

CLAS-ANALYSIS 2002-109
ripani@jlab.org

Measurement of Two Pion Decay of Electroproduced Light Quark Baryon States with CLAS

M. Ripani^a, V. Burkert^b, V. Mokeev^c

^aIstituto Nazionale di Fisica Nucleare,
Via Dodecanneso 33, I-16146 Genova (Italy)

^bThomas Jefferson National Accelerator Facility,
12000 Jefferson Avenue, Newport News, Virginia, 23606

^cNuclear Physics Institute of Moscow State University,
119899, Vorob'evy Gory, Moscow, Russia

December 11, 2002

Contents

| | |
|--|----------|
| I Motivations and Procedures for the Raw Data Analysis | 4 |
| 1 Physics Motivations, Theoretical and Experimental Aspects | 6 |
| 1.1 Physics Issues | 6 |
| 1.2 Phenomenology | 6 |
| 1.3 Physics and Kinematics | 7 |
| 2 E1C (1999) analysis | 8 |
| 2.1 Detector and Reconstruction features | 8 |
| 2.1.1 Electron Identification: Calorimeter | 8 |
| 2.1.2 Electron Identification: Cherenkov | 10 |
| 2.1.3 Effect of calorimeter cut | 12 |
| 2.1.4 Hadron Identification | 12 |
| 2.1.5 Quality Checks | 19 |
| 2.2 Evaluation of CLAS Acceptance and Efficiency | 19 |
| 2.2.1 General issues in the cross section calculation | 19 |
| 2.2.2 The Monte Carlo event generator | 23 |
| 2.2.3 Geometrical and Kinematic Acceptance: Fiducial Cuts | 24 |
| 2.2.4 Detection and reconstruction efficiency | 30 |
| 2.2.5 Radiative Corrections | 35 |
| 2.2.6 Comparison between data and Monte Carlo | 36 |
| 2.3 Check of Missing Mass Dependence on Hadronic Variables | 42 |
| 2.4 Momentum Corrections | 42 |
| 2.5 Multipion backgrounds | 57 |
| 2.6 Cuts summary | 57 |
| 2.7 Cross Sections | 57 |
| 2.8 Systematic errors | 62 |
| 2.8.1 Dependence on Monte Carlo Assumptions | 62 |
| 2.8.2 Dependence on Monte Carlo Throwing Region | 62 |
| 2.8.3 Integration | 66 |
| 2.8.4 Fiducial Cuts | 66 |
| 2.8.5 Kinematic Coverage | 66 |

| | | |
|-----------|--|------------|
| 2.8.6 | Radiative Corrections | 67 |
| 2.8.7 | Global Sector Uniformity Correction | 67 |
| 2.8.8 | Photoelectron Cut | 67 |
| 2.8.9 | Missing Mass Cuts | 67 |
| 2.8.10 | Summary of Systematics | 68 |
| 3 | Concluding Remarks | 69 |
| II | Resonance Analysis | 70 |
| 4 | Generalities | 72 |
| 4.1 | Introduction | 72 |
| 4.2 | Kinematics and observables | 72 |
| 4.3 | Model calculations | 73 |
| 5 | The Analysis of E-93-006 data | 75 |
| 5.0.1 | Genova-Moscow Model Description | 75 |
| 5.0.2 | Technical Details on the Two Pion Code | 76 |
| 5.0.3 | Fixing Model Free Parameters | 78 |
| 5.0.4 | Nominal Model Calculation | 80 |
| 5.0.5 | Basic Features of Fitting Procedure | 100 |
| 5.0.6 | Resonance Analysis: Conventional States | 105 |
| 5.0.7 | Resonance Analysis: Missing States Search Strategy and Detailed Analysis | 122 |
| 5.0.8 | Resonance Analysis: Missing States Further Search | 135 |
| 5.1 | Evaluation of uncertainties for extracted form factors $A_{1/2}$, $A_{3/2}$ | 146 |
| 5.2 | Quasi-two-body channel and resonant/background separation | 160 |
| 5.2.1 | Resonance Analysis: Further Work After Discussion within SoN Review Committee and Final Fits to be Reported in the Paper . . . | 173 |
| 6 | Conclusions | 187 |

Part I

Motivations and Procedures for the Raw Data Analysis

Chapter 1

Physics Motivations, Theoretical and Experimental Aspects

1.1 Physics Issues

The excitation of baryon resonances is genuinely a non-perturbative phenomenon. Measurements of the transition amplitudes from the nucleon to its excited states are sensitive to the spatial and spin structure of the transition. Many of the nucleon excited states in the mass region around and above 1.7 GeV tend to decouple from the single-pion and eta channels, while πN scattering experiments have shown that many of them decay predominantly in multipion channels, such as $\Delta\pi$ or $N\rho$, leading to $N\pi\pi$ final states[1]. A measurement of the transition form factors of these states is very important for testing symmetry properties of the quark model. Moreover, SU(6) symmetric quark models[2, 3] predict more states than have been found in experiments. QCD mixing effects could decouple many of these states from the pion-nucleon channel[2], with consequent lack of evidence in elastic πN scattering, while strongly coupling them to two-pion channels such as $\Delta\pi$ [2, 4, 5, 6]. However, other models such as the Quark Cluster Model[7] predict a fewer number of states than the symmetric model, more in accordance with experimental observation. Search for the states still missing from the experimental evidence is therefore crucial in understanding the basic degrees of freedom in baryon structure.

1.2 Phenomenology

Main contributions to the double pion production are isobar channels like $\Delta(1236)\pi$ and ρN [8]: $eN \rightarrow e'\Delta\pi \rightarrow e'N'\pi\pi$, $eN \rightarrow e'\rho N \rightarrow e'N'\pi\pi$. All isobar production channels can proceed through continuum processes, or through the excitation of baryon resonances with a cascade like $eN \rightarrow e'N^* \rightarrow e'\Delta\pi \rightarrow e'N'\pi\pi$. The double pion production data come mainly from bubble chamber experiments with real photons[8, 9], where data about

various charge channels were collected. Another experiment at DESY[10] measured the electroproduction of $p\pi^+\pi^-$ off the proton with very poor statistics and large binning. Recent photoproduction measurements up to slightly above the $D_{13}(1520)$ have been performed at Mainz[11, 12], using the DAPHNE large angle detector, while data in a wider energy range have been collected in Bonn using the SAPHIR[12, 13] detector.

1.3 Physics and Kinematics

The main feature evident from all the two pion production data collected in the past experiments[8, 10, 11, 12] is the presence of the isobar "quasi-two-body" states $\Delta\pi$ and ρN . A typical approach for separating such different isobar contributions is to simply fit their bumps in the invariant masses, obtaining approximate cross sections. This was the data analysis adopted in most of the past experiments with electromagnetic probes[8, 10], being interested essentially in the gross features and being the data affected by high statistical uncertainty. However, the correct description of a three-body collision is based on five independent kinematical variables in the most general case[14] and moreover the isobar quasi-two-body production and subsequent decay involves all of them[15]. Moreover, as discussed in chapter 2, the cross section calculation from the data requires to possibly correct for detector acceptance in each bins in the hadronic variables; therefore it is necessary to choose a complete set of independent kinematic variables, in order to apply the appropriate detector corrections to the data and immediately access the underlying physics. Among different possible sets of variables, we chose to use the following ones, which are quite convenient for a physical interpretation of the data: we introduced three sets of variables, defined in the CM frame, each one composed by two invariant masses and three angles; the first set contains the invariant mass of the $p\pi^+$ pair and the invariant mass of the $\pi^+\pi^-$ pair, then the polar angles θ and ϕ of the proton and finally the rotation freedom ψ of the pion pair with respect to the so-called hadronic plane defined by the incoming virtual photon, incoming proton and the outgoing proton; the second set contains the invariant mass of the $p\pi^+$ pair and the invariant mass of the $\pi^+\pi^-$ pair, then the polar angles θ and ϕ of the π^- and finally the rotation freedom ψ of the $p\pi^+$ pair with respect to the so-called hadronic plane defined by the incoming virtual photon, incoming proton and the outgoing π^- ; the third set contains the invariant mass of the $p\pi^-$ pair and the invariant mass of the $\pi^+\pi^-$ pair, then the polar angles θ and ϕ of the π^+ and finally the rotation freedom ψ of the $p\pi^-$ pair with respect to the so-called hadronic plane defined by the incoming virtual photon, incoming proton and the outgoing π^+ . The first set of variables is more appropriate for the analysis of the resonance decay into $\Delta^{++}\pi^-$, while the second set is more appropriate for the analysis of the resonance decay into $\rho^0 p$; the third set is used just for completeness and to help understanding the systematic errors (see corresponding section).

Chapter 2

E1C (1999) analysis

2.1 Detector and Reconstruction features

We started to analyse data taken in the so-called 'e1c' running period, corresponding to spring 1999. Energy selected was first 2.567 GeV at a field of 1500 A ('low' field), with the goal of obtaining the first data at a Q^2 between 0.5 and 0.8 GeV^2/c^2 and W up to 1.9 GeV, to be compared with the previous DESY experiment. Then we analysed Q^2 between 0.8 and 1.1 GeV^2/c^2 from the same data set and finally Q^2 between 1.1 and 1.5 using data at 4.247 GeV at a field of 2250 A ('low' field). We used cooked files obtained from the PROD-1-9 version of the code and reduced to HBOOK ntuples as "quasi-DST" format with smaller size, containing the basic information.

We discuss in this first section various aspects of the event reconstruction and identification in the CLAS detector, as well as the data selection we performed to arrive to cross sections.

2.1.1 Electron Identification: Calorimeter

The hardware trigger in CLAS was based on a coincidence between Cherenkov counter and electromagnetic forward calorimeter. Discriminator threshold in the Cherenkov was put at a signal level of less than a single photoelectron produced on the photocathode, to avoid losing good events and to perform some rejection of pion background. Threshold in the calorimeter was set such to cut off events as close as possible to the kinematic edges of the W and Q^2 domain covered by the measurement, but far enough to keep the low energy contamination within reasonable limits.

So first of all it was necessary to study the calorimeter response to identified "electrons" and develop appropriate cuts to partly eliminate pion contamination. In figure 2.1 we show, for particles identified as electrons by the reconstruction program, the plot of the outer energy released in the calorimeter (normalised to the momentum) versus the inner energy (also normalised to the momentum); the cut used to reject the (mostly minimum

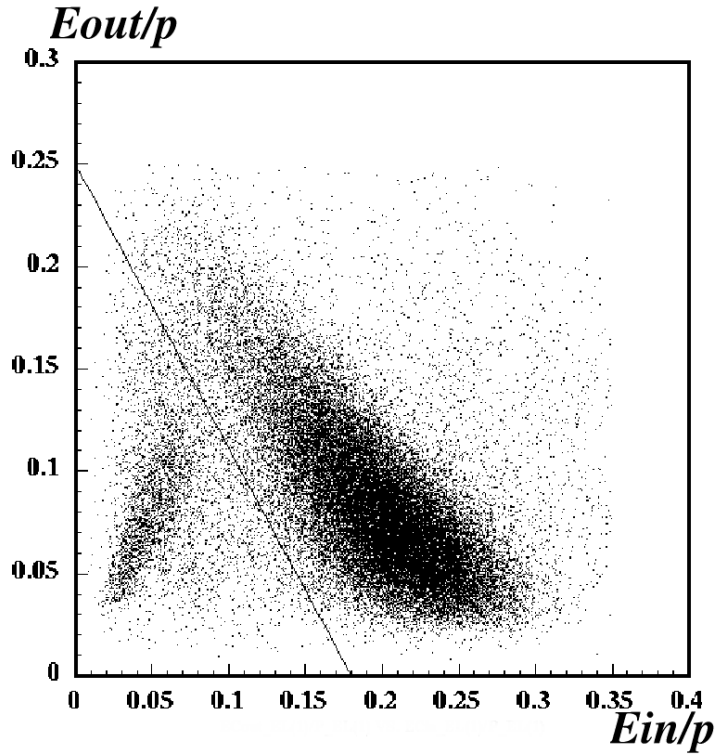


Figure 2.1: Forward calorimeter outer energy versus inner energy deposition, both normalised to the particle's momentum; the cut to reject most of the pions in the lower left spot is shown.

ionizing) pions is also shown and it is given by the formula

$$\frac{EC_{out}}{P} > 0.28 - 1.65 * \frac{EC_{in}}{P} \quad (2.1)$$

for the 2.567 GeV data and by

$$\frac{EC_{out}}{P} > 0.31 - 1.8 * \frac{EC_{in}}{P} \quad (2.2)$$

for the 4.247 GeV data. One may expect that this calorimeter cut, besides removing most unwanted pions, may have some effect on the electron detection efficiency: this was studied by means of the Cherenkov photoelectron distribution, as reported in section 2.1.3. Threshold effects from the calorimeter were controlled applying Kim Egiyan's function[16] as a fiducial cut on the outgoing electron energy.

2.1.2 Electron Identification: Cherenkov

Considering its primary role in the trigger, it was obviously very important to study the photoelectron response in the Cherenkov and eliminate any pion contamination left in the data. In figure 2.2 we report (six plots above) the distributions of the photoelectron yield in the Cherenkov counter for each CLAS sector, inside the fiducial regions (see subsection 2.2.3 about fiducial cuts), for Q^2 between 0.5 and 0.8 GeV^2 , which was the first interval we wanted to investigate and for W between 1.8 and 1.9 GeV (the scale of the photoelectron number is multiplied by 10, therefore 10 means actually 1 photoelectron). It is quite clear from the pictures that at higher W an increase in the low photoelectron part of the distribution takes place: subsequent studies on the kinematics proved that such pronounced low photoelectron yield is due to pion contamination which survives the calorimeter cut.

Therefore, a cut was applied requiring the photoelectron number to be more than 2.5, then the remaining distribution was fitted with a curve of the type

$$y = A \left(\frac{L^{\frac{x}{P}}}{\Gamma \left(\frac{x}{P} + 1 \right)} \right) e^{-L} \quad (2.3)$$

which represents a Poisson distribution where the sigma is no more constrained to the mean value and A , P , L are the free parameters; such a curve gives a pretty good fit which is shown by the thick blue curve in picture 2.2; then, the curve was extrapolated to zero (thin blue curve) to recover the amount of events cut off below 2.5 photoelectrons; this way we derived a correction factor for each sector which represents a particular contribution to the electron detection efficiency. Assuming that this correction can recover the electron inefficiency due to the shape of the photoelectron distribution and the photoelectron cut, we then plotted the amount of inclusive electron events in each sector (plot labeled ph_EL EXP in figure 2.2): certainly this distribution has not to be uniform because of the difference among fiducial cuts (see corresponding section) in different sectors; we therefore simulated the effect of the fiducial cuts on the electron yield sector by sector (plot labeled ph_EL SIM in figure 2.2), as well as the effect of the target shift with respect to the nominal position; then we normalised the experimental electron yield sector by sector to the simulated one (plot labeled ph_EL EXP/SIM in figure 2.2): this way we eliminated the non-uniformity due to fiducial cuts and one would expect that the sector distribution from the normalised data should be uniform in the six sectors: instead, as shown in the plot "ph_EL EXP/SIM", some non-uniformity is still present, typically of the order of 10%: part of this is certainly of statistical origin, but part may be an actual difference between the sectors, indicating that either our extrapolation method does not recover completely the events rejected by the photoelectron cut, or that there is some other source of loss in the reconstruction, not visible through the photoelectron distribution.

To further investigate this aspect, we plotted the scintillator number versus the CM energy W for the three Q^2 bins used in the analysis and for all six sectors separately, to

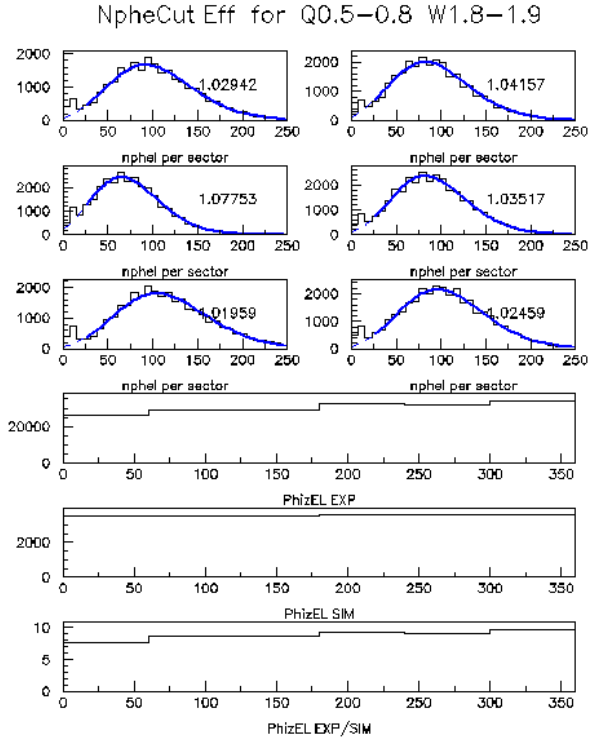


Figure 2.2: Cherenkov photoelectron distributions in the six sectors at the kinematics indicated on top of figure (six plots at the top); the fit of the distributions is reported; the first plot of the three plots at the bottom ($\phi_{\text{EL}} \text{ EXP}$) shows the electron yield sector by sector (inside fiducial cuts) after correcting for the photoelectron cut through the above fits; the second plot at the bottom shows the simulated electron yield sector by sector (inside fiducial cuts); the last plot shows the experimental electron yield sector by sector, renormalised to the simulated yield to eliminate the effect of fiducial cuts: still a small global non-uniformity is present.

check for specific problems. In figure 2.3 through 2.5 the black points show all electrons detected in the various ToF paddles, while the red points show those inside fiducial cuts. From these plots, no evidence is present of additional anomalous behaviour besides what fiducial cuts take care of. We therefore decided to apply a global factor to correct for the final non-uniformity in the sector distribution, renormalising the yield sector by sector to the maximum.

2.1.3 Effect of calorimeter cut

In order to study the effect of the above mentioned calorimeter cut on the electron detection efficiency, we assumed that all signals in the Cherenkov corresponding to more than 5 photoelectrons have to be associated with electrons. Then we applied our calorimeter cut and measured the depletion in the number of events above 5 photoelectrons. This depletion turned out to be not more than 5 %. In picture 2.6 we report the photoelectron distribution for the six sectors, before and after applying the calorimeter cut. The derived correction was fitted by a second order polynomial: an example is reported in fig. 2.7

2.1.4 Hadron Identification

For the particle identification (PID), we started from the reconstruction contained in the EVNT bank, which is produced by the SEB (Simple Event Builder) package, routinely called by the reconstruction program A1C. The SEB routines automatically apply the PID procedure based on the Time-Of-Flight (TOF) calculation, plus a correction related to the actual time reference given by the radiofrequency of the machine (RF correction). It turned out that the RF correction is sometimes ambiguous, due to tails in the time distribution of the signal from one bunch: it therefore produces some side “jets” in the velocity distributions. Picture 2.8 namely shows the plot of the particle velocity β , given by the TOF measurement, versus the particle momentum measured by the track in the drift chambers; in the left bottom plot (“OUR”), β is recalculated without using the radiofrequency, while the right bottom plot reports the quantities derived from the SEB output (EVNT bank): it is clearly seen that the side tails or double bands appearing in the right plot are eliminated in the left plot; the price to pay for that is a slight worsening of the time (β) resolution, which is however not quite important at least for medium energies. The two plots at the top show the particle mass distributions obtained in the two cases by calculating the mass through the well known formula

$$m = \frac{p\sqrt{1 - \beta^2}}{\beta} \quad (2.4)$$

In figure 2.9 we report the cuts used to select pions and protons in the β versus momentum plot: we devoted particular care to developing the upper cut for pions, as this has the important effect of eliminating the low momentum electron-positron component,

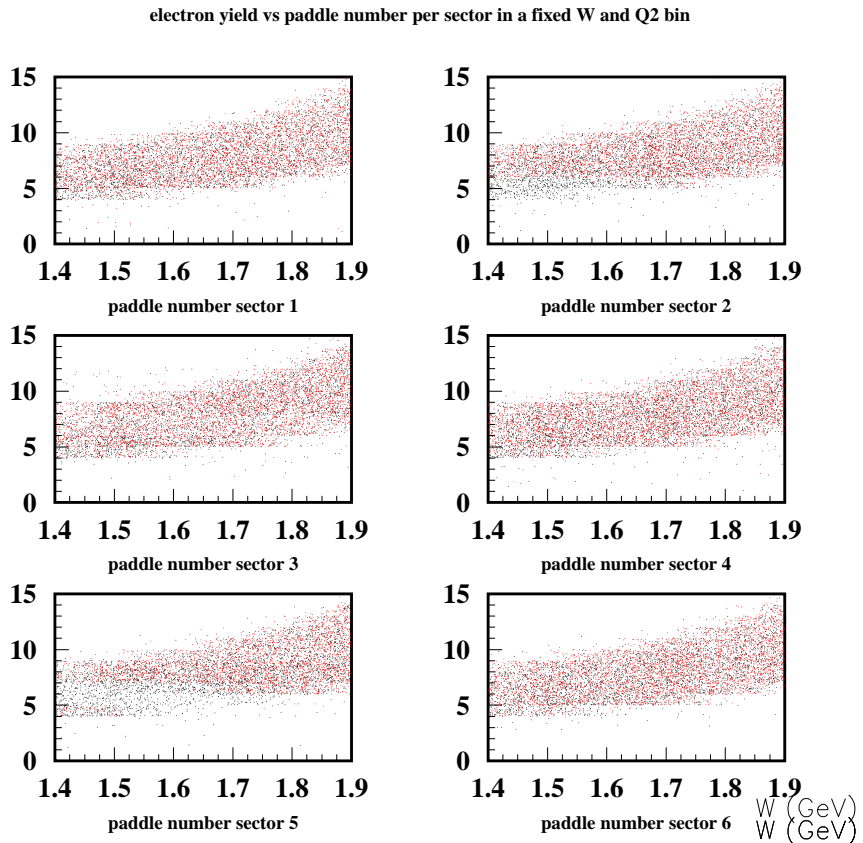


Figure 2.3: Electron yield plotted against W (X) and ToF paddle number (Y), for all six sectors of CLAS; beam energy 2.567 GeV, torus current 1500 A, Q^2 between 0.5 and 0.8 GeV^2/c^2 . Black points are without, red points are with electron fiducial cuts applied.

electron yield vs paddle number per sector in a fixed W and Q2 bin

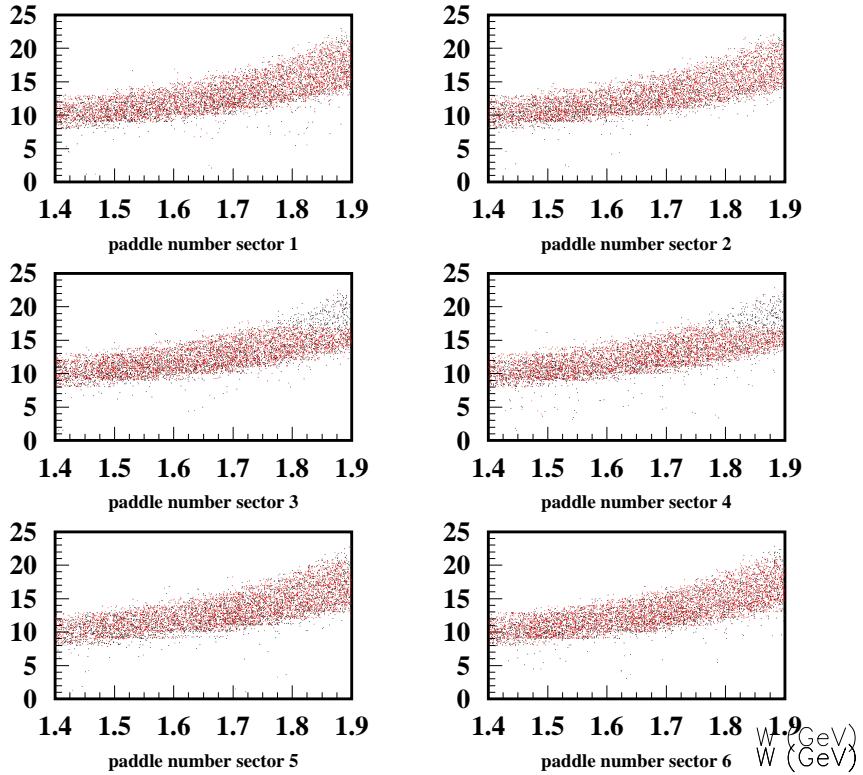


Figure 2.4: Electron yield plotted against W (X) and ToF paddle number (Y), for all six sectors of CLAS; beam energy 2.567 GeV, torus current 1500 A, Q^2 between 0.8 and 1.1 GeV^2/c^2 . Black points are without, red points are with electron fiducial cuts applied.

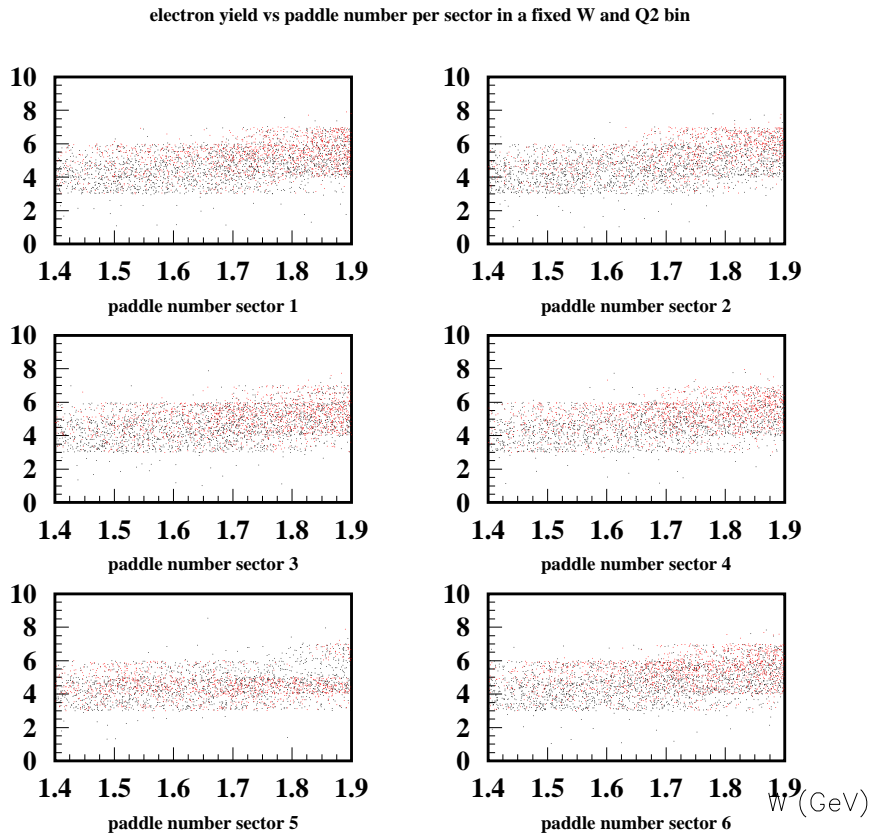


Figure 2.5: Electron yield plotted against W (X) and ToF paddle number (Y), for all six sectors of CLAS; beam energy 4.247 GeV, torus current 2250 A, Q^2 between 1.1 and 1.5 GeV^2/c^2 . Black points are without, red points are with electron fiducial cuts applied.

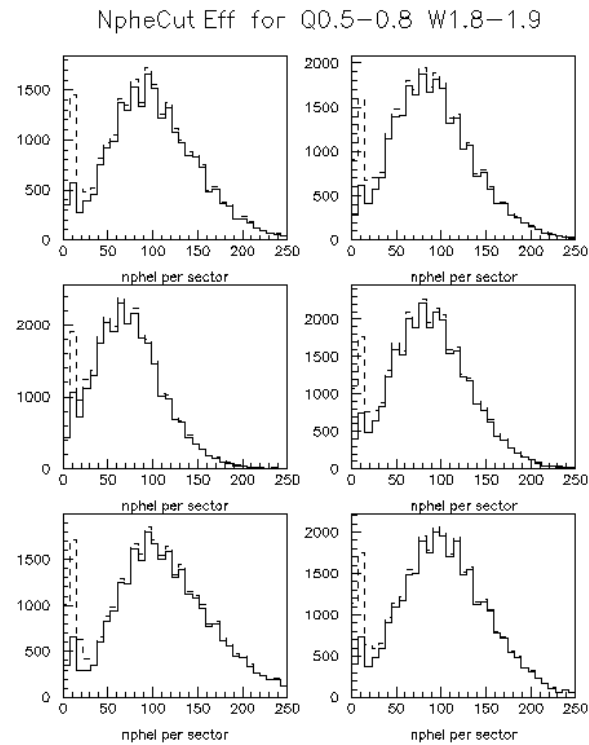


Figure 2.6: Photoelectron distribution for the six sectors, before (dashed) and after (full) applying the calorimeter cut; kinematics indicated above the picture.

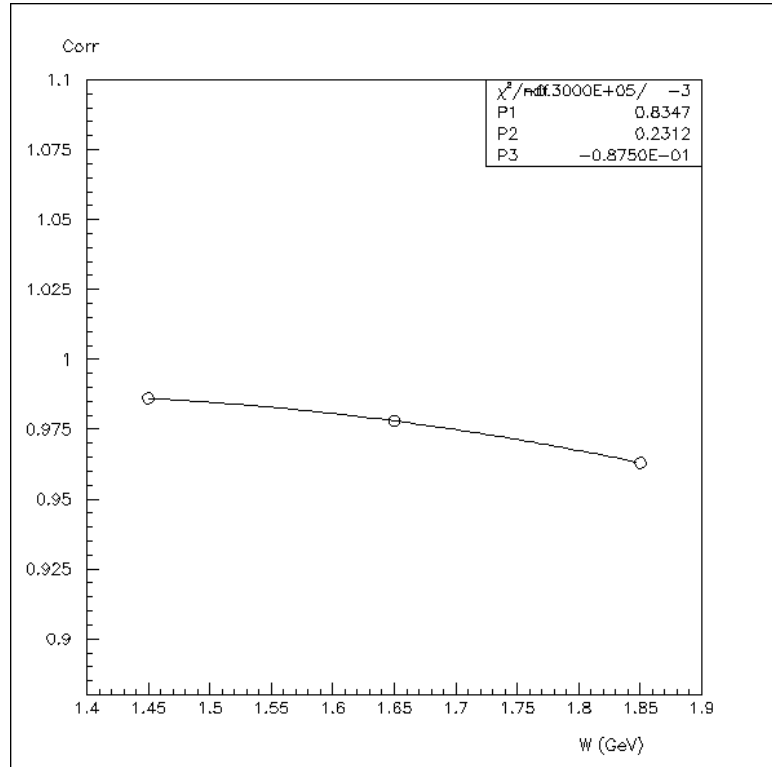


Figure 2.7: Electron efficiency correction due to the calorimeter cut at 2.567 beam energy, 1500 A field and Q^2 between 0.5 and 0.8 GeV^2 . The fit is a parabola and the coefficients found are reported in the legend.

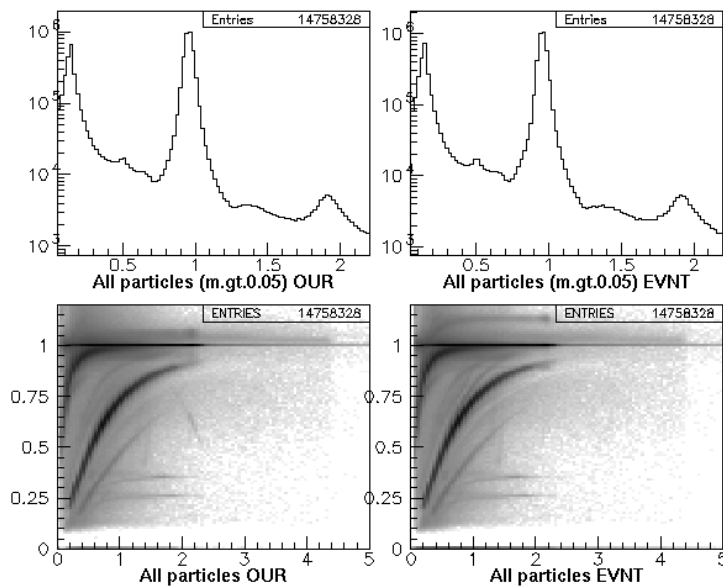


Figure 2.8: Particle velocity β , given by the TOF measurement, versus the particle momentum measured by the track in the drift chambers; in the left bottom plot (“OUR”), β is recalculated without using the radiofrequency, while the right bottom plot reports the quantities derived from the SEB output (EVNT bank). The two plots at the top show the particle mass distributions.

visible in the picture as a spot at low momentum and β around unity, which may pollute the identified pions. However, as shown in figure 2.10, the backward scintillator paddles, those corresponding to the CLAS numbering from 40 to 51, have a problem in determining the time for pions; therefore in this case for the pion selection we used a looser cut to avoid losing events; the cut is also shown in figure 2.10 and it is clear that the looser selection cut in our PID keeps all pion candidates.

2.1.5 Quality Checks

For the analysis, only “golden runs” according to the definition of the E1C chef (S. Barrow) were considered. Nevertheless we performed our own quality checks on all files. In order to check the stability of CLAS in the detection of different reactions, we defined a set of histograms representing various reaction yields, i.e. electron inclusive, electron-proton inclusive, electron elastic (W cut), electron-proton elastic (W plus θ - ϕ correlation cut), electron-proton from the Δ (W cut) and finally electron-proton- π^+ with a cut on the missing π^- , each single yield being normalised to the Faraday cup charge obtained from the so called “live-gated” signal, where the signal from the Faraday cup is only integrated during the live-time: this way, the charge is already corrected for the data acquisition dead-time. Such normalised yields were calculated, using the PID procedures described in the previous subsection, for each cooked file inside a run, therefore providing a very accurate monitoring of stability even inside a single run. “Good files” were selected requiring that the normalised yield for a single file should not deviate more than a few percent from the average. Subsequent analysis was performed only on the good files.

We report in figure 2.11 only a sample of files from the 2.567 GeV and 1500 A running period, plotting only the normalised inclusive electron yield and the normalized inclusive two pion yield.

2.2 Evaluation of CLAS Acceptance and Efficiency

2.2.1 General issues in the cross section calculation

To obtain a reliable cross section from the detector raw data, it is necessary to correct for distortion effects due to detector non-uniformity, which has origin both in the geometry and in the response of the equipment to particles (see following subsections). The geometrical and kinematic non-uniformity can be very well described by means of fiducial cuts that describe regions of the detector where the response of the various subsystems is well known; of course, fiducial cuts will eliminate dead regions like the torus coils in the first place. Then, the detector response inside the fiducial regions can be simulated using a code containing a detailed description of particle interactions with the various subsystems (see following subsections). Non-uniformities in the detector response (both of geometrical and hardware nature) will be in general different for different configurations of the

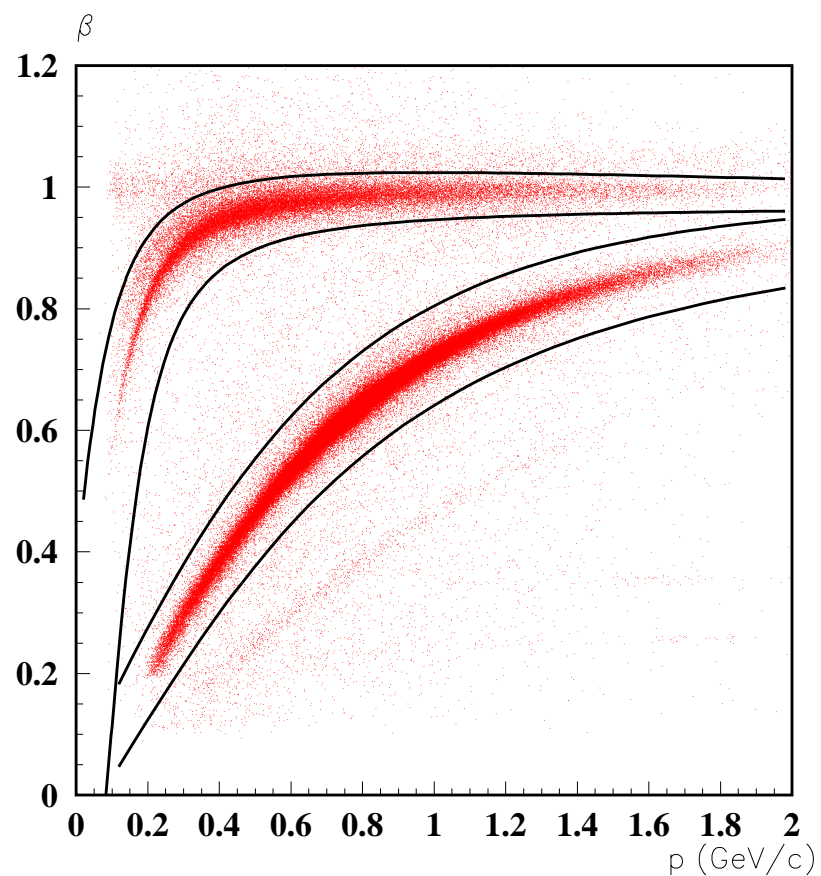


Figure 2.9: β versus momentum plot for hadrons; lines show the cuts used to identify pions and protons for small to medium angle scintillators.

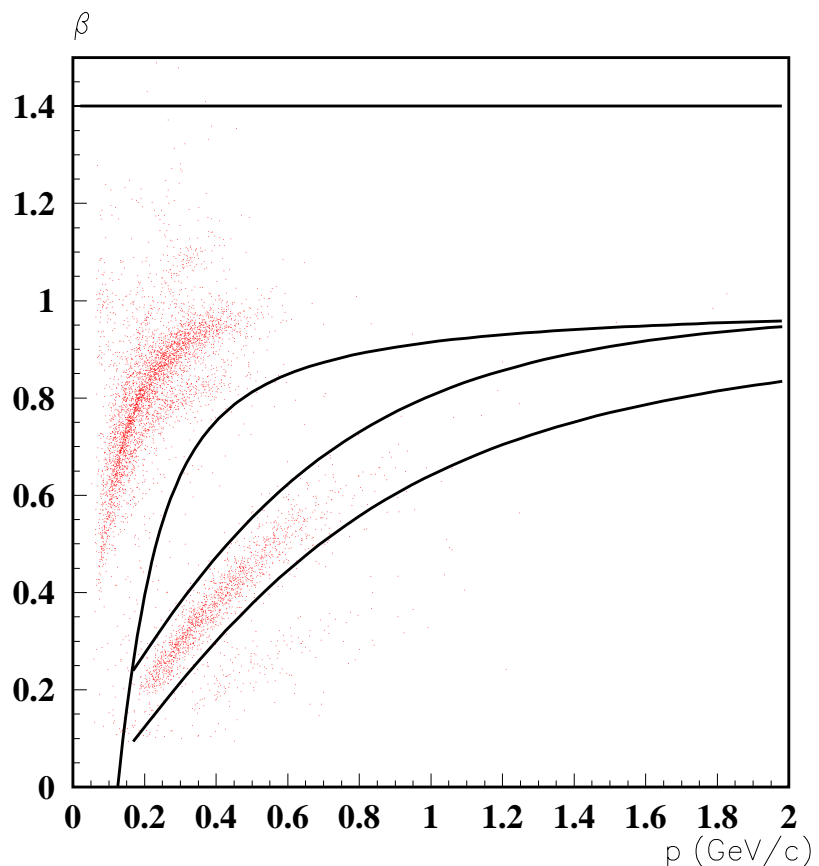


Figure 2.10: β versus momentum plot for hadrons; lines show the cuts used to identify pions and protons for large angle scintillators.

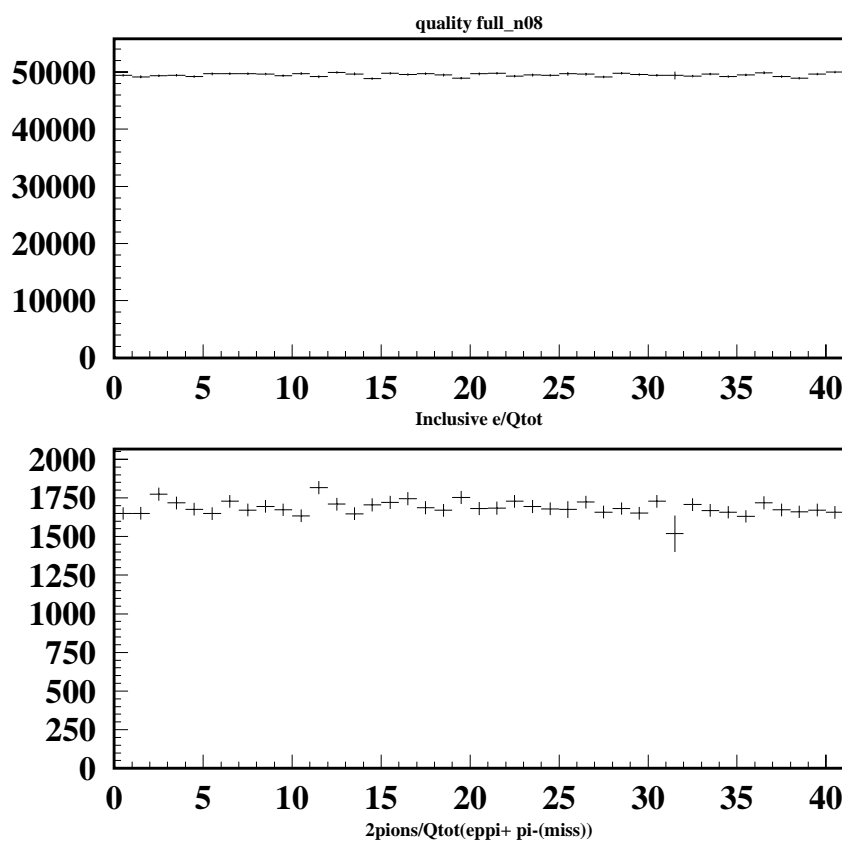


Figure 2.11: Stability of runs.

detected final state, like multiplicities, momenta, etc; therefore, if we fold the detector corrections for a particular reaction with the differential cross section for that reaction, the resulting average correction will be normally quite strongly dependent on the cross section assumed; on the other hand, using a Monte Carlo code to generate events and evaluate the detector acceptance and response, one is making assumptions on the differential cross sections; certainly one can use cross sections which are “realistic” and possibly based on available measurements, but in any case, using only average corrections can lead to bigger systematic errors and, ultimately, to a “model-dependent” cross section.

From the above discussion, it is clear that the correct procedure to evaluate detector corrections and derive cross sections is to divide the particle yield in kinematic bins, using a complete set of independent kinematic variables, in other words a set such that fixing all values inside it completely fixes all four-momenta of the particles involved. This way, choosing kinematic bins for these set of variables will correspond to determining narrow regions of the detector where the particles are travelling through, thereby limiting the extent of non-uniformity present in each bin; with such procedure the folding over detector geometry and response is done only inside a bin, where both cross sections and detector features will have a smoother variation: the dependence of the results on the assumed particle distributions will therefore be much reduced and will most likely be quite small. However, events still have to be generated according to a realistic Monte Carlo, in order to minimize systematic errors even more. The code we adopted for this analysis is briefly described in the following paragraph.

When dealing with unpolarised electron scattering as in the present case, it easily seen that the cross section cannot depend on the electron azimuthal angle ϕ_{el} ; therefore, one can safely integrate events over this angle, deriving a detector correction which will be averaged over ϕ_{el} , without introducing any model dependence.

2.2.2 The Monte Carlo event generator

The event generator used for simulations in this experiment contains several electroproduction cross sections, including single, double and triple pion electroproduction. The code relies on cross section tables that describe measured total and differential cross sections from the literature, scaled by a virtual photon flux and a dipole form factor to provide a reasonable fall off with Q^2 . Therefore our code gives a realistic description of cross sections and their relative weights, as well as backgrounds generated from competitive channels. Radiative effects were introduced in the code, either, as described in section 2.2.5. Being based on cross section tables, the code is still executed at acceptable speed, even when radiative effects are included. Typically, about 200,000 two pion events per hour are generated in the full phase space on a Pentium III processor at 750 MHz clock speed.

2.2.3 Geometrical and Kinematic Acceptance: Fiducial Cuts

The CLAS detector has an active detection solid angle obviously smaller than 2π , being part of the space filled with the torus field coils: the angles covered by the coils are not equipped with any detection system and therefore form a “dead” area for detection. Moreover, different studies and analyses have shown that also the edges of the active area do not provide a safe region for particle reconstruction, being affected by rescattering from the coils, field distortions and similar effects. Therefore it is now common practice to *accept* for the analysis only events inside specific *fiducial cuts*, i.e. cuts on the kinematic variables (momentum and angles) of each particle, such to guarantee that the reconstructed events accepted in the analysis include only particles detected in “safe” areas of the detector, that is where the acceptance is thought to be well understood. These cuts produce a reduction factor in the number of events accepted in each kinematic bin that we will call *detector acceptance*.

We performed a specific inspection of the data to see whether modifications to the fiducial cuts developed for the E1B (1998) data were necessary; for electrons we started from the fiducial cuts developed by V. Burkert; for positive hadrons, we started from the fiducial cuts developed by the UVa and Pittsburgh groups: these new hadron fiducial cuts, which we will call ”skewed” for simplicity, are non-symmetric with respect to the sector mid-plane, to account for the non-symmetric distribution of positive hadrons actually seen in the data. Our fiducial cuts did not contain parts referring to dead or malfunctioning ToF scintillators: their rejection was performed both in the data and in the Monte Carlo using an explicit list containing the bad paddle numbers.

A particular care is required by the Cherenkov detector, that provides the primary information for electron discrimination, as it was found that some areas of the Cherenkov counters are affected by inefficiencies: the above mentioned fiducial cuts for the electron detection eliminate the main areas of inefficiency. For the Cherenkov counter, we maintained the general shape of the cuts; modifications were instead applied to the strip cuts whose purpose is to remove particular bad regions (corresponding to a dead photomultiplier or a low efficiency region connected to some other hardware problem): we removed a strip cut in sectors 2, 3 and 4, which looked to be no more necessary in E1C, while we applied a new strip cut in sector 3, where a slight depletion in the electron yield had been noticed; we report in figure 2.12 the new electron fiducial cuts for all CLAS sectors in the ϕ versus θ angle plane for a particular momentum interval. The analytical shape of

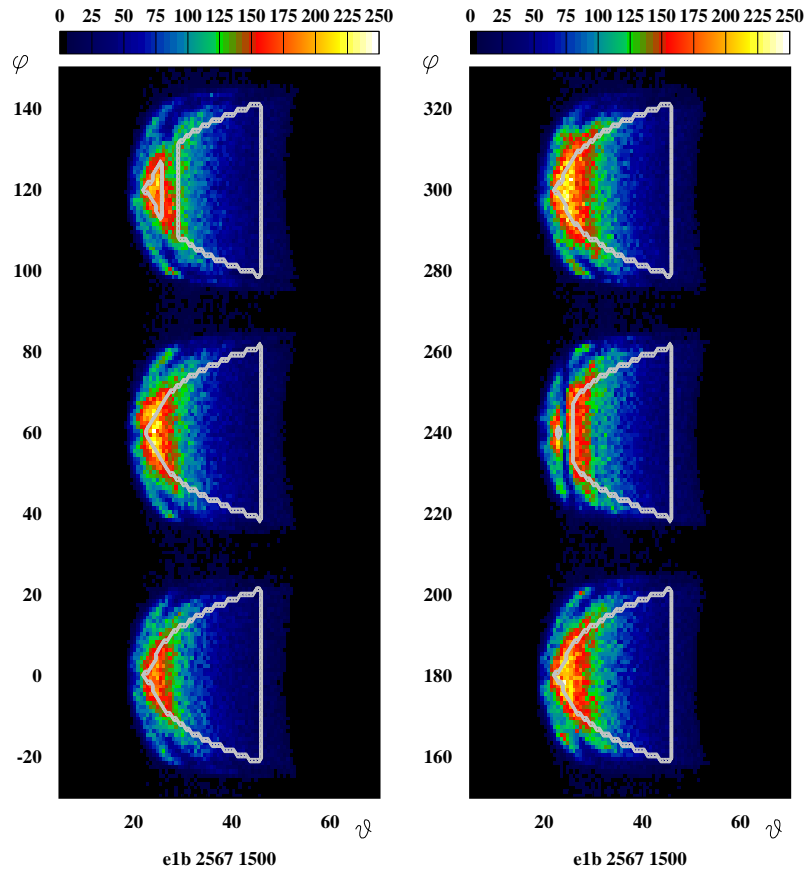


Figure 2.12: Plot of angles ϕ versus θ for electrons detected in the 6 CLAS sectors at 2.567 GeV beam energy and 1500 A field, with momentum between 0.7 and 1 GeV/c; the curve showing the fiducial cuts (calculated at the same average momentum) is also superimposed on the plots. The label says e1b, but the picture actually refers to 1999 data.

the electron fiducial cuts is given by the following formulas:

$$\delta\phi_e = 30 \sin((\theta - \theta_{min})d2r)^{0.35(p(\frac{I_{max}}{I}+0.15))}$$

$$\begin{aligned}\theta_{min} &= \theta_1 + \frac{\theta_2}{p(I_{max}/I)+0.15} \\ \theta_{max} &= 50.0^\circ\end{aligned}$$

$$d2r = 0.01745$$

$$\theta_1 = 15.5^\circ$$

$$\theta_2 = 15.0^\circ$$

$$I_{max} = 3375$$

where $\delta\phi_e$ represents the portion of the polar angle ϕ_e accepted by the fiducial cut, or in other words if $\theta_{min} < \theta < \theta_{max}$ and $|\phi| < \delta\phi$ then the electron is accepted.

For positive hadrons, as mentioned above we did not use strip cuts related to bad scintillators, replacing them with an explicit cut on the paddle number in the analysis program. We then checked the situation with the proton and π^+ event population inside the previous fiducial cut shape; we found that some slight modifications with respect to the UVa-UPitt version were necessary and hence we developed a new version of the cuts for positive hadrons; as an example, we show in figure 2.13 the new positive hadron fiducial cuts for all CLAS sectors in the ϕ versus θ plane, together with proton data integrated over momentum. In figure 2.14 the new positive hadron fiducial cuts for all CLAS sectors in the ϕ versus θ plane (data integrated over momentum) are again reported, this time together with positive pion data (integrated over momentum). The analytical shape of the positive hadron fiducial cuts is given by the following formulas:

$$\begin{aligned}\delta\phi_p^+ &= A^+(s)(1 - e^{-B^+(s)(\theta-C^+(s))}) \\ \delta\phi_p^- &= A^-(s)(1 - e^{-B^-(s)(\theta-C^-(s))})\end{aligned}$$

$$\theta_{min} = 10^\circ$$

If $\delta\phi^- < \phi < \delta\phi^+$ and $\theta > \theta_{min}$ then the positive hadron is accepted. In tables 2.1 and 2.2, the parameters used at the two different beam energies and fields are reported.

To give a precise definition of acceptance, suppose that A is the number of MC theoretically generated $ep\pi^+\pi^-$ events; then suppose that B is the number of such MC events for which $ep\pi^+$ fall inside the fiducial cuts (we don't care about the π^-); then our definition of geometrical and kinematic acceptance is just the ratio $\frac{B}{A}$. The geometric and kinematic acceptance of CLAS corresponding to the fiducial cuts were evaluated in each kinematic bin using the Genova event generator. The effect of radiation is discussed in section 2.2.5.

A particularly important issue regards the percentage of events lost in the binning process due to bins with zero acceptance: of course, for such bins it is not possible to correct the data and obtain a cross section; being the kinematic variable space multidimensional in the case of double pion production, extrapolating the cross sections from neighboring

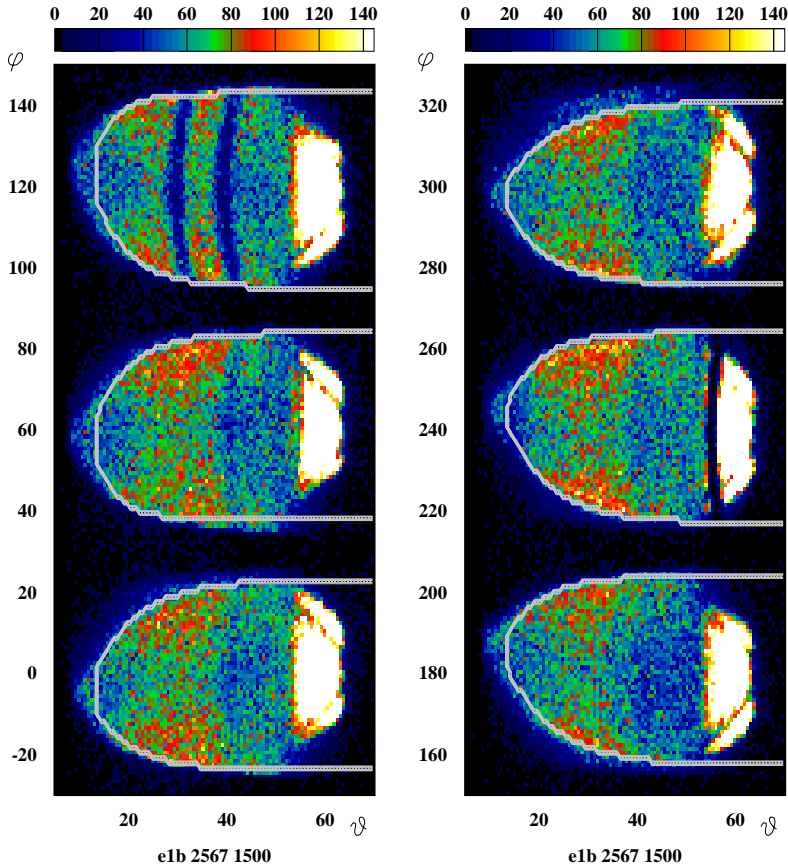


Figure 2.13: Plot of angles ϕ versus θ for protons detected in the 6 CLAS sectors at 2.567 GeV beam energy and 1500 A field, with momentum between 0.7 and 1 GeV/c; the curve showing the fiducial cuts is also superimposed on the plots. The label says e1b, but the picture actually refers to 1999 data.

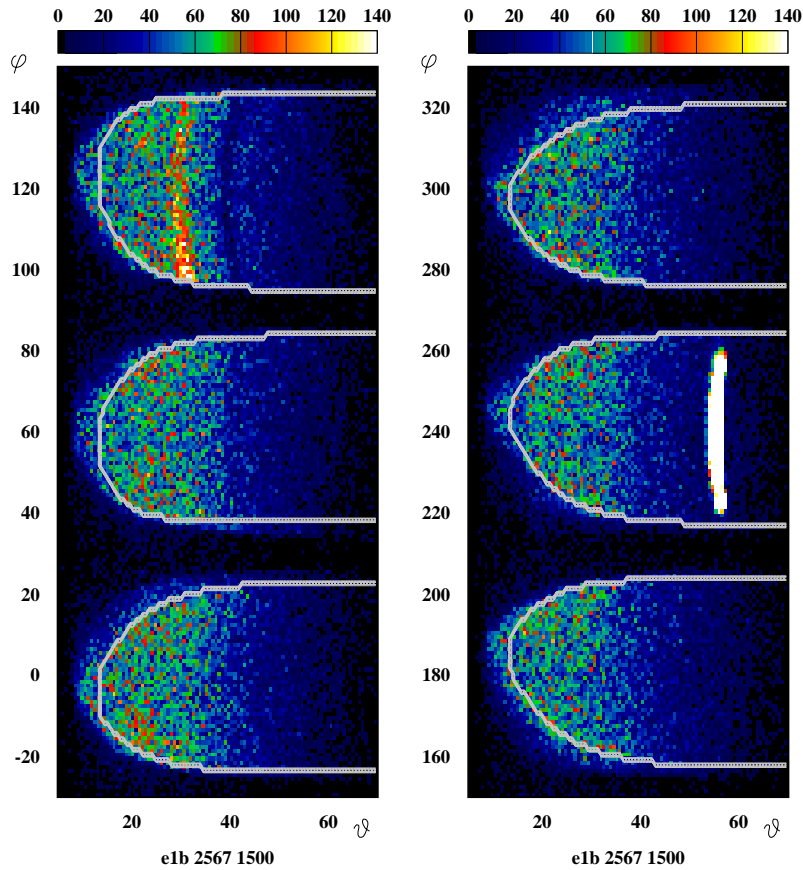


Figure 2.14: Plot of angles ϕ versus θ for positive pions detected in the 6 CLAS sectors at 2.567 GeV beam energy and 1500 A field, with momentum between 0.7 and 1 GeV/c; the curve showing the fiducial cuts is also superimposed on the plots. The label says e1b, but the picture actually refers to 1999 data.

Table 2.1: Parameters in the fiducial cut analytic form for 2.567 GeV beam energy and 1500 A field

| Parameter | Sector 1 | Sector 2 | Sector 3 | Sector 4 | Sector 5 | Sector 6 |
|-----------|----------|----------|----------|----------|----------|----------|
| A^+ | 23 | 24 | 23 | 24 | 24 | 21 |
| B^+ | 0.09 | 0.11 | 0.17 | 0.11 | 0.12 | 0.08 |
| C^+ | 10 | 9 | 7 | 6 | 8 | 10 |
| A^- | 24 | 22 | 25 | 23 | 23 | 24 |
| B^- | 0.10 | 0.18 | 0.11 | 0.08 | 0.09 | 0.1 |
| C^- | 5 | 8 | 9 | 11 | 11 | 8 |

Table 2.2: Parameters in the fiducial cut analytic form for 4.247 GeV beam energy and 2250 A field

| Parameter | Sector 1 | Sector 2 | Sector 3 | Sector 4 | Sector 5 | Sector 6 |
|-----------|----------|----------|----------|----------|----------|----------|
| A^+ | 23 | 24 | 23 | 22 | 24 | 23 |
| B^+ | 0.07 | 0.11 | 0.17 | 0.18 | 0.14 | 0.06 |
| C^+ | 11 | 9 | 7 | 6 | 8 | 12 |
| A^- | 22 | 21.5 | 25 | 23 | 24 | 25 |
| B^- | 0.18 | 0.18 | 0.11 | 0.08 | 0.07 | 0.09 |
| C^- | 8 | 8 | 9 | 11 | 13 | 8 |

bins with non-zero acceptance to bins with zero acceptance can be tricky and unreliable. Therefore, we checked carefully, using our realistic Monte Carlo, the percentage of cross section lost because of bins with zero acceptance. It turned out that with the adopted binning, typically a few percent of the simulated cross section was lost, sometimes with a maximum below 10 %. Actually, the fact that a cell has zero acceptance or efficiency may be just connected to insufficient statistics in the simulation, as many cells end up with very few generated events; nevertheless, for those cells it is not possible to perform a correction to the data. To get the final cross sections, we therefore performed an extrapolation to the empty bins using the MonteCarlo distributions as an estimate of the missing cross section. This extrapolation is typically only a few percent and we quoted as systematic error a quantity equal to one half of the extrapolation, assuming that the extrapolated cross section may be wrong by plus or minus 50 %, due to the assumptions in the MonteCarlo.

It was observed by V. Burkert that the "skewed" UVa-Pitt fiducial cuts do not contain the shrinking in ϕ as θ increases, adopted for instance in Hovanes' analysis of single π^+ electroproduction. Therefore, we implemented this shrinking for both protons and positive pions and recalculated all detector corrections and the final cross sections once again. Since this was done applying the above described extrapolation procedure, this further step gave the possibility of checking the validity of the extrapolation when changing fiducial cuts and also to recheck the systematic error associated with the choice of the fiducial cuts itself (see later discussion of systematic errors in section 2.7). Figure 2.15 reports once again the "skewed" fiducial cuts previously described (the same like figure 2.14): in this case, θ angles up to 120 degrees are reported to emphasize the subsequent difference with Hovanes' cuts that shrink in ϕ . Figure 2.16 reports instead the fiducial cuts adopted by Hovanes Egiyan in his analysis of single π^+ electroproduction: also here, θ angles up to 120 degrees are reported, to evidentiate the shrinking in ϕ . Hovanes' cuts were implemented in our analysis as well, all simulations reanalysed to derived to new corresponding corrections to the data and finally all cross sections were recalculated. Results are discuss in section 2.6 and following, but we can anticipate here that changes in the final results are very little and certainly inside the statistical and systematic uncertainty, which gives confidence in the extrapolation procedure and suggest a relative insensitivity of the results to the choice of hadron fiducial cuts.

2.2.4 Detection and reconstruction efficiency

Our definition of *efficiency* of the detector is the following: given a particular kinematics of the reaction under study such that the event falls inside the above mentioned fiducial cuts, the efficiency is a product of

- the probability for each particle in this event of giving a correlated signal in the different detector parts

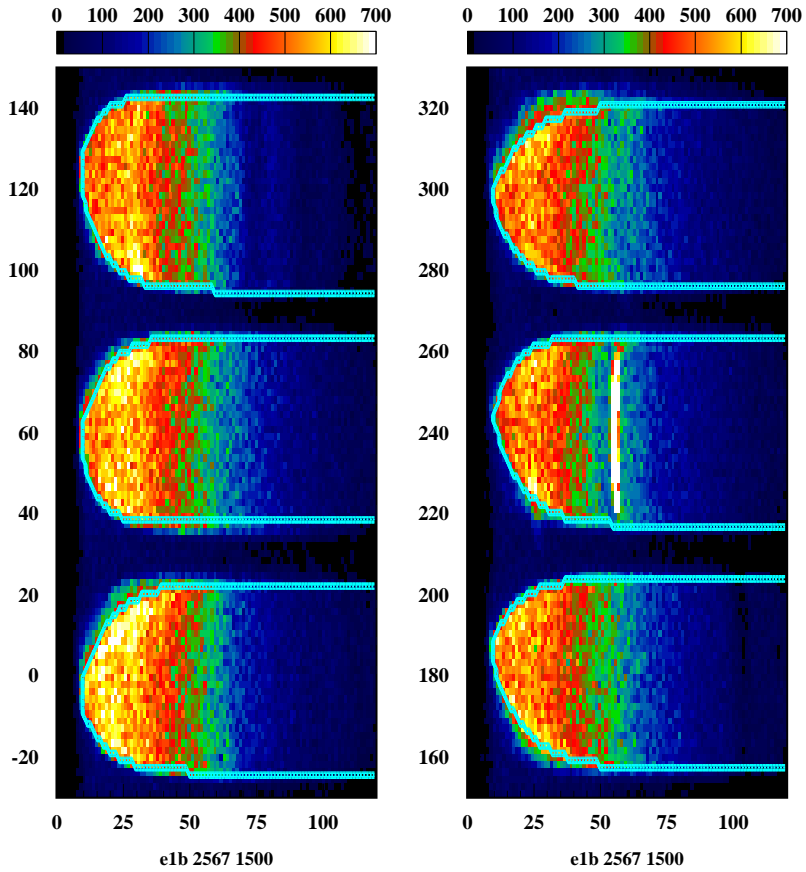


Figure 2.15: Plot of angles ϕ versus θ for positive pions detected in the 6 CLAS sectors at 2.567 GeV beam energy and 1500 A field, with all momenta. The curve shows once again the "skewed" fiducial cuts adopted at first in the analysis reported in the note and described in section 2.2.3. The label says e1b, but the picture actually refers to 1999 data.

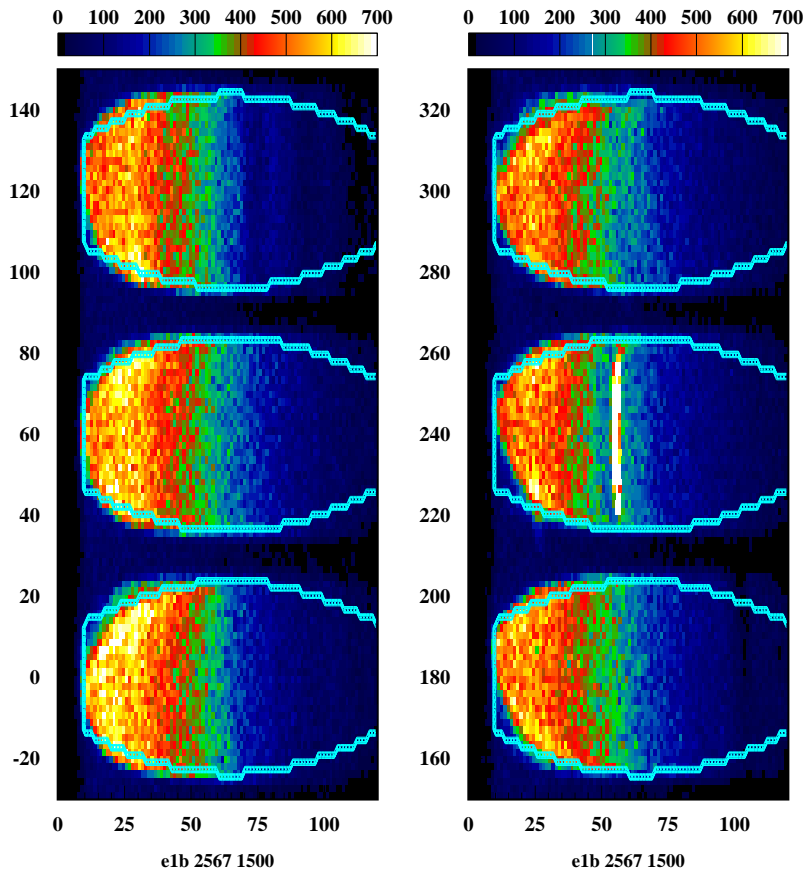


Figure 2.16: Plot of angles ϕ versus θ for positive pions detected in the 6 CLAS sectors at 2.567 GeV beam energy and 1500 A field, with all momenta. The curve shows the fiducial cuts adopted by H. Egiyan in his analysis, calculated at a typical momentum of 1 GeV/c (anyway, momentum dependence is quite soft). The label says e1b, but the picture actually refers to 1999 data.

- the probability for having the different signals sufficiently well-matched in space and time to be accepted by a reconstruction program
- a software factor of merit indicating the ability of the program itself in reconstructing good events
- a factor introduced by the missing mass cuts applied: in our case, being the final state detected $ep\pi^+$, we applied a missing mass cut (see the corresponding sections) to pick up the missing π^- and reject the multipion background; this cut of course is eliminating some good events too, contributing to what we call reconstruction efficiency.

Our definition above partly includes other distortion effects, such as for instance the probability that an event produced at the target in a particular kinematic bin be shifted to another bin because of physical or computational reasons (bin migration). All these effects combined can be concisely called the *reconstruction efficiency*. In order to give a more precise definition, suppose that C is the number of MC theoretically generated $ep\pi^+\pi^-$ events requiring that $ep\pi^+$ fall inside the fiducial cuts (same kind of events accepted as B in the previous paragraph); then let those events be processed by the GSIM code and then suppose that D is the number of events for which $ep\pi^+$ are detected and identified, each of them falling inside the fiducial cuts and being the missing mass $M_x(ep\pi^+)$ inside a chosen π^- window; then our definition of reconstruction efficiency is just the ratio $\frac{D}{C}$. The effect of radiation is discussed in section 2.2.5.

In our analysis, we calculated the reconstruction efficiency inside the regions defined by the fiducial cuts using the Genova event generator as an input to the GSIM CLAS simulation code based on Geant and containing the detector description. To avoid boundary effects on the efficiency, we generated events in a wider region containing the fiducial cuts well inside, then we calculated the ratio $\frac{D}{C}$ only in the region delimited by the actual fiducial cuts: this way, bin migration can occur in both directions at the edges of the fiducial cuts, therefore the efficiency is not distorted. Analogously to the acceptance case, some bins may turn out to have zero efficiency, basically due to insufficient statistics in the simulation: for them, again we rely on the MonteCarlo to perform an extrapolation, which again represents typically a small amount, on the few percent scale. In figure 2.17 we compare such a broader region used to generate events to H. Egiyan's fiducial region: it is clear how the events generated in our Monte Carlo occupy a wider kinematic region than the actual fiducial cuts applied in data analysis, thereby avoiding boundary effects; as visible in the figure, in this case positive pions are generated everywhere in ϕ only for θ greater than about 55 degrees, while for smaller values of θ they are delimited by the yellow curve reported in the picture.

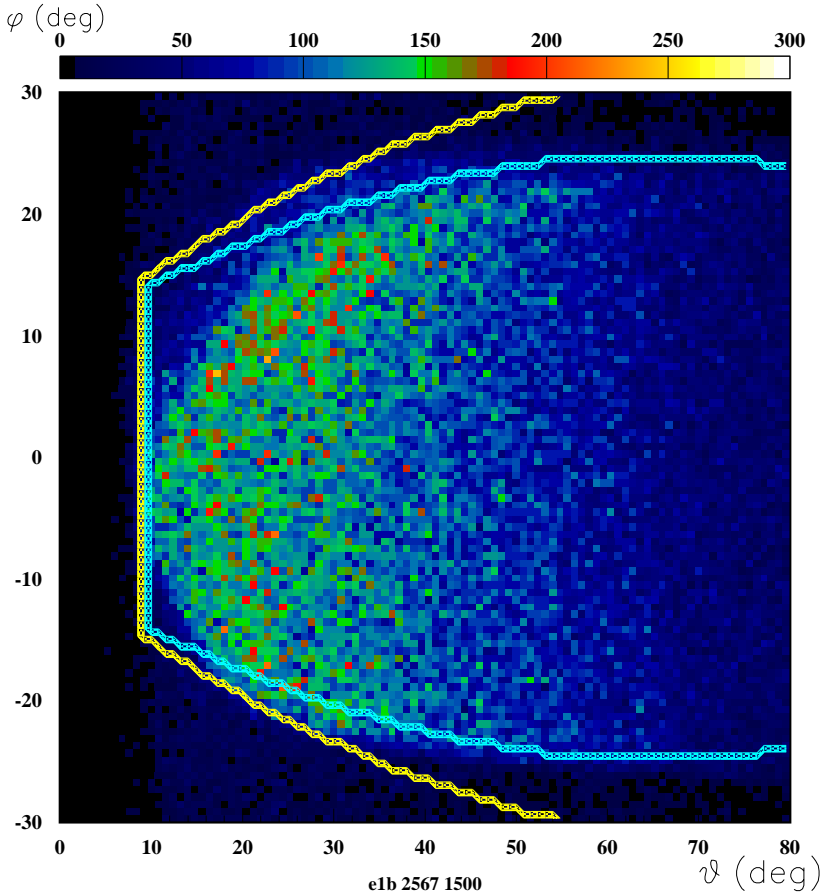


Figure 2.17: Plot of angles ϕ versus θ for positive pions detected in the CLAS sector 1 at 2.567 GeV beam energy and 1500 A field, with all momenta. The yellow curve shows the broader fiducial cuts used in the event generator to throw events; the cyan curve shows instead the above mentioned fiducial cuts from H. Egiyan's analysis. The label says e1b, but the picture actually refers to 1999 data.

2.2.5 Radiative Corrections

To obtain absolute cross sections, it is of course necessary to correct the data for radiative effects; to this purpose, our Monte Carlo event generator was modified to incorporate radiation, using the built-in cross section tables to produce events where the actual kinematic variables at the lepton-hadron vertices are shifted due to photon emission before or after the scattering. Both soft and hard photon emission were included according to the well known Mo and Tsai paper[17]. One of the most noticeable effects of radiation is to produce a tail in the missing mass distribution of reaction $ep \rightarrow ep\pi^+\pi^-\gamma$, when electron, proton and π^+ are detected and where the γ ray is namely coming from electron radiation. The tail is present both in the theoretical missing mass distribution and in the experimental or simulated detector response.

Since both electron and hadron angular distributions are distorted by radiation, radiative effects have to be taken into account when evaluating the geometrical and kinematic acceptance of the detector. Therefore we will modify our *acceptance* definition as follows: suppose that A is the number of MC theoretically generated $ep\pi^+\pi^-\gamma$ events with missing mass $M_x(ep\pi^+)$ inside a chosen π^- window (which means a cut-off in the hardness of the radiated photon); then suppose that B is the number of such MC events for which $ep\pi^+$ fall inside the fiducial cuts; then our definition of geometrical and kinematic acceptance is just the ratio $\frac{B}{A}$. For the particular final state under consideration here, we found that the global effect (integrated over all hadronic variables) of radiation on the acceptance was of the order of a few %.

Reconstruction efficiency can be also affected by radiation, being the missing mass distribution distorted and a tail produced. Therefore we will modify our definition of *reconstruction efficiency* as follows: suppose that C is the number of MC theoretically generated $ep\pi^+\pi^-\gamma$ events requiring that $ep\pi^+$ fall inside the fiducial cuts and that the missing mass $M_x(ep\pi^+)$ be inside a chosen π^- window (same kind of events accepted as B in the previous paragraph); then let those events be processed by the GSIM code and then suppose that D is the number of events for which $ep\pi^+$ are detected and identified, each of them falling inside the fiducial cuts and being the missing mass $M_x(ep\pi^+)$ inside the chosen π^- window; then our definition of reconstruction efficiency is just the ratio $\frac{D}{C}$. We found actually that, keeping the missing mass window fixed in all plots, the global efficiency values does not depend much on radiation, at the level of percent. In any case, radiation was included in the simulations.

Correcting for efficiency and acceptance means to go back to events of type A: this means that after those corrections we will obtain a radiated cross section integrated over radiated photon energies up to the a cut-off corresponding to the chosen missing mass window; the final step is therefore to relate the extracted radiated cross section with the non-radiated one; this is done again by means of the Monte Carlo event generator in the following way: two simulations are performed, with the same number of primary extractions, (where primary means before accepting or rejecting the event according to the cross section weights), the first without radiation, the second with radiation; this way, the number

of generated events will obviously be proportional to the absolute non-radiated and radiated cross sections, respectively; then a cut is performed on the missing mass distribution in the radiated case, equal to the cut performed in the theoretical distributions when correcting the data for acceptance and efficiency; the ratio between events inside the cut-off and events in the non-radiated case will provide the final radiative correction necessary to extract the pure non-radiated electron scattering cross section. In summary, the full acceptance-efficiency-radiative correction procedure is illustrated by the following complete formula, where F is the complete correction factor that data should be multiplied for:

$$F = \frac{N_{MC,norad}}{N_{MC,rad,soft}} \frac{N_{MC,rad,soft}}{N_{MC,rad,soft,accepted}} \frac{N_{MC,rad,soft,accepted}}{N_{MC,rad,soft,accepted,reconstructed}} \quad (2.5)$$

where the rightmost fraction represents the reconstruction efficiency correction, the middle fraction represents the geometrical and kinematic acceptance correction, while the leftmost fraction is the final theoretical correction for “soft” photon emission (“soft” meaning that we keep events inside a relatively narrow missing mass cut). We found that the leftmost fraction is of the order of 1.1 to 1.15 and therefore it is the most important factor among radiative effects.

In the following, we will denote with C the correction represented by acceptance and efficiency (that contains some of the radiative effects)

$$C = \frac{N_{MC,rad,soft}}{N_{MC,rad,soft,accepted}} \frac{N_{MC,rad,soft,accepted}}{N_{MC,rad,soft,accepted,reconstructed}} \quad (2.6)$$

and with R the “theoretical” radiative correction factor

$$R = \frac{N_{MC,norad}}{N_{MC,rad,soft}} \quad (2.7)$$

To give an idea about the extent of the radiative correction R , in figure 2.18, 2.19 and 2.20 we report the correction, averaged over all hadronic variables, as a function of W , for the three analysed Q^2 bins.

2.2.6 Comparison between data and Monte Carlo

We report here the comparison between some quantities calculated in the data and in the Monte Carlo. We begin by analysing the missing mass for the final state where electron, proton and π^+ are detected. Calorimeter energy cut, Cherenkov photoelectron cut and fiducial cuts previously described were applied to produce the plot. In figure 2.21, we report the missing mass for detection of $ep \rightarrow ep\pi^+$, for 6 different W bins at 2.567 GeV beam energy, 1500 A field and at Q^2 between 0.5 and 0.8 GeV 2 , after subtraction of empty target counts, properly normalized to the Faraday cup live-time-gated charge. After

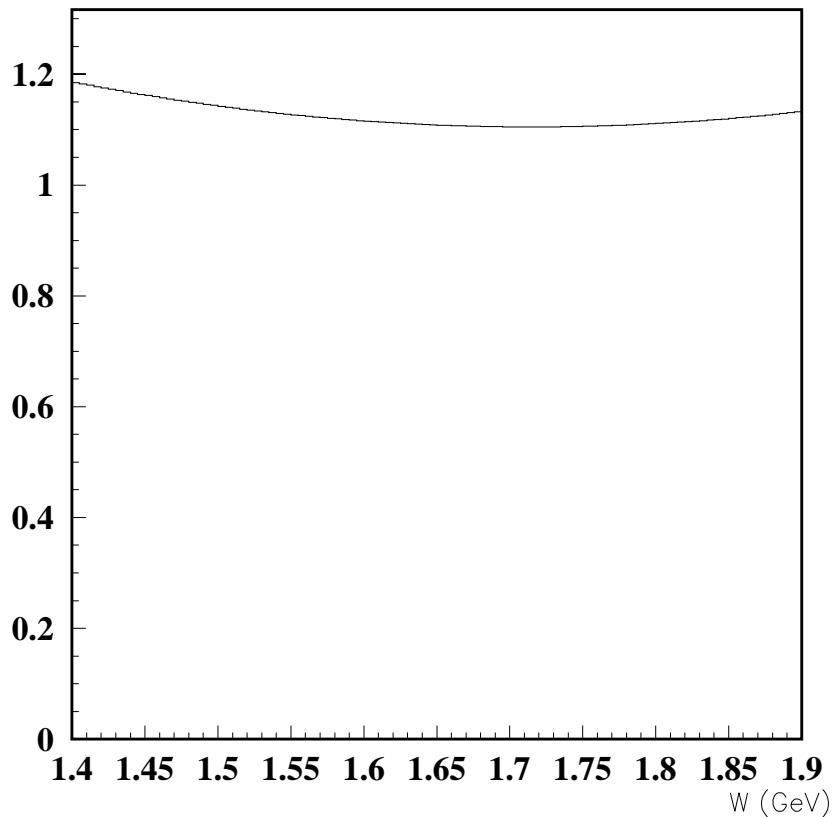


Figure 2.18: Radiative correction factor, averaged over all hadronic variables, as a function of W for Q^2 between 0.5 and 0.8 GeV^2/c^2 .

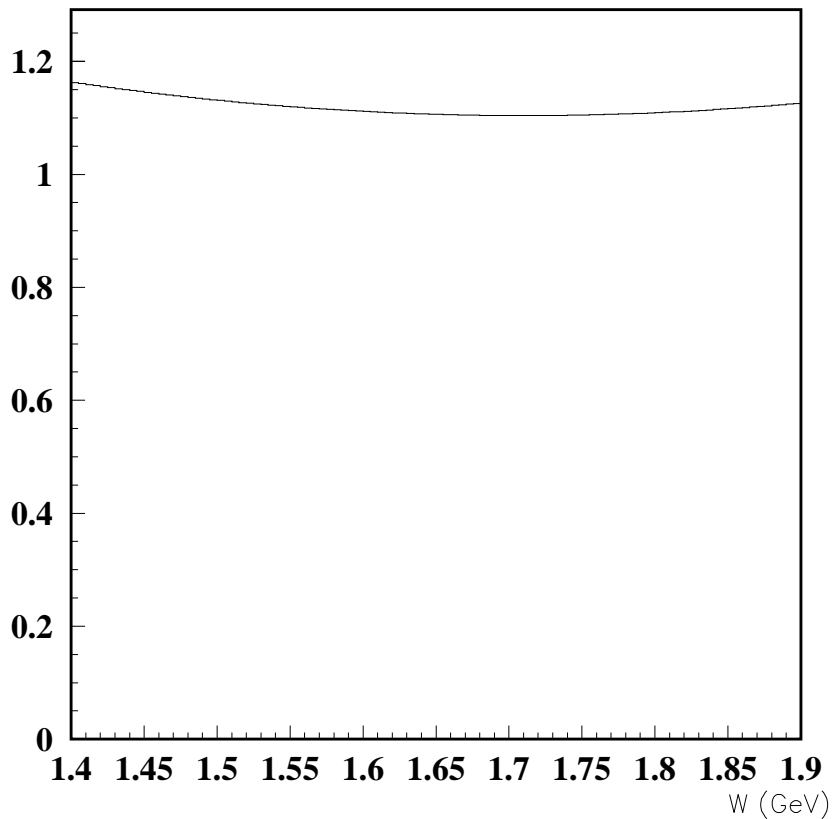


Figure 2.19: Radiative correction factor, averaged over all hadronic variables, as a function of W for Q^2 between 0.8 and 1.1 GeV^2/c^2 .

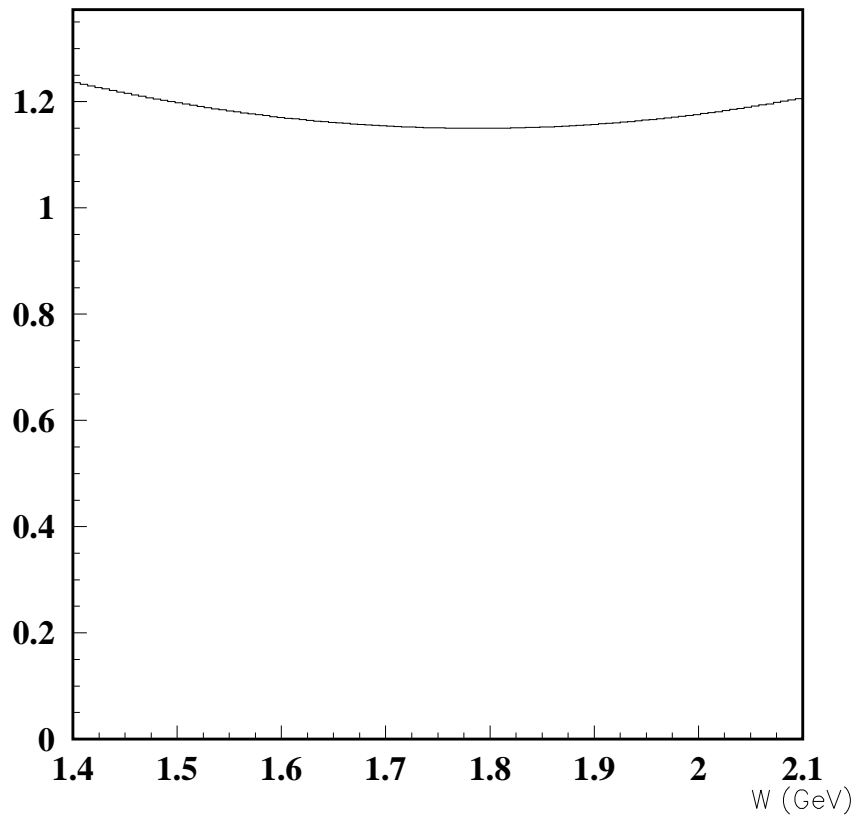


Figure 2.20: Radiative correction factor, averaged over all hadronic variables, as a function of W for Q^2 between 1.1 and 1.5 GeV^2/c^2 .

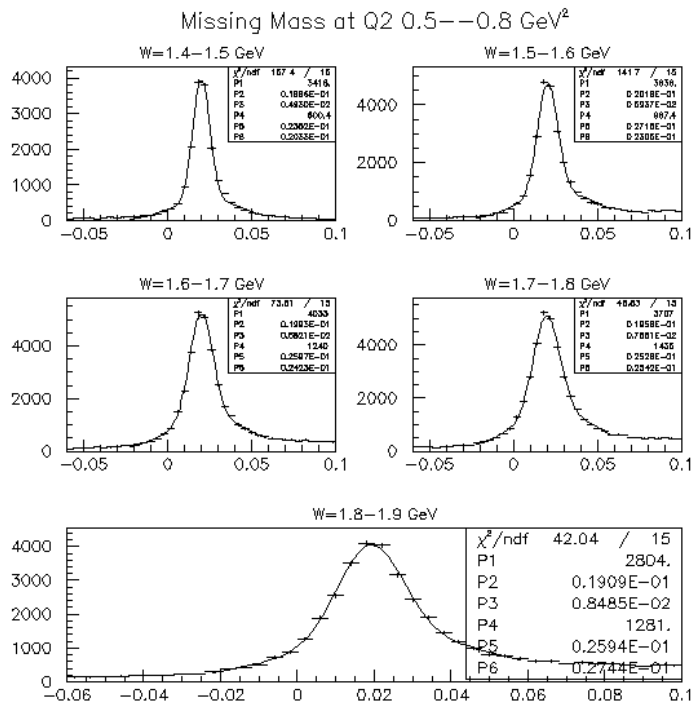


Figure 2.21: Measured missing mass for detection of $e p \pi^+$, for 6 energy bins at 2.567 GeV beam energy, 1500 A field and Q^2 between 0.5 and 0.8 GeV^2/c^2 .

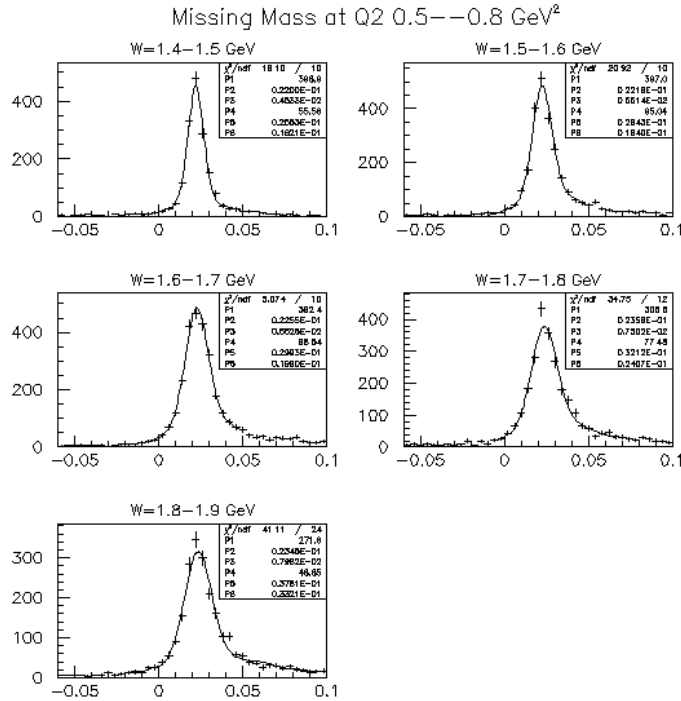


Figure 2.22: Simulated missing mass for detection of $ep\pi^+$, for 5 energy bins at 2.567 GeV beam energy, 1500 A field and Q^2 between 0.5 and 0.8 GeV^2/c^2 .

application of all cuts and after empty target subtraction, a very clean missing π^- peak shows up in the histogram, with a right-side tail obviously due to electron radiation and to higher multiplicity channels like $ep \rightarrow ep\pi^+\pi^-\pi^0$: it is clear how this background rises as the CMS energy W increases. The fit reported in the plots is the sum of two gaussian, where the primary gaussian accounts very well for the main width of the missing pion peak: the parameters obtained from the fit, especially those from the primary gaussian, are used to tune the MC and obtain the same width as in the data. In figure 2.22, we report the same missing mass for detection of $ep \rightarrow ep\pi^+$, such as obtained from the MonteCarlo simulation through the GEANT parametrisation of particle interactions. In this case, no background represented by additional channels other than 2π production was put in the simulation, as the effect of such background was separately studied to derive the missing mass cuts (see section 2.4). To obtain a width in the simulated missing mass comparable to the data, we tuned the DOCA smearing parameters in the GSIM Post Processor code for region 1,2,3 together. As the peak position in the Monte Carlo is slightly different than the data, we shifted the missing mass cuts correspondingly to avoid biasing the efficiency. A similar tuning was performed for the other kinematics and data

sets analysed.

As mentioned before, our correction procedure for acceptance and reconstruction effects takes care of each single bin in the hadronic space, therefore reducing the dependence on Monte Carlo ingredients to a very small, if not negligible amount. Nevertheless, we want here to give an idea of how our Monte Carlo can reproduce the main features seen in the data themselves, like invariant mass distributions and so on. As an example, we chose the 2.567 GeV beam energy, 1500 A field data and corresponding simulation. First of all we produced some plots for a sampling W energy of 1.6-1.625 GeV and Q^2 between 0.5 and 0.8 GeV^2/c^2 . Figure 2.23 shows the invariant mass distribution for the pion-pion pair. Figure 2.24 shows the invariant mass distribution for the proton- π^+ pair. Figure 2.25 shows the CM angle of the $\pi\pi$ pair (which would correspond to the CM angle of the ρ meson in the specific case that a ρ is produced). Figure 2.26 shows the CM angle of the $p - \pi^-$ pair (which would correspond to the CM angle of a Δ^0 in the specific case that a Δ^0 is produced).

2.3 Check of Missing Mass Dependence on Hadronic Variables

To check that we applied appropriate missing mass cuts, we checked the kinematic dependence of the missing mass, i.e. how much the missing mass distribution depends on the hadronic variables used in the analysis. It is very clear that once again, the multi-fold nature of the hadronic kinematic space prevents from plotting such a dependence on all hadronic CM variables at once, at variance with the familiar two-body case of single meson production (even the available statistics would not be enough for such a study); therefore we report here the dependence of the missing mass distribution on each of the five kinematic variables used in the analysis. Pictures 2.27 through 2.31 show namely those dependences in the six W bins for the 2.567 GeV, 1500 A data, from which it is clear that the missing mass is generally well defined and the use of a fixed cut is safe.

For comparison, we report the same series of plots from the MC simulation (at low statistics): the MC events reconstructed after the GEANT processing seem to reproduce well what seen in the data.

2.4 Momentum Corrections

Due to possible slight misalignments in the DC position and to small inaccuracies in the description of the torus magnetic field, the momentum and angle of particles may have some systematic deviation from the real value. To correct this deviation, “ad hoc” corrections to the particle momenta were introduced first by Volker Burkert. We followed a similar path, developing corrections to the particle momenta with the purpose of obtaining

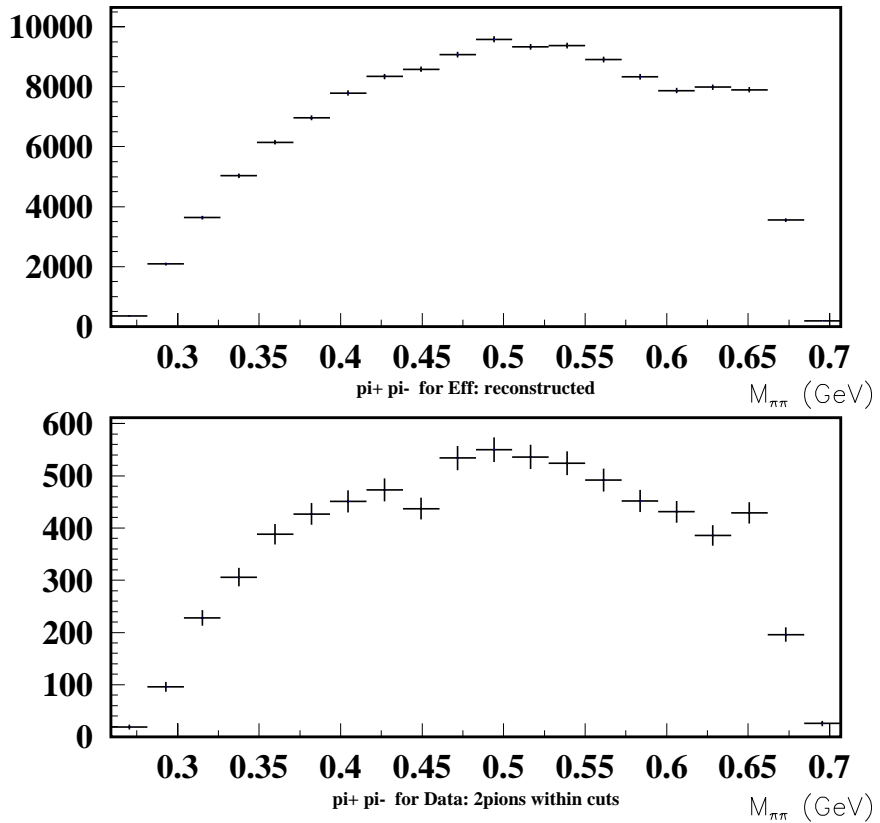


Figure 2.23: Simulated (top) and measured (bottom) invariant mass for the pion-pion pair, when detecting $e\pi^+$, at 2.567 GeV beam energy, 1500 A field, W between 1.6 and 1.625 GeV and Q^2 between 0.5 and 0.8 GeV^2/c^2 .

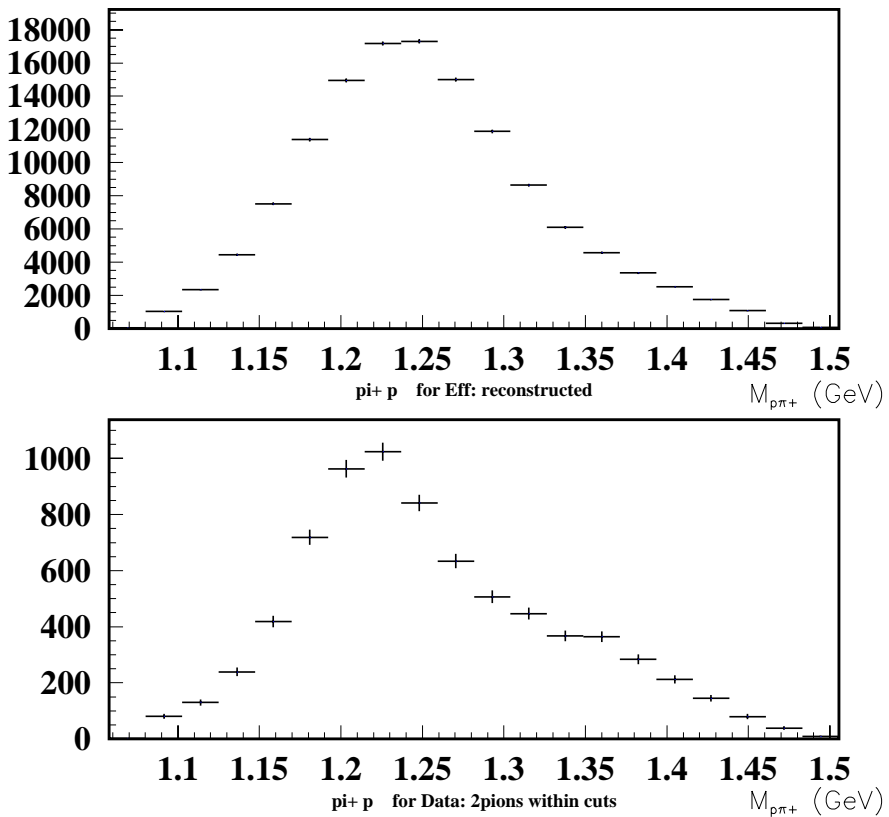


Figure 2.24: Simulated (top) and measured (bottom) invariant mass for the proton- π^+ pair, when detecting $ep\pi^+$, at 2.567 GeV beam energy, 1500 A field, W between 1.6 and 1.625 GeV and Q^2 between 0.5 and 0.8 GeV^2/c^2 .

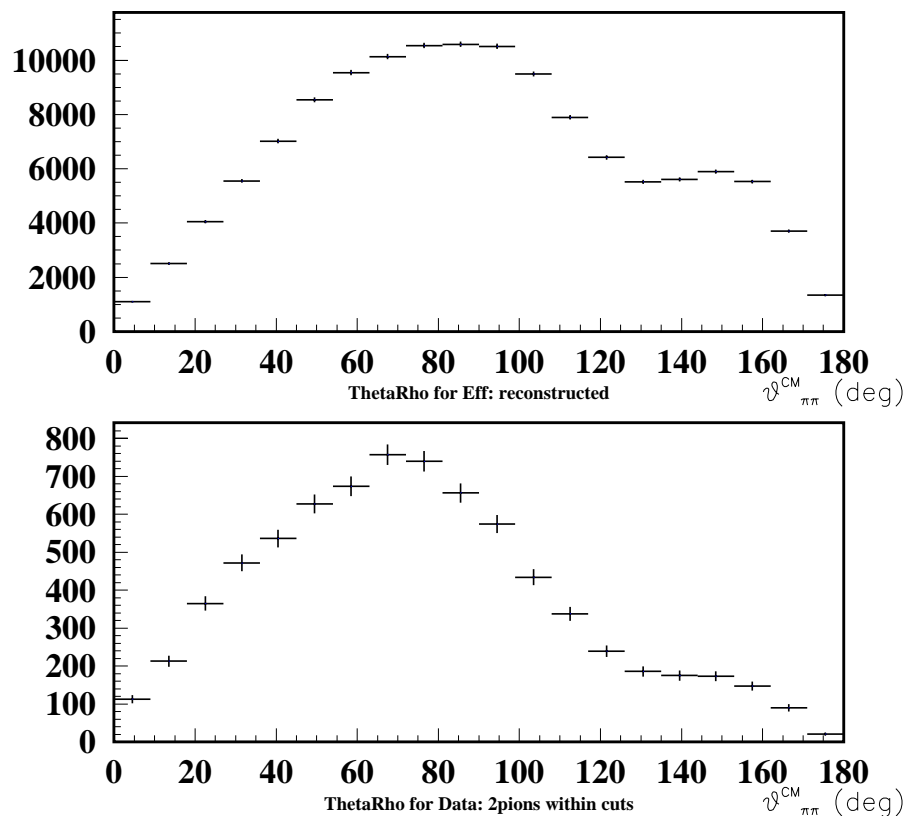


Figure 2.25: Simulated (top) and measured (bottom) angular distribution of the $\pi^+\pi^-$ pair in the CM system, when detecting $ep\pi^+$, at 2.567 GeV beam energy, 1500 A field, W between 1.6 and 1.625 GeV and Q^2 between 0.5 and 0.8 GeV^2/c^2 .

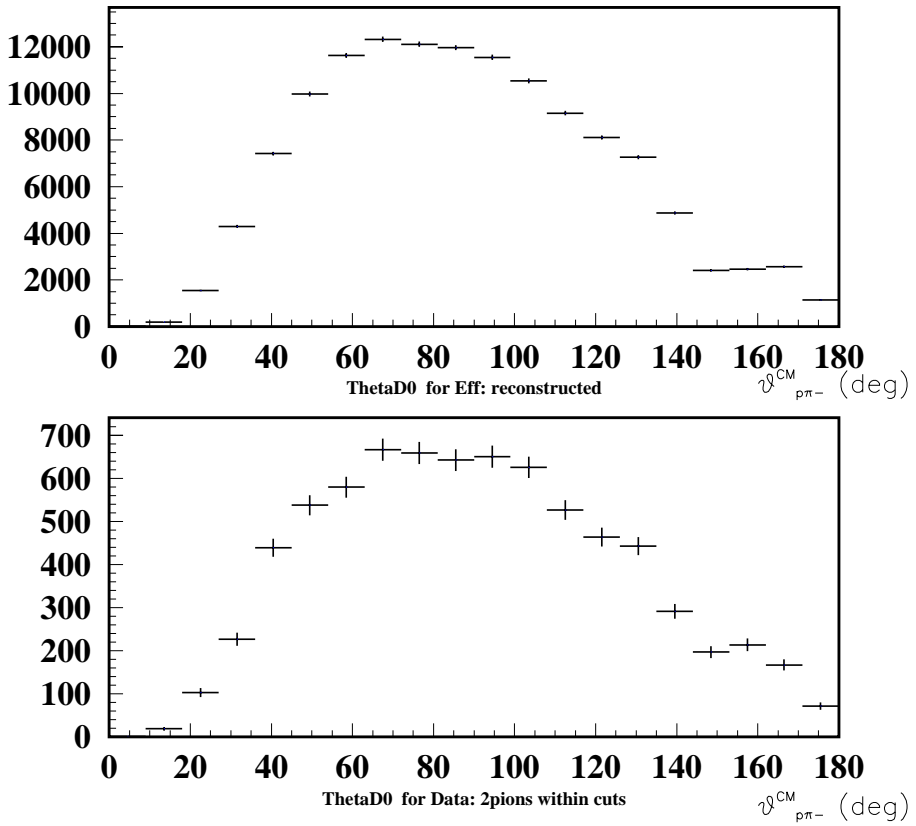


Figure 2.26: Simulated (top) and measured (bottom) angular distribution of the $p - \pi^-$ pair in the CM system, when detecting $ep\pi^+$, at 2.567 GeV beam energy, 1500 A field, W between 1.6 and 1.625 GeV and Q^2 between 0.5 and 0.8 GeV^2/c^2 .

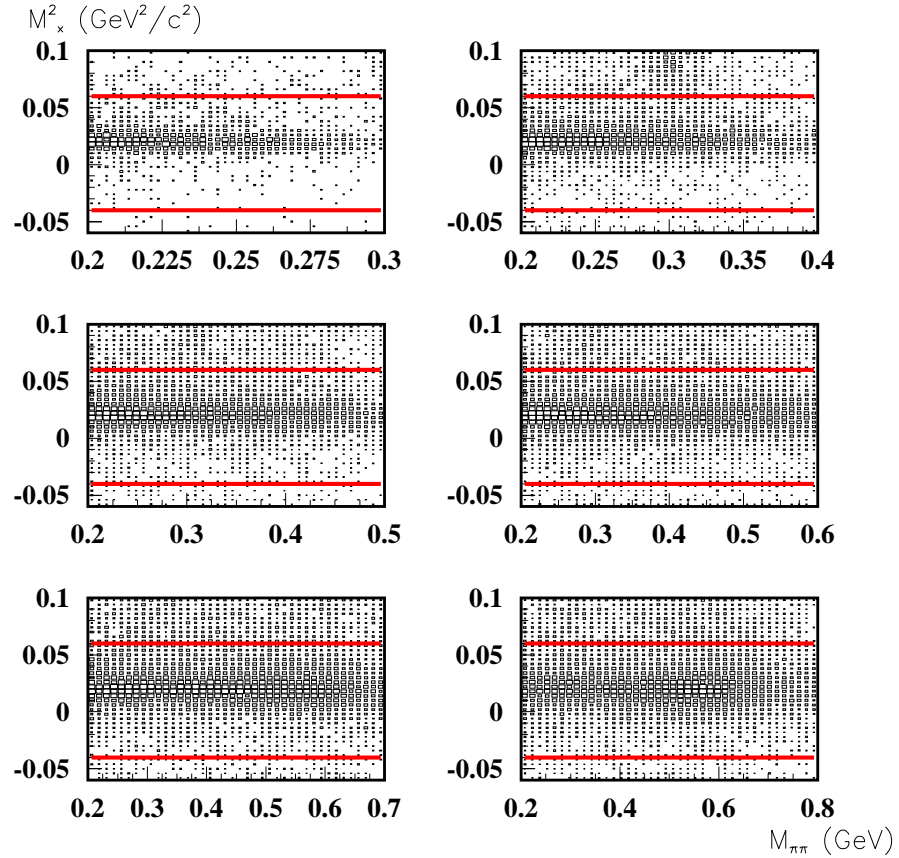


Figure 2.27: Missing mass distribution when detecting $ep\pi^+$, at 2.567 GeV beam energy, 1500 A field, as a function of the pion-pion invariant mass, for six W bins (1.4-1.5 GeV, top left, through 1.9-2.0 GeV, bottom right (only the first five W bins were actually used in the analysis). Q^2 between 0.5 and 0.8 GeV^2/c^2 . Red lines across the plot illustrate the missing mass cut used throughout the analysis.

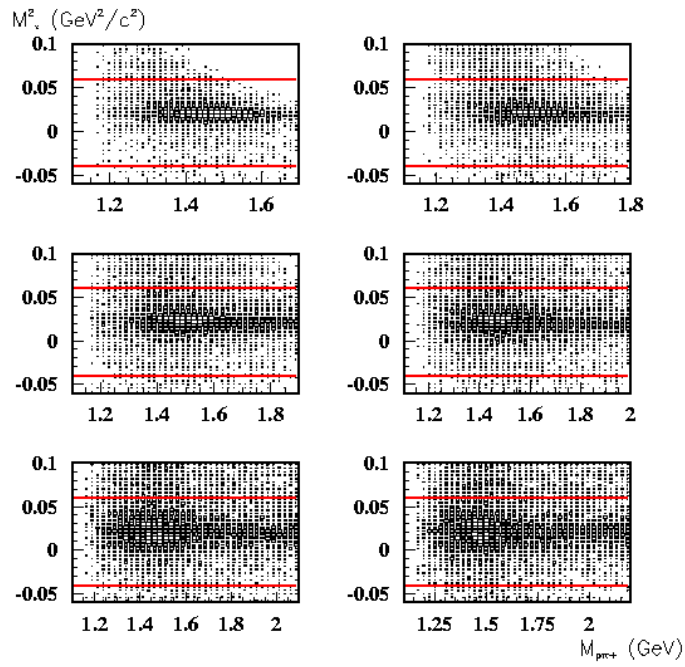


Figure 2.28: Missing mass distribution when detecting $e p \pi^+$, at 2.567 GeV beam energy, 1500 A field, as a function of the $p\pi^+$ invariant mass, for six W bins (1.4-1.5 GeV, top left, through 1.9-2.0 GeV, bottom right (only the first five W bins were actually used in the analysis). Q^2 between 0.5 and 0.8 GeV^2/c^2 . Red lines across the plot illustrate the missing mass cut used throughout the analysis.

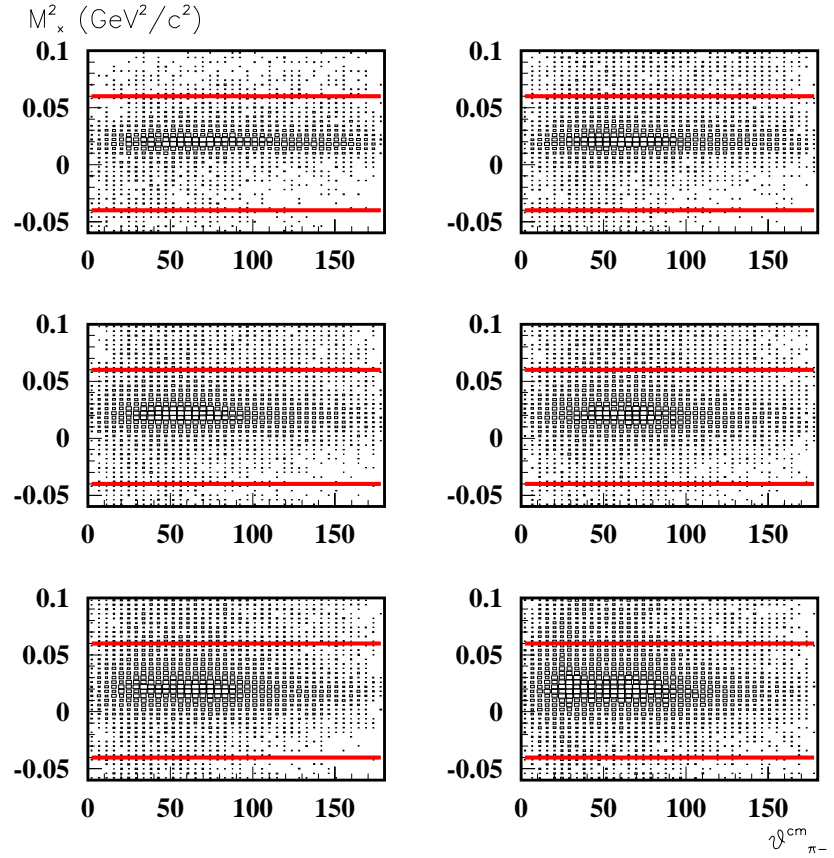


Figure 2.29: Missing mass distribution when detecting $ep\pi^+$, at 2.567 GeV beam energy, 1500 A field, as a function of the CM azimuthal angle of the π^- , for six W bins (1.4-1.5 GeV, top left, through 1.9-2.0 GeV, bottom right (only the first five W bins were actually used in the analysis). Q^2 between 0.5 and 0.8 GeV^2/c^2 . Red lines across the plot illustrate the missing mass cut used throughout the analysis.

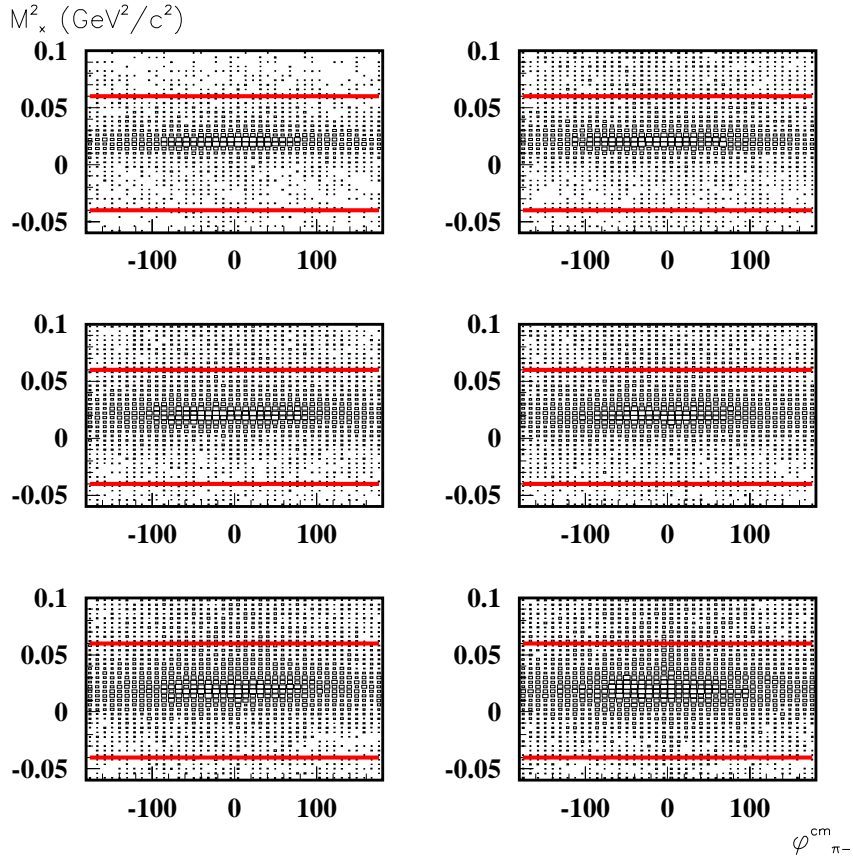


Figure 2.30: Missing mass distribution when detecting $e p \pi^+$, at 2.567 GeV beam energy, 1500 A field, as a function of the CM polar angle of the π^- , for six W bins (1.4-1.5 GeV, top left, through 1.9-2.0 GeV, bottom right (only the first five W bins were actually used in the analysis). Q^2 between 0.5 and 0.8 GeV^2/c^2 . Red lines across the plot illustrate the missing mass cut used throughout the analysis.

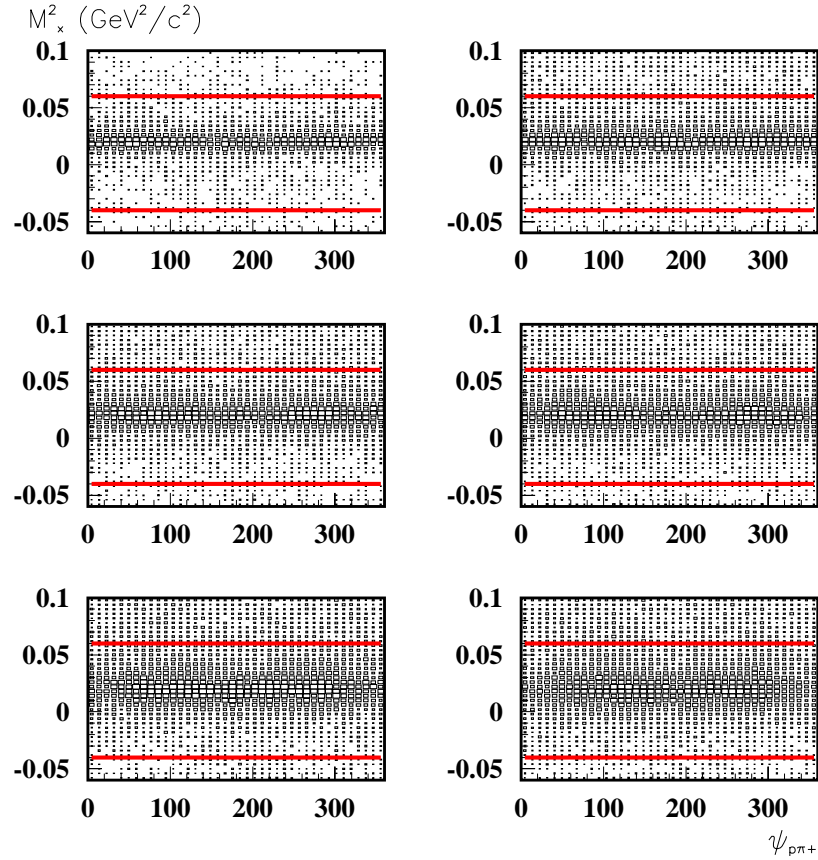


Figure 2.31: Missing mass distribution when detecting $ep\pi^+$, at 2.567 GeV beam energy, 1500 A field, as a function of the polar angle of the $\rho\pi^+$ pair with respect to the hadronic plane, for six W bins (1.4-1.5 GeV, top left, through 1.9-2.0 GeV, bottom right (only the first five W bins were actually used in the analysis). Q^2 between 0.5 and 0.8 GeV^2/c^2 . Red lines across the plot illustrate the missing mass cut used throughout the analysis.

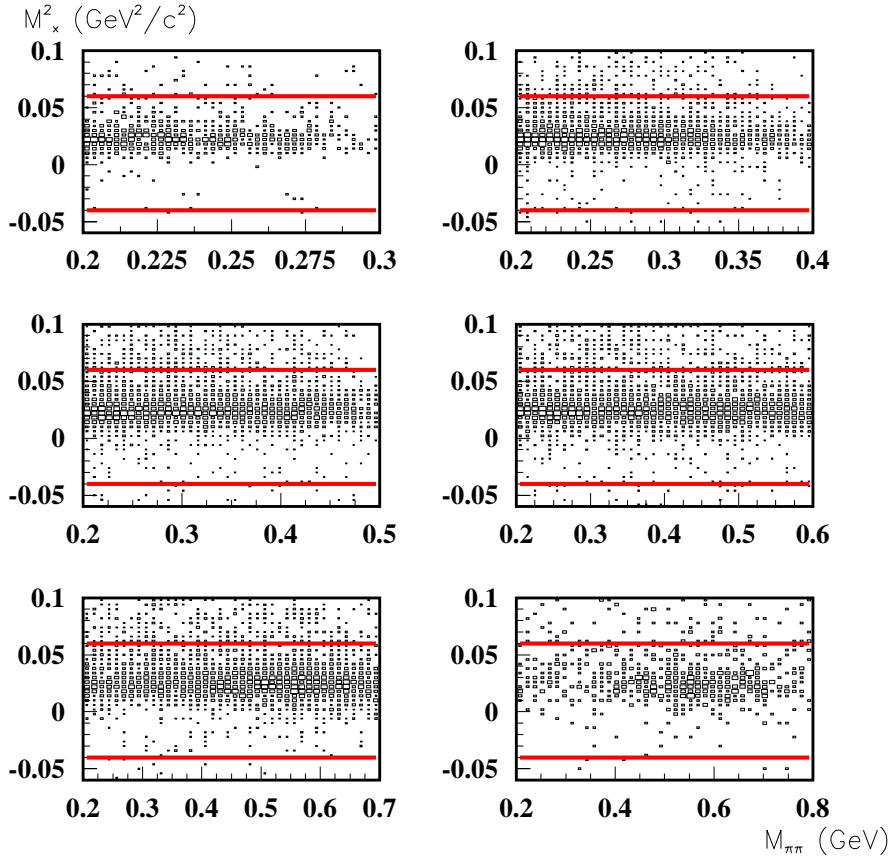


Figure 2.32: Simulated missing mass distribution for $ep\pi^+$, at 2.567 GeV beam energy, 1500 A field, as a function of the pion-pion invariant mass, for six W bins (1.4-1.5 GeV, top left, through 1.9-2.0 GeV, bottom right (only the first five W bins were actually simulated, the last is populated only by bin migration)). Q^2 between 0.5 and 0.8 GeV^2/c^2 . Red lines across the plot illustrate the missing mass cut used throughout the analysis.

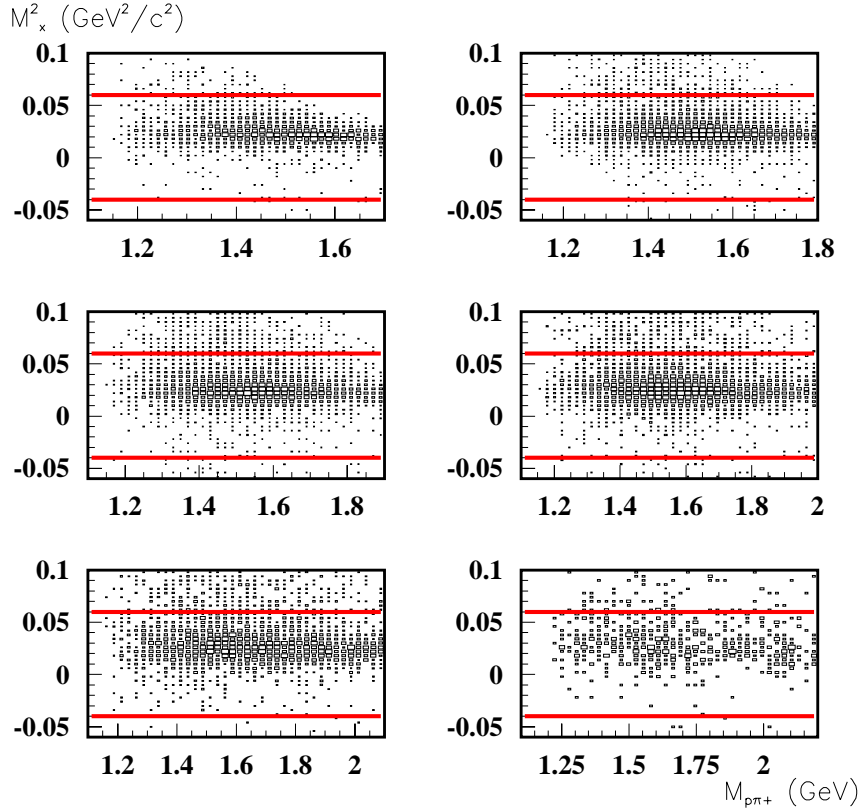


Figure 2.33: Simulated missing mass distribution for $ep\pi^+$, at 2.567 GeV beam energy, 1500 A field, as a function of the $p\pi^+$ invariant mass, for six W bins (1.4-1.5 GeV, top left, through 1.9-2.0 GeV, bottom right (only the first five W bins were actually simulated, the last is populated only by bin migration). Q^2 between 0.5 and 0.8 GeV $^2/c^2$. Red lines across the plot illustrate the missing mass cut used throughout the analysis.

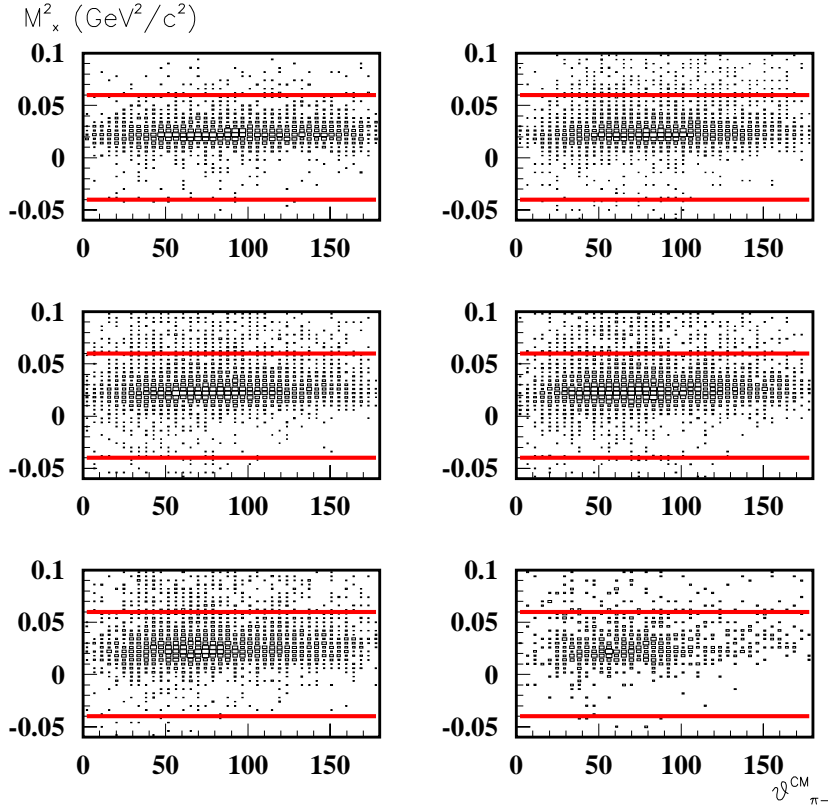


Figure 2.34: Simulated missing mass distribution for $ep\pi^+$, at 2.567 GeV beam energy, 1500 A field, as a function of the CM azimuthal angle of the π^- , for six W bins (1.4-1.5 GeV, top left, through 1.9-2.0 GeV, bottom right (only the first five W bins were actually simulated, the last is populated only by bin migration). Q^2 between 0.5 and 0.8 GeV^2/c^2 . Red lines across the plot illustrate the missing mass cut used throughout the analysis.

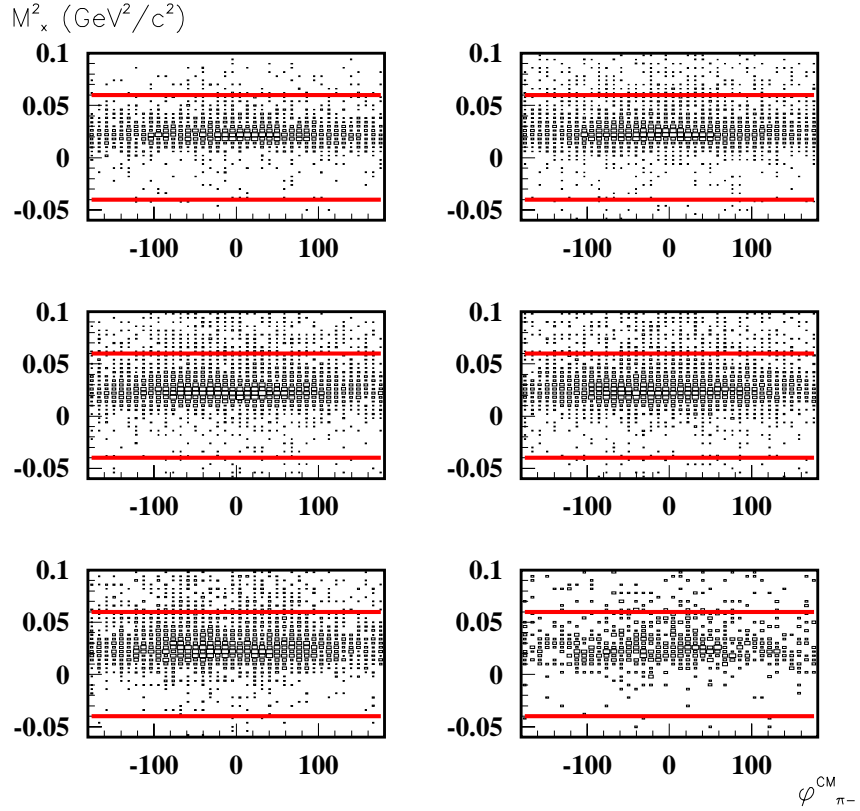


Figure 2.35: Simulated missing mass distribution for $ep\pi^+$, at 2.567 GeV beam energy, 1500 A field, as a function of the CM polar angle of the π^- , for six W bins (1.4-1.5 GeV, top left, through 1.9-2.0 GeV, bottom right (only the first five W bins were actually simulated, the last is populated only by bin migration)). Q^2 between 0.5 and 0.8 GeV $^2/c^2$. Red lines across the plot illustrate the missing mass cut used throughout the analysis.

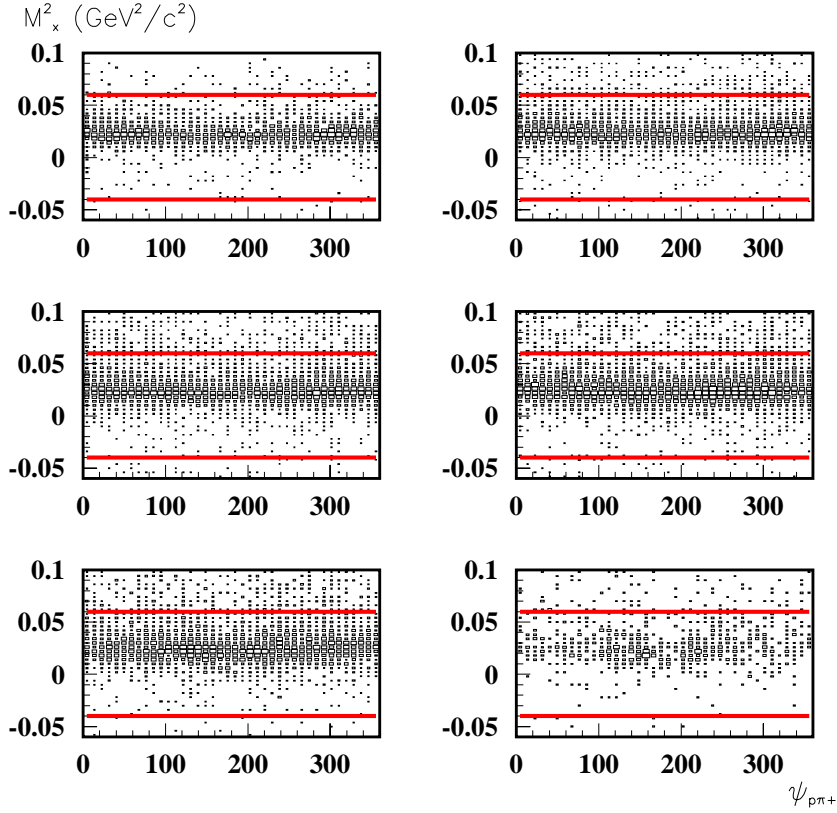


Figure 2.36: Simulated missing mass distribution for $ep\pi^+$, at 2.567 GeV beam energy, 1500 A field, as a function of the polar angle of the $p\pi^+$ pair with respect to the hadronic plane, for six W bins (1.4-1.5 GeV, top left, through 1.9-2.0 GeV, bottom right (only the first five W bins were actually simulated, the last is populated only by bin migration)). Q^2 between 0.5 and 0.8 GeV^2/c^2 . Red lines across the plot illustrate the missing mass cut used throughout the analysis.

a correct position for the elastic electron scattering peak and shrinking a bit more the width of missing mass peaks. It turned out that for our double pion analysis, the most important correction was to the electron momentum, in order to have the correct energy scale in the invariant mass spectrum, while momentum corrections to proton and π^+ were only slightly affecting the π^- peak in the missing mass distribution.

2.5 Multipion backgrounds

We performed a simulation of multipion backgrounds, using our MC event generator and simulating reactions like $ep \rightarrow ep\pi^+\pi^-\pi^0$; we found that, when detecting $ep\pi^+$, the missing mass distribution for the multipion events was not producing any contamination below a missing mass squared of $0.07 \text{ GeV}^2/\text{c}^2$. To make sure that really no multipion contamination was included in our analysis, we decided to use an even more conservative cut of $0.06 \text{ GeV}^2/\text{c}^2$.

2.6 Cuts summary

From the above discussion, we can draw the conclusions on what kind of cuts to use in the analysis. First of all, all particles were required to be detected inside the fiducial cuts previously described. To ensure that electrons are properly identified, we first applied the above mentioned calorimeter cut, applying a specific correction for the corresponding electron loss as reported section 2.1.3; threshold effects from the calorimeter were controlled applying Kim Egiyan's function as an energy fiducial cut; then, we applied the photoelectron cut for the Cherenkov detector, again correcting the yield with the fit previously mentioned. In order to identify pions properly, the above mentioned cut in the β -vs-p plot was applied for forward and medium angle scintillators, where there were no problems of double bands. We then applied a missing mass cut for the detected $ep\pi^+$ state, requiring the missing mass to be between -0.04 and $0.06 \text{ GeV}^2/\text{c}^2$ (this cut was slightly shifted in the MC to account for the different missing pion mass seen). Finally, a rejection list was applied to bad ToF scintillators, both in data and Monte Carlo simulations.

2.7 Cross Sections

Using the full statistics collected in the second electron scattering run (1999) at 2.567 GeV beam energy and 1500 A magnetic field setting, as well as 4.247 GeV beam energy and 2250 A magnetic field setting, two pion event candidates were extracted from the data and analysed. With the above described correction procedure, data were binned in W with 25 MeV steps and in few Q^2 intervals as described later on. Our analysis program was able to calculate the acceptance/efficiency corrections in the full hadronic kinematic space, binning in the following 3 sets of variables

1. invariant mass of the $p\pi^+$ pair, invariant mass of the $\pi^+\pi^-$ pair, proton polar angles θ and ϕ and rotation freedom ψ of the pion pair with respect to the hadronic plane;
2. invariant mass of the $p\pi^+$ pair, invariant mass of the $\pi^+\pi^-$ pair, π^- polar angles θ and ϕ and rotation freedom ψ of the $p\pi^+$ pair with respect to the hadronic plane;
3. invariant mass of the $p\pi^-$ pair, invariant mass of the $\pi^+\pi^-$ pair, π^+ polar angles θ and ϕ and rotation freedom ψ of the $p\pi^-$ pair with respect to the hadronic plane;

The full differential cross section derived has therefore the form (for instance if we consider the kinematic set 1)

$$\frac{d\sigma}{dW dQ^2 dM_{p\pi^+} dM_{\pi^+\pi^-} d\Omega_p d\psi_{\pi\pi}} = \Gamma_v \frac{d\sigma}{dM_{p\pi^+} dM_{\pi^+\pi^-} d\Omega_p d\psi_{\pi\pi}} \quad (2.8)$$

where Γ_v is the virtual photon flux, given by

$$\Gamma_v = \frac{\alpha}{4\pi} \frac{1}{E_{beam}^2 M_p^2} \frac{W(W^2 - M_p^2)}{(1-\epsilon)Q^2} \quad (2.9)$$

where α is the fine structure constant ($\frac{1}{137}$), M_p is the proton mass and ϵ is the virtual photon transverse polarisation, given by

$$\epsilon = \left(1 + 2 \left(1 + \frac{\omega^2}{Q^2} \right) \tan^2 \left(\frac{\theta_{el}}{2} \right) \right)^{-1} \quad (2.10)$$

where $\omega = E_{beam} - E_{el}$. The experimental definition of (2.5) is

$$\frac{d\sigma}{dW dQ^2 dM_{p\pi^+} dM_{\pi^+\pi^-} d\Omega_p d\psi_{\pi\pi}} = \frac{\Delta N}{(Q/e)_A^{\rho x} N_0 \Delta W \Delta Q^2 \Delta \tau} CR \quad (2.11)$$

where ΔN is the number of events inside the multidimensional bin, C is the correction factor coming from the acceptance and efficiency calculated via Monte Carlo simulations, R is the "theoretical" radiative correction illustrated in section 2.2.5), Q is the integrated Faraday Cup charge, e is the elementary charge, ρ is the target density in $\frac{gr}{cm^2}$, x is the target length in cm, A is the target atomic weight in grams, N_0 is Avogadro's number and ΔW , ΔQ^2 are the electron kinematics bins and $\Delta \tau$ is the hadronic multidimensional bin given by

$$\Delta \tau = \Delta M_{p\pi^+} \Delta M_{\pi^+\pi^-} \Delta \cos(\theta_p) \Delta \phi_p \Delta \psi_{\pi\pi} \quad (2.12)$$

The virtual photon cross section is therefore given by

$$\frac{d\sigma}{dM_{p\pi^+} dM_{\pi^+\pi^-} d\Omega_p d\psi_{\pi\pi}} = \frac{\Delta N}{< \Gamma_v > (Q/e)_A^{\rho x} N_0 \Delta W \Delta Q^2 \Delta \tau} CR \quad (2.13)$$

where $\langle \Gamma_v \rangle$ is an average virtual photon flux inside the electron bins considered. Obviously, no binning in the electron polar angle ϕ_{el} was performed, although a sector dependent electron correction was applied, as outlined in section 2.1.2. (2.11) is then integrated to get partially differential cross sections or the total cross section. The adopted hadronic binning for the E1C analysis was: 10 bins for the invariant masses, 10 bins for the primary angular variable (for instance θ_p), 5 bins for the other angular variables, for a total of 25,000 hadronic bins. To evaluate absolute statistical errors in all plots, we used the following formula

$$\delta_{stat}(M_{p\pi^+}, M_{\pi^+\pi^-}, \theta_p, \phi_p, \psi_{\pi\pi}) = \frac{\sqrt{\Delta N}}{\langle \Gamma_v \rangle (Q/e) \frac{\rho_x}{A} N_0 \Delta W \Delta Q^2 \Delta \tau} CR \quad (2.14)$$

then propagating the errors quadratically when performing integrations over variables; we want to remark here that the final statistical error obtained for instance on the total cross section points is exceeding in percentage the usual $\frac{1}{\sqrt{N_{tot}}}$ because of the non-uniformity of the detector correction C in (2.11). Another source of statistical fluctuations is connected to the limited statistics in the Monte Carlo: looking at formula (2.11), it is clear that the error in the knowledge of the correction factor C is affecting the cross section value. If we write $\frac{1}{C}$ as a product of the acceptance α and the efficiency ϵ , that we calculate separately, we can then propagate their respective statistical errors in the sequence of integrals of (2.11). Here we have to spend a few words about the statistical error in the simulation; let's consider for instance the acceptance α ; its definition is simply

$$\alpha = \frac{N. \text{ events accepted}}{N. \text{ events generated}} = \frac{N_{acc}}{N_{gen}} \quad (2.15)$$

It turns out[18] that the absolute statistical error on α is given by

$$\delta(\alpha) = \sqrt{\frac{N_{acc}(N_{gen} - N_{acc})}{N_{gen}^3}} \quad (2.16)$$

If we write the correction coefficient $\frac{1}{C}$ as the product of acceptance α and efficiency ϵ , and if we call $\delta(\alpha)$ and $\delta(\epsilon)$ the corresponding absolute errors, then the error on the cross section due to the limited Monte Carlo statistics will be given by

$$\delta_{stat,MC}(\tau) = \frac{d\sigma}{dM_{p\pi^+} dM_{\pi^+\pi^-} d\Omega_p d\psi_{\pi\pi}} \left[\left(\frac{\delta\alpha}{\alpha} \right)^2 + \left(\frac{\delta\epsilon}{\epsilon} \right)^2 \right] \quad (2.17)$$

A remark here is necessary: looking at expression (2.5) which we report here,

$$F = RC = \frac{N_{MC,norad}}{N_{MC,rad,soft}} \frac{N_{MC,rad,soft}}{N_{MC,rad,soft,accepted}} \frac{N_{MC,rad,soft,accepted}}{N_{MC,rad,soft,accepted,reconstructed}} \quad (2.18)$$

one would argue that intermediate terms cancel out and one is left with the simple ratio

$$F = \frac{N_{MC,norad}}{N_{MC,rad,soft,accepted,reconstructed}} \quad (2.19)$$

Therefore, in principle errors from the Monte Carlo should be calculated starting from this simple expression for the radiative-acceptance correction; in practice, however, the above cancellation does certainly not take place in the last two ratios: actually, the last ratio, that corresponds to the calculation of the reconstruction efficiency, involves the use of the GEANT simulation and therefore takes a much longer time than the evaluation of the middle ratio (geometrical and kinematic acceptance) that involves only our Monte Carlo event generator; therefore we practically simulated less events to calculate the last ratio than we simulated to calculate the second (middle) one; in other words, the number $N_{MC,rad,soft,accepted}$ in the second ratio is actually quite bigger than the same quantity appearing in the last ratio; in fact, also the number $N_{MC,rad,soft}$ in the first ratio may be slightly different from the same quantity in the second ratio, as in our procedure all the three ratios were obtained in separate simulations for practical reasons. To better understand the numerical aspects, let's therefore write the correction factor as

$$F = RC = \frac{N_{MC,norad}}{N_{MC,rad,soft}} \frac{N'_{MC,rad,soft}}{N_{MC,rad,soft,accepted}} \frac{N'_{MC,rad,soft,accepted}}{N_{MC,rad,soft,accepted,reconstructed}} \quad (2.20)$$

In summary, in our evaluation of the Monte Carlo errors, we calculated and combined the statistical errors from the second and third ratio, while we neglected the contribution from the first one (radiative factor): since its numerator and denominator don't involve any acceptance cuts, its contribution to the total error is certainly negligible, as we will show in a moment.

To give some numerical estimates that help to understand the figures involved, let's calculate F as a global correction factor, depending only on W and Q^2 and integrated over all hadronic variables: this is much easier to do and gives an idea of the underlying algebra. For a particular bin in W and Q^2 , we had

- 6.5 million events generated without radiation, everywhere in kinematic space
- 5.4 million events generated with (soft) radiation, everywhere in kinematic space, from which
 - 330,000 events fall inside fiducial cuts
 - 130,000 million events generated separately inside fiducial cuts for subsequent GEANT processing, from which
 - 50,000 are fully reconstructed and identified as belonging to the reaction under analysis

As global numbers, the above figures correspond to an acceptance of 0.062 and a reconstruction efficiency of 0.38; errors on these two quantities, calculated according to (2.16), are 0.16 % and 0.26 %, respectively; their quadratic combination is 0.3 %. Suppose now that we did only one simulation to calculate acceptance and efficiency at once, therefore having the same numbers in the denominator of the second ratio and the numerator of the third, respectively, such to produce a cancellation in the quantity

$$\frac{N_{MC,rad,soft}}{N_{MC,rad,soft,accep}} \frac{N_{MC,rad,soft,accep}}{N_{MC,rad,soft,accep,reconstr}} = \frac{N_{MC,rad,soft}}{N_{MC,rad,soft,accep,reconstr}} \quad (2.21)$$

To obtain that, one should have reduced the number of events in the primary generation, to maintain the same execution time which is dominated by the GEANT processing; in explicit numbers, $N_{MC,rad,soft}$ would have been equal to about 2.1 million events instead of 5.4; it is straightforward to calculate, using (2.16) that in this case the error on the above quantity would have been 0.4 %, clearly bigger than the error obtained in our procedure (0.3 %) where the two ratios are separately simulated and calculated, as well as their respective errors.

As further evaluation, in the framework of our procedure, let's calculate the contribution of the first ratio

$$R = \frac{N_{MC,norad}}{N_{MC,rad,soft}} \quad (2.22)$$

to the total error, which was neglected in our analysis; in our specific numerical example, numerator and denominator correspond to 6.5 and 5.4 million events, respectively; since these two quantities come from two different and independent simulations, one has to combine their errors quadratically instead of using (2.16); this produces an error of 0.06 %, which is indeed negligible.

One may object that in fact in our procedure, even though we made separate simulations, numerically the quantities $N_{MC,rad,soft}$ and $N'_{MC,rad,soft}$ are very close to each other and therefore we should calculate the errors on the simplified factor

$$\frac{N_{MC,norad}}{N_{MC,rad,soft,accepted}} \frac{N'_{MC,rad,soft,accepted}}{N_{MC,rad,soft,accepted,reconstructed}} \quad (2.23)$$

In this case, while obviously the second ratio and its error are exactly the same as before, for the first ratio (a combination of radiative and acceptance corrections) again we have independent quantities in numerator and denominator and the corresponding error has to be calculated from the customary quadratic combination. It is straightforward to calculate the error on the first ratio using the figures previously mentioned and we found in this case 0.18 %, to be quadratically combined with 0.26 % for the second ratio: it is very clear that the difference with our actual evaluation is totally negligible, as our previous number to combine was 0.16 % instead of 0.18 %.

It is also important to notice that the statistical error from the Monte Carlo, calculated with our procedure, was found to be typically 10 to 20 % smaller than the "experimental" statistical errors obtained from (2.14), which means that any small variation in the Monte Carlo error due to the use of slightly different procedures would not lead to an appreciable difference in the final error quoted in the plots. Indeed, we finally combined quadratically the two statistical errors coming from fluctuations in the data (represented by (2.14)) and from the MonteCarlo (represented by (2.17)). All statistical errors reported in the data plots were obtained with this combination. In figure 2.37, 2.38 and 2.39 we report the final results for the total cross section at Q^2 between 0.5 and 0.8 GeV 2 , between 0.8 and 1.1 GeV 2 and between 1.1 and 1.5 GeV 2 , respectively. In all pictures we compare the data points obtained with our previous "skewed" fiducial cuts and the new version modified according to H. Egiyan's recipe. Moreover in these pictures we report as a grey band the systematic error calculated as discussed in the next section.

2.8 Systematic errors

2.8.1 Dependence on Monte Carlo Assumptions

The first source of systematic errors we took into account was the dependence of the cross section on the Monte Carlo used. In principle, using a full binning of the events in W , Q^2 and all hadronic variables, the dependence of the acceptance and efficiency corrections on the distributions used in the event generator is minimal. However, to check this point more quantitatively, we repeated both the acceptance and efficiency simulation for all W and Q^2 bins, changing the physical content of the Monte Carlo: instead of simulating all channels $\Delta^{++}\pi^-$, $\Delta^0\pi^+$, $\rho^0 p$ and $p\pi^+\pi^-$, we simulated only the first three, removing the phase space. To be able to perform this analysis in a reasonable time, we simulated only a limited amount of events and looked at integrated quantities, such to obtain a conservative upper limit to the actual changes in acceptance and efficiency. From this study we derived a systematic error that, combined from acceptance and efficiency, ranges from 3 to 4 %. This errors were computed and tabulated for each single W and Q^2 bin.

2.8.2 Dependence on Monte Carlo Throwing Region

As mentioned previously, to speed up the simulation procedure a little bit, events were thrown in CLAS using a geometric region in θ and ϕ larger than the fiducial cuts, rather than using the full phase space, basically to avoid processing events hitting dead regions like the torus coils. However, bin migration may occur from these areas outside our simulation region, especially in the case of protons undergoing large angle scattering, and affect our results if those areas are not covered by the Monte Carlo. We checked this point by performing a short simulation with hadrons generated in the full phase space and comparing to our technique: in this way, we obtained a systematic error ranging from

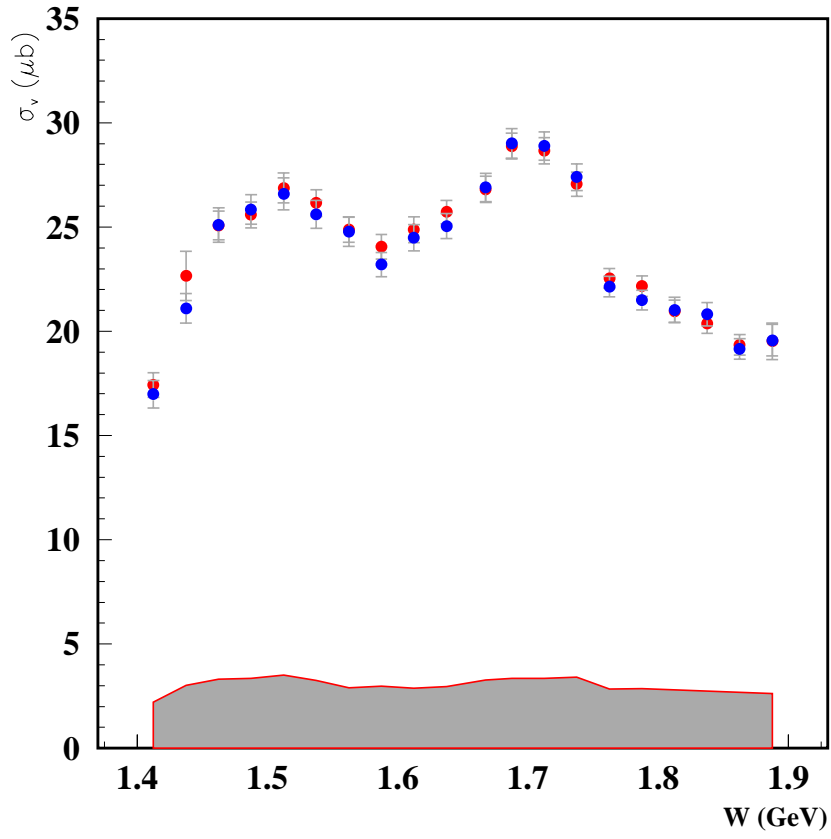


Figure 2.37: Total virtual photon cross section as a function of the CMS energy W for $ep \rightarrow ep\pi^+\pi^-$ at Q^2 between 0.5 and 0.8 GeV^2 ; red points: CLAS data from the e1c (1999) running period, obtained with our previous "skewed" fiducial cuts; blue points: same, but using H. Egiyan's recipe. Error bars are statistical only, while the grey band represents the systematic error.

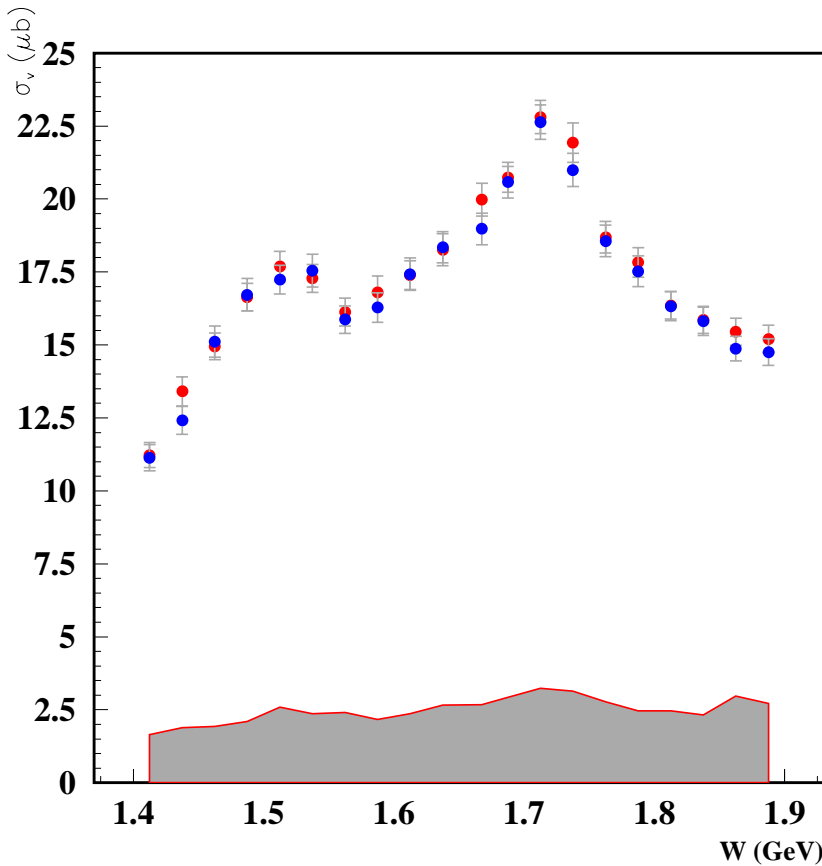


Figure 2.38: Total virtual photon cross section as a function of the CMS energy W for $ep \rightarrow ep\pi^+\pi^-$ at Q^2 between 0.8 and 1.1 GeV^2 ; red points: CLAS data from the e1c (1999) running period, obtained with our previous "skewed" fiducial cuts; blue points: same, but using H. Egiyan's recipe. Error bars are statistical only.

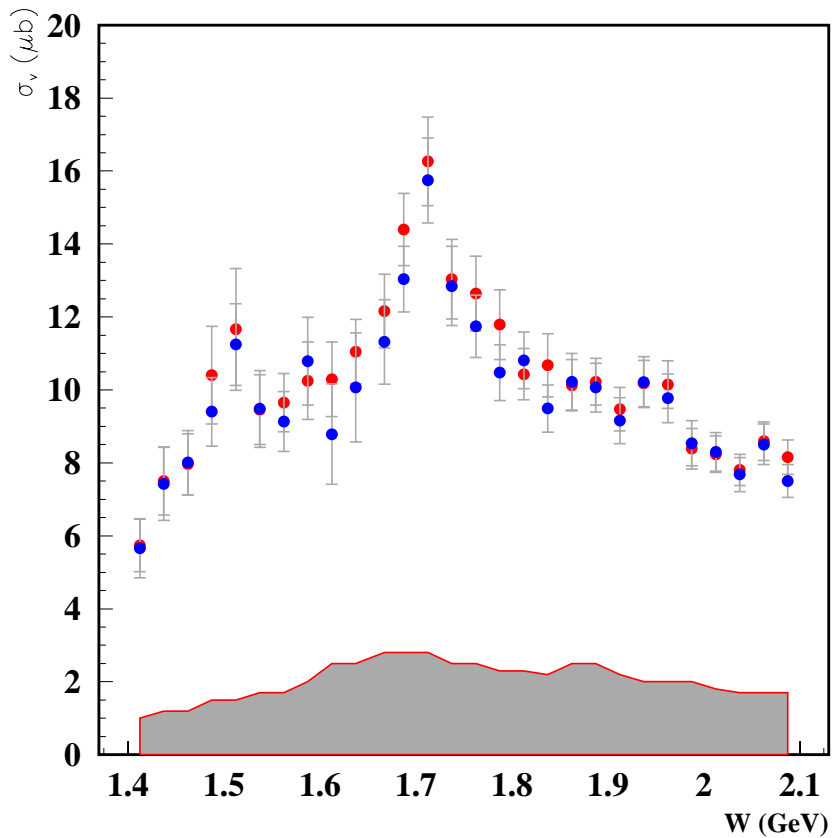


Figure 2.39: Total virtual photon cross section as a function of the CMS energy W for $ep \rightarrow ep\pi^+\pi^-$ at Q^2 between 1.1 and 1.5 GeV^2 ; red points: CLAS data from the e1c (1999) running period, obtained with our previous "skewed" fiducial cuts; blue points: same, but using H. Egiyan's recipe. Error bars are statistical only.

zero up to 8 %. A more detailed analysis of differential cross sections used in the physics analysis did not show any significant distortion effects due to such particular cases of bin migrations, considering that this analysis is after big unexpected multipoles and is not concerned with small effects at level of a few percent.

2.8.3 Integration

To estimate the systematic error due to the integration of finite bins, we performed the analysis using the three different sets of hadronic variables previously discussed and we calculated the same total cross section integrating differential cross sections from the three sets: therefore, the discrepancy in the total cross section numbers obtained may be an indication of the systematic error connected with the numerical integration procedure. For E1C, this systematic effect is typically of the order of 5 to 10 %. Thanks to the complete cross section calculation done for all three sets of hadronic variables, we have been able to compute and tabulate this systematic error for each W and Q^2 bin.

2.8.4 Fiducial Cuts

As mentioned in section 2.2.3, we calculated the total cross section using both the "skewed" fiducial cuts derived from UVa-Upitt as well as a modified version based on H. Egiyan π^+ analysis. Basically, the point here was that the "skewed" UVa-Pitt fiducial cuts do not contain the shrinking in ϕ as θ increases, adopted in Hovanes' analysis of single π^+ electroproduction. Therefore, as described in section 2.2.3 we implemented this shrinking to both protons and positive pions and recalculated all detector corrections and the final cross sections once again. Having obtained our cross sections from two different sets of fiducial cuts, we used the two sets of results as a measure of the systematic error associated to a change in the fiducial cuts; even though this difference appears to possibly be only of statistical origin (see previous cross section plots), we adopted a conservative point of view and decided to consider the difference (small, on the other hand) between the two sets of data points as a source of systematic error to be added in quadrature to the others, for each W and Q^2 bin.

2.8.5 Kinematic Coverage

As mentioned in section 2.2.3, we introduced a systematic error connected with the extrapolation procedure that we used to recover hadronic bins with zero acceptance. This was made possible by the estimate, given by the analysis of our Monte Carlo, of the percentage of events lost because of acceptance cuts; as a criterion to evaluate this systematic error, we decided to assume that the amount of events coming from the extrapolation may be wrong by as much as 50 %, being of course dependent on specific assumptions in the

Monte Carlo model cross sections. We therefore calculated the corresponding systematic error for each W and Q^2 bin, to be added to the other sources.

2.8.6 Radiative Corrections

Again our correction procedure is based on our Monte Carlo, which is certainly realistic but does not contain the exact cross sections that one should use in principle to calculate the radiated processes. Certainly the model dependence here is minimal as we extract from the data only a cross section corresponding to relatively "soft" photons that correspond to values of W and Q^2 very close to the ones under analysis; nevertheless, we made an estimate of how much the radiative effects change when modifying the cross sections in our Monte Carlo generator. For this purpose, we recalculated the radiative corrections switching off the phase space channel in the Monte Carlo and regenerating all events based on this modified cross section. From these tests, we derived a typical 3% systematic error.

2.8.7 Global Sector Uniformity Correction

In section 2.1.2 we showed that, despite the normalisation to the fiducial cuts acceptance and the fine details introduced in the simulation, most significantly the target shift with respect to the nominal position, we got an electron yield sector by sector which is not uniform; we therefore applied a global renormalisation factor referring to the most populated sector: from there, we estimated a systematic error of the order of 10%, essentially coming from the fitting error when deriving the electron yield sector by sector and thereby the renormalisation factor.

2.8.8 Photoelectron Cut

We performed the analysis varying the photoelectron cut from 2.5 to 2 and correspondingly correcting the data with the above described procedure. The resulting cross section change was about 1 %, demonstrating a relatively small sensitivity of our photoelectron fitting procedure to the applied cut; nevertheless, this small systematic error was included in the list of errors to be combined.

2.8.9 Missing Mass Cuts

Based on the GPP tuning procedure to get the right missing mass width in the MonteCarlo simulation, we estimated a 2 % systematic error related to the missing mass shape and the corresponding cuts; basically, we obtained this number looking at the different amount of events captured by the missing mass cut while slightly changing the peak width by tuning the GPP DOCA smearing parameters.

2.8.10 Summary of Systematics

From our studies, it turns out that the biggest sources of systematic error in particular W and Q^2 bins are the integration over hadronic variables (which may be partly correlated with the Monte Carlo model dependence), the extrapolation procedure and the bin migration from regions outside the domain of the GSIM simulation. Although some of the systematic errors discussed may be partly correlated and therefore our final estimate is likely to be a conservative one, we summed up all the errors above reported in quadrature to obtain the total systematic error: this quantity is reported as a grey band in the total cross section pictures, 2.37, 2.38 and 2.39.

Chapter 3

Concluding Remarks

We have presented in the first part of this document the data analysis technique to extract two pion electroproduction cross sections from the CLAS raw data. Only total cross sections as a function of W at different momentum transfers have been reported here. Some differential cross sections involved in our resonance analysis are extensively reported, together with the results of the analysis itself, in the second part of this document.

Part II

Resonance Analysis

Chapter 4

Generalities

4.1 Introduction

This analysis is aimed to extract the Q^2 dependence of N^* electromagnetic form factors $A_{1/2}(Q^2)$, $A_{3/2}(Q^2)$ as well as to search for possible signals from missing baryon states in the data about double charged pion production on proton by virtual photons, collected in experiment E93-006. Input information for this analysis are:

- ($p\pi^+$) and ($\pi^+\pi^-$) invariant mass distributions;
- π^- angular distributions

measured in various W and Q^2 bins. A specific phenomenological model, relating measured differential cross sections with N^* electromagnetic form factors $A_{1/2}(Q^2)$ and $A_{3/2}(Q^2)$, has been developed and used to extract N^* electromagnetic form factors from data fit.

4.2 Kinematics and observables

Two pion production from other experiments[19, 10, 22] shows the presence of isobar "quasi-two-body" states, $\Delta\pi$ and ρN , on top of an $N\pi\pi$ continuum which uniformly populates the Dalitz plot of the invariant masses $M_{p\pi^+}$ and $M_{\pi^+\pi^-}$. The description of a three-body final state is based on five independent kinematical variables in the most general case[14] and moreover the isobar quasi-two-body production and subsequent decay involves all of them[15]. In particular, it is necessary to choose a complete set of independent kinematic variables, in order to apply the appropriate acceptance corrections to the data. For instance, a convenient set is made up from the invariant mass of the $p\pi^+$ and the $\pi^+\pi^-$ pair, then the polar angles θ and ϕ of the π^- and finally the rotation freedom ψ of the $p\pi^+$ pair with respect to the so-called hadronic plane defined by the incoming virtual photon (incoming proton) and the outgoing π^- ; this set of variables is very appropriate for the analysis of resonance decay into $\Delta^{++}\pi^-$. We chose this method,

instead of applying a maximum likelihood procedure on an event-by-event basis, because in the analysis of data in the resonance region it is not sure *a priori* that models employed in the physics analysis are correctly describing the measured data distributions; on the other hand, a general partial-wave expansion is certainly very complicated and affected by strong ambiguities; instead, we derived experimental cross sections by binning and correcting the data in the full kinematic space: the observables derived can then be compared to any model calculation, knowledge of specific experimental features of the detector being not necessary.

4.3 Model calculations

Remarkable aspects of double pion electromagnetic production are the presence of many sizeable non-resonant mechanisms, characterized by a large number of partial waves; moreover, many overlapping resonances contribute to this cross section and their contribution is typically not dominant, but rather comparable to the non-resonant background; all these features give rise to ambiguities that make the model-independent extraction of partial waves not unique as experiments are limited to a restricted set of unpolarised observables; therefore only a model can guide to the extraction of the resonant amplitudes, but needs first to be tested on cross sections derived in a model-independent way. To be able to give at least a first interpretation of the data on two pion electroproduction, it is therefore necessary to have a model containing a description of the different possible production processes, in terms of both non-resonant mechanisms (Born terms and corrections to them) as well as resonance excitation, whose signal we want to pin down. The description of the non-resonant mechanisms is quite important because, at variance for instance with π^0 production in the $\Delta(1232)$ region, the continuum turns out to be a relevant contribution to the total cross section in this channel. Moreover, a treatment of the coupling of initial and final states to open inelastic channels in describing non-resonant mechanisms becomes increasingly important at increasing W .

There has been recently an increasing theoretical and phenomenological activity in the field of double pion electromagnetic production; a preliminary survey was done in [20]; an accurate model for this reaction, with a comprehensive description of all isospin channels, has been developed at low energy ($W \leq 1.6$ GeV) by the Valencia group[21] and compared to the recent precise data from MAMI[22]; however, due to the limited number of N^* included, as well as the absence of ISI and FSI treatment, this approach can be considered applicable only for relatively low W values (< 1.6 GeV): it is clear that this model is of little use in this experiment, where we look especially for resonant contributions *above* 1.6 GeV. A similar approach has been discussed in [23], focusing on specific non-resonant diagrams, but again, due to the reasons specified above for [21], the calculation is applicable to low energies only. ρ meson electroproduction has been calculated by [24], introducing σ meson exchange as the main contributor in the N^* region; as far as we know, this calculation does not contain N^* resonances and moreover other important

double pion mechanisms, as $\Delta\pi$ production, essential in the resonance region, are absent; ρ meson photoproduction has been also calculated in the framework of a quark model[25]: again other important production mechanisms are not accounted for; since the goal of our analysis is the extraction of N^* form factors from data with minimal model assumptions on hadron structure, clearly it does not look much appropriate to use a specific quark model of baryons. Given that all these activities date back to relatively recent times, it is clear how a comprehensive approach to treat several production mechanisms as well as low and high energies (especially important for the missing states search) was still to come on the theoretical side, when we started analysing CLAS data.

Foreseeing that the theoretical evolution was going to be not sufficient for a timely analysis and interpretation of the new data, we developed a phenomenological model, in cooperation with a Moscow State University group[27, 28], providing an extensive description of two pion cross sections both for real and virtual photons; a specific goal of our work was the initial interpretation of data from E-93-006 at JLAB that needs to accompany a first publication. The Genova-Moscow model provides a reasonable description of the two important intermediate isobar production mechanisms, $\gamma p \rightarrow \Delta\pi \rightarrow p\pi^+\pi^-$ and $\gamma p \rightarrow \rho^0 p \rightarrow p\pi^+\pi^-$; a third mechanism, the direct $\gamma p \rightarrow p\pi^+\pi^-$, often called “phase space”, was included as a pure phase space amplitude and fitted from the data as described below. (The presence of isobars (Δ and ρ meson) in the final two pion state can be observed looking at the cross section differential in the invariant mass of the $p\pi^+$ pair and of the $\pi\pi$ pair, respectively). Our model relates quantities of physical interest: N^* electromagnetic form factors, contributions from different quasi-two-body channels ($\Delta\pi$, ρp , phase space), resonant and non-resonant mechanisms, with measured observables like cross sections and spin asymmetries, allowing to extract those physical quantities from the data fit.

In the following subsections, we will briefly describe the main ingredients of our analysis code.

Chapter 5

The Analysis of E-93-006 data

5.0.1 Genova-Moscow Model Description

The main charged double pion production mechanisms were parametrized at level of meson-baryon tree diagrams. The reaction amplitude was assumed to be a superposition of $\gamma p \rightarrow \pi^- \Delta^{++}$, $\gamma p \rightarrow \pi^+ \Delta^0$ and $\gamma p \rightarrow \rho p$ quasi-two-body processes with subsequent decay of intermediate Δ and ρ . The remaining mechanisms were parametrized as an amplitude $C(W, Q^2)$ independent from the final state particle's quantum numbers and four-momenta, but representing a function of W and Q^2 to be determined from the data fit in each W and Q^2 bin. Three body amplitudes for each mentioned above quasi- two-body channel were estimated in Breit-Wigner ansatz as a product of quasi-two-body production amplitude, decay amplitude and Breit-Wigner propagator for the unstable particle in the intermediate state[27, 28]. The decay amplitudes for Δ and ρ were calculated from effective Lagrangians[27, 28] with mass-dependent form factors taken from [30]. The model for evaluation of quasi-two-body production amplitudes is described in details in [27, 28]. Here we present only the main ingredients.

The quasi-two-body amplitudes were treated as a superposition of N^* excitations and non-resonant mechanisms. We included 12 resonances with 3 or 4 stars according to the PDG listing, and a relevant contribution to the double pion channel, estimated based on the following figure of merit: the product of the square root of the radiative width and square root of two pion decay width, divided by the total width. N^* excitation was estimated in Breit-Wigner ansatz, where N^* decay amplitudes to $\pi\Delta$ and ρp final state in resonant point were taken from analysis [44]. W evolution of these amplitudes was described assuming as usually barrier penetration effects as a dominant factor. Electromagnetic vertices could be estimated from electromagnetic $A_{1/2,3/2}$ N^* form factors, taken either from experimental data or from any quark model prediction; on the other hand, they could be considered as free parameters to be extracted from data fit: the extraction of $A_{1/2,3/2}$ from the data represents the goal of our phenomenological analysis. To first make realistic predictions of the resonant content, we took PDG values[32] for real photons and a Single Quark Transition Model (SQTM) fit[43] for virtual photons as starting

point to describe N^* 's electromagnetic excitation. Non-resonant processes for $\gamma p \rightarrow \rho p$ channel were described in the frame of diffractive vector dominance model[33]; the magnitude of the non-resonant ρ meson diffractive production amplitude was assumed to be a free parameter, independent from W , to be determined from data fit. Non-resonant contributions for $\gamma p \rightarrow \pi^- \Delta^{++}$, channel were described by a superposition of Born terms initially proposed in [34]; to treat photon and pion off-shell behavior we implemented in the pion-exchange amplitude an electromagnetic pion form factor taken from [35] and a $\pi N \Delta$ vertex function obtained in NN scattering analysis[36]. To describe $\pi \Delta$ production at W above 1.7 GeV we substituted the pion propagator in the pion-in-flight term by a pion Regge trajectory as proposed in [37], with subsequent restoration of gauge invariance; the effective value of reggeon coupling is considered as W -independent free parameter to be determined from data fit.

We developed a specific approach to describe the interaction with open inelastic channel in the initial and final states[27, 28] for the $\pi \Delta$ channel: ISI and FSI effects were treated as a partial absorption of incoming γp (ρ p in the spirit of vector meson dominance) and outgoing $\pi^- \Delta^{++}$ particles; the penetration (absorption) coefficients were related with elastic ρp and $\pi \Delta$ scattering amplitudes, estimated in the frame of an isobar model[27, 28] based on world data on πN scattering.

As a test of our model, in figure 5.1 we present the comparison between ABBHHM data[19] on the energy dependence of the total cross section for $\gamma p \rightarrow p \pi^+ \pi^-$ at the photon point and our model calculation. Free model parameters, reggeon coupling, magnitude of non-resonant rho production amplitude and 3-body phase space were determined from simultaneous fit of $(p \pi^+)$ and $(\pi^+ \pi^-)$ invariant mass distributions. As follows from figure 5.1, our model succeeds in reproducing both the overall double charged pion production cross section as well as the contribution of $\gamma p \rightarrow \pi^- \Delta^{++}$ and $\gamma p \rightarrow \rho p$ quasi-two-body channels. We found[27, 28] that our model is able to reproduce all available world data on energy and momentum transfer dependence of overall and quasi-two-body cross sections, as well as the main features of invariant mass and angular distributions. Therefore we concluded that our model is treating properly the main mechanisms of double charged pion production in the kinematical range of our interest ($W < 2.0$ GeV, Q^2 , $-t \sim$ few GeV 2) and can be used for CLAS data analysis.

5.0.2 Technical Details on the Two Pion Code

From the previous paragraphs, it is quite clear that the treatment of the complete three-body state based on the different isobar intermediate channels is a rather complicated task, also from the computing point of view. To give an idea of the issues and figures involved, here we want to describe briefly the machinery of the code and the technical solutions adopted to repeat the calculations several times, as it happens for instance in fitting steps. The calculations are performed in the following way: a large kinematic grid is established for the five hadronic variables mentioned several times[39], consisting of 12 points for

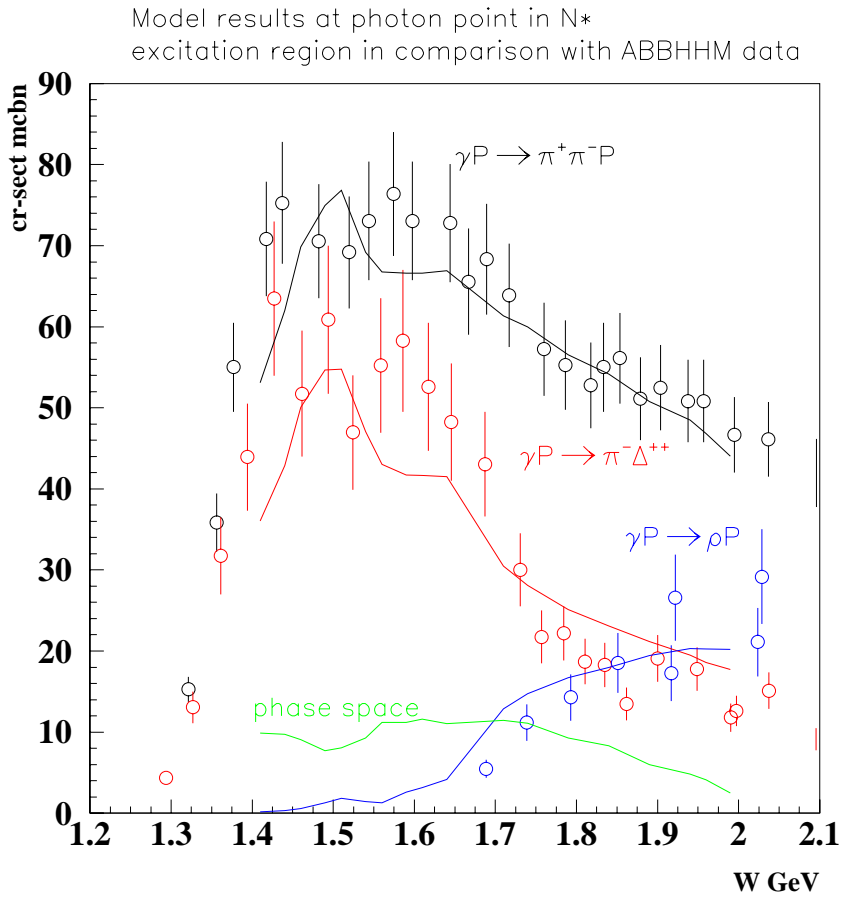


Figure 5.1: Charged double pion production total cross section for real photons as a function of W. Data from [19]. Curves from the Genova-Moscow code.

each invariant mass, 8 points for the CM θ_{π^-} angle and 8 points for the $\psi_{p\pi^+}$ rotation angle, therefore a total of 9216 kinematic points per W and Q^2 point; there is no need to consider explicitly the CM ϕ_{π^-} angle as the dependence of the cross section on it has a well known analytical form and can therefore be integrated at level of cross section formulas, while cross sections points in between the reference grid are calculated using a standard interpolation algorithm. In turn, considering approximately the number of processes and resonances involved, it is necessary to calculate something like a thousand different helicity amplitudes in each kinematic point or a couple of thousand double precision real numbers, for a total of about 18 million double precision real numbers; moreover, for the $\Delta\pi$ amplitudes it is necessary to compute all unitarity corrections, which means that each helicity amplitude has to be expanded in partial waves, corrected wave by wave and then reconstructed, which increases the quantity of real numbers to treat by about a factor 10: so we arrive to something like a 100 million double precision real numbers, whose calculation involves several floating point operations; it is clear that we can easily arrive to billions of floating point operations for the complete evaluation of the differential cross section in all hadronic kinematic points. To compute all quasi-two-body $\Delta\pi$ and $\rho\rho$ intermediate amplitudes for all resonances and non-resonant processes, as well as the Δ and ρ decay amplitudes and then put them all together to form the three-body overall 2π amplitudes for one W and Q^2 point takes about ???? hours on a Pentium III at 650 MHz running Linux. Therefore, our technical approach to perform several repeated calculations with different input parameters was to calculate once at the beginning all amplitudes and write them to very large lookup tables in form of disk-resident files: each subsequent calculation is then initiated reading these tables and downloading all amplitudes to the computer RAM; to do that for one W and Q^2 point takes about 120 Mbytes RAM; to achieve the capability of calculating more than one W and/or Q^2 point at once, the machines in the Genova Linux farm were equipped with a RAM ranging from 0.5 to 1 Gbyte and the disk swap space in each machine was increased to 1 Gbyte.

Concerning the search for the best parameters in our fits to the data, being them free parameters of non-resonant processes or resonance couplings, we adopted the standard criterion of χ^2 minimization, where χ^2 was calculated summing over all differential cross section points under analysis, at all W values for one or more Q^2 intervals, considering as degrees of freedom all parameters subject to variation.

5.0.3 Fixing Model Free Parameters

Our approach contains free parameters, that we do not know how to calculate: therefore they should be extracted from the data fit. These parameters are:

1. the Regge trajectory coupling appearing as a scale factor (Reggeon coupling) in the "pion-in-flight" Born term for the $\pi\Delta$ quasi-two-body channel; this factor appears since Regge trajectory effectively accounts for exchange of many mesons (belonging to the pion Regge trajectory) with different strong and electromagnetic couplings.

We assume this scale factor to be independent from W , however we assume a possible Q^2 dependence of this coupling.

2. In our description of non-resonant ρ diffractive production we take the diffractive slope in t from experimental data collected above N^* excitation region[33], considering their value as W -independent. Since in the N^* excitation region the total ρp production amplitude is determined by a coherent superposition of resonant and non-resonant mechanisms and we overlap the ρ production threshold, we prefer to keep the magnitude of the diffractive production amplitude as a free parameter, instead of fixing it at the value extracted from fit of data above the N^* excitation region: we assume that this parameter is W -independent, however we did not exclude a possible Q^2 -dependence.
3. The third free parameter of our approach is the three-body phase space $C(W, Q^2)$, representing as discussed above a phenomenological parametrisation for all remaining mechanisms not accounted for by our explicit amplitudes for $\pi\Delta$ and ρp production.

In order to keep this first physical analysis as simple and clear as possible, we decided to adopt a simple fitting procedure, based on the three most important experimental distributions: two invariant masses describing the intermediate isobar production and one azimuthal angular distribution in the CM; as angle, we chose θ_{π^-} , being this angle directly connected with the $\Delta\pi$ production process in the sense that a quasi-two-body description of this channel can be done using namely θ_{π^-} (of course, this angle reflects also the presence of the other mechanisms, but in a more indirect way).

Our procedure was therefore to first fit the model parameters at each Q^2 in the whole range of W to derive their best value: this first fit was performed varying at the same time the coupling of a few resonances relevant in the particular W bin under analysis, to ensure that the fit was flexible enough to allow for a good reproduction of the experimental distributions already at this stage; then the analysis was repeated keeping the non-resonant parameters fixed and focusing on specific resonance contributions. Needless to say, with this procedure a separation between the various isobar channels is also obtained. As examples, we report in figures 5.2 through 5.11 the fitted differential cross sections, for all three Q^2 intervals and for the W intervals where there is an appreciable sensitivity to the fitted parameters. As it follows from the figures, the forward angle slope in angular distributions is strongly affected by non-resonant process contributions: this slope at high W depends both on the Reggeon coupling for the $\pi\Delta$ channel as well as on the magnitude of ρ diffractive production. The good description of angular distributions that we got from our calculation provides confidence in the proper treatment of non-resonant processes, while the simultaneous reproduction of ρ and Δ peaks in $(\pi^+\pi^-)$ and $(p\pi^+)$ invariant mass distributions ensures that we can properly distinguish between $\pi\Delta$ and ρp channels. We found that data could be described by W and Q^2 independent Reggeon coupling

and diffractive amplitude. We observed sizeable interference effects between resonant and non-resonant mechanisms for W bins between 1.79 and 1.89 GeV. Good reproduction of angular distributions in these bins suggests a proper treatment of interference effects.

5.0.4 Nominal Model Calculation

Based on the free-parameter fit described in the previous section, we first calculated the cross section predicted in our model, using as input for the resonance photocouplings as a function of Q^2 the SQTM/empirical fit by V. Burkert[43]: we will refer to this comparison as the "nominal" calculation, in the sense that in this case we make a model prediction based on conventional resonances and existing experimental information, plus of course some theoretical assumptions that are behind the SQTM fits of the N^* photocouplings. In figure 5.12 we report the results of such nominal calculation for all three momentum transfers, as a function of W, compared to the experimental data from CLAS. It is evident how, while the second resonance region, dominated by the Roper resonance and the $D_{13}(1520)$, is well reproduced at all Q^2 using namely the existing experimental information on the resonance photocouplings, we have a sizeable missing strength in the third resonance region around 1.7 GeV for the two lower momentum transfers and perhaps some missing strength for the last momentum transfer, too. The results of 1-differential cross section description for W bins between 1.49 and 1.61 GeV at $Q^2 = 0.65 \text{ GeV}^2$ are shown in figures 5.13 through 5.17, together with decomposition into contributions of different quasi-two-body channels. The complete set of plots for all W and Q^2 bins under the SQTM assumption can be found in http://www.jlab.org/Hall-B/secure/e1/mokeev/ps_final/sqtm: the files *sqtmc[xxx]_[yyy].ps* contain 1-differential cross section plots with decomposition into quasi-two-body channels $\gamma p \rightarrow \pi^- \Delta^{++}$ (red curves), $\gamma p \rightarrow \rho p$ (green curves), $\gamma p \rightarrow \pi^+ \Delta^0$ (blue curves) and 3-body phase space (magenta curves). The W dependence of the total cross-section is presented in *w_sqtm.ps*.

Another remarkable feature of the comparison between nominal calculation and data is that, due to the specific contribution of the $P_{13}(1720)$, we obtain a quite prominent ρ meson production peak in the $\pi\pi$ invariant mass, which is not seen in the CLAS data: this is very well visible in pictures 5.18 through 5.20, where the two experimental mass distributions are reported in the first two plots, together with our calculation, at the three momentum transfer values: the pion-pion calculated mass plot is evidently affected by a large ρ production peak, absent in the data. In pictures 5.21 through 5.23 we report the same data together with our calculation, but this time subdivided into overall resonant and non-resonant contributions: it is evident in these last three pictures that the overshoot in ρ meson production is namely coming from resonance excitation and a closer inspection shows that the $P_{13}(1720)$ is indeed responsible for that, being the state among those contributing in the region around 1.7 GeV with the largest branching ratio to the ρp channel ($87 \pm 5 \%$ [44]). The branching ratios of this particular state in the two pion

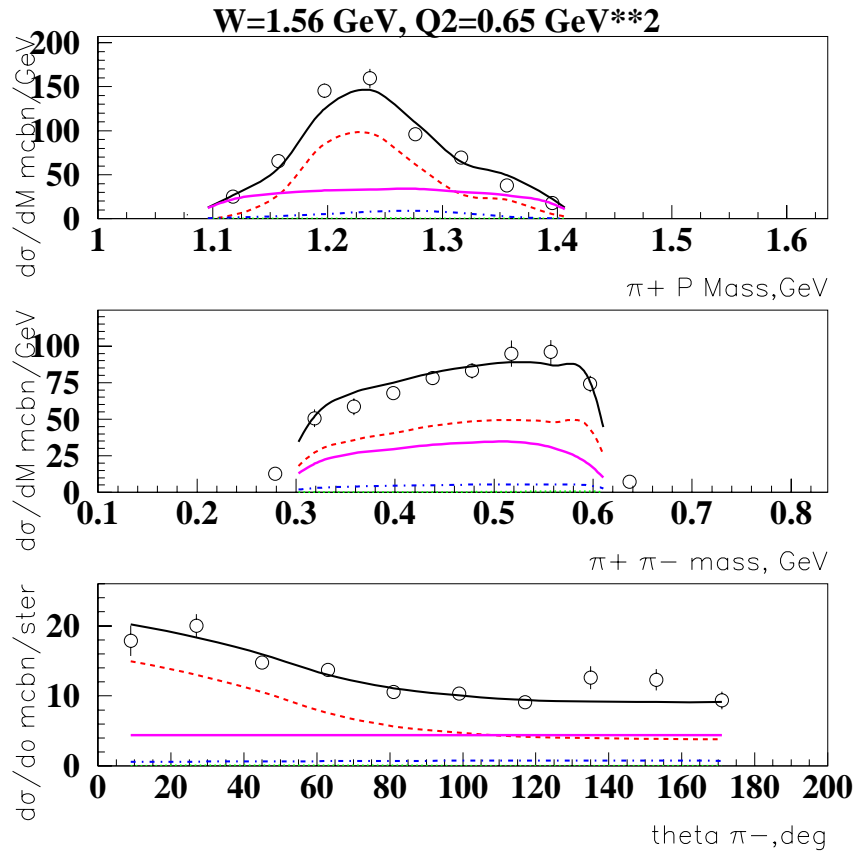


Figure 5.2: Virtual photon cross section for $ep \rightarrow ep\pi^+\pi^-$ at Q^2 between 0.5 and 0.8 GeV^2 and W between 1.55 and 1.575 GeV , differential in (top to bottom): proton- π^+ invariant mass; $\pi^+\pi^-$ invariant mass; π^- angle θ . Data from CLAS; red dashed line: $\Delta^{++}\pi^-$ contribution estimated in our fit; blue dot-dashed line: $\Delta^0\pi^+$ contribution estimated in our fit; green dotted line: ρ meson contribution estimated in our fit; magenta full line: phase space contribution estimated in our fit; black full line: total of all contributions estimated in our fit.

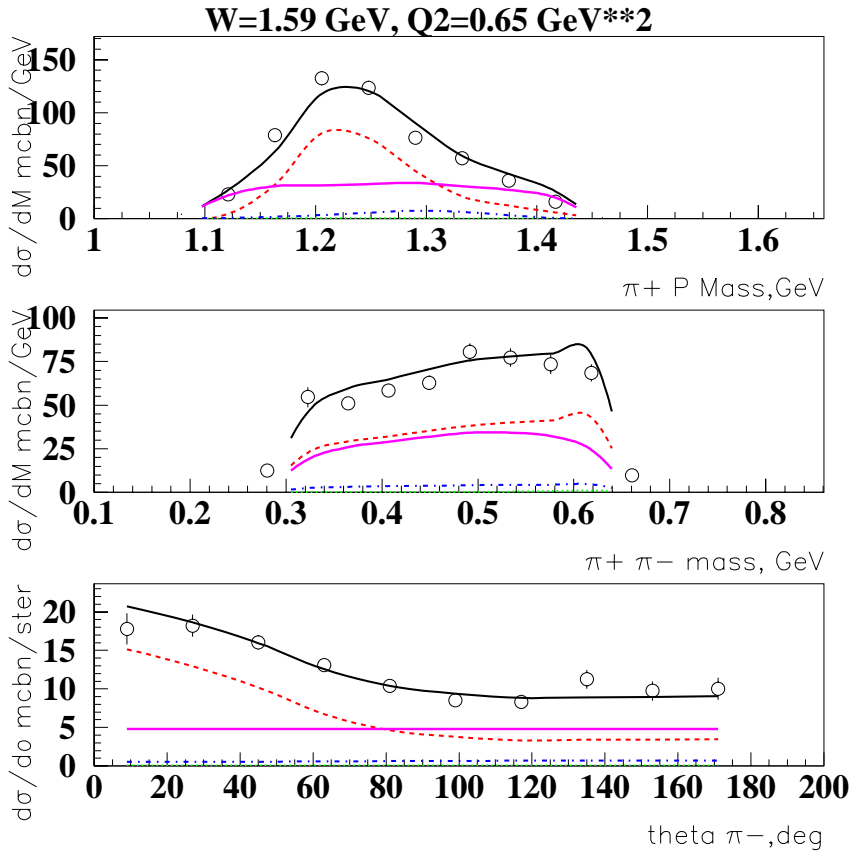


Figure 5.3: Virtual photon cross section for $ep \rightarrow ep\pi^+\pi^-$ at Q^2 between 0.5 and 0.8 GeV^2 and W between 1.55 and 1.575 GeV , differential in (top to bottom): proton- π^+ invariant mass; $\pi^+\pi^-$ invariant mass; π^- angle θ . Data from CLAS; red dashed line: $\Delta^{++}\pi^-$ contribution estimated in our fit; blue dot-dashed line: $\Delta^0\pi^+$ contribution estimated in our fit; green dotted line: ρ meson contribution estimated in our fit; magenta full line: phase space contribution estimated in our fit; black full line: total of all contributions estimated in our fit.

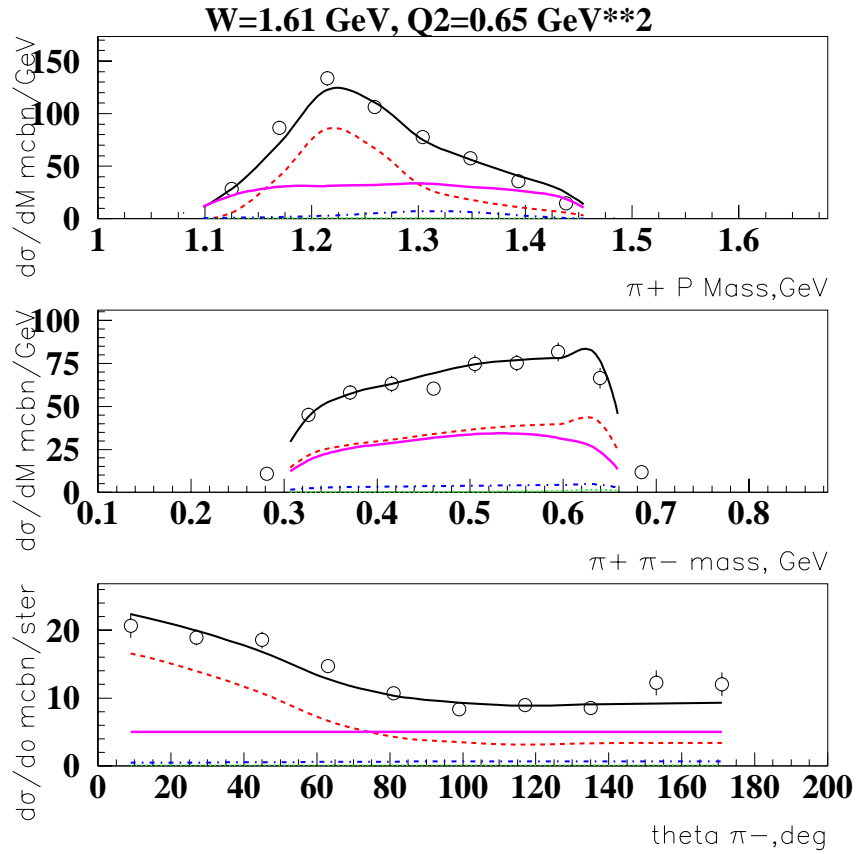


Figure 5.4: Virtual photon cross section for $ep \rightarrow ep\pi^+\pi^-$ at Q^2 between 0.5 and 0.8 GeV^2 and W between 1.55 and 1.575 GeV , differential in (top to bottom): proton- π^+ invariant mass; $\pi^+\pi^-$ invariant mass; π^- angle θ . Data from CLAS; red dashed line: $\Delta^{++}\pi^-$ contribution estimated in our fit; blue dot-dashed line: $\Delta^0\pi^+$ contribution estimated in our fit; green dotted line: ρ meson contribution estimated in our fit; magenta full line: phase space contribution estimated in our fit; black full line: total of all contributions estimated in our fit.

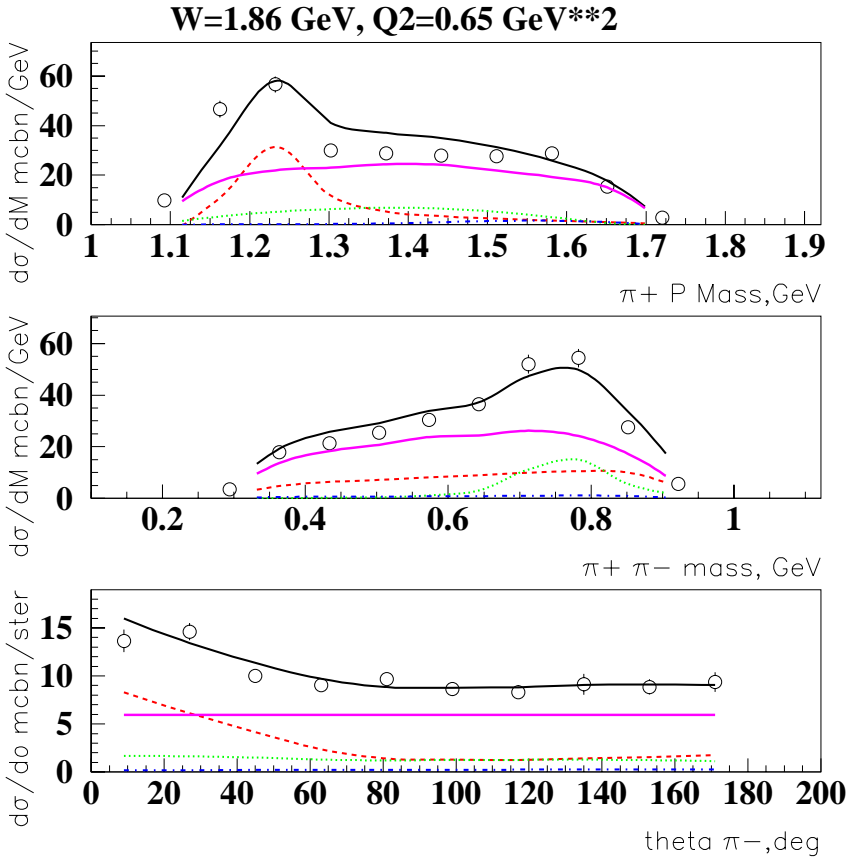


Figure 5.5: Virtual photon cross section for $ep \rightarrow ep\pi^+\pi^-$ at Q^2 between 0.5 and 0.8 GeV^2 and W between 1.55 and 1.575 GeV , differential in (top to bottom): proton- π^+ invariant mass; $\pi^+-\pi^-$ invariant mass; π^- angle θ . Data from CLAS; red dashed line: $\Delta^{++}\pi^-$ contribution estimated in our fit; blue dot-dashed line: $\Delta^0\pi^+$ contribution estimated in our fit; green dotted line: ρ meson contribution estimated in our fit; magenta full line: phase space contribution estimated in our fit; black full line: total of all contributions estimated in our fit.

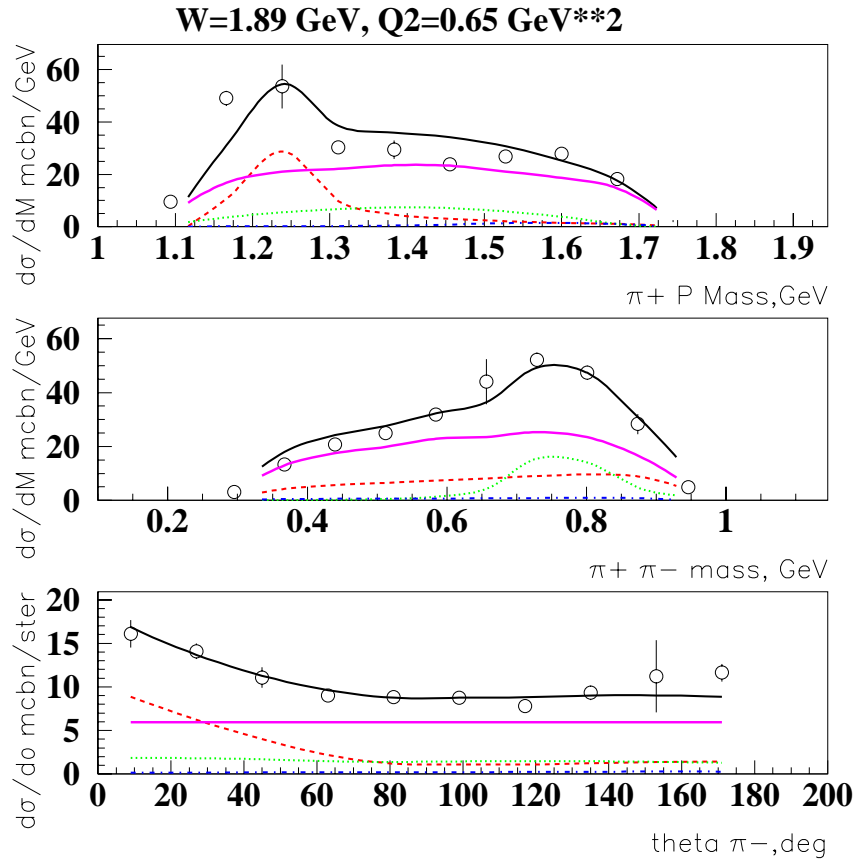


Figure 5.6: Virtual photon cross section for $ep \rightarrow ep\pi^+\pi^-$ at Q^2 between 0.5 and 0.8 GeV^2 and W between 1.55 and 1.575 GeV , differential in (top to bottom): proton- π^+ invariant mass; $\pi^+\pi^-$ invariant mass; π^- angle θ . Data from CLAS; red dashed line: $\Delta^{++}\pi^-$ contribution estimated in our fit; blue dot-dashed line: $\Delta^0\pi^+$ contribution estimated in our fit; green dotted line: ρ meson contribution estimated in our fit; magenta full line: phase space contribution estimated in our fit; black full line: total of all contributions estimated in our fit.

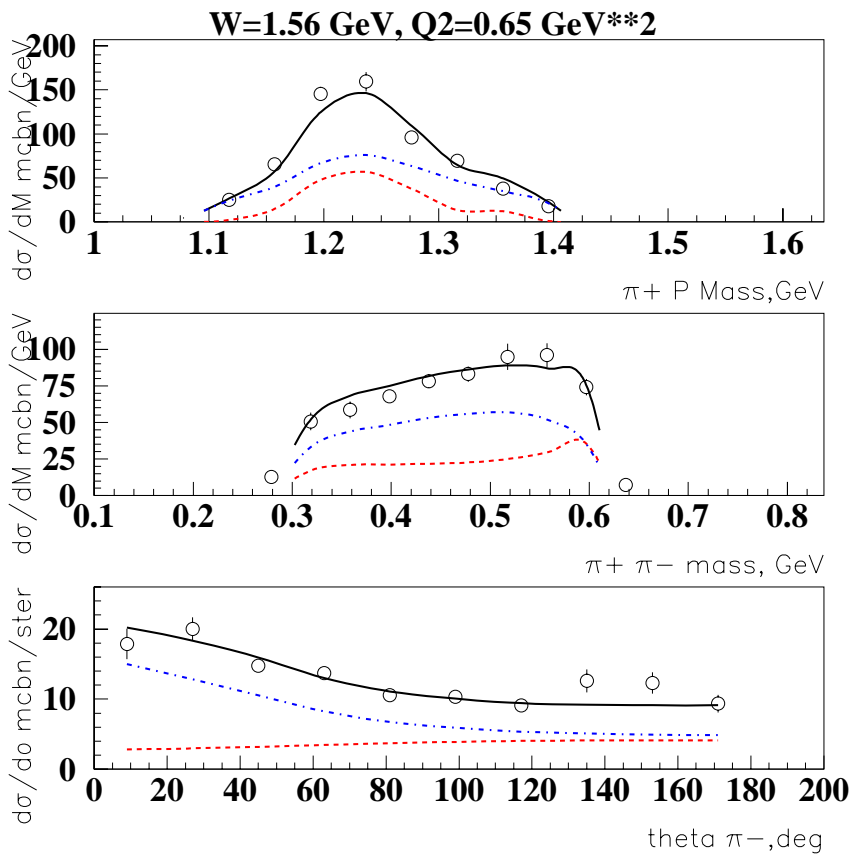


Figure 5.7: Virtual photon cross section for $ep \rightarrow ep\pi^+\pi^-$ at Q^2 between 0.5 and 0.8 GeV^2 and W between 1.55 and 1.575 GeV , differential in (top to bottom): proton- π^+ invariant mass; $\pi^+ \pi^-$ invariant mass; π^- angle θ . Data from CLAS; red dashed line: all resonant contributions estimated in our fit; blu dot-dashed line: all non-resonant contributions estimated in our fit; black full line: sum of all terms estimated in our fit.

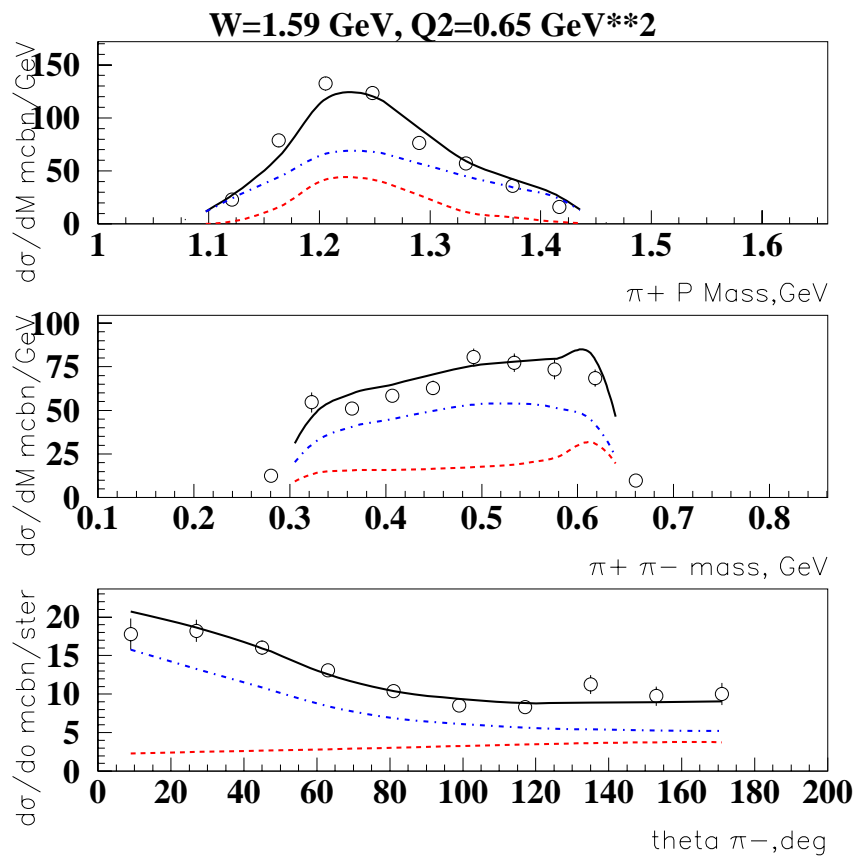


Figure 5.8: Virtual photon cross section for $ep \rightarrow ep\pi^+\pi^-$ at Q^2 between 0.5 and 0.8 GeV^2 and W between 1.55 and 1.575 GeV , differential in (top to bottom): proton- π^+ invariant mass; $\pi^+\pi^-$ invariant mass; π^- angle θ . Data from CLAS; red dashed line: all resonant contributions estimated in our fit; blu dot-dashed line: all non-resonant contributions estimated in our fit; black full line: sum of all terms estimated in our fit.

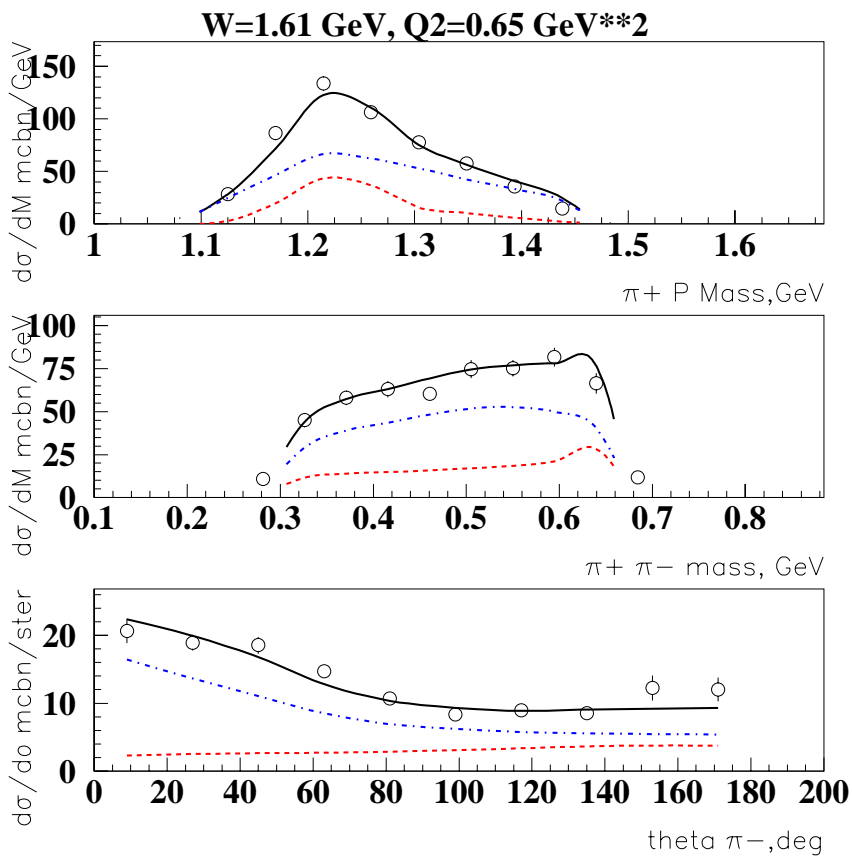


Figure 5.9: Virtual photon cross section for $ep \rightarrow ep\pi^+\pi^-$ at Q^2 between 0.5 and 0.8 GeV^2 and W between 1.55 and 1.575 GeV , differential in (top to bottom): proton- π^+ invariant mass; $\pi^+-\pi^-$ invariant mass; π^- angle θ . Data from CLAS; red dashed line: all resonant contributions estimated in our fit; blu dot-dashed line: all non-resonant contributions estimated in our fit; black full line: sum of all terms estimated in our fit.

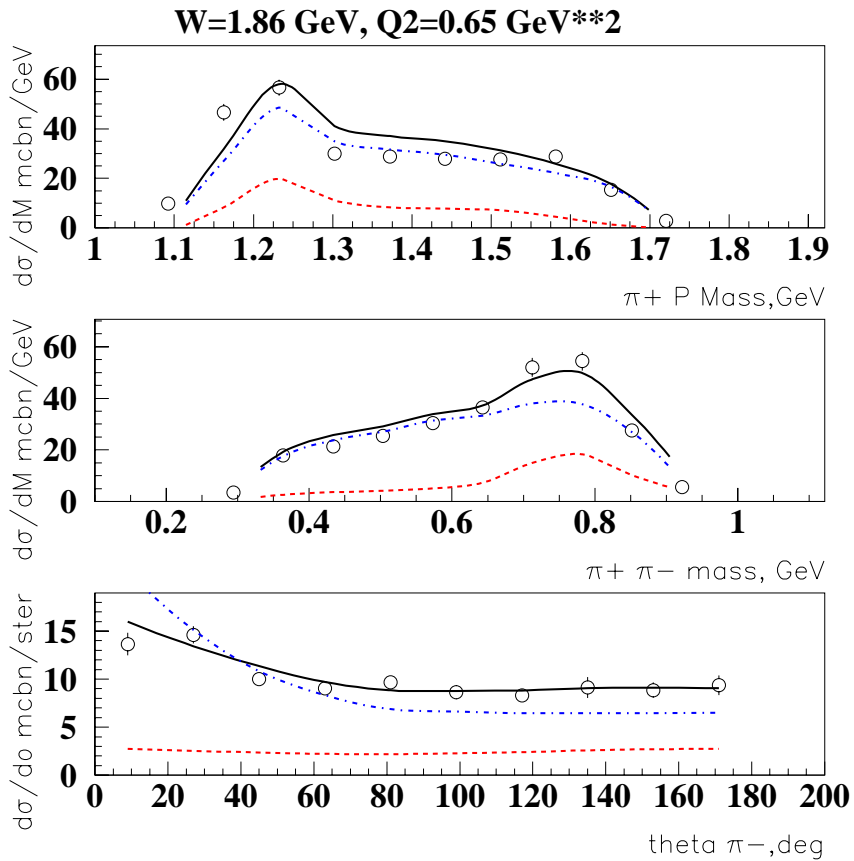


Figure 5.10: Virtual photon cross section for $ep \rightarrow ep\pi^+\pi^-$ at Q^2 between 0.5 and 0.8 GeV 2 and W between 1.55 and 1.575 GeV, differential in (top to bottom): proton- π^+ invariant mass; $\pi^+\pi^-$ invariant mass; π^- angle θ . Data from CLAS; red dashed line: all resonant contributions estimated in our fit; blue dot-dashed line: all non-resonant contributions estimated in our fit; black full line: sum of all terms estimated in our fit.

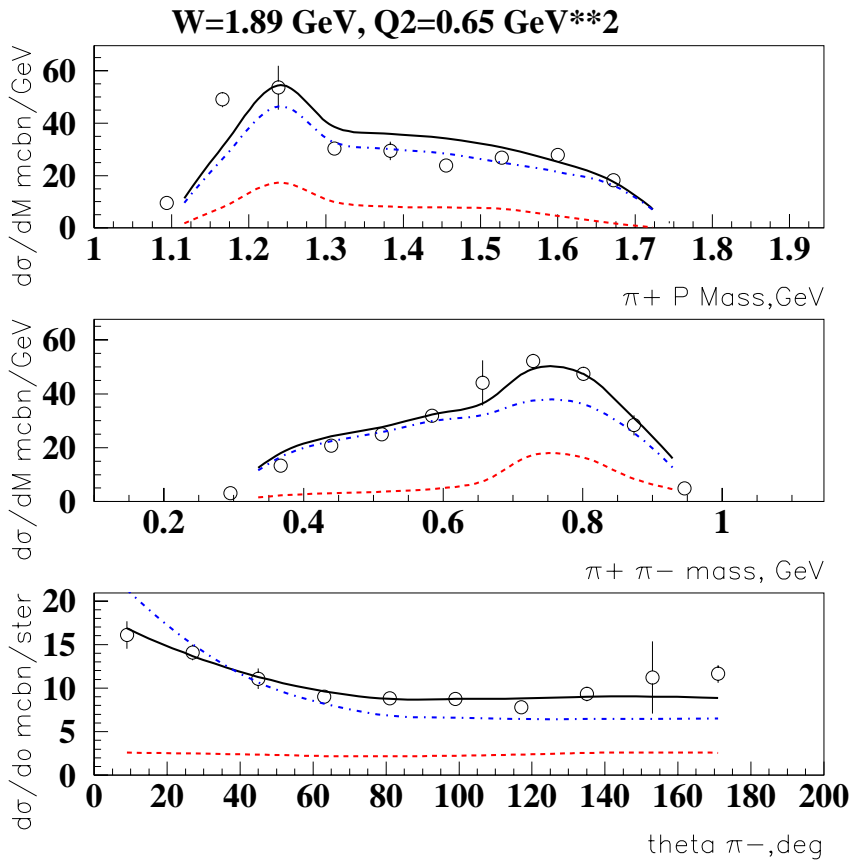


Figure 5.11: Virtual photon cross section for $ep \rightarrow ep\pi^+\pi^-$ at Q^2 between 0.5 and 0.8 GeV^2 and W between 1.55 and 1.575 GeV , differential in (top to bottom): proton- π^+ invariant mass; $\pi^+\pi^-$ invariant mass; π^- angle θ . Data from CLAS; red dashed line: all resonant contributions estimated in our fit; blu dot-dashed line: all non-resonant contributions estimated in our fit; black full line: sum of all terms estimated in our fit.

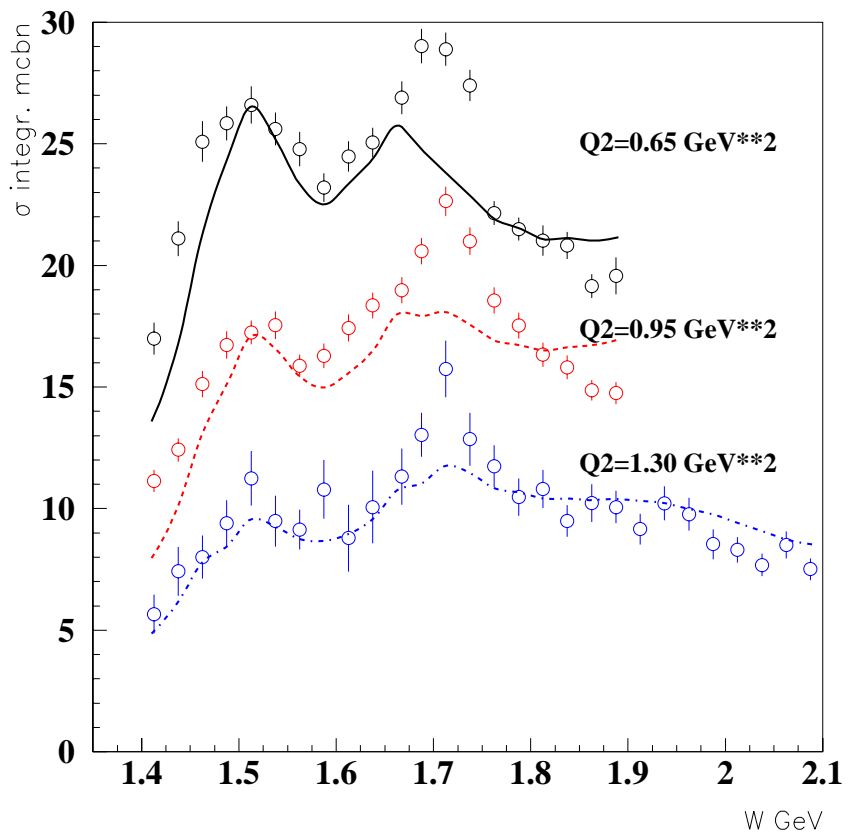


Figure 5.12: Total virtual photon cross section for $ep \rightarrow ep\pi^+\pi^-$ for all Q^2 as a function of W . Data from CLAS; Curves represent our "nominal" calculation as described in the text.

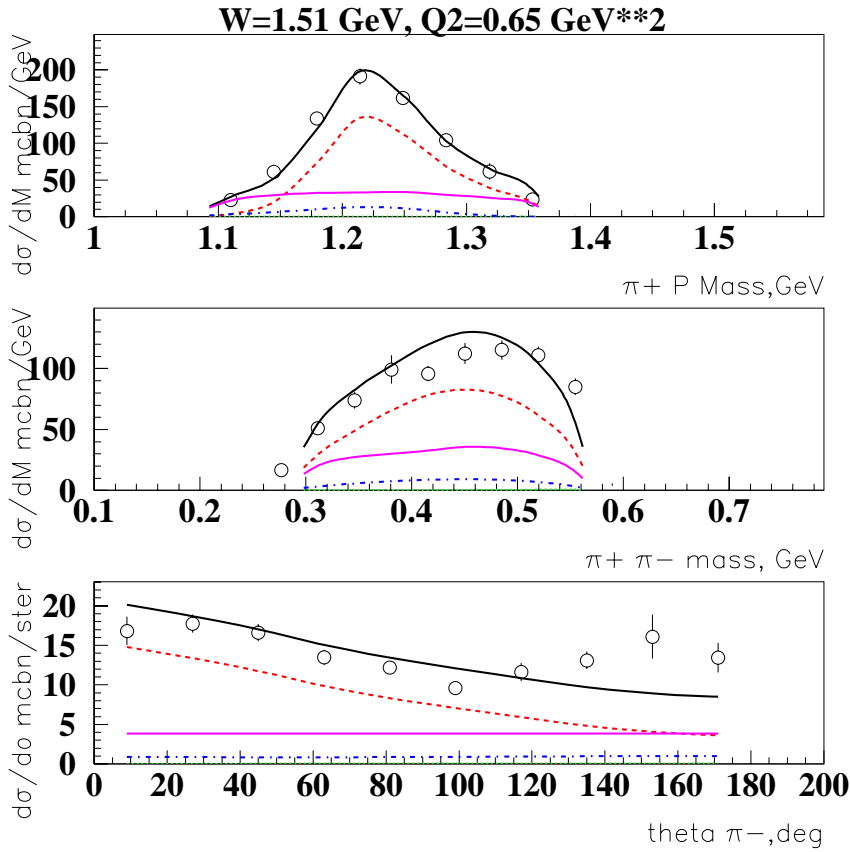


Figure 5.13: Virtual photon cross section for $ep \rightarrow ep\pi^+\pi^-$ at Q^2 between 0.5 and 0.8 GeV^2 and W between 1.5 and 1.525 GeV , differential in (top to bottom): proton- π^+ invariant mass; $\pi^+-\pi^-$ invariant mass. Data from CLAS; red dashed line: all $\Delta^{++}\pi^-$ contributions in our "nominal" calculation; blu dot-dashed line: all $\Delta^0\pi^+$ contributions in our "nominal" calculation; green dot-dashed line: all $\rho^0\rho$ contributions in our "nominal" calculation; magenta full line: phase space contribution in our "nominal" calculation; black full line: sum of all sub-channels in our "nominal" calculation.

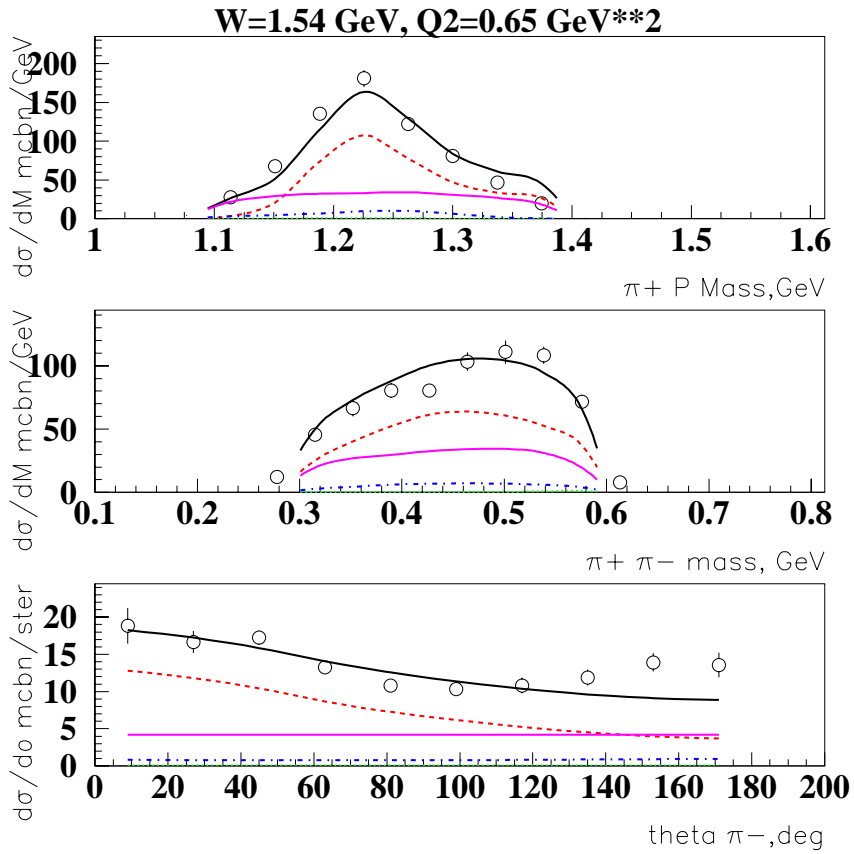


Figure 5.14: Virtual photon cross section for $ep \rightarrow ep\pi^+\pi^-$ at Q^2 between 0.5 and 0.8 GeV^2 and W between 1.525 and 1.550 GeV , differential in (top to bottom): proton- π^+ invariant mass; $\pi^+\pi^-$ invariant mass. Data from CLAS; red dashed line: all $\Delta^{++}\pi^-$ contributions in our "nominal" calculation; blue dot-dashed line: all $\Delta^0\pi^+$ contributions in our "nominal" calculation; green dot-dashed line: all $\rho^0 p$ contributions in our "nominal" calculation; magenta full line: phase space contribution in our "nominal" calculation; black full line: sum of all sub-channels in our "nominal" calculation.

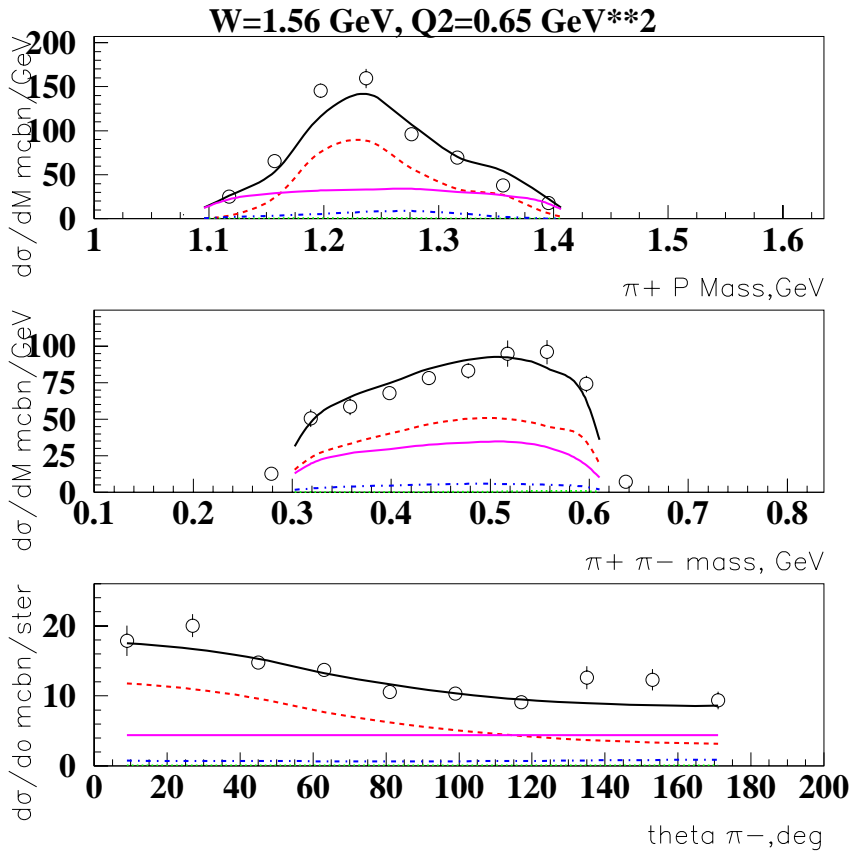


Figure 5.15: Virtual photon cross section for $ep \rightarrow ep\pi^+\pi^-$ at Q^2 between 0.5 and 0.8 GeV^2 and W between 1.550 and 1.575 GeV , differential in (top to bottom): proton- π^+ invariant mass; $\pi^+\pi^-$ invariant mass. Data from CLAS; red dashed line: all $\Delta^{++}\pi^-$ contributions in our "nominal" calculation; blu dot-dashed line: all $\Delta^0\pi^+$ contributions in our "nominal" calculation; green dot-dashed line: all $\rho^0\rho$ contributions in our "nominal" calculation; magenta full line: phase space contribution in our "nominal" calculation; black full line: sum of all sub-channels in our "nominal" calculation.

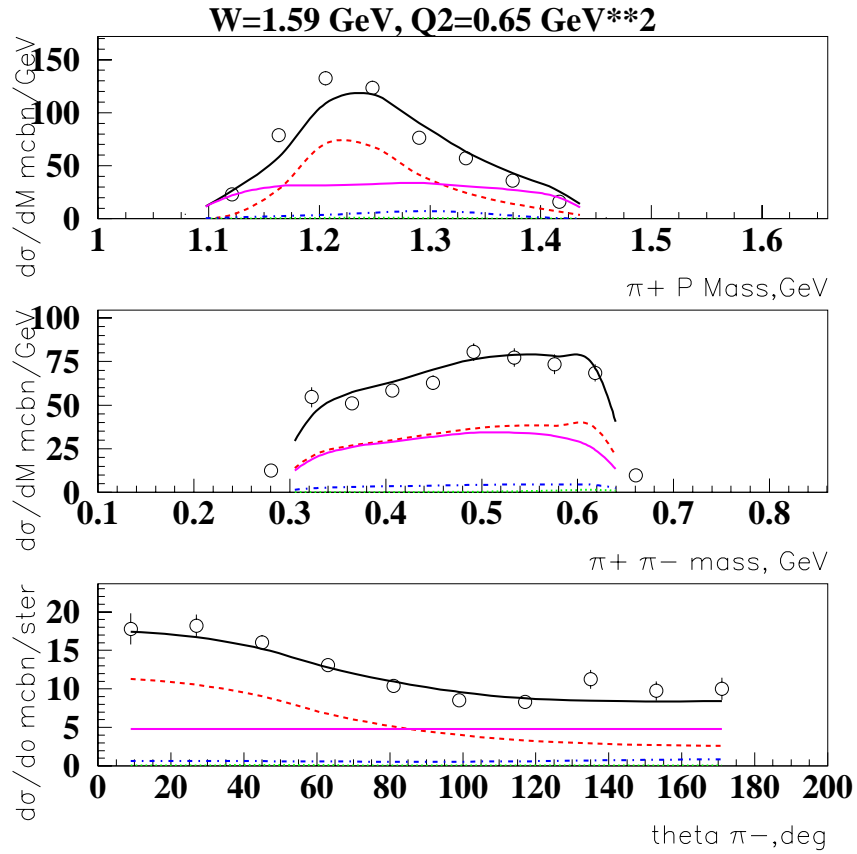


Figure 5.16: Virtual photon cross section for $ep \rightarrow ep\pi^+\pi^-$ at Q^2 between 0.5 and 0.8 GeV^2 and W between 1.575 and 1.6 GeV , differential in (top to bottom): proton- π^+ invariant mass; $\pi^+\pi^-$ invariant mass. Data from CLAS; red dashed line: all $\Delta^{++}\pi^-$ contributions in our "nominal" calculation; blue dot-dashed line: all $\Delta^0\pi^+$ contributions in our "nominal" calculation; green dot-dashed line: all $\rho^0 p$ contributions in our "nominal" calculation; magenta full line: phase space contribution in our "nominal" calculation; black full line: sum of all sub-channels in our "nominal" calculation.

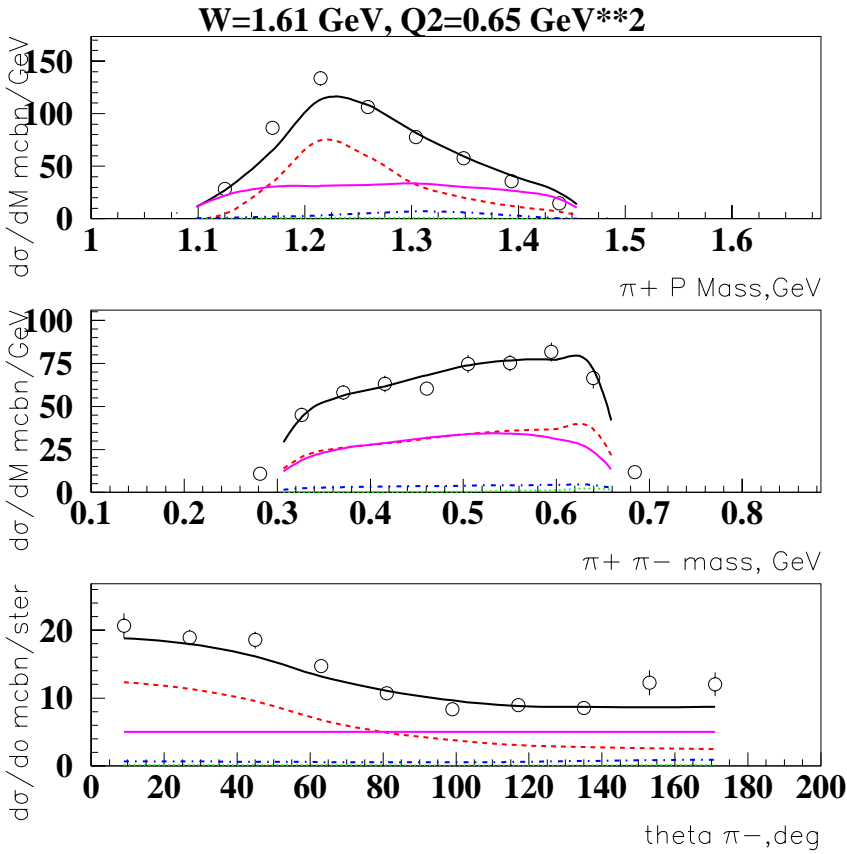


Figure 5.17: Virtual photon cross section for $ep \rightarrow ep\pi^+\pi^-$ at Q^2 between 0.5 and 0.8 GeV^2 and W between 1.6 and 1.625 GeV , differential in (top to bottom): proton- π^+ invariant mass; $\pi^+ \pi^-$ invariant mass. Data from CLAS; red dashed line: all $\Delta^{++}\pi^-$ contributions in our "nominal" calculation; blue dot-dashed line: all $\Delta^0\pi^+$ contributions in our "nominal" calculation; green dot-dashed line: all $\rho^0\rho$ contributions in our "nominal" calculation; magenta full line: phase space contribution in our "nominal" calculation; black full line: sum of all sub-channels in our "nominal" calculation.

channels was taken from ref. [44], where it is quite clear that, according to the error reported, there is not much space to reduce the branching ratio of 80 % to the ρ meson channel. Instead, our data show a lack of strength in the $\Delta\pi$ channel, that would require an increase of this branch for the $P_{13}(1720)$, again incompatible with analysis [44]. A more recent and more sophisticated global analysis of hadronic data[45], finds a similar result for the ρ branching ratio, therefore we assumed that we should not change the hadronic decay of this state to interpret our data. Instead, we assumed that for this particular state there may be a failure of the SQTM predictions and therefore the electromagnetic form factors should be modified: accordingly we decreased its two helicity couplings to reflect the CLAS experimental mass distributions, as discussed in the section 2.0.6. Moreover, the measured excess of total cross section around 1.7 GeV cannot be filled by enhancing the $P_{13}(1720)$ electromagnetic coupling with respect to SQTM prediction, since that would give rise to the above discussed ρ peak in the $\pi^+\pi^-$ invariant mass distributions around 1.7 GeV, not supported by CLAS data.

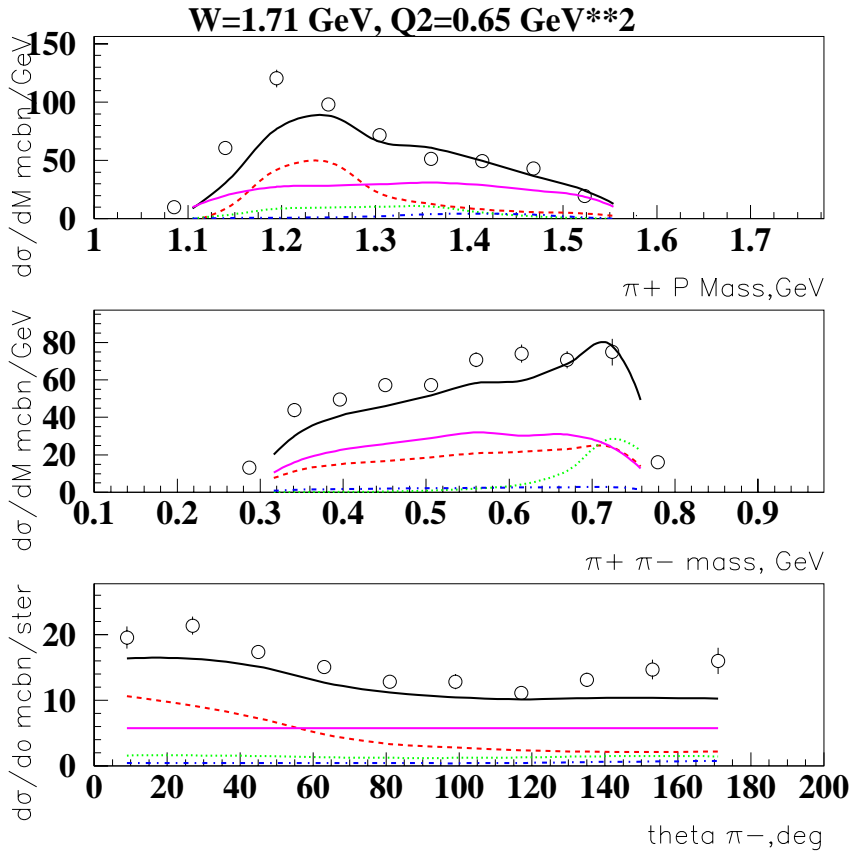


Figure 5.18: Virtual photon cross section for $ep \rightarrow ep\pi^+\pi^-$ at Q^2 between 0.5 and 0.8 GeV^2 and W between 1.7 and 1.725 GeV , differential in (top to bottom): proton- π^+ invariant mass; $\pi^+-\pi^-$ invariant mass. Data from CLAS; red dashed line: all $\Delta^{++}\pi^-$ contributions in our "nominal" calculation; blu dot-dashed line: all $\Delta^0\pi^+$ contributions in our "nominal" calculation; green dot-dashed line: all $\rho^0\rho$ contributions in our "nominal" calculation; magenta full line: phase space contribution in our "nominal" calculation; black full line: sum of all sub-channels in our "nominal" calculation.

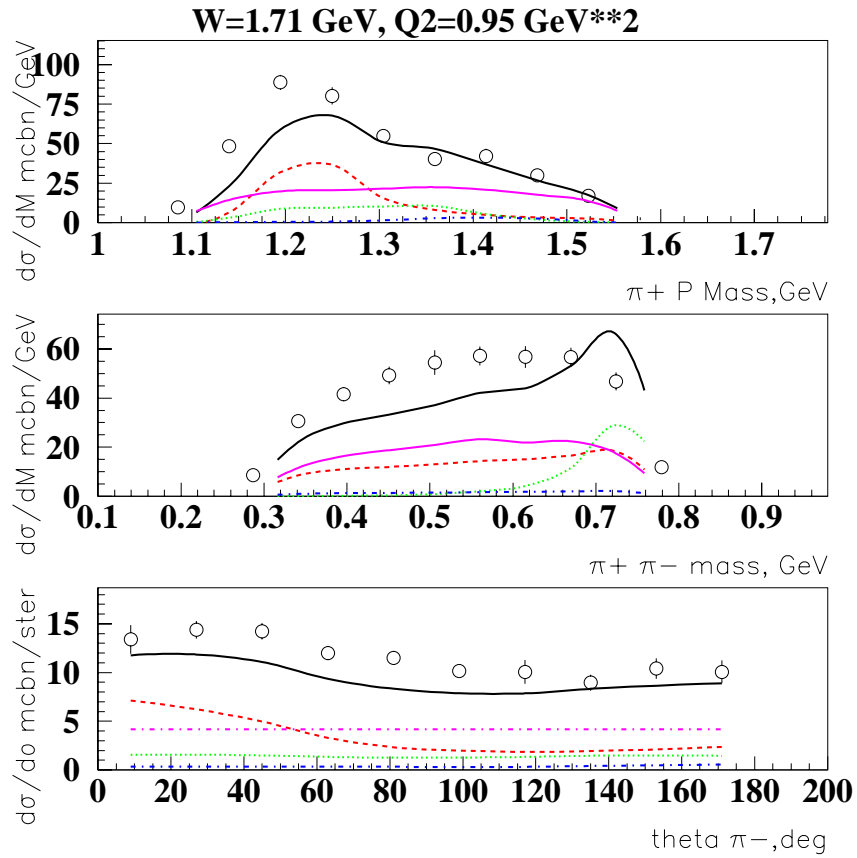


Figure 5.19: Virtual photon cross section for $ep \rightarrow ep\pi^+\pi^-$ at Q^2 between 0.8 and 1.1 GeV^2 and W between 1.7 and 1.725 GeV , differential in (top to bottom): proton- π^+ invariant mass; $\pi^+\pi^-$ invariant mass. Data from CLAS; red dashed line: all $\Delta^{++}\pi^-$ contributions in our "nominal" calculation; blue dot-dashed line: all $\Delta^0\pi^+$ contributions in our "nominal" calculation; green dot-dashed line: all $\rho^0 p$ contributions in our "nominal" calculation; magenta full line: phase space contribution in our "nominal" calculation; black full line: sum of all sub-channels in our "nominal" calculation.

5.0.5 Basic Features of Fitting Procedure

N^* electromagnetic form factors $A_{1/2,3/2}(Q^2)$ were extracted from a fit of $\pi^+\pi^-$ and $p\pi^+$ invariant mass and π^- angular distributions in all available W and Q^2 bins. The use of standard fitting techniques as MINUIT, however, faces severe obstacles both from the technical point of view: in our approach we evaluated all 1-differential cross-sections after proper integration of 5-differential cross-section, completely describing the final $\pi^+\pi^-p$ state; in each W and Q^2 bin we estimate the 5-differential cross-section in 9216 kinematical points corresponding to the kinematical net mentioned above; our data are collected at 20 W points for $Q^2=0.65, 0.95 \text{ GeV}^2$ and at 28 points for $Q^2=1.30 \text{ GeV}^2$; therefore, to fit the measured 1-differential cross-sections we had to calculate the 5-differential cross-section in 184320 points either at $Q^2=0.65$ or at $Q^2=0.95 \text{ GeV}^2$, and in 258048 points at $Q^2=1.30 \text{ GeV}^2$; that for each trial attempt of the fit. First of all in this way we faced the restrictions imposed by computer RAM: in our calculation available RAM was restricted to 1 Gbyte and allowed to store the look-up table for process amplitudes for up to W and Q^2 bins; we found that even just to vary electromagnetic amplitudes for a single N^* and in 6 W and Q^2 bins, MINUIT was converging to a solution after roughly 1 day of running. Therefore, even for this simplified fit, considering only a single state parameter variation, we needed roughly 3 days to get MINUIT solutions for $Q^2 = 0.65, 0.95 \text{ GeV}^2$ and 4 days for $Q^2 = 1.30 \text{ GeV}^2$; if we assume variation of parameters for 12 N^* 's included in our code, time consumption becomes definitely unaffordable. Moreover, as it was mentioned above, quantity of W bins fitted simultaneously can not exceed 6, due to the RAM restriction, while we had 20 W bins for $Q^2 = 0.65, 0.95 \text{ GeV}^2$ and 28 W bins for $Q^2 = 1.30 \text{ GeV}^2$. Therefore we should have fitted our data piece by piece, subdividing W bins in groups of up to 6 bins. Actually, it happens that $A_{1/2,3/2}(Q^2)$ for $D_{13}(1520)$ state (for instance), extracted in fit of W bins between 1.41 and 1.54 GeV (6 bins totally), differ from values extracted in the fit of another group of W bins, for instance between 1.49 and 1.64 GeV (6 bins again): the value of N^* electromagnetic form factors by definition should be W -independent and it is not clear how to match different values obtained from fits of different groups of W bins. Finally, we found that if we varied $A_{1/2,3/2}$ amplitudes for a few N^* 's simultaneously in a wide range of values, (for instance between -200 and $+200 10^{-3} \text{ GeV}^{-1/2}$, the solutions become too ambiguous and difficult to interpret. All this difficulties make unfeasible to use directly a MINUIT-based procedure or similar for extraction of N^* electromagnetic form factors from data fit and therefore we developed a special procedure to overcome these problems.

In our procedure, as initial values for $N^* A_{1/2,3/2}(Q^2)$ electromagnetic form factors we used SQTM[43] results, since they represent SU(6)-based fit of available world data on N^* electromagnetic form factor Q^2 -dependence. As input for strong decay amplitudes we used the results of analysis[44] for LS partial decay width of N^* , obtained from world data on $\pi N \rightarrow \pi\pi N$ reactions. Considering PDG values as the results of a more comprehensive analysis, we assumed N^* 's LS partial widths to be a product of PDG total width and branching ratio taken from[44]. To extract N^* 's electromagnetic form factors

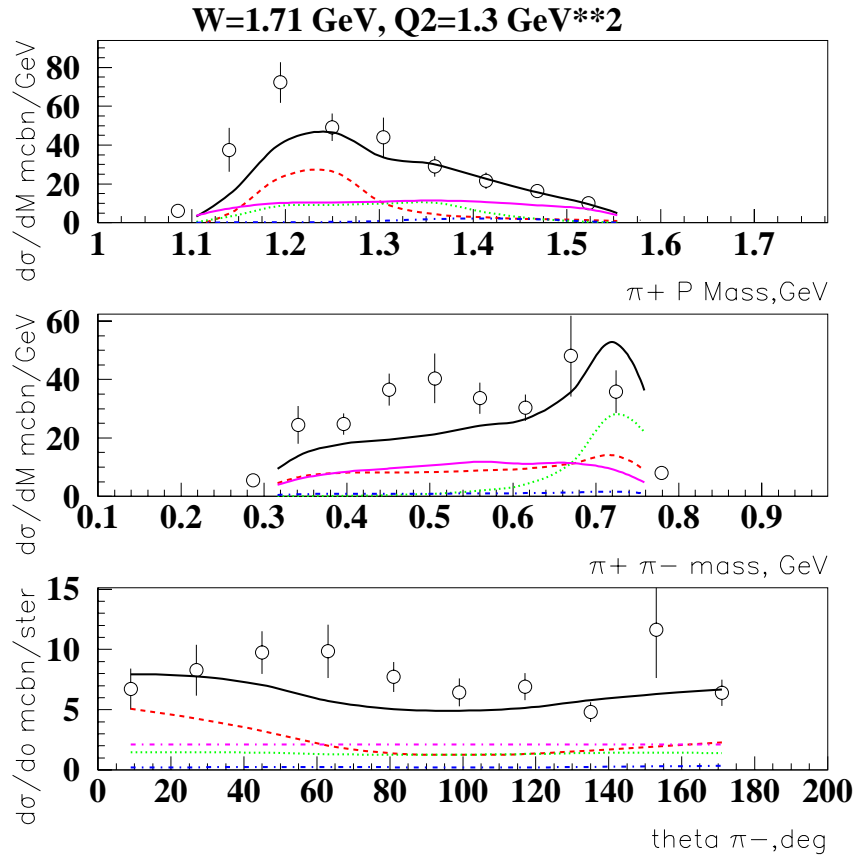


Figure 5.20: Virtual photon cross section for $ep \rightarrow ep\pi^+\pi^-$ at Q^2 between 1.1 and 1.5 GeV^2 and W between 1.7 and 1.725 GeV , differential in (top to bottom): proton- π^+ invariant mass; $\pi^+\pi^-$ invariant mass. Data from CLAS; red dashed line: all $\Delta^{++}\pi^-$ contributions in our "nominal" calculation; blue dot-dashed line: all $\Delta^0\pi^+$ contributions in our "nominal" calculation; green dot-dashed line: all $\rho^0 p$ contributions in our "nominal" calculation; magenta full line: phase space contribution in our "nominal" calculation; black full line: sum of all sub-channels in our "nominal" calculation.

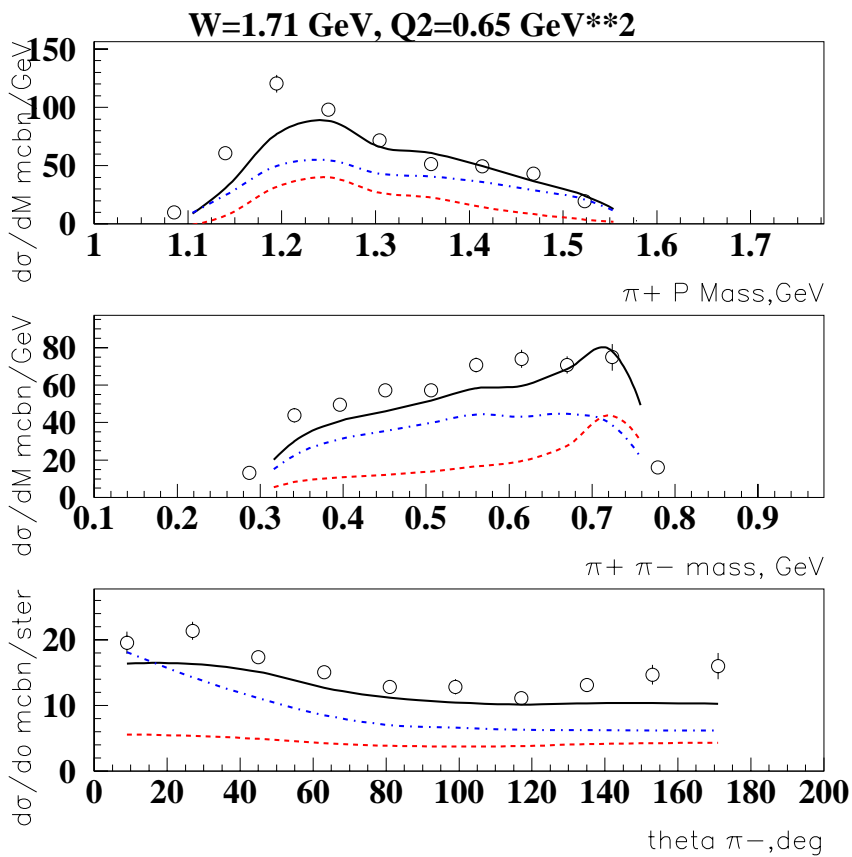


Figure 5.21: Virtual photon cross section for $ep \rightarrow ep\pi^+\pi^-$ at Q^2 between 0.5 and 0.8 GeV 2 and W between 1.7 and 1.725 GeV, differential in (top to bottom): proton- π^+ invariant mass; $\pi^+\pi^-$ invariant mass. Data from CLAS; red dashed line: all resonant contributions in our "nominal" calculation; blu dot-dashed line: all non-resonant contributions in our "nominal" calculation; black full line: sum of all terms in our "nominal" calculation.

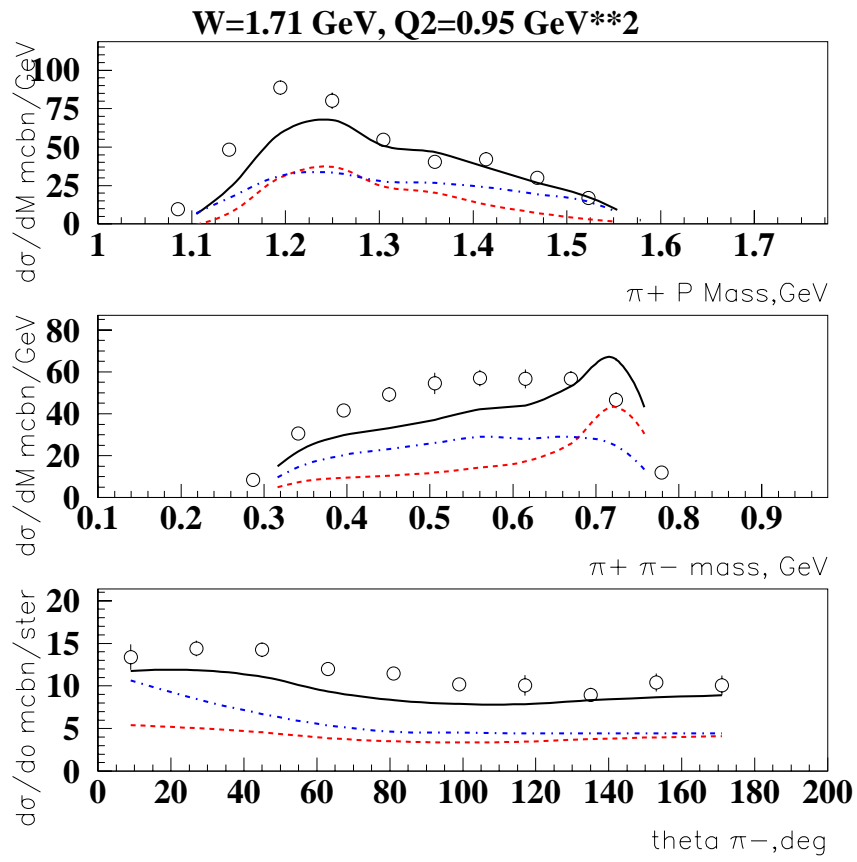


Figure 5.22: Virtual photon cross section for $ep \rightarrow ep\pi^+\pi^-$ at Q^2 between 0.8 and 1.1 GeV^2 and W between 1.7 and 1.725 GeV , differential in (top to bottom): proton- π^+ invariant mass; $\pi^+\pi^-$ invariant mass. Data from CLAS; red dashed line: all resonant contributions in our "nominal" calculation; blu dot-dashed line: all non-resonant contributions in our "nominal" calculation; black full line: sum of all terms in our "nominal" calculation.

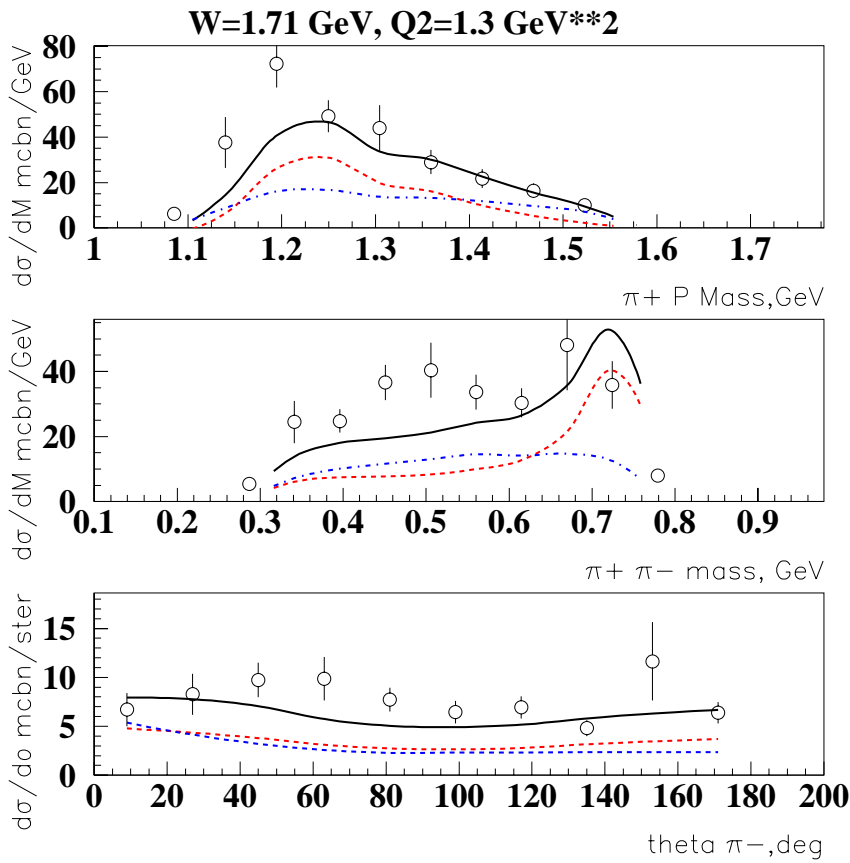


Figure 5.23: Virtual photon cross section for $ep \rightarrow ep\pi^+\pi^-$ at Q^2 between 1.1 and 1.5 GeV 2 and W between 1.7 and 1.725 GeV, differential in (top to bottom): proton- π^+ invariant mass; $\pi^+\pi^-$ invariant mass. Data from CLAS; red dashed line: all resonant contributions in our "nominal" calculation; blu dot-dashed line: all non-resonant contributions in our "nominal" calculation; black full line: sum of all terms in our "nominal" calculation.

from experimental data, we randomly fluctuated their values by 20 % (standard deviation) around SQTM values[43], which corresponds to SQTM prediction uncertainties[40]. For $D_{15}(1675)$ and $D_{13}(1700)$ states, SQTM predicts zero electromagnetic form factors (being in this case the fit of [43] based on pure $SU(6)$); however, other models, including $SU(6)$ breaking terms from the beginning, predict for these states non-vanishing electromagnetic form factor values, comparable with strengths of other excited states. Therefore we decided to fluctuate electromagnetic form factors for $D_{15}(1675)$ and $D_{13}(1700)$ around Non-Relativistic Quark Model values (NRQM)[43] by 20 % (standard deviation). For each random extraction of N^* electromagnetic form factor values we calculated $\pi^+\pi^-$, $p\pi^+$ invariant mass and π^- angular distributions in each W and Q^2 bin; then we calculated χ^2 for each Q^2 bin separately, averaging over all W bins involved. We then picked-up the best solution according to the minimum χ^2 and considered $A_{1/2,3/2}$ form factors corresponding to this solution as values extracted from experimental data fit. One trial calculation for all W -values in a single Q^2 bin takes not more than 15 minutes: it gives the opportunity to perform 100 trial attempts during 1 day, as well as to perform final fine parameter tuning optionally, by hand adjustment. The accuracy reported in [44] for N^* 's strong decay branching ratio is typically a few percent for all states except $D_{13}(1700)$, whose position and strong decay branching ratio are poorly known: therefore, we extracted position and strong partial decay widths of this particular state from a simultaneous fit of all Q^2 bins in a limited W range, between 1.61 and 1.81 GeV, being the range for partial width variation taken from [44]. At variance with the case of $D_{13}(1700)$, in varying electromagnetic form factors for all other N^* 's, we kept LS strong partial decay branching ratio fixed at values from [44], while for $D_{13}(1700)$ we used our best values got in the above described data fit.

In the case of a sizeable departure of N^* electromagnetic form factors from SQTM predictions (above 30%) as well as in the case of missing baryon state search (see below), we also extracted N^* electromagnetic form factors using MINUIT in the following way: we assumed a variation of electromagnetic form factors for such particular state in a wide range (typically between -0.2 and +0.2 $\text{GeV}^{-1/2}$) and used MINUIT to extract them from data fit in the most sensitive 6 W and Q^2 bins, keeping parameters of all other states at values extracted on in the fit method previously described. So, in practice, we used MINUIT to check for alternative solutions in particular cases, but in a restricted energy region.

5.0.6 Resonance Analysis: Conventional States

The following step was to investigate the resonance contributions in terms of modifications to the couplings of conventional states. At first, we decreased both electromagnetic helicity couplings for $P_{13}(1720)$ by a factor 2, to reproduce the experimental mass distributions from CLAS. For the states $D_{13}(1700)$ and $D_{15}(1675)$, the SQTM is predicting the photocouplings to vanish; however non-relativistic as well as relativistic quark models[43] predict non-zero couplings for these states; moreover, predicted couplings for $D_{13}(1700)$

are comparable with our suppressed $P_{13}(1720)$ couplings mentioned above. Therefore, as a first attempt, we decided to replace the photocoupling values from the SQTM for these two states with values from Non-Relativistic Quark Model predictions (NRQM)[43]. To proceed in the analysis of conventional states, as further step we took into account the possible uncertainty in the SQTM photocoupling fit[43]: according to V. Burkert, one may assume an uncertainty of the order of 10% for the $D_{13}(1520)$ and the $S_{11}(1535)$, while for all other states a 20% can be estimated; of course, for the two states $D_{13}(1700)$ and $D_{15}(1675)$ for which the SQTM predicts vanishing photocouplings and for which we switched to using a NRQM prediction, a 20 % variation was applied to the NRQM values. We therefore varied, using a random extraction procedure, each single resonance photocoupling according to the above mentioned uncertainty (interpreted as standard deviation σ) and picked up the best solution in terms of χ^2 minimization; χ^2 was calculated from all three differential cross section plots at all W values for a particular Q^2 interval, considering as degrees of freedom all resonance photocouplings that were varied in this "Monte Carlo" procedure, a total of 22 in our case.

In order to eliminate the discrepancy observed at low W values, we implemented as a free parameter the longitudinal coupling $C_{1/2}$ of the Roper resonance and determined its value from data fit; however, since our fit involved a limited number of kinematic variables, it is not possible to separate transverse and longitudinal coupling for the Roper without ambiguity; therefore, our fit in this case simply means that, if we assume for $A_{1/2}$ the value given by the SQTM prediction and then fill any discrepancy with the $P_{11}(1440)$ longitudinal coupling, we see that we get a large value for $C_{1/2}$. Although some ambiguity between Roper excitation and phase space may still exist due to the limited range in the Dalitz plot, from our fit it looks like increasing the phase space results in a slightly worse fit quality: also by inspection of the $p\pi^+$ mass distributions around 1.44 GeV, it looks like the missing strength is not uniformly distributed but may rather result from an insufficient $\Delta\pi$ contribution, which is namely what we get from the Roper.

Considering the poor knowledge of strong couplings for $D_{13}(1700)$ state[44, 45], we also fluctuated the strong decay partial widths for this state only, inside uncertainties of [44], as well as its position, according to the PDG uncertainty. In figure 5.24 we report the W dependence of the total cross section obtained in the above described fitting procedure: we reached a good agreement with data everywhere, apart from the structure around 1.7 GeV. The corresponding 1-differential cross sections at $W=1.71$ GeV bin and all 3 available Q^2 bins are shown in figures 5.25 through 5.27. Reducing the $P_{13}(1720)$ electromagnetic excitation strengths allows to improve the shape of the $\pi\pi$ invariant mass distribution, eliminating the ρ peak, however we still have a sizeable lack of $\Delta\pi$ strength in $p\pi^+$ mass distributions. The complete set of pictures on our fit quality under variation of conventional states can be found in http://www.jlab.org.Hall-B/secure/e1/mokeev/ps_final/step2. Pictures $stp2ch[qqq]_[nnn].ps$ contain the 1-differential cross-sections in the [qqq] $\text{GeV}^2 Q^2$ bin and the [nnn] GeV W bin as well as the cross-section decomposition into different quasi-two-body channel contributions. The parameters extracted in our fit for the most

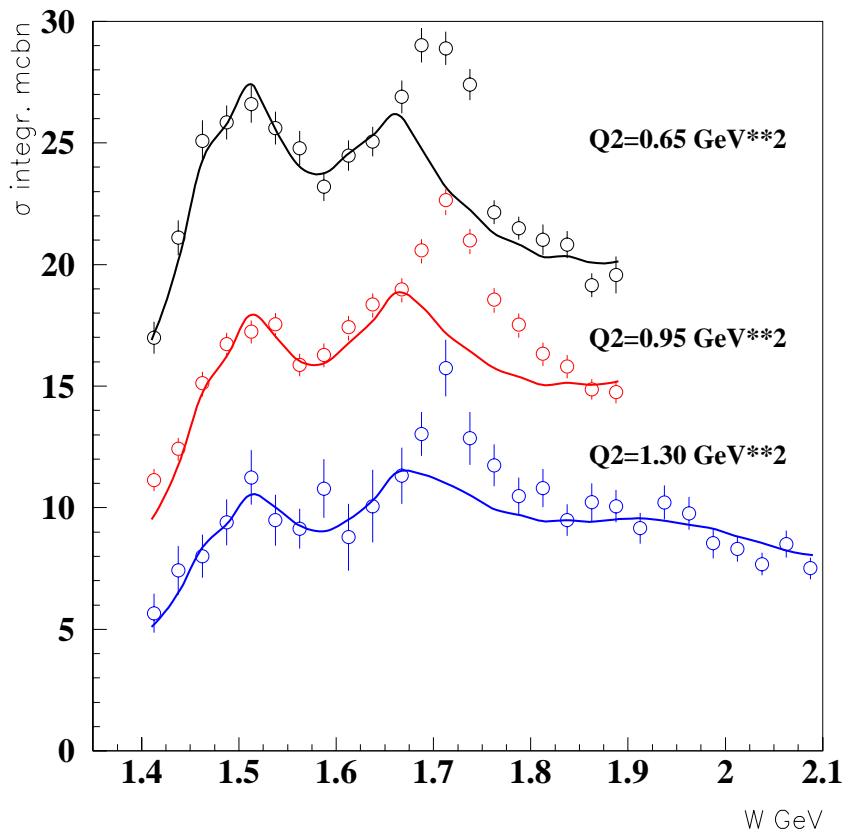


Figure 5.24: Total virtual photon cross section for $ep \rightarrow ep\pi^+\pi^-$ at all Q^2 as a function of W . Data from CLAS. Curves represent our best solution when fluctuating resonance couplings within some limits as described in the text.

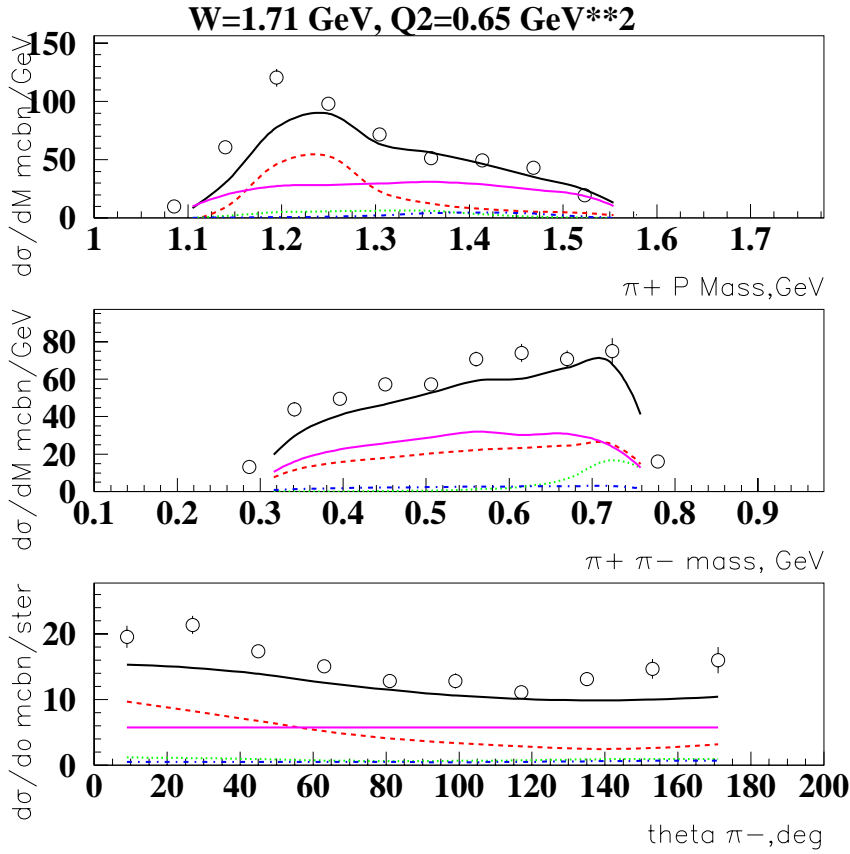


Figure 5.25: Virtual photon cross section for $ep \rightarrow ep\pi^+\pi^-$ at Q^2 between 0.5 and 0.8 GeV^2 and W between 1.7 and 1.725 GeV , differential in (top to bottom): proton- π^+ invariant mass; $\pi^+\pi^-$ invariant mass. Data from CLAS; red dashed line: all $\Delta^{++}\pi^-$ contributions in our "nominal" calculation; blu dot-dashed line: all $\Delta^0\pi^+$ contributions in our "nominal" calculation; green dot-dashed line: all $\rho^0 p$ contributions in our "nominal" calculation; magenta full line: phase space contribution in our "nominal" calculation; black full line: sum of all sub-channels in our "nominal" calculation. Data from CLAS. Curves represent our best solution when fluctuating resonance couplings within some limits as described in the text.

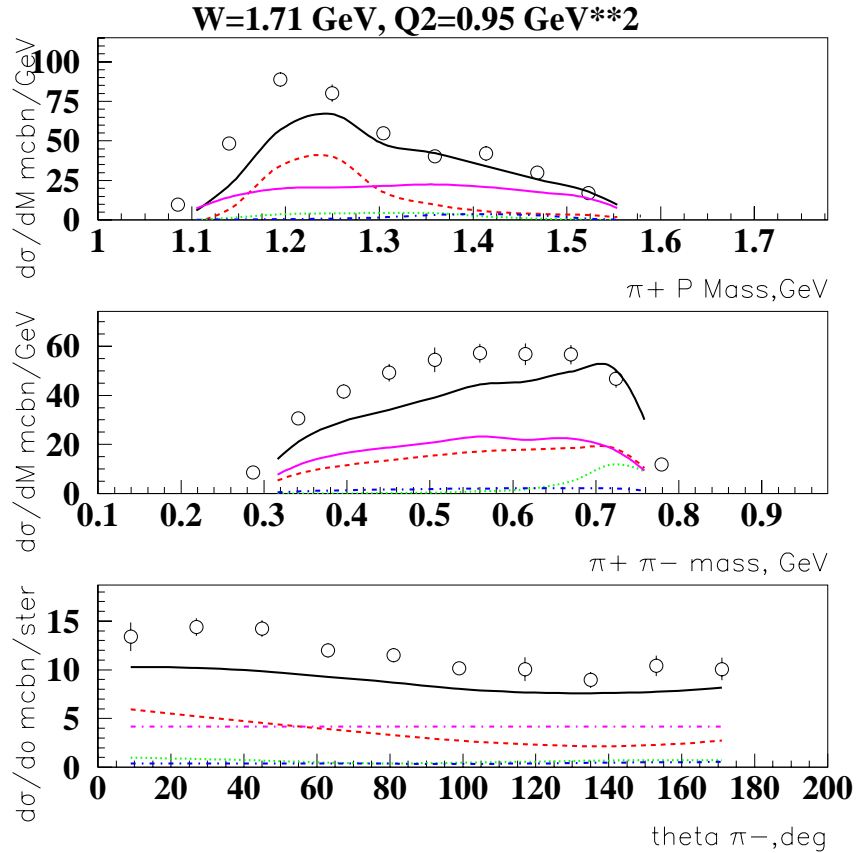


Figure 5.26: Virtual photon cross section for $ep \rightarrow ep\pi^+\pi^-$ at Q^2 between 1.1 and 1.5 GeV^2 and W between 1.7 and 1.725 GeV , differential in (top to bottom): proton- π^+ invariant mass; $\pi^+\pi^-$ invariant mass. Data from CLAS; red dashed line: all $\Delta^{++}\pi^-$ contributions in our "nominal" calculation; blu dot-dashed line: all $\Delta^0\pi^+$ contributions in our "nominal" calculation; green dot-dashed line: all $\rho^0 p$ contributions in our "nominal" calculation; magenta full line: phase space contribution in our "nominal" calculation; black full line: sum of all sub-channels in our "nominal" calculation. Curves represent our best solution when fluctuating resonance couplings within some limits as described in the text.

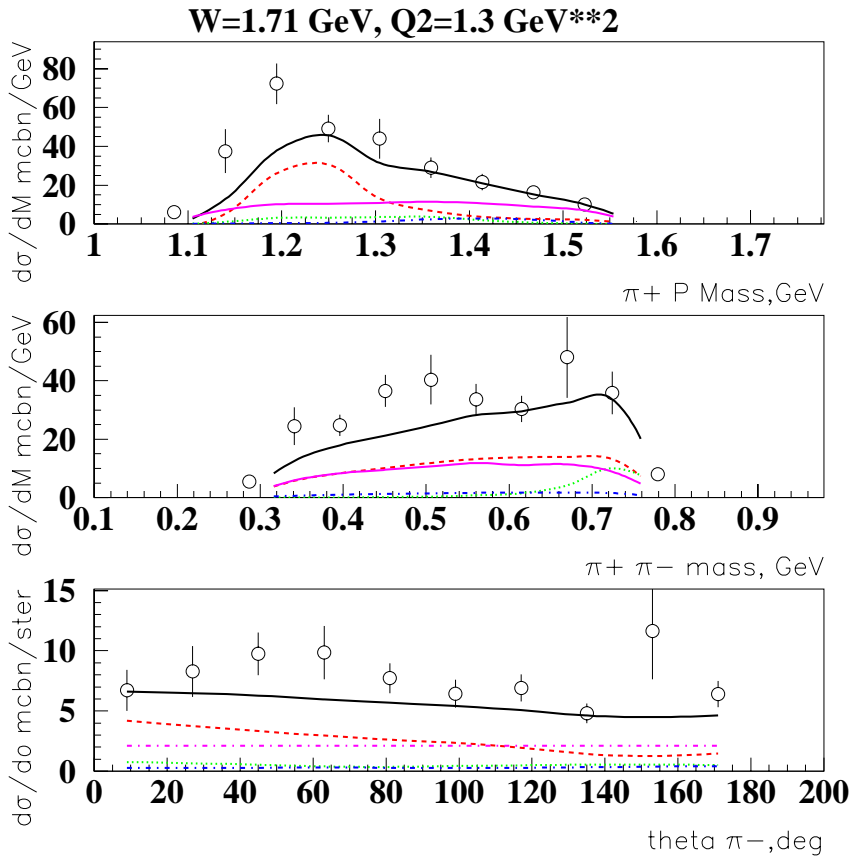


Figure 5.27: Virtual photon cross section for $ep \rightarrow ep\pi^+\pi^-$ at Q^2 between 1.1 and 1.5 GeV^2 and W between 1.7 and 1.725 GeV , differential in (top to bottom): proton- π^+ invariant mass; $\pi^+-\pi^-$ invariant mass. Data from CLAS; red dashed line: all $\Delta^{++}\pi^-$ contributions in our "nominal" calculation; blu dot-dashed line: all $\Delta^0\pi^+$ contributions in our "nominal" calculation; green dot-dashed line: all $\rho^0 p$ contributions in our "nominal" calculation; magenta full line: phase space contribution in our "nominal" calculation; black full line: sum of all sub-channels in our "nominal" calculation. Curves represent our best solution when fluctuating resonance couplings within some limits as described in the text.

Table 5.1: The electromagnetic couplings for the $P_{13}(1720)$

| Q^2 (GeV^2/c^2) | $A_{1/2}$ SQTM prediction ($10^{-3} \text{ GeV}^{-1/2}$) | $A_{3/2}$ SQTM prediction ($10^{-3} \text{ GeV}^{-1/2}$) | $A_{1/2}$ our fit ($10^{-3} \text{ GeV}^{-1/2}$) | $A_{3/2}$ our fit ($10^{-3} \text{ GeV}^{-1/2}$) |
|--------------------------|--|--|--|--|
| 0.65 | -38. | -65. | -25. | -39. |
| 0.95 | -36. | -63. | -23. | -21. |
| 1.30 | -35. | -59. | -21. | -21. |

 Table 5.2: The longitudinal coupling for the $P_{11}(1440)$

| Q^2 (GeV^2/c^2) | $C_{1/2}$ our fit ($10^{-3} \text{ GeV}^{-1/2}$) |
|--------------------------|--|
| 0.65 | -250. |
| 0.95 | -190. |
| 1.30 | -130. |

strongly modified states with respect to SQTM ($P_{13}(1720)$) and $C_{1/2}$ for $P_{11}(1440)$) are presented in Tables 5.1 and 5.2 .

Therefore we found that the CLAS data can be described everywhere, except the structure around 1.7 GeV, using electromagnetic form factors for all conventional states as expected from SQTM predictions within 20% standard deviation, except the case of $P_{13}(1720)$, whose electromagnetic form factors are strongly reduced with respect to SQTM as clearly indicated by CLAS data on $\pi\pi$ invariant mass distribution around 1.7 GeV: absence of ρ peak: this may be interpreted as an indication of a particular nature of the $P_{13}(1720)$ conventional state. At this stage of the analysis, we still have a sizeable excess of measured cross section around 1.7 GeV, which can not be filled neither by enhancing the electromagnetic excitation of the $P_{13}(1720)$, nor of the $D_{33}(1700)$ state: in first case we would create the unobserved ρ peak in the $\pi\pi$ invariant mass distributions, not supported by data as we stressed many times above; in the second case, being the $D_{33}(1700)$ very broad (~ 300 MeV total width), we would spoil the W dependence of cross section both at W below and above the 1.7 GeV structure.

In order to fully explore the possibility of interpreting the CLAS data only in terms of conventional states, we tried to vary photocouplings and strong decay widths of conventional $D_{13}(1700)$ state. First, we pumped $A_{1/2,3/2}$ for this state by a factor 2.5 with respect to NRQM and then we fluctuated them by 20% (σ), keeping the photocouplings of all other states on best values extracted on the above described previous fitting step. Simultaneously we also varied its strong decay partial widths within uncertainties of [44].

Table 5.3: The electromagnetic couplings for the $D_{13}(1700)$ from our fitting procedure, starting from NRQM values and keeping the parameter variation in a restricted range

| Q^2 (GeV^2/c^2) | $A_{1/2}$ NRQM prediction ($10^{-3} \text{ GeV}^{-1/2}$) | $A_{3/2}$ NRQM prediction ($10^{-3} \text{ GeV}^{-1/2}$) | $A_{1/2}$ our fit ($10^{-3} \text{ GeV}^{-1/2}$) | $A_{3/2}$ our fit ($10^{-3} \text{ GeV}^{-1/2}$) |
|--------------------------|--|--|--|--|
| 0.65 | -18.60 | 5.50 | -64. | 13. |
| 0.95 | -17.60. | 4.30. | -58. | 11. |
| 1.30 | -16.00. | 3.20. | -40. | 8.5 |

Table 5.4: Parameters for $D_{13}(1700)$ from MINUIT "free" fit

| position (GeV) | total width (MeV) | $A_{1/2}$ MINUIT fit ($10^{-3} \text{ GeV}^{-1/2}$) | $A_{3/2}$ MINUIT fit ($10^{-3} \text{ GeV}^{-1/2}$) |
|-------------------|----------------------|---|---|
| 1.72 | 72. | 4.5 | -56 |

Based on the above described fitting procedure, we picked-up best solution with minimal χ^2 : the corresponding $D_{13}(1700)$ photocouplings obtained in our fit in comparison with NRQM predictions are listed in Table 5.3.

In figure 5.28 we present the total cross section as a function of W , for all momentum transfer bins, evaluated in the assumption of a stronger excitation of the conventional $D_{13}(1700)$ state: we succeeded to approximately reproduce the W spectrum in all 3 Q^2 bins, as well as to approximately reproduce the invariant mass distributions (pictures 5.29 through 5.31), but we still have a poor description of angular distributions (pictures 5.29 through 5.31).

We also analysed the possibility to describe data varying couplings of $D_{13}(1700)$ state in a very wide range using MINUIT in a restricted energy range: we varied $A_{1/2,3/2}$ couplings of $D_{13}(1700)$ within -100 and +100 in units of $10^{-3} \text{ GeV}^{-1/2}$, strong decay widths within the above mentioned limits and position between 1.65 and 1.75 GeV (PDG limits), keeping couplings of all other N^* at values extracted in the previous fittin step. We left to the MINUIT routines to find the best solution from simultaneous fit of $\pi\pi$, $p\pi^+$ invariant mass and π^- angular distributions in W bins 1.64, 1.66, 1.69, 1.71, 1.74, 1.76 GeV for $Q^2=0.65 \text{ GeV}^2$ (a total of 156 points for 6 parameters). We found in this case the best solution for the $D_{13}(1700)$ parameters presented in the Table 5.4, with a χ^2 value approximately 30% lower than obtained in the previously discussed parameter search. W spectra are as usually well reproduced, like in the previous step. The comparison with 1-differential cross sections is presented in figures 5.32 through 5.36: MINUIT provides a better description of angular distributions at $W=1.69, 1.71, 1.74 \text{ GeV}$, while it appears to

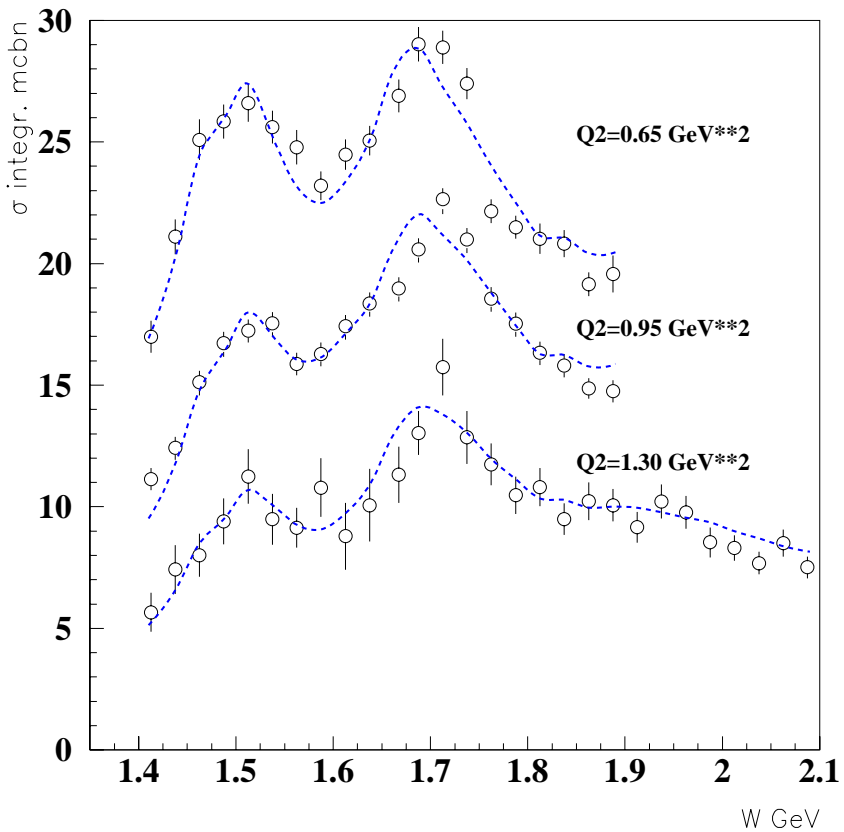


Figure 5.28: Total virtual photon cross section for $ep \rightarrow ep\pi^+\pi^-$ at all Q^2 as a function of W . Data from CLAS. Curves represent our best solution when modifying the conventional $D_{13}(1700)$ as described in the text.

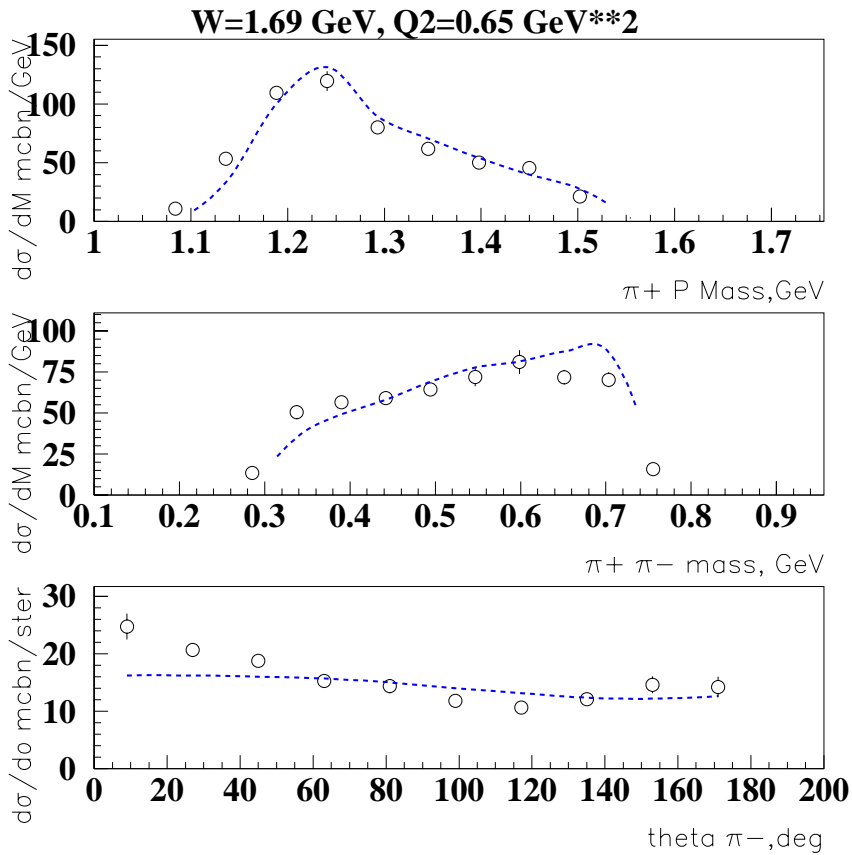


Figure 5.29: Virtual photon cross section for $ep \rightarrow ep\pi^+\pi^-$ at Q^2 between 0.5 and 0.8 GeV 2 and W between 1.7 and 1.725 GeV, differential in (top to bottom): proton- π^+ invariant mass; $\pi^+ \pi^-$ invariant mass. Data from CLAS. Curves represent our best solution when modifying the conventional $D_{13}(1700)$ as described in the text.

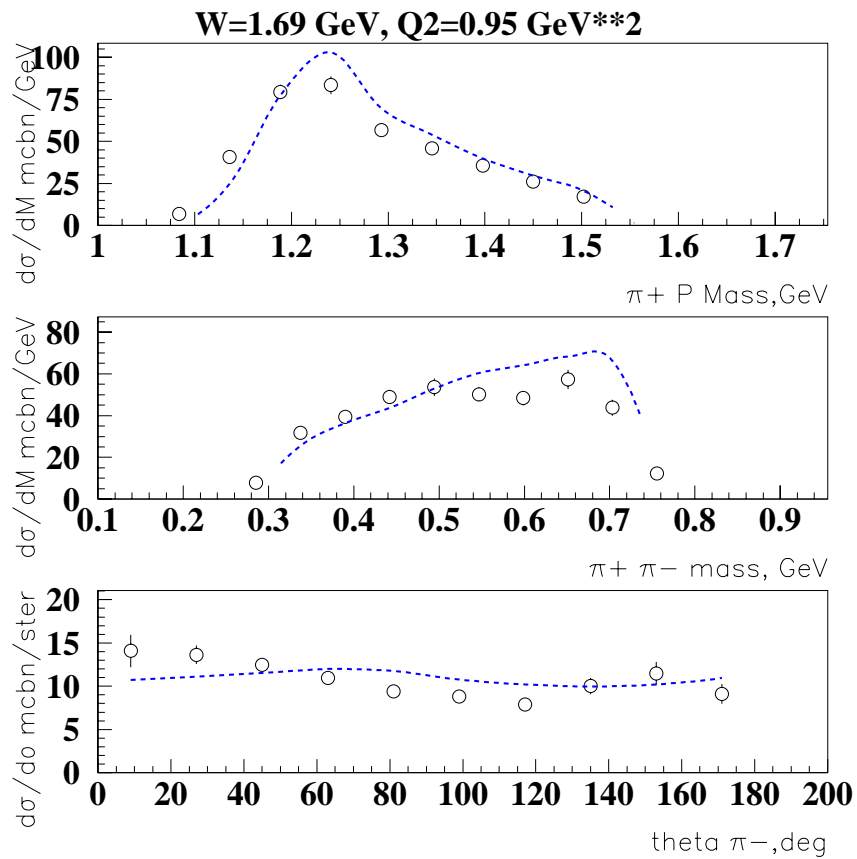


Figure 5.30: Virtual photon cross section for $ep \rightarrow ep\pi^+\pi^-$ at Q^2 between 0.8 and 1.1 GeV^2 and W between 1.7 and 1.725 GeV , differential in (top to bottom): proton- π^+ invariant mass; $\pi^+\pi^-$ invariant mass. Data from CLAS. Curves represent our best solution when modifying the conventional $D_{13}(1700)$ as described in the text.

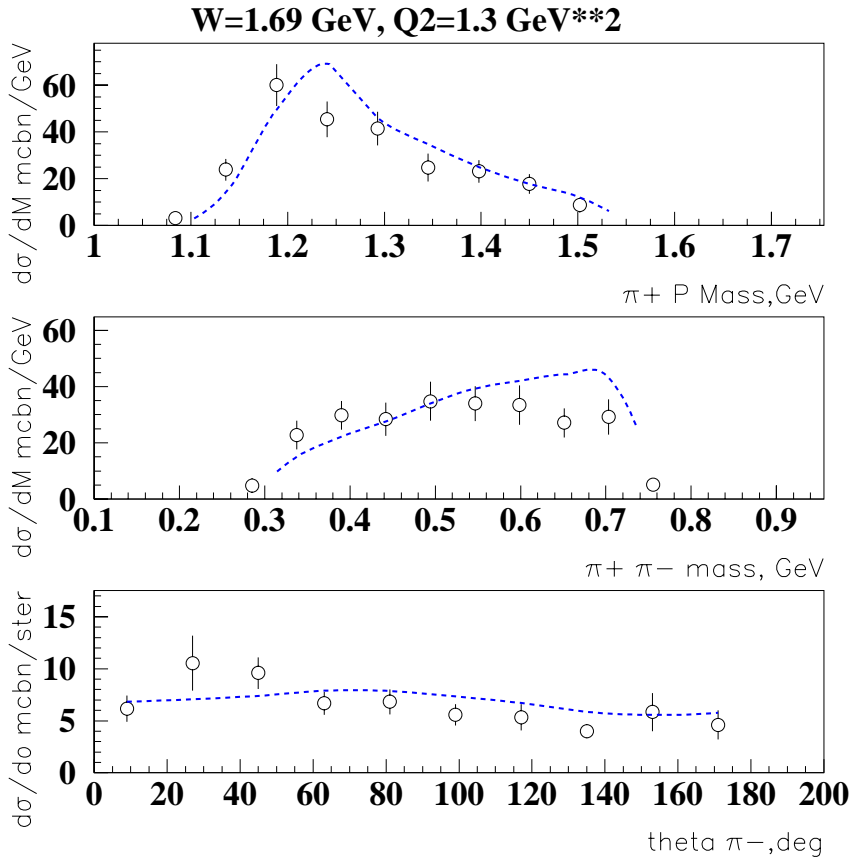


Figure 5.31: Virtual photon cross section for $ep \rightarrow ep\pi^+\pi^-$ at Q^2 between 1.1 and 1.5 GeV 2 and W between 1.7 and 1.725 GeV, differential in (top to bottom): proton- π^+ invariant mass; $\pi^+-\pi^-$ invariant mass. Data from CLAS. Curves represent our best solution when modifying the conventional $D_{13}(1700)$ as described in the text.

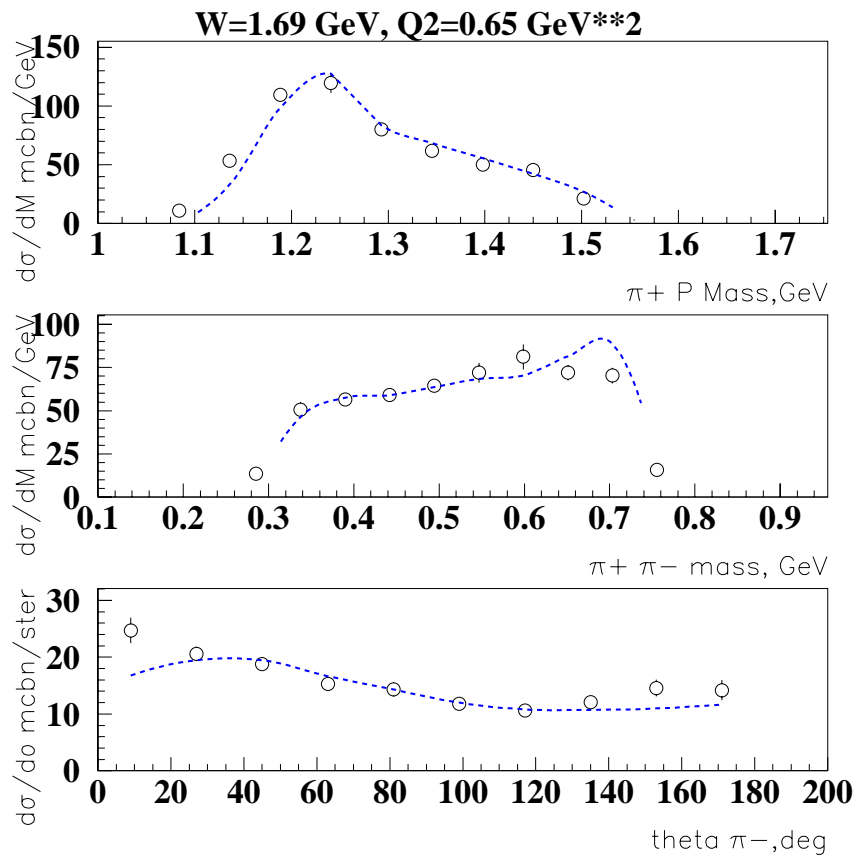


Figure 5.32: Virtual photon cross section for $ep \rightarrow ep\pi^+\pi^-$ at Q^2 between 0.5 and 0.8 GeV^2 and W between 1.7 and 1.725 GeV , differential in (top to bottom): proton- π^+ invariant mass; $\pi^+\pi^-$ invariant mass. Data from CLAS. Curves represent our best solution from MINUIT when modifying the conventional $D_{13}(1700)$ as described in the text.

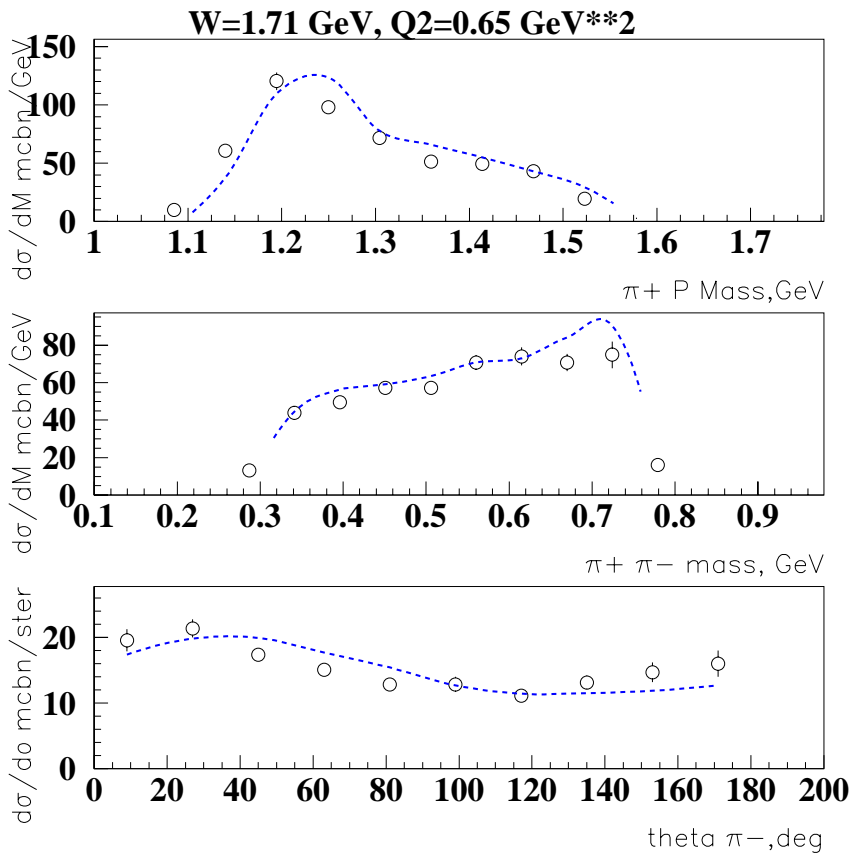


Figure 5.33: Virtual photon cross section for $ep \rightarrow ep\pi^+\pi^-$ at Q^2 between 0.8 and 1.1 GeV 2 and W between 1.7 and 1.725 GeV, differential in (top to bottom): proton- π^+ invariant mass; $\pi^+ \pi^-$ invariant mass. Data from CLAS. Curves represent our best solution from MINUIT when modifying the conventional $D_{13}(1700)$ as described in the text.

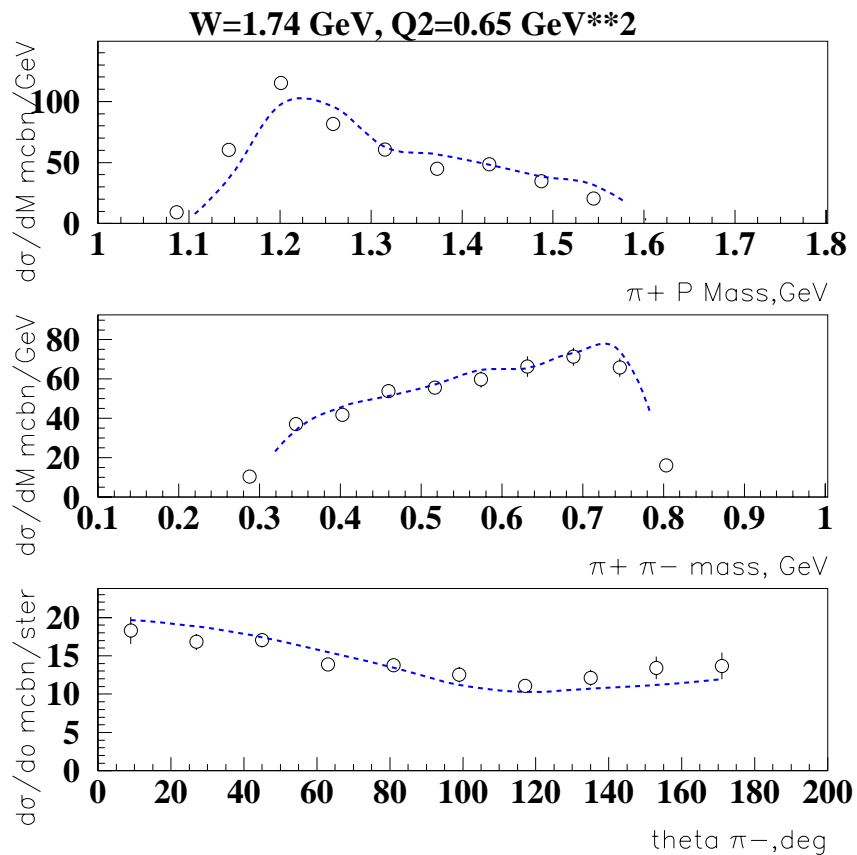


Figure 5.34: Virtual photon cross section for $ep \rightarrow ep\pi^+\pi^-$ at Q^2 between 1.1 and 1.5 GeV^2 and W between 1.7 and 1.725 GeV , differential in (top to bottom): proton- π^+ invariant mass; $\pi^+\pi^-$ invariant mass. Data from CLAS. Curves represent our best solution from MINUIT when modifying the conventional $D_{13}(1700)$ as described in the text.

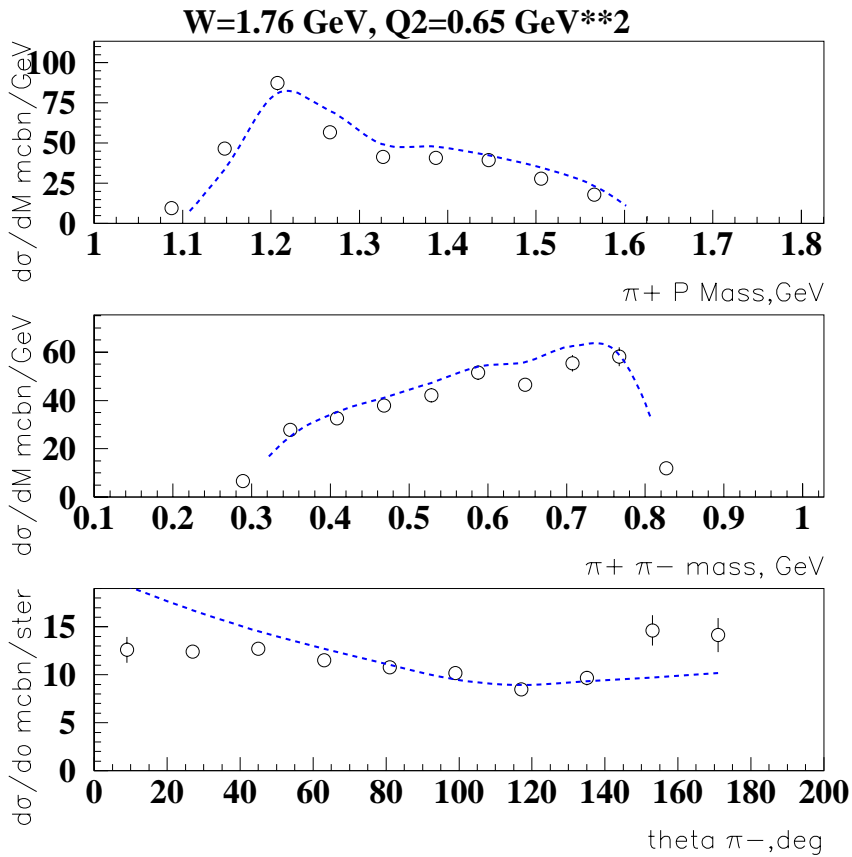


Figure 5.35: Virtual photon cross section for $ep \rightarrow ep\pi^+\pi^-$ at Q^2 between 1.1 and 1.5 GeV 2 and W between 1.7 and 1.725 GeV, differential in (top to bottom): proton- π^+ invariant mass; $\pi^+\pi^-$ invariant mass. Data from CLAS. Curves represent our best solution from MINUIT when modifying the conventional $D_{13}(1700)$ as described in the text.

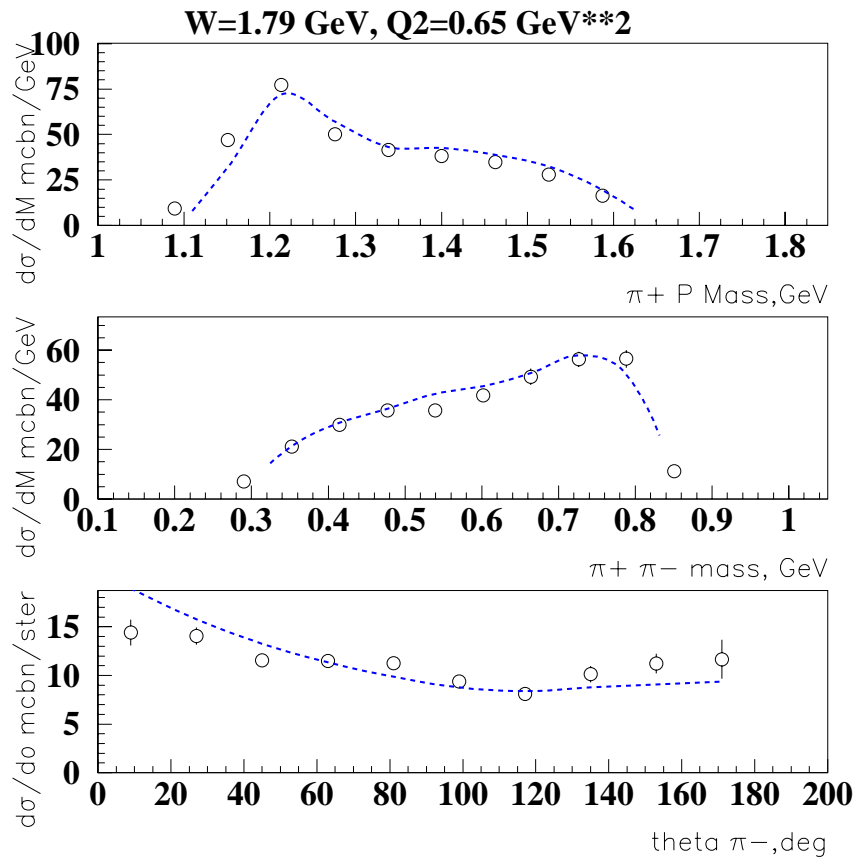


Figure 5.36: Virtual photon cross section for $ep \rightarrow ep\pi^+\pi^-$ at Q^2 between 1.1 and 1.5 GeV^2 and W between 1.7 and 1.725 GeV , differential in (top to bottom): proton- π^+ invariant mass; $\pi^+\pi^-$ invariant mass. Data from CLAS. Curves represent our best solution from MINUIT when modifying the conventional $D_{13}(1700)$ as described in the text.

completely miss the data for angular distributions at $W=1.76, 1.79$ GeV. Moreover, the extracted $D_{13}(1700)$ parameters (Table 5.4) are strongly different from *any* quark model predictions: $A_{1/2}$ absolute values are about a factor 5 lower, while $A_{3/2}$ is about a factor 8 higher. Typical total widths of N^* 's situated around 1.7 GeV are in the range 150-300 MeV, while the $D_{13}(1700)$ width extracted from fit turns out to be 72 MeV. Considering the strong departure from angular distribution data at $W=1.76, 1.79$ GeV as well as the unexpected extracted parameters, we decided to drop this solution with free variation of $D_{13}(1700)$ couplings got by MINUIT and in further analysis we only considered the previously discussed solution corresponding to $A_{1/2,3/2}$ pumped with respect to NRQM, with resulting parameters in Table 5.3.

We also tested the possibility of fitting in a restricted energy region both $D_{13}(1700)$ and $P_{13}(1720)$ using MINUIT and again leaving the parameters free in a very wide range, but the final result did not change.

As mentioned above, our fit using the parameter fluctuation in the full W range gives a good description of total cross sections as a function of W , as well as invariant mass distributions, but fails to describe angular distributions. The reason for such failure appears to be the following: for D-states with $\text{abs}(A_{1/2}) > \text{abs}(A_{3/2})$, the resonant decay partial wave interferes with the non-resonant mechanisms destructively at forward and backward pion emission angles and constructively at central angles; this gives rise to a suppression of cross section in angular distributions at forward and backward angles and a growth at central angles, which is in contradiction with experimental angular distributions trends around 1.7 GeV in W . Therefore enhancing electromagnetic couplings for D-states in the attempt to fill the gap around 1.7 GeV spoils angular distributions, if $\text{abs}(A_{1/2}) > \text{abs}(A_{3/2})$, as expected for $D_{13}(1700)$ and $D_{33}(1700)$ states in any model prediction. Moreover, as follows from Table 5.3, electromagnetic couplings for $D_{13}(1700)$ state required to fill gap around 1.7 GeV appear to be close to maximal values among all N^* states, while any model predicts weak electromagnetic couplings for this state and exactly zero in SU(6) limit.

We still checked the possibility of pumping the $D_{15}(1675)$ and the $F_{15}(1680)$, but their mass is too low and well established to provide strength at or above 1.7 GeV: increasing the strength of such states produces a shoulder at the left of our bump, clearly not supported by data. Moreover, sizeable modifications of the properties of the $F_{15}(1680)$ are not quite acceptable, as its properties are well known from a number of previous experiments[46]. Based on all the previous discussion, we were led to the attempt of filling the gap around 1.7 GeV implementing a missing baryon state.

5.0.7 Resonance Analysis: Missing States Search Strategy and Detailed Analysis

Considering the energy range of the bump observed in the data and looking at quark model predictions for the masses of missing states[5], as well as considering a recent indi-

cation from the literature[47], we decided to start our investigation of the missing strength assuming that the observed gap could be filled by one of the lightest and narrowest missing baryon states predicted in[5]. There are two such states: $P_{11}(1880)$ and $P_{13}(1870)$. Since, according to [48], accuracy of missing state position evaluation is roughly 200 MeV and their strong decay widths should be decreased according to phase space shrinkage, if we shift these states toward 1.7 GeV, we can consider them as possible candidates to fill the gap around 1.7 GeV. Another interesting possibility is suggested by flux tube models[49], that predict for instance a $qqqq$ hybrid with a mass of 1870 ± 100 MeV: the behavior of form factors as a function of Q^2 should allow us to distinguish between ordinary and hybrid baryons. Since our data contains only the charged pion isospin channel, we are not able to distinguish between $1/2$ and $3/2$ isospin. However, in our code, for strong decay strengths we put Clebsch-Gordan isospin coefficients corresponding to isospin $1/2$ of missing state, based on quark model predictions[5]; however, substitution by $3/2$ isospin simply causes a renormalization of partial strong decay widths for missing state extracted in our analysis, keeping data description unchanged. Therefore, for definitive conclusion about missing state isospin, comparative studies of different isospin channels are necessary. We started our analysis from attempting to fill the gap implementing a missing baryon state with quantum numbers P_{13} around 1.7 GeV in W . As an initial value for strong decay widths, we used predictions [5] for the $P_{13}(1870)$ $[\frac{3}{2}^+]$ missing state, being it the lowest P_{13} missing state. The initial $A_{1/2,3/2}$ for this new state were put equal for both helicities and their absolute values as well as the initial mass position were determined from manual adjustment of the peak in the total cross section as a function of W around 1.7 GeV. Then we fluctuated simultaneously strong decay width and position of the new state and of the conventional $D_{13}(1700)$ state. The strong decay widths for $D_{13}(1700)$ were fluctuated again inside uncertainties of [44], while for P_{13} missing state we assumed a range of partial strong decay width fluctuation corresponding to a total decay width variation between 40 and 600 MeV. The position of conventional $D_{13}(1700)$ state was again fluctuated between 1.65 and 1.75 GeV (PDG uncertainty), while position of missing state was varied between 1.68 and 1.76 GeV. The parameters of all other conventional states were fixed at values obtained in our previous best fit. For each choice of the above mentioned parameters we calculated all 1-differential cross sections in the limited energy range between 1.64 and 1.81 GeV in all available W and Q^2 bins. According to minimal χ^2 we extracted in this fitting procedure values for strong decay widths and positions for conventional $D_{13}(1700)$ and for missing P_{13} baryon states. In this first step only the strong couplings were varied independently, while the photocouplings were varied in such a way to keep their ratio constant; in other words, partial and total widths were free to change, while the electromagnetic amplitudes were changed only by an overall renormalisation, to compensate for the strong parameter change and preserve the total strength seen in the data. In a further step we fluctuated $A_{1/2,3/2}$ for missing baryon state within 50% in σ , extracting their best value according to minimal χ^2 : in this case of course, the fit was performed for each Q^2 bin separately. Finally, we performed a fine tuning of $A_{1/2,3/2}$ amplitudes for P_{13} missing and

Table 5.5: Strong parameters for $P_{13}(1720)$ missing state

| position (GeV) | total width (MeV) | Branching ratio $\pi\Delta$ | Branching ratio ρp |
|-------------------|----------------------|--------------------------------|-----------------------------|
| 1.72 ± 0.02 | 88 ± 12 | $(47 \pm 15) \%$ | $(9 \pm 10) \%$ |

Table 5.6: Strong parameters for conventional $D_{13}(1700)$ state

| position (GeV) | total width (MeV) | Branching ratio $\pi\Delta$ | Branching ratio ρp |
|-------------------|----------------------|--------------------------------|-----------------------------|
| 1.74 ± 0.03 | 185 ± 27 | $(53 \pm 25) \%$ | $(45 \pm 30) \%$ |

$D_{13}(1700)$, $D_{33}(1700)$, $P_{13}(1720)$, $F_{15}(1860)$ conventional states, through slight manual adjustments, calculating several times the dependence on W as well as the complete set of 1-differential cross sections in separate single Q^2 bin. In picture 5.37 the total cross sections from CLAS at all three momentum transfers are reported, together with both our fit in terms of conventional states (see section 2.05) and in terms of the missing P_{13} ; in pictures 5.38 through 5.46 the same comparison is reported for the 1-differential cross sections. The complete 1-differential cross section plots for this second unusual solution are presented in http://www.jlab.org/Hall-B/secure/e1/mokeev/ps_final/missp13. As follows from the reported plots, the quality of our description of the total cross section as a function of W is very close both enhancing conventional $D_{13}(1700)$ state or implementing the missing $P_{13}(1720)$, while implementation of missing state provides a systematic improvement in angular distribution description. The overall improvement of fit quality caused by $P_{13}(1720)$ missing state implementation can be seen in Table 5.10, where χ^2 values in each W and Q^2 bin are compared for both options in data description.

The extracted final strong parameters for missing and conventional $D_{13}(1700)$ states are listed in Table 5.5 and Table 5.6, respectively. Instead, electromagnetic $A_{1/2,3/2}$ helicity couplings are reported in section 2.1, where we discuss the error evaluation for these quantities.

Position and J^P quantum numbers of missing $P_{13}(1720)$ turn out to coincide with conventional $P_{13}(1720)$, however for the conventional state the strong decays are completely different: $87 \pm 5 \%$ to ρp and 0% to $\Delta\pi$, according to [44] and confirmed by [45]: considering the big imaginary part of P_{13} ρp partial wave and the consequently very large branching ratio presented in the mentioned literature, it is difficult to conceive that the

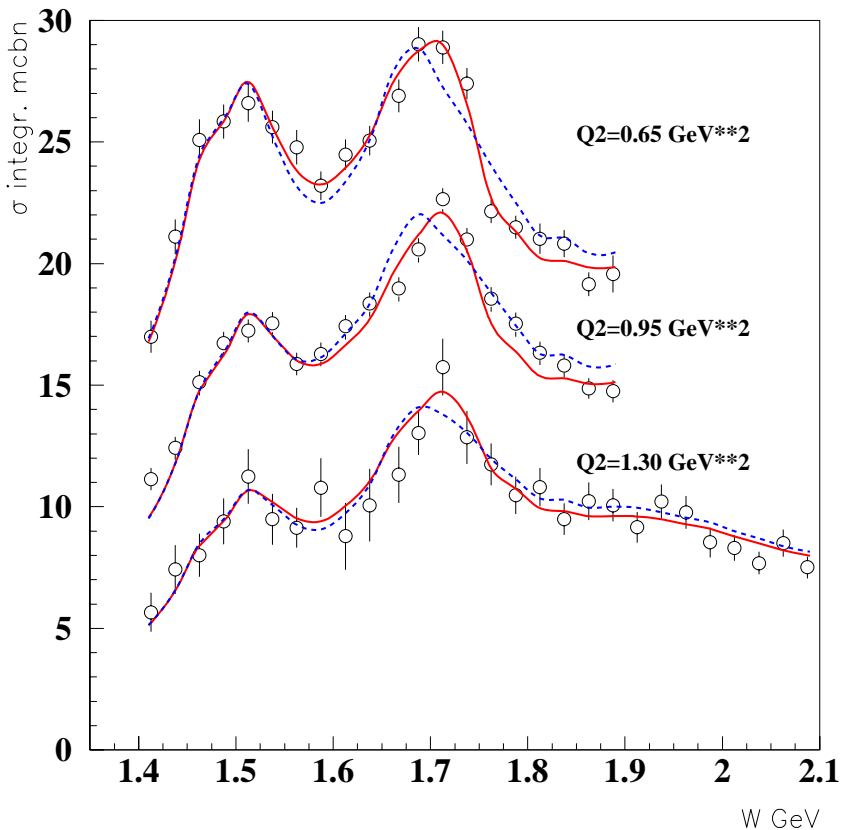


Figure 5.37: Total virtual photon cross section for $ep \rightarrow ep\pi^+\pi^-$ at all Q^2 as a function of W . Data from CLAS. Red full line: our resonance fit using a missing $P_{13}(1720)$; blue dashed line: our resonance fit modifying the conventional $D_{13}(1700)$.

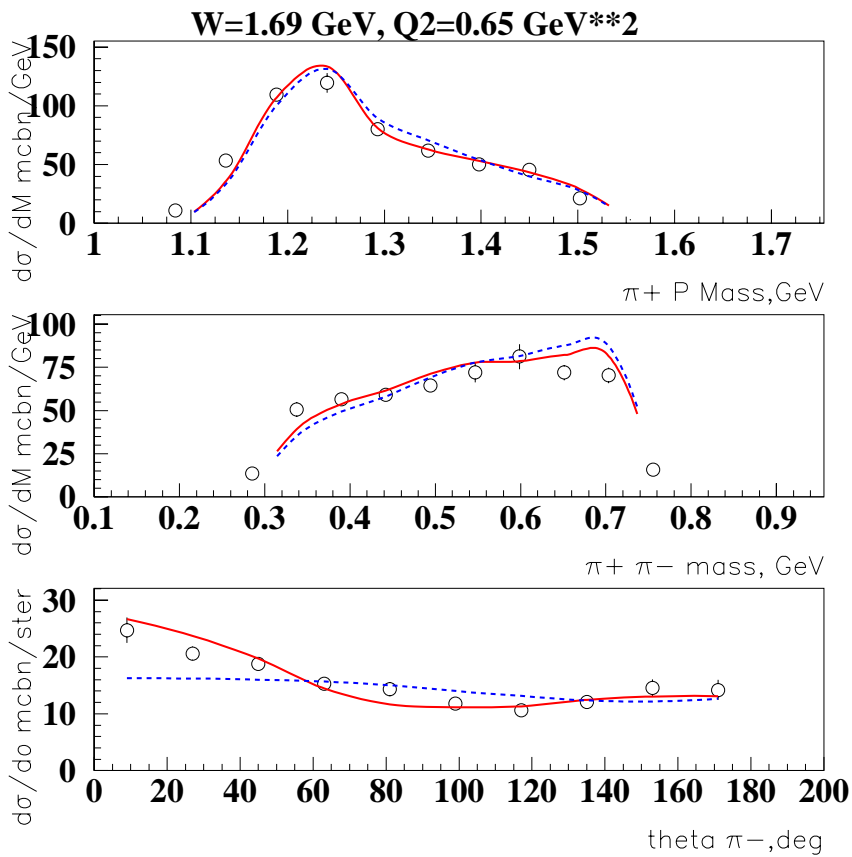


Figure 5.38: Virtual photon cross section for $ep \rightarrow ep\pi^+\pi^-$ at Q^2 between 0.5 and 0.8 GeV^2 and W between 1.675 and 1.7 GeV , differential in (top to bottom): proton- π^+ invariant mass; $\pi^+\pi^-$ invariant mass; π^- angle θ . Data from CLAS; red full line: our resonance fit using a missing $P_{13}(1720)$; blue dashed line: our resonance fit modifying the conventional $D_{13}(1700)$.

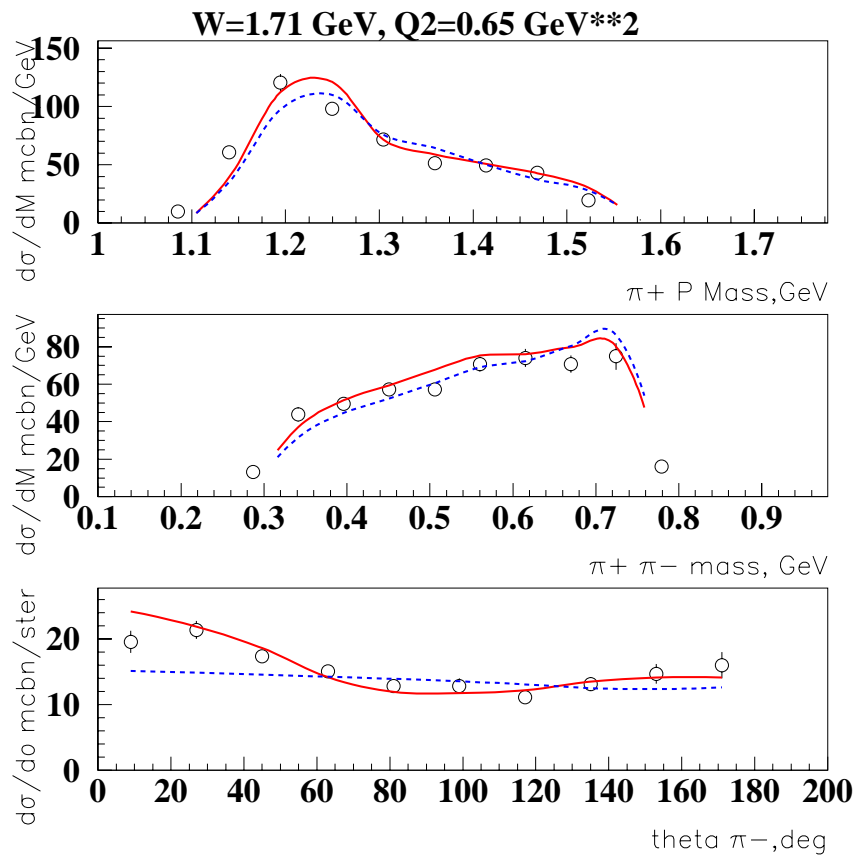


Figure 5.39: Same as previous picture, for W between 1.7 and 1.725 GeV.

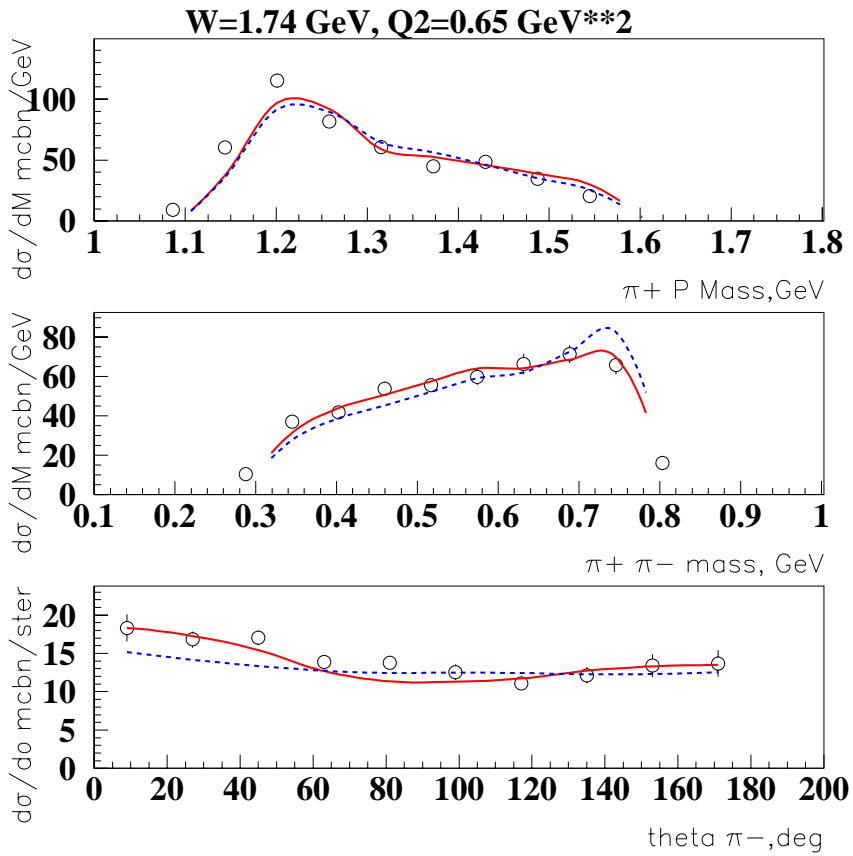


Figure 5.40: Same as previous picture, for W between 1.725 and 1.750 GeV.

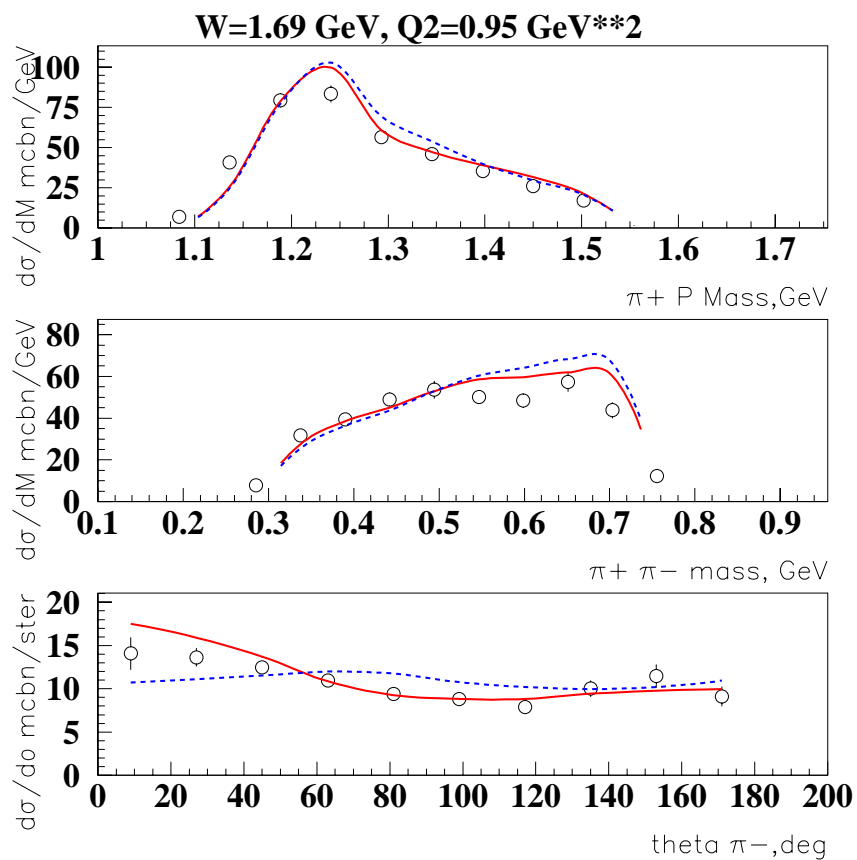


Figure 5.41: Same as previous picture, for Q^2 between 0.8 and 1.1 GeV^2 and W between 1.675 and 1.7 GeV .

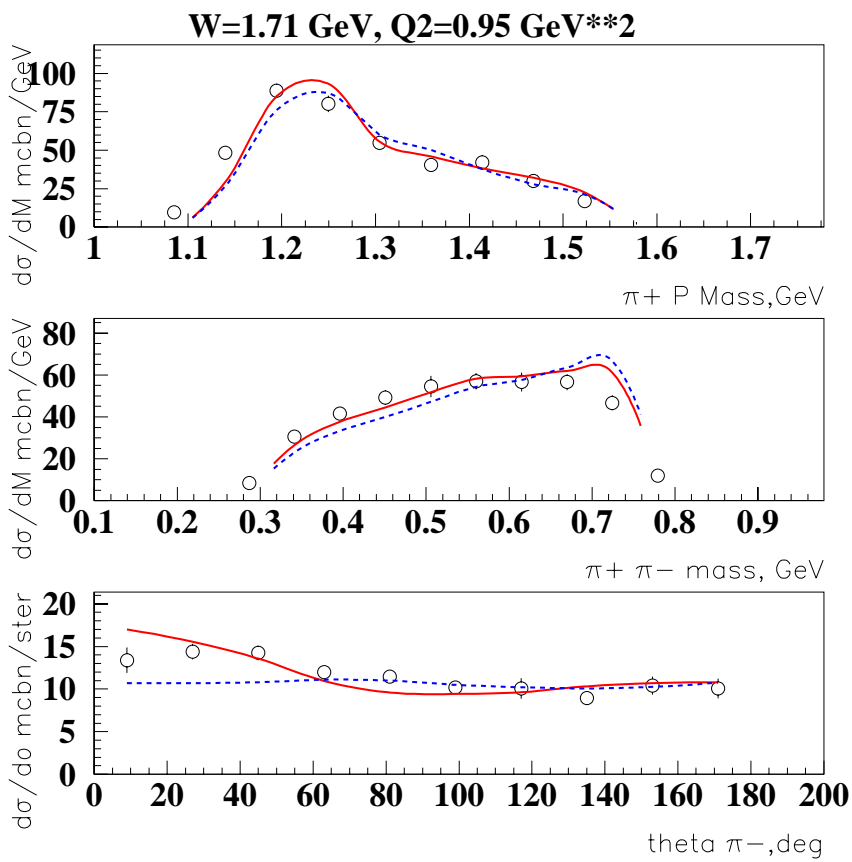


Figure 5.42: Same as previous picture, for W between 1.7 and 1.725 GeV.

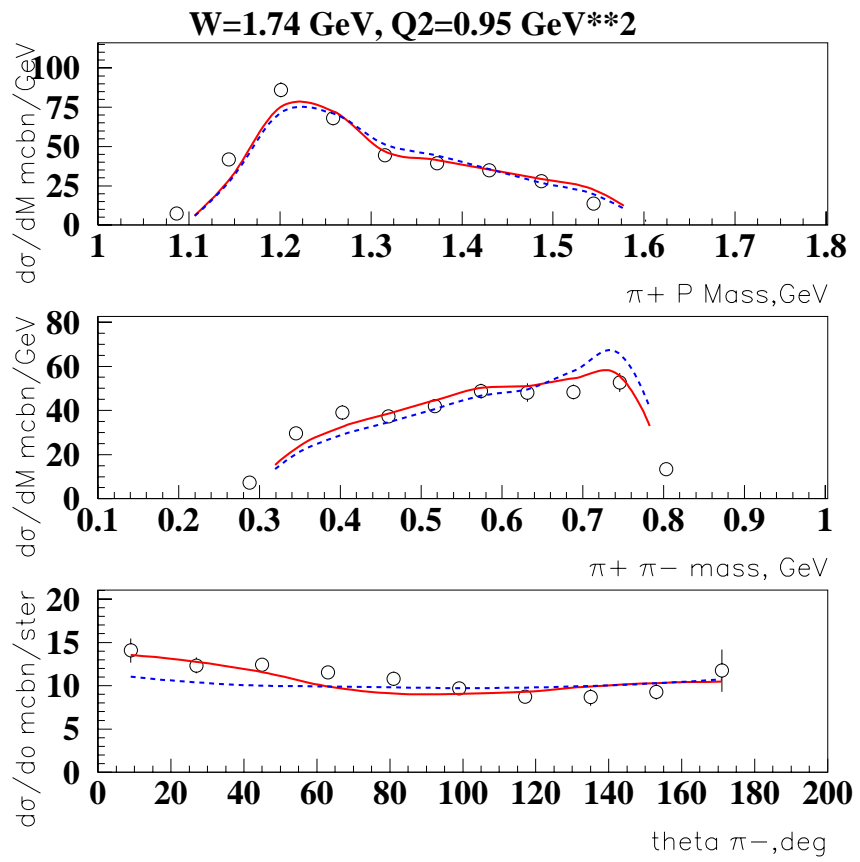


Figure 5.43: Same as previous picture, for W between 1.725 and 1.750 GeV.

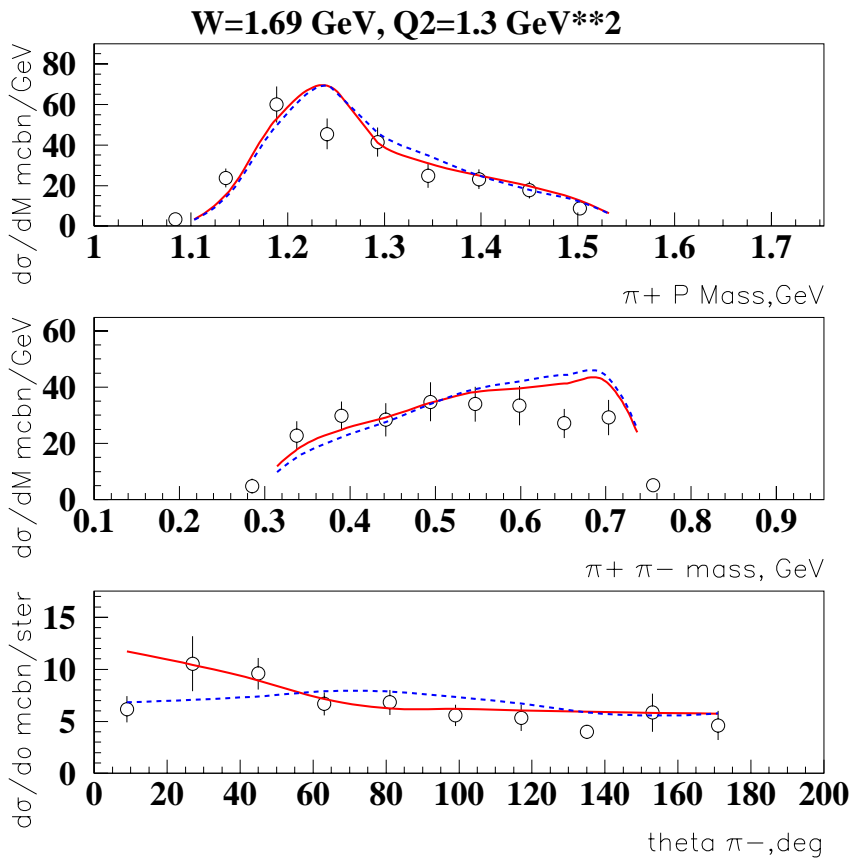


Figure 5.44: Same as previous picture, for Q^2 between 1.1 and 1.5 GeV^2 and W between 1.675 and 1.7 GeV .

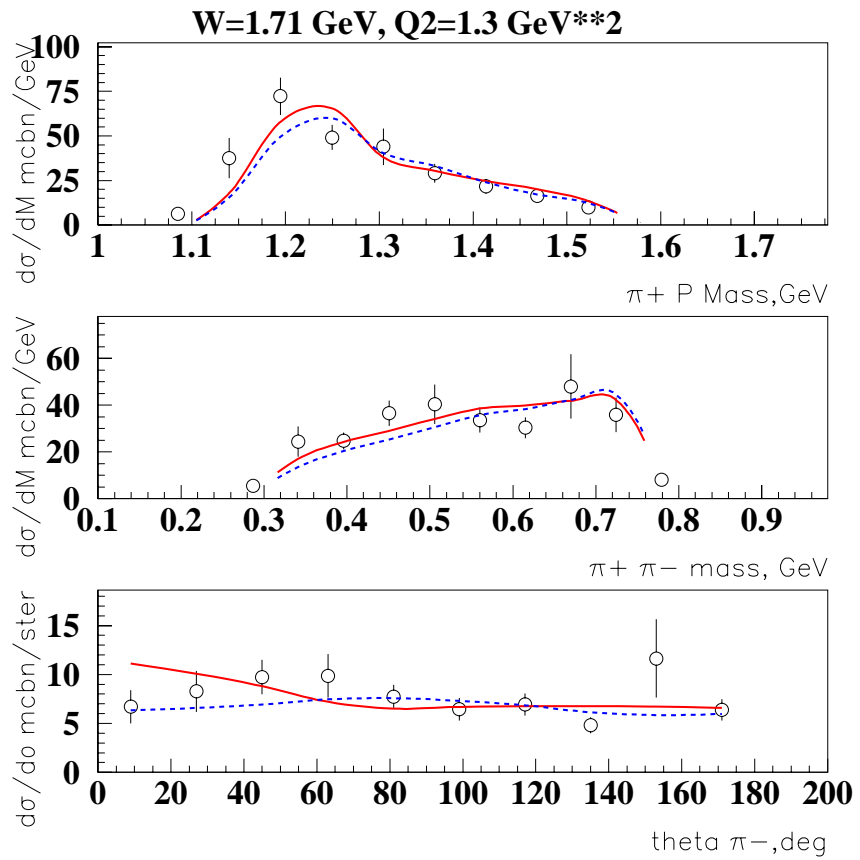


Figure 5.45: Same as previous picture, for W between 1.7 and 1.725 GeV.

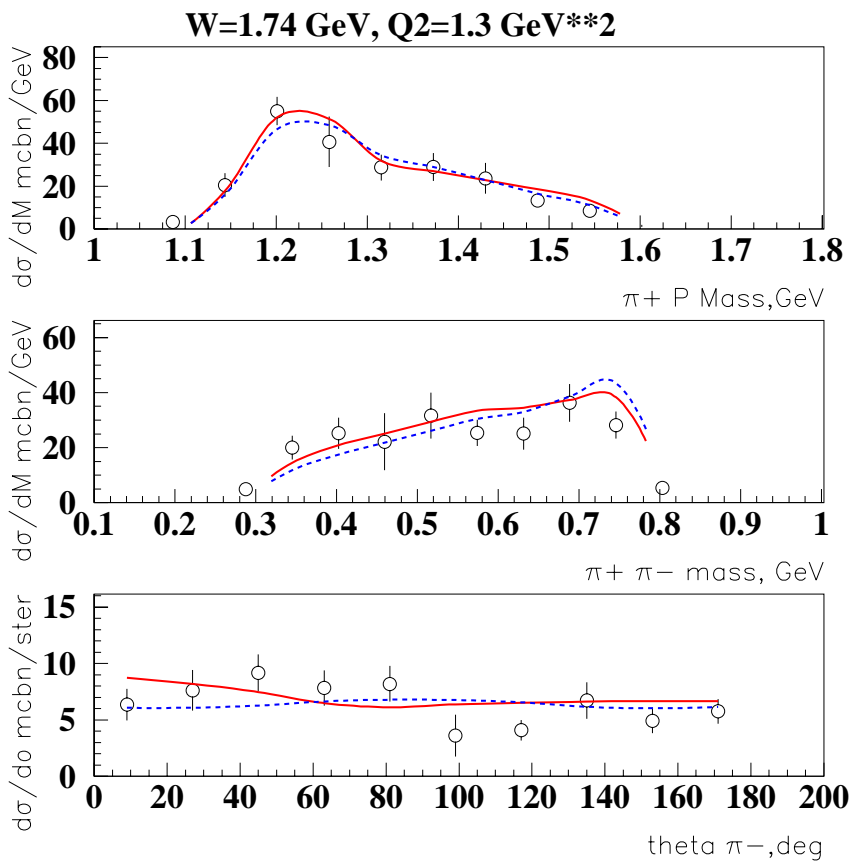


Figure 5.46: Same as previous picture, for W between 1.725 and 1.750 GeV.

extraction of this quantities could be wrong by such a large amount.

We also investigated the possibility for alternative solutions, varying $A_{1/2,3/2}$ form factors for missing state $P_{13}(1720)$ in a very wide range (between -100 and +100 in 10^{-3} GeV $^{-1/2}$ units). Using our MINUIT-based code version we fitted simultaneously 1-differential cross sections in a limited energy range, between 1.64 and 1.76 GeV at $Q^2=0.65$ GeV 2 . The variation range for missing state strong decay widths and position was the same as described above. The parameters of all other N^* 's were kept on the previously found best fit values. We found that MINUIT converged to the same solution as the full W fit with more limited parameter variation described above. The coincidence of both methods provides confidence in missing state parameter reliability. We also varied $A_{1/2,3/2}$ in a wide range simultaneously for $D_{13}(1700)$ conventional state and $P_{13}(1720)$ missing state at $Q^2=0.65$ GeV 2 . For this case we found two minima: the first one coincides with previous fit results for conventional $D_{13}(1700)$ and missing $P_{13}(1720)$ states separately fitted; the second gives drastically different $A_{1/2,3/2}$ amplitudes for $D_{13}(1700)$ state ($A_{1/2}=5.9*10^{-3}$ GeV $^{-1/2}$, $A_{1/2}=45*10^{-3}$ GeV $^{-1/2}$) with respect to the values expected from NRQM and other quark models; however in this case χ^2 appears to be 10 % lower. This second solution provides better description of angular distributions at W=1.66 GeV bin and a comparable with previous fit in all other W and Q^2 bins. Therefore, fit quality improvement is not significant, but $A_{1/2,3/2}$ for $D_{13}(1700)$ are strongly different from any quark model prediction; moreover, for this fit the total width of missing $P_{13}(1720)$ appears a bit too narrow, being 60 MeV: for all these reasons, we decided to keep this solution as a complementary opportunity and in all further analysis we restricted ourselves to solutions obtained in our "traditional" fit, over all W range and with parameter fluctuation in limited range. The complete 1-differential cross section plots for this second unusual solution are presented in http://www.jlab.org/Hall-B/secure/e1/mokeev/ps_final/minuit.

After having obtained the best solution when reproducing our data with a missing P_{13} , we proceeded in examining the following list of alternative quantum numbers: S_{11} , P_{11} , F_{15} , F_{17} . A D_{13} was not taken into consideration as our analysis of the conventional $D_{13}(1700)$ had shown that such a state could not fit our angular distributions well; a D_{15} was also ruled out assuming that the experimental value of the mass should be far from quark model predictions by not more than about 200 MeV: instead, the lowest missing D_{15} is predicted around 2.1 GeV, which would imply a shift of about 400 MeV if such a state was found instead at 1.7 GeV.

5.0.8 Resonance Analysis: Missing States Further Search

As a next step, we tried to implement different quantum numbers for the missing state to see how much sensitivity we have to its spin and parity; to choose what spin-parity to test, we followed the quark model predictions on the missing baryon masses, with the requirement that the mass of the candidates should not depart from the bump seen in the data by more than 200 MeV, which is the typical uncertainty attributed to such theoretical

models[48]; therefore, following predictions in [5], our next candidates were P_{11} , S_{11} , D_{15} , F_{15} , F_{17} .

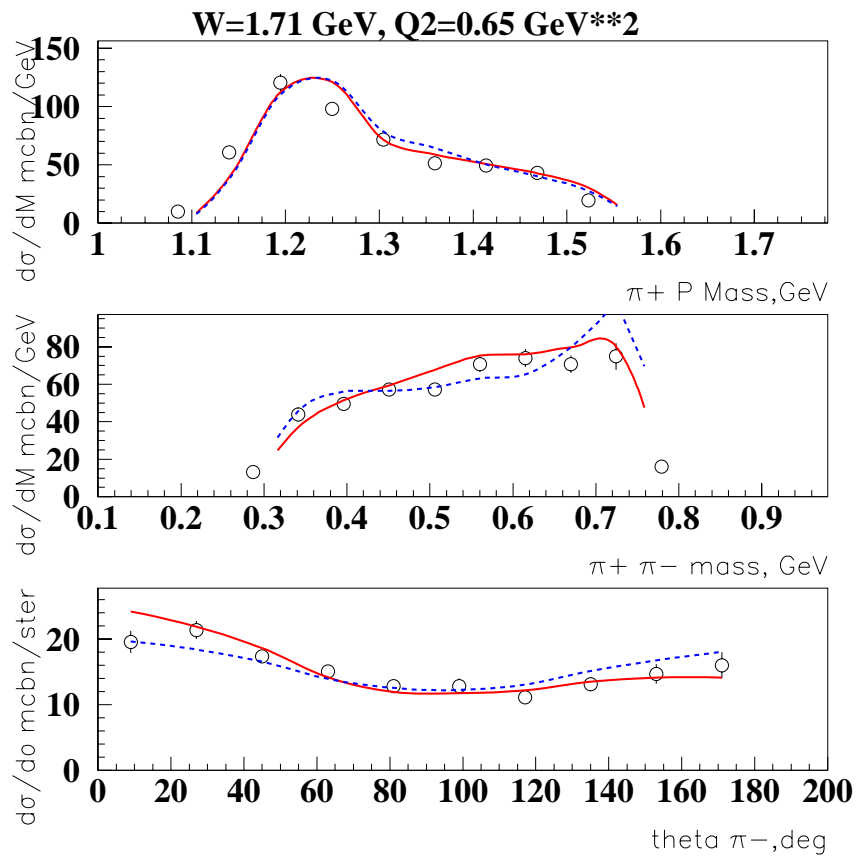


Figure 5.47: Virtual photon cross section for $ep \rightarrow ep\pi^+\pi^-$ at Q^2 between 0.5 and 0.8 GeV^2 and W between 1.7 and 1.725 GeV , differential in (top to bottom): proton- π^+ invariant mass; $\pi^+\pi^-$ invariant mass; π^- angle θ . Data from CLAS; red full line: our resonance fit using a missing P_{13} ; blue dashed line: our resonance fit using a missing P_{11} .

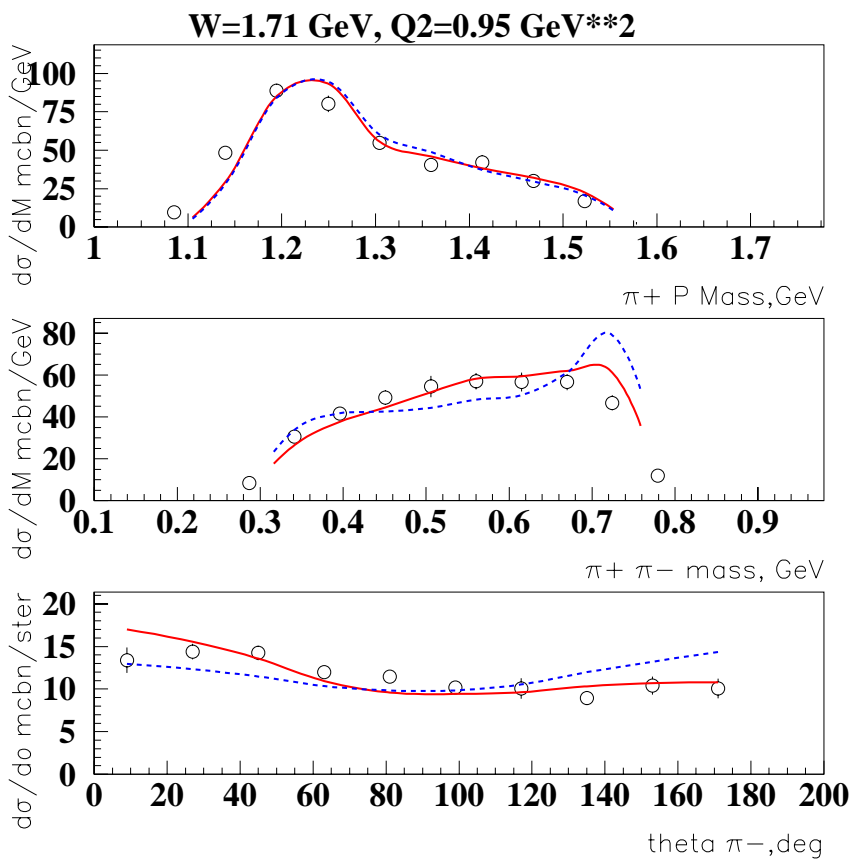


Figure 5.48: Same as previous picture, but for Q^2 between 0.8 and 1.1 GeV^2 .

We repeated the procedure of searching the resonance parameters, but starting from strong coupling values and position found in the case of the P_{13} ; the electromagnetic couplings $A_{1/2,3/2}$ were instead fixed requiring $A_{1/2}^2(J^P) + A_{3/2}^2(J^P) = A_{1/2}^2(P_{13}) + A_{3/2}^2(P_{13})$, which means to initially preserve the total electromagnetic excitation strength. We also assumed the subchannel decay width to $\pi\Delta$ and $\rho\rho$ final state for J^P missing resonances under investigation to be equal to the corresponding values established in fit for the missing $P_{13}(1720)$. To assign initial values for strong decay LS partial waves we subdivided the overall subchannel width equally among all LS waves. For N^* 's with spin greater than $\frac{1}{2}$, as initial values of $A_{1/2,3/2}$ we subdivided the total electromagnetic strength equally between the two helicities. Again we varied first the decay couplings and position and in a second pass the electromagnetic coupling to reproduce the overall strength. Figures 5.47 through 5.61 report the result of our search for all alternative quantum numbers, for the most significant energy bins at the three momentum transfers. Although the difference between these two states is not pronounced, based on the χ^2 we can still establish a preference for the P_{13} hypothesis. Complete information on 1-differential cross section description, implementing missing baryon states with different quantum numbers can be found in http://www.jlab.org/Hall-B/secure/e1/mokeev/ps_final/comparison. In all plots the red solid line always corresponds to $P_{13}(1720)$ missing state hypothesis, while cross sections obtained with alternative missing states are shown by blue dashed lines.

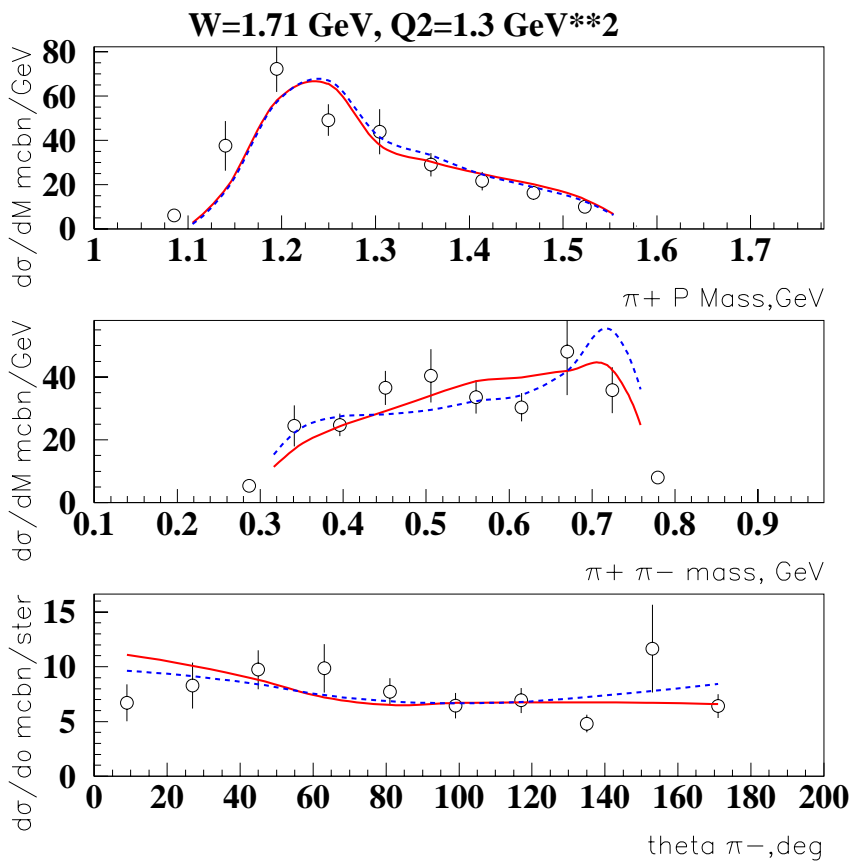


Figure 5.49: Same as previous picture, but for Q^2 between 1.1 and 1.5 GeV^2 .

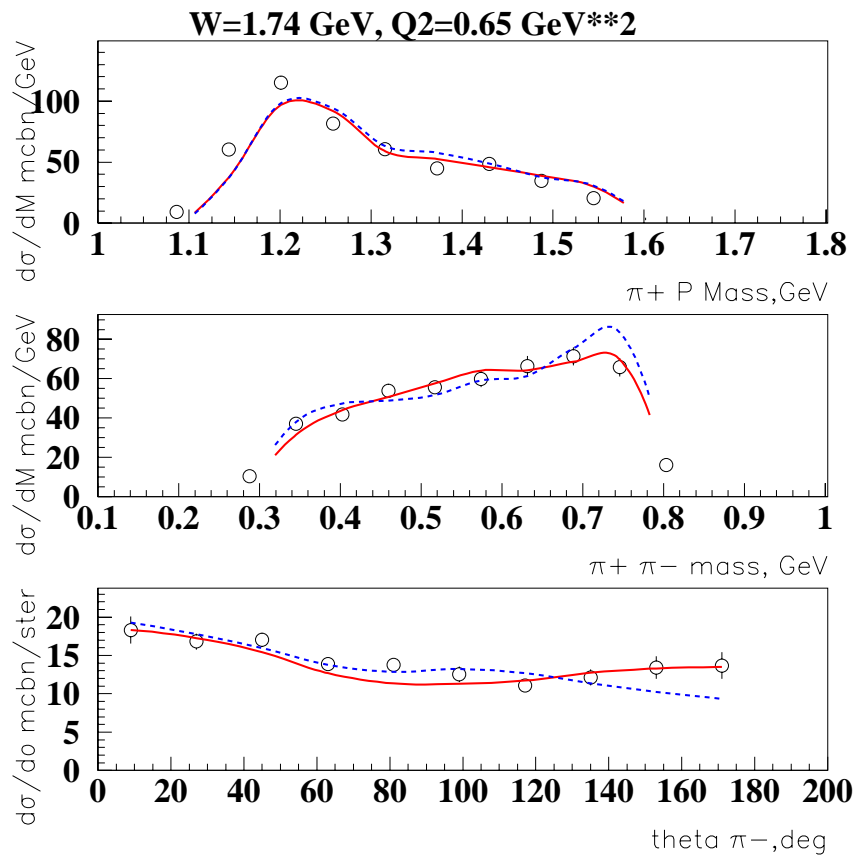


Figure 5.50: Virtual photon cross section for $ep \rightarrow ep\pi^+\pi^-$ at Q^2 between 0.5 and 0.8 GeV^2 and W between 1.725 and 1.750 GeV, differential in (top to bottom): proton- π^+ invariant mass; $\pi^+\pi^-$ invariant mass; π^- angle θ . Data from CLAS; red full line: our resonance fit using a missing P_{13} ; blue dashed line: our resonance fit using a missing S_{11} .

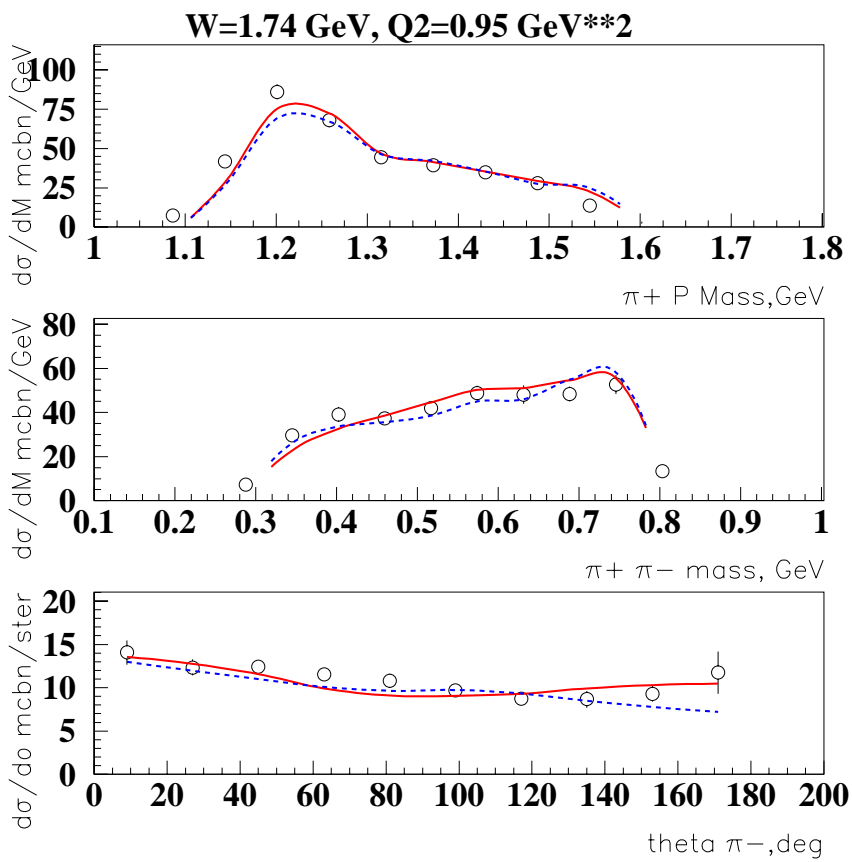


Figure 5.51: Same as previous picture, but for Q^2 between 0.8 and 1.1 GeV^2 .

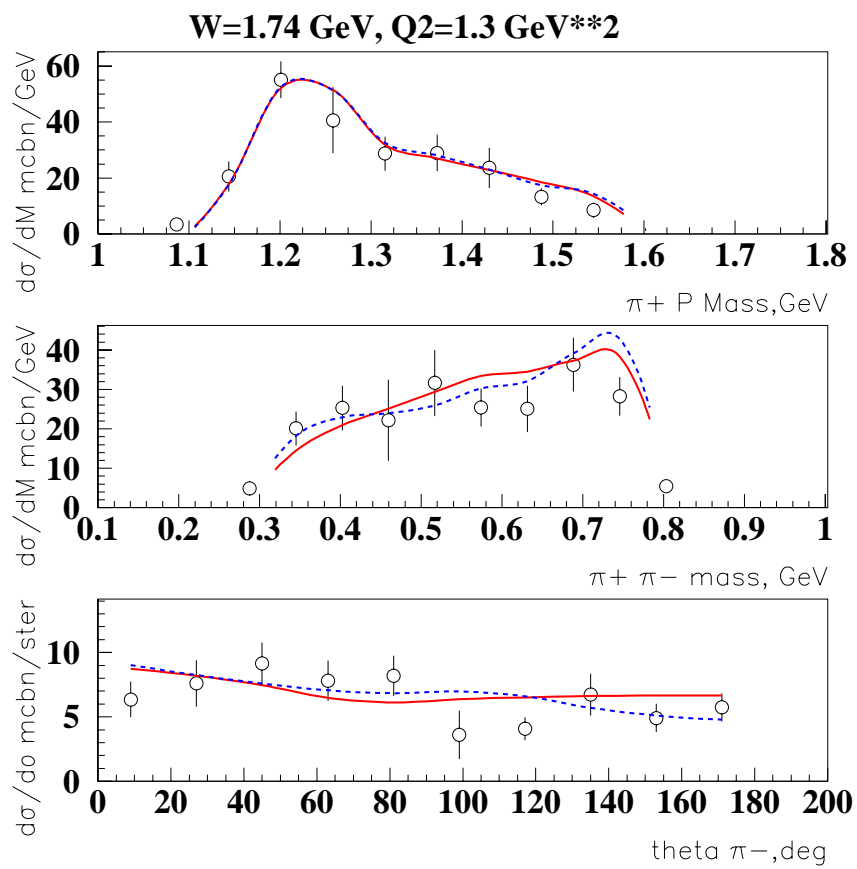


Figure 5.52: Same as previous picture, but for Q^2 between 1.1 and 1.5 GeV².

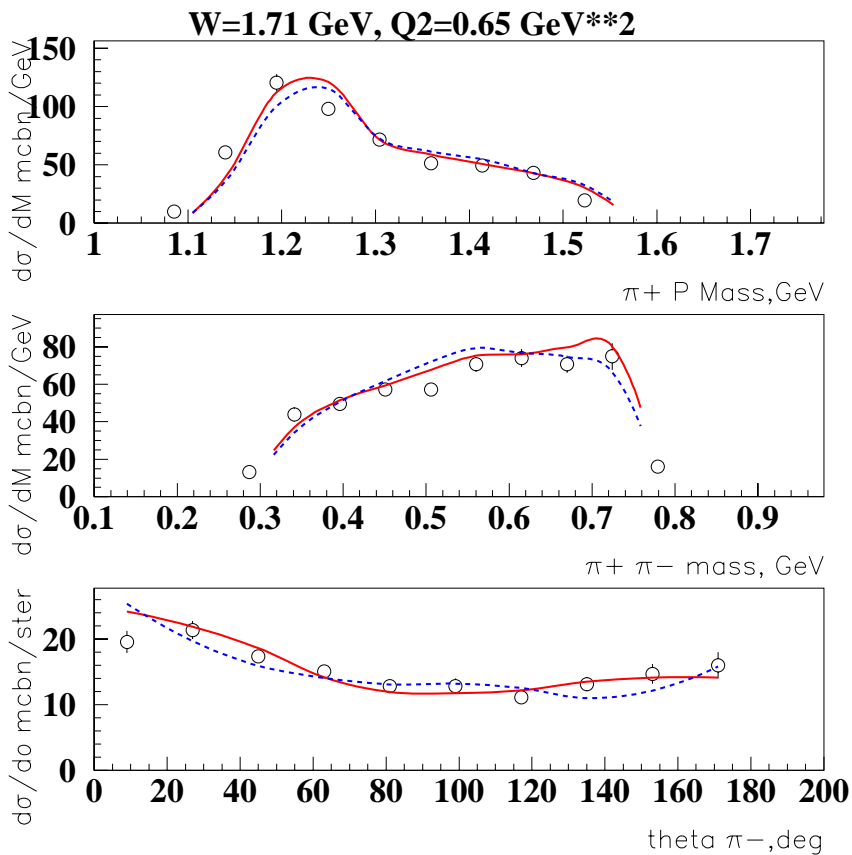


Figure 5.53: Virtual photon cross section for $ep \rightarrow ep\pi^+\pi^-$ at Q^2 between 0.5 and 0.8 GeV^2 and W between 1.7 and 1.725 GeV , differential in (top to bottom): proton- π^+ invariant mass; π^+ - π^- invariant mass; π^- angle θ . Data from CLAS; red full line: our resonance fit using a missing P_{13} ; blue dashed line: our resonance fit using a missing D_{15} .

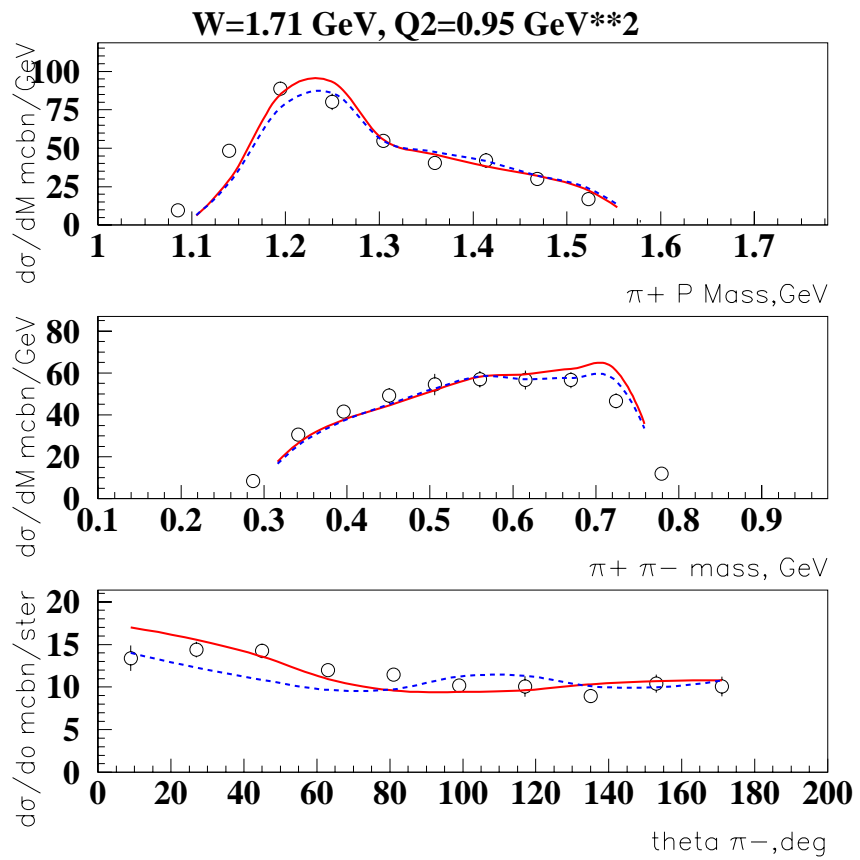


Figure 5.54: Same as previous picture, but for Q^2 between 0.8 and 1.1 GeV².

Table 5.7: χ^2 values for the conventional resonance hypothesis, at several W and Q^2 values

| Resonance state | W (GeV) | Q^2 (GeV^2/c^2) | χ^2 |
|-----------------|---------|-----------------------|----------|
| $D_{13}(1700)$ | 1.69 | 0.65 | 9.6 |
| | 1.69 | 0.95 | 7.6 |
| | 1.69 | 1.3 | 1.8 |
| | 1.71 | 0.65 | 16 |
| | 1.71 | 0.95 | 17 |
| | 1.71 | 1.3 | 4.3 |
| | 1.74 | 0.65 | 15 |
| | 1.74 | 0.95 | 13 |
| | 1.74 | 1.3 | 1.7 |
| | average | average | 9.5 |

In tables 5.7 through 5.13 we present χ^2 calculated from the three distributions for a few W values around the bump and at all three momentum transfers, both for the conventional state hypothesis as well as for the various missing states tested with different quantum numbers.

5.1 Evaluation of uncertainties for extracted form factors $A_{1/2}$, $A_{3/2}$

The following procedure was developed to estimate uncertainties on the extracted $A_{1/2,3/2}$ electromagnetic form factors. First we varied $A_{1/2,3/2}$ for each state by 80% in σ around best values obtained in our fit. For each choice of $A_{1/2,3/2}$, we calculated the total cross section as a function of W and the corresponding χ^2 , obtained from comparison of estimated and measured 1-differential cross-sections, averaged over the full W range at each single Q^2 bin separately. The corresponding band of estimated total cross section uncertainties for $Q^2=0.95$ GeV 2 is shown in figure 5.62. We then selected only those solutions corresponding to an increase of χ^2 by unity. The accepted band of solutions under this requirement for $Q^2=0.95$ GeV 2 is shown in figure 5.63. Then we averaged $A_{1/2,3/2}$ form factor values for each N^* from the accepted solutions, attributing the obtained mean values and dispersions with mean values and statistical uncertainties for extracted N^* form factors. The results obtained together with SQTM expectations[43] are shown in figures 5.64 through 5.75, together with the curves calculated from SQTM or NRQM[43]. For the main part of states, $A_{1/2,3/2}$ values extracted in fit deviate within 30% from SQTM or NRQM prediction, while to get correct description of $\pi\pi$ invariant mass distributions in

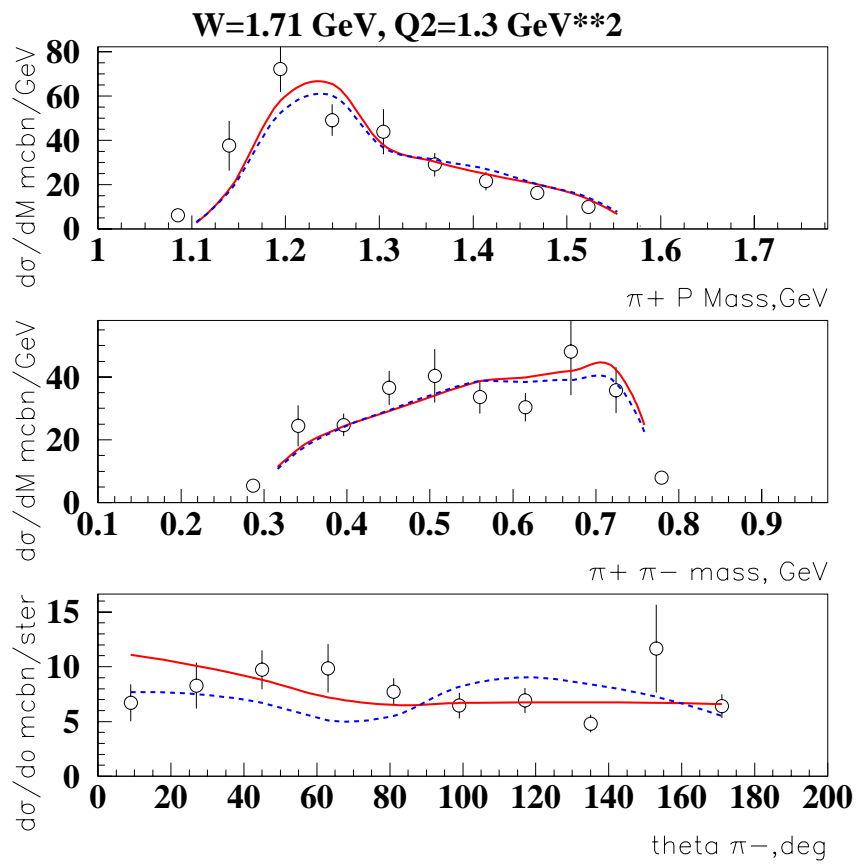


Figure 5.55: Same as previous picture, but for Q^2 between 1.1 and 1.5 GeV².

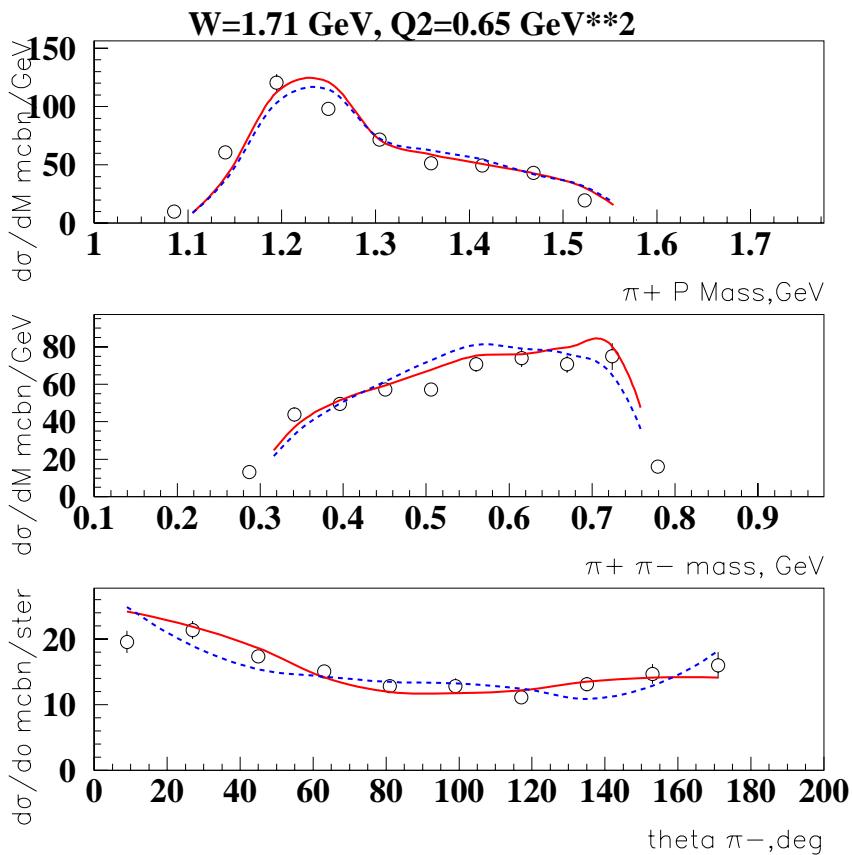


Figure 5.56: Virtual photon cross section for $ep \rightarrow ep\pi^+\pi^-$ at Q^2 between 0.5 and 0.8 GeV^2 and W between 1.7 and 1.725 GeV , differential in (top to bottom): proton- π^+ invariant mass; $\pi^+\pi^-$ invariant mass; π^- angle θ . Data from CLAS; red full line: our resonance fit using a missing P_{13} ; blue dashed line: our resonance fit using a missing F_{15} .

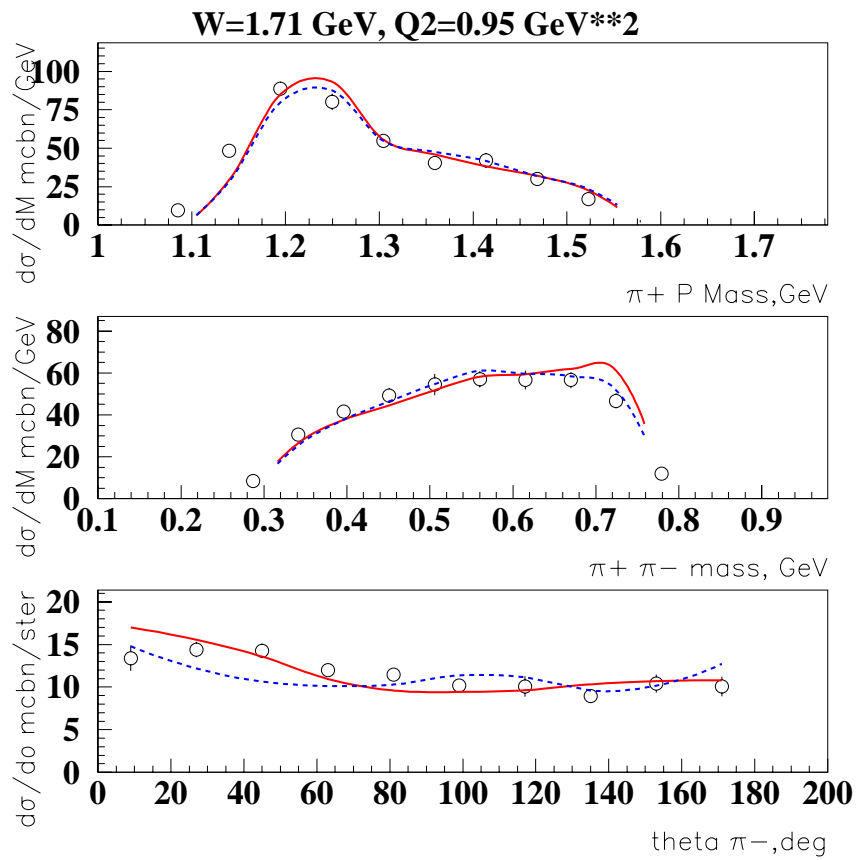


Figure 5.57: Same as previous picture, but for Q^2 between 0.8 and 1.1 GeV 2 .

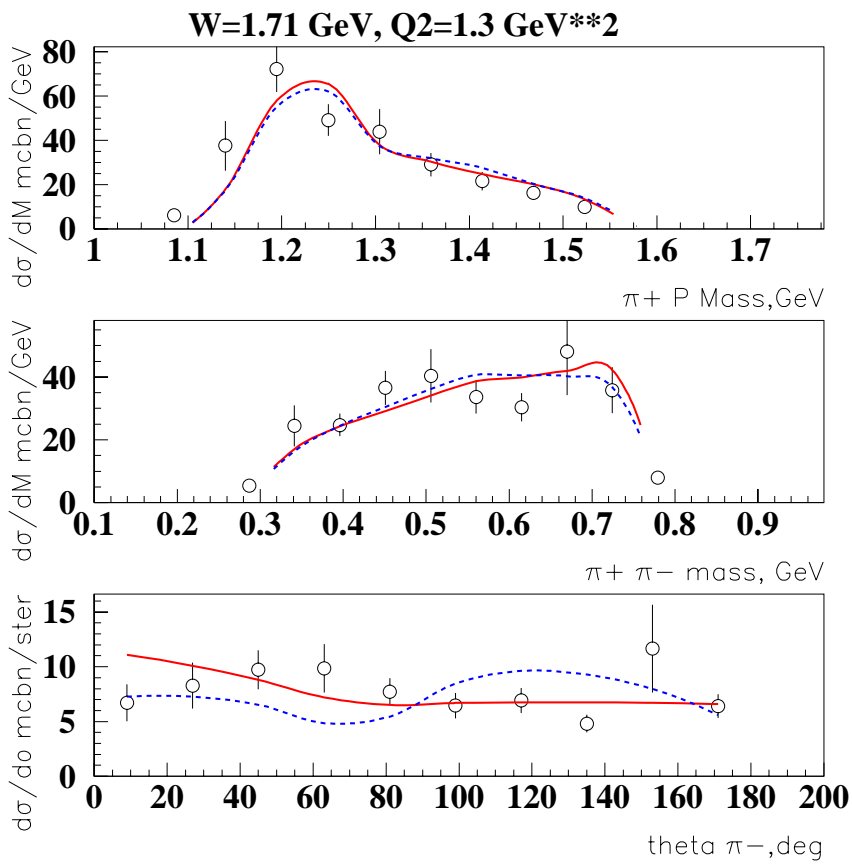


Figure 5.58: Same as previous picture, but for Q^2 between 1.1 and 1.5 GeV^2 .

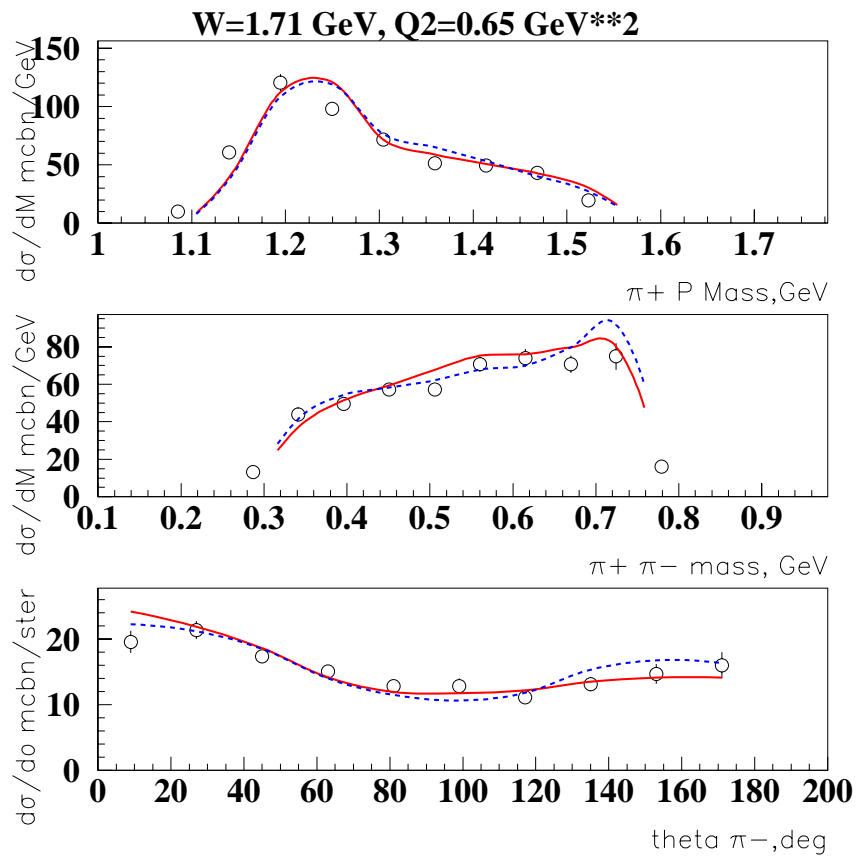


Figure 5.59: Virtual photon cross section for $ep \rightarrow ep\pi^+\pi^-$ at Q^2 between 0.5 and 0.8 GeV^2 and W between 1.7 and 1.725 GeV , differential in (top to bottom): proton- π^+ invariant mass; $\pi^+\pi^-$ invariant mass; π^- angle θ . Data from CLAS; red full line: our resonance fit using a missing P_{13} ; blue dashed line: our resonance fit using a missing F_{17} .

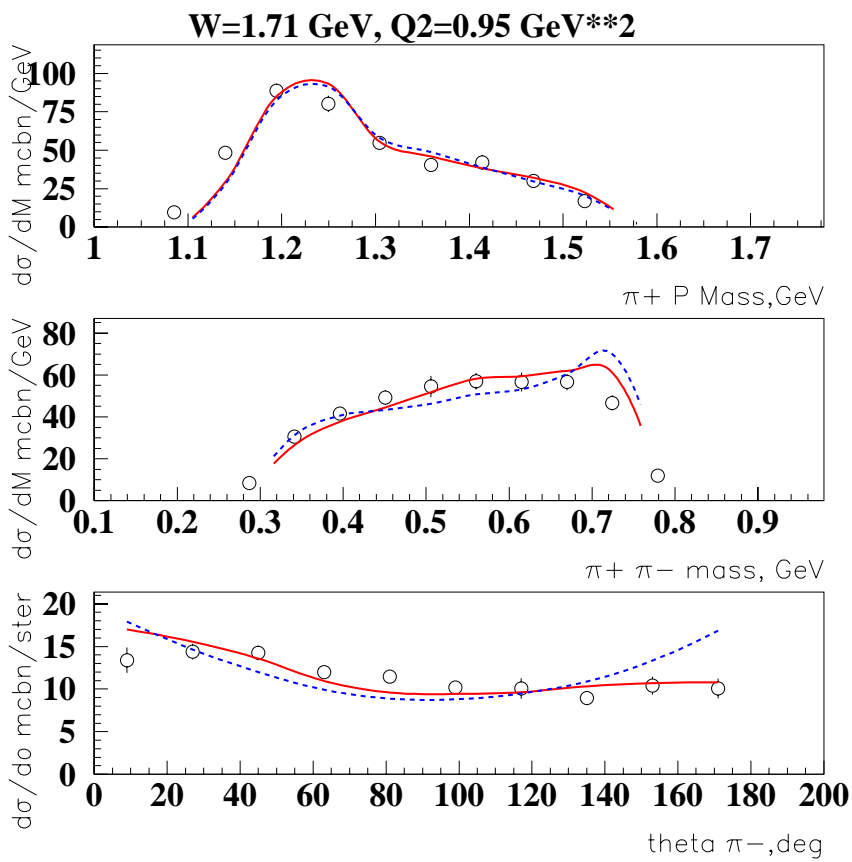


Figure 5.60: Same as previous picture, but for Q^2 between 0.8 and 1.1 GeV^2 .

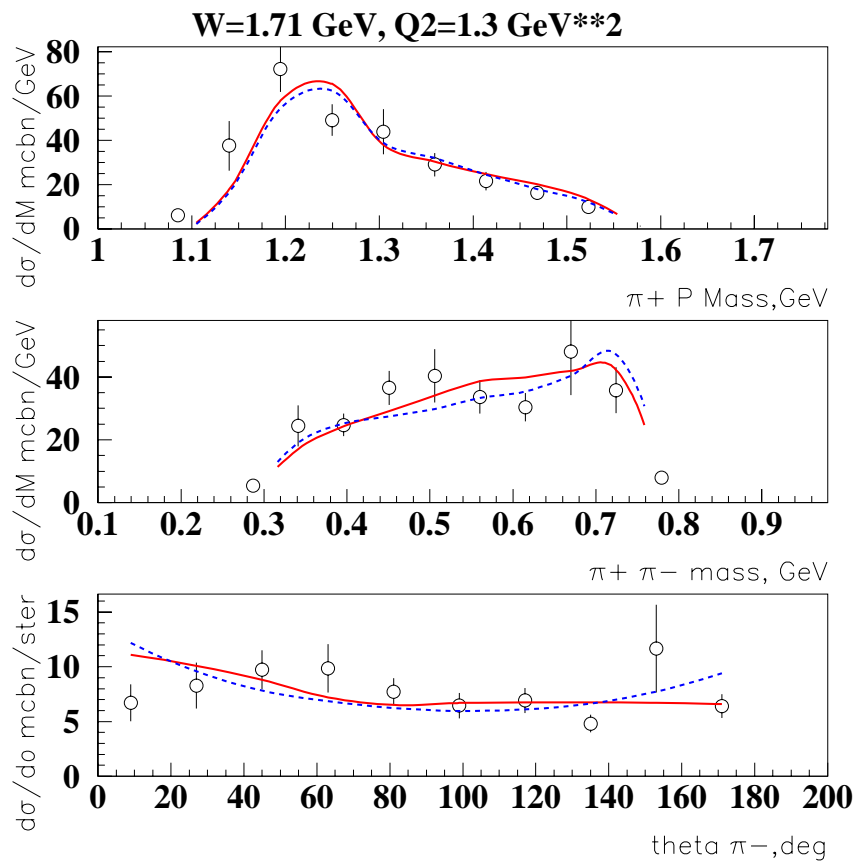


Figure 5.61: Same as previous picture, but for Q^2 between 1.1 and 1.5 GeV².

Table 5.8: χ^2 values for the missing S_{11} hypothesis, at several W and Q^2 values

| Resonance state | W (GeV) | Q^2 (GeV^2/c^2) | χ^2 |
|-----------------|---------|-----------------------|----------|
| $S_{11}(1720)$ | 1.69 | 0.65 | 4.8 |
| | 1.69 | 0.95 | 6.4 |
| | 1.69 | 1.3 | 3.2 |
| | 1.71 | 0.65 | 7.8 |
| | 1.71 | 0.95 | 6.5 |
| | 1.71 | 1.3 | 2.2 |
| | 1.74 | 0.65 | 7.2 |
| | 1.74 | 0.95 | 4.5 |
| | 1.74 | 1.3 | 1.4 |
| | average | average | 4.9 |

Table 5.9: χ^2 values for the missing P_{11} hypothesis, at several W and Q^2 values

| Resonance state | W (GeV) | Q^2 (GeV^2/c^2) | χ^2 |
|-----------------|---------|-----------------------|----------|
| $P_{11}(1720)$ | 1.69 | 0.65 | 5.4 |
| | 1.69 | 0.95 | 8.2 |
| | 1.69 | 1.3 | 3.5 |
| | 1.71 | 0.65 | 8.9 |
| | 1.71 | 0.95 | 10 |
| | 1.71 | 1.3 | 2.7 |
| | 1.74 | 0.65 | 7.8 |
| | 1.74 | 0.95 | 4.9 |
| | 1.74 | 1.3 | 1.6 |
| | average | average | 5.9 |

Table 5.10: χ^2 values for the missing P_{13} hypothesis, at several W and Q^2 values

| Resonance state | W (GeV) | Q^2 (GeV^2/c^2) | χ^2 |
|-----------------|---------|-----------------------|----------|
| $P_{13}(1720)$ | 1.69 | 0.65 | 3.4 |
| | 1.69 | 0.95 | 5.3 |
| | 1.69 | 1.3 | 2.9 |
| | 1.71 | 0.65 | 5.5 |
| | 1.71 | 0.95 | 4.5 |
| | 1.71 | 1.3 | 2.2 |
| | 1.74 | 0.65 | 5.5 |
| | 1.74 | 0.95 | 3.3 |
| | 1.74 | 1.3 | 1.5 |
| | average | average | 3.8 |

Table 5.11: χ^2 values for the missing D_{15} hypothesis, at several W and Q^2 values

| Resonance state | W (GeV) | Q^2 (GeV^2/c^2) | χ^2 |
|-----------------|---------|-----------------------|----------|
| $D_{15}(1720)$ | 1.69 | 0.65 | 4.9 |
| | 1.69 | 0.95 | 8.5 |
| | 1.69 | 1.3 | 5.4 |
| | 1.71 | 0.65 | 7.7 |
| | 1.71 | 0.95 | 5.2 |
| | 1.71 | 1.3 | 3.2 |
| | 1.74 | 0.65 | 8.2 |
| | 1.74 | 0.95 | 5.0 |
| | 1.74 | 1.3 | 1.8 |
| | average | average | 5.6 |

Table 5.12: χ^2 values for the missing F_{15} hypothesis, at several W and Q^2 values

| Resonance state | W (GeV) | Q^2 (GeV^2/c^2) | χ^2 |
|-----------------|-----------|-----------------------|----------|
| $F_{15}(1720)$ | 1.69 | 0.65 | 4.2 |
| | 1.69 | 0.95 | 7.0 |
| | 1.69 | 1.3 | 5.7 |
| | 1.71 | 0.65 | 7.6 |
| | 1.71 | 0.95 | 4.6 |
| | 1.71 | 1.3 | 3.6 |
| | 1.74 | 0.65 | 8.3 |
| | 1.74 | 0.95 | 4.5 |
| | 1.74 | 1.3 | 2.2 |
| | average | average | 5.3 |

Table 5.13: χ^2 values for the missing F_{17} hypothesis, at several W and Q^2 values

| Resonance state | W (GeV) | Q^2 (GeV^2/c^2) | χ^2 |
|-----------------|-----------|-----------------------|----------|
| $F_{17}(1720)$ | 1.69 | 0.65 | 4.0 |
| | 1.69 | 0.95 | 7.1 |
| | 1.69 | 1.3 | 3.3 |
| | 1.71 | 0.65 | 6.7 |
| | 1.71 | 0.95 | 8.9 |
| | 1.71 | 1.3 | 2.8 |
| | 1.74 | 0.65 | 6.8 |
| | 1.74 | 0.95 | 4.2 |
| | 1.74 | 1.3 | 1.7 |
| | average | average | 5.1 |

W bins around 1.7 GeV, we should decrease $A_{1/2,3/2}$ form factors of $P_{13}(1720)$ conventional state more than a factor 2: this could be an indication of a particular nature of $P_{13}(1720)$ resonance structure. For many states, the Q^2 dependence of form factors is much steeper at Q^2 below 0.6 GeV 2 with respect to higher momentum transfer values: this is normally interpreted as indication of the role of additional degrees of freedom in the photon-proton interaction at low Q^2 , in particular the role of sea quarks or a meson cloud contribution created by flux tube breaking[50].

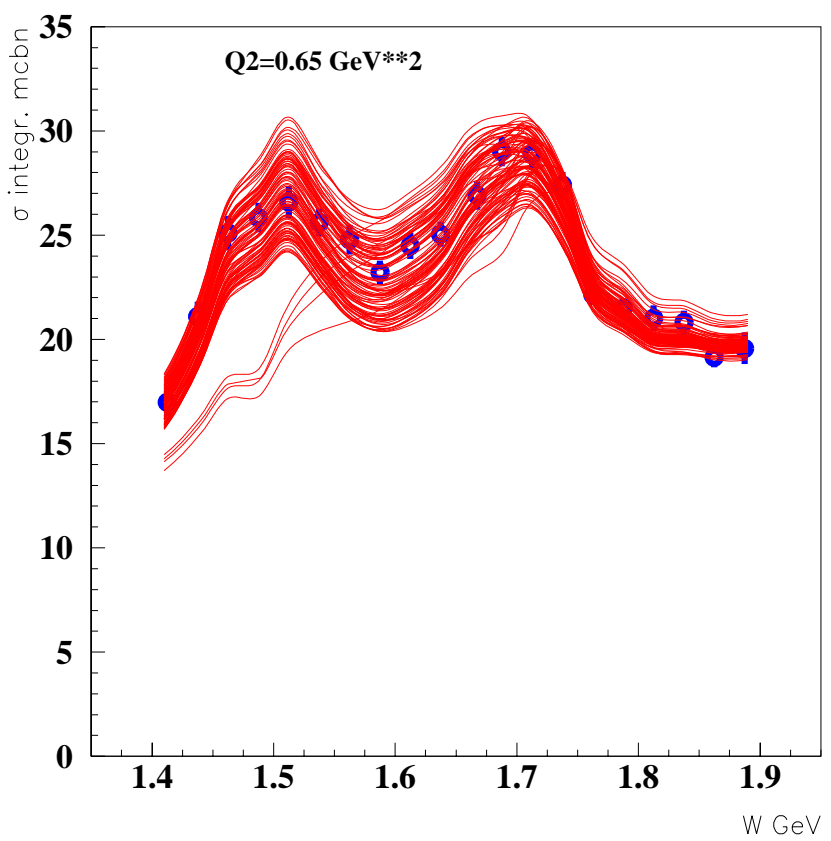


Figure 5.62: Band of solutions when allowing $A_{1/2,3/2}$ to fluctuate by 80 %, at $Q^2=0.95$ GeV^2 .

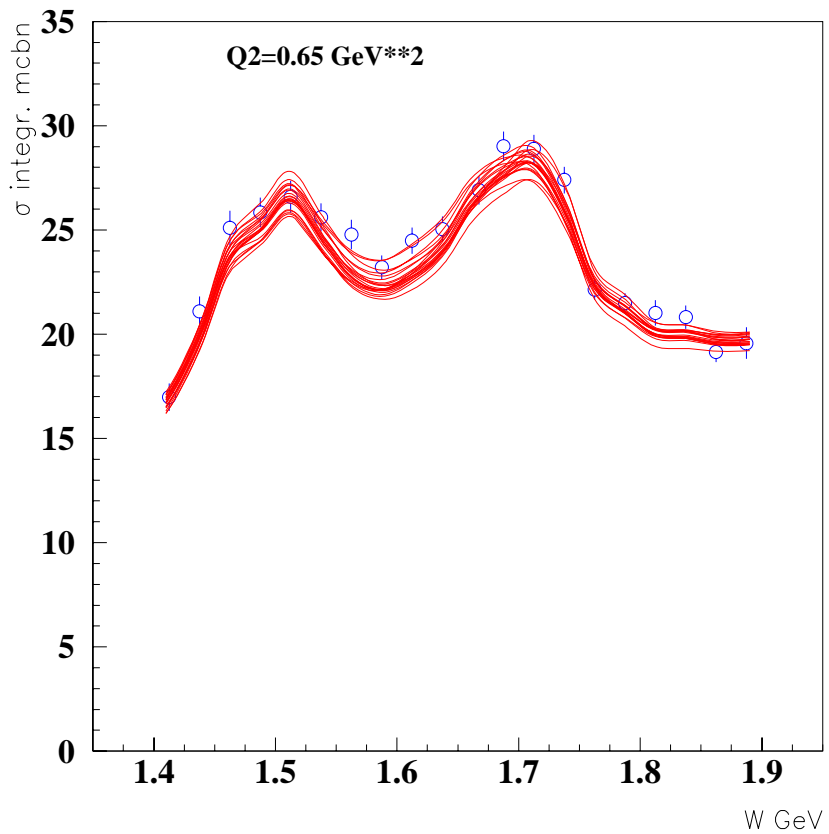


Figure 5.63: Band of solutions when selecting solutions corresponding to experimental uncertainties, at $Q^2=0.95 \text{ GeV}^2$.

5.2 Quasi-two-body channel and resonant/background separation

Isolating the amplitudes of particular quasi-two-body channels as well as the overall amplitudes for resonant and non-resonant mechanisms, we subdivided total and 1-differential cross sections into contributions of different quasi-two-body channels as well as contributions of resonant and non resonant mechanisms. Since our calculations were fitted to the data and the fit obtained is rather good, we can consider our channel separation and our resonance-background separation as quite realistic. The dependence of different quasi-two-body cross sections on W as well as the results for the resonance-background separation, together with the overall double charged pion production cross section for the case of the best fit with a missing $P_{13}(1720)$ state are shown in figure 5.76 through 5.78. For $W < 1.75$ GeV, $\pi^- \Delta^{++}$ channel provides the main contribution, while at W above 1.85 GeV the contributions of $\pi^- \Delta^{++}$, ρp and phase space appear to be comparable, however $\pi^- \Delta^{++}$ production decreases and ρp channel increases with W at all Q^2 values. The $\gamma p \rightarrow \rho p$ cross section exhibits a resonance-like bump around 1.9 GeV in W ($Q^2 = 1.3$ GeV 2): therefore there is the opportunity to study high-lying N^* 's with $M > 1.9$ GeV in double charged pion production exclusive channel even at Q^2 above 1 GeV 2 . A remarkable feature in our resonance-background separation (figure 5.79 through 5.81) is the growth of the N^* contribution with Q^2 . It could be interesting to study such resonant mechanism at higher Q^2 to reach kinematic domain where N^* 's relative contribution becomes small in comparison to photon interaction with quark without formation of a resonant bound state, assuming that deep-inelastic-like picture becomes dominant at such high momentum transfers[51].

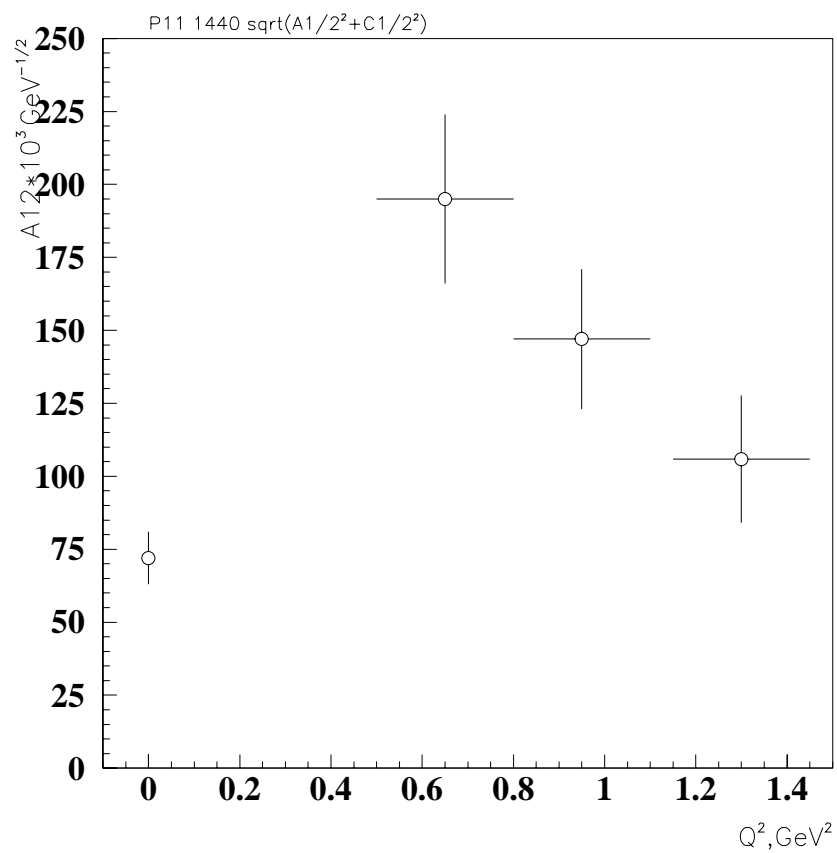


Figure 5.64: Total photoexcitation strength of $P_{11}(1440)$ as a function of Q^2 from our fit; photon point is from PDG.

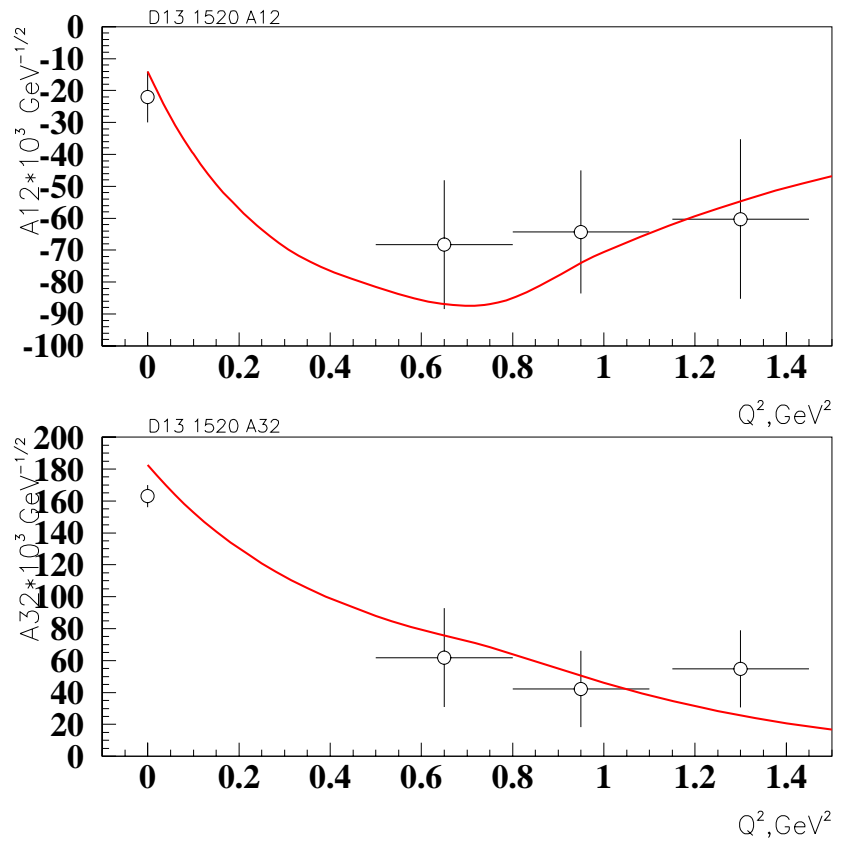


Figure 5.65: Photocouplings of $D_{13}(1520)$ as a function of Q^2 from our fit; photon point is from PDG.

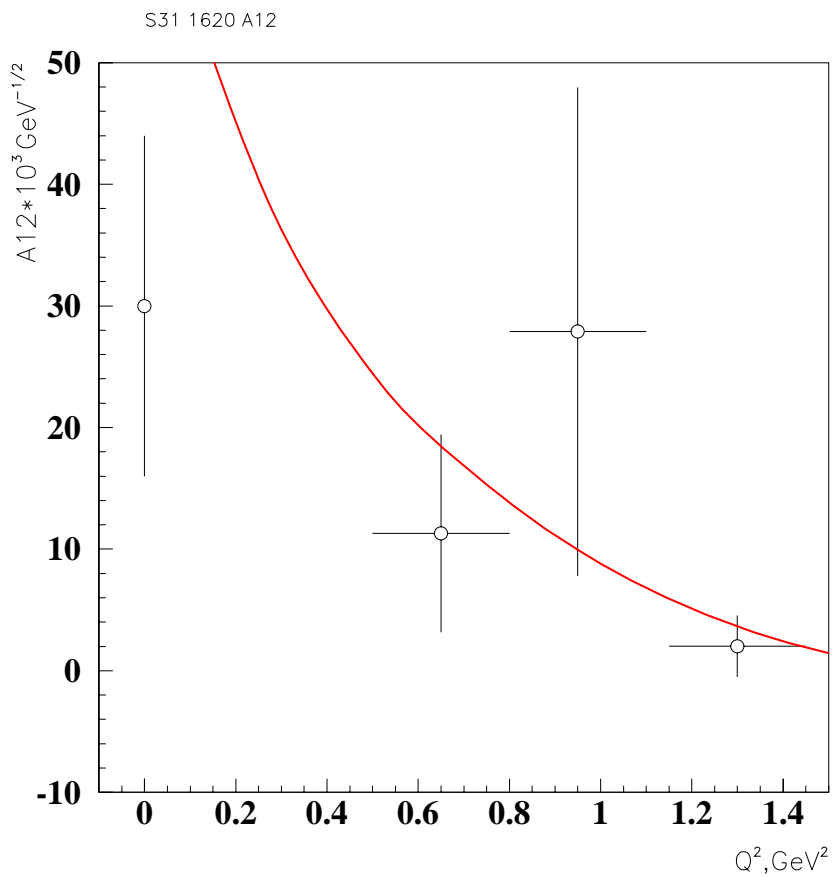


Figure 5.66: Photocouplings of $S_{31}(1620)$ as a function of Q^2 from our fit; photon point is from PDG.

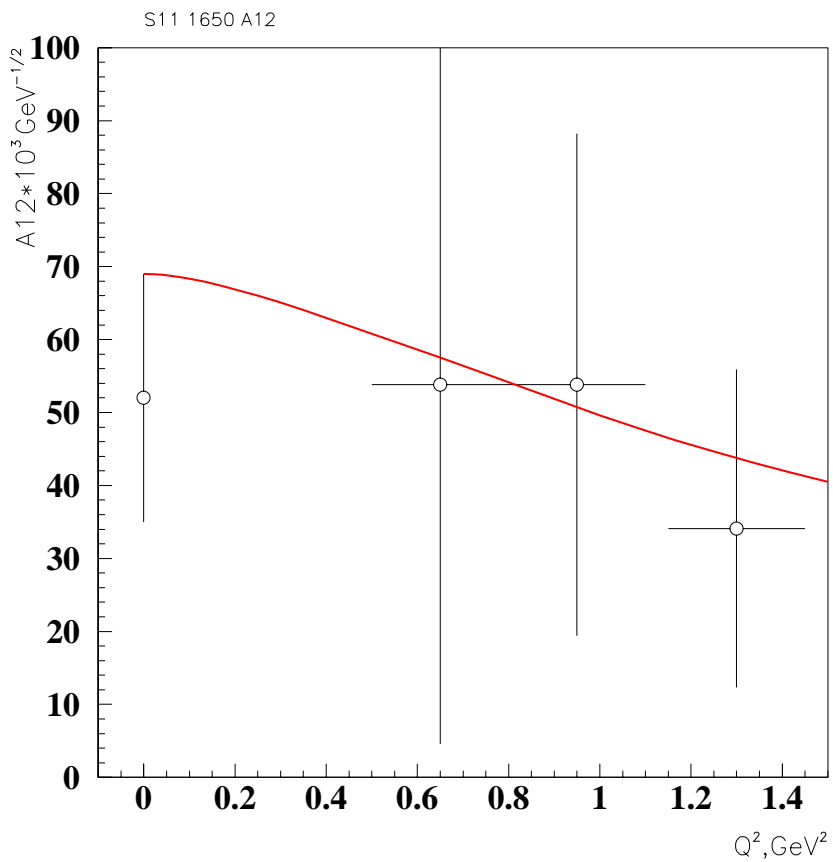


Figure 5.67: Photocouplings of $S_{11}(1650)$ as a function of Q^2 from our fit; photon point is from PDG.

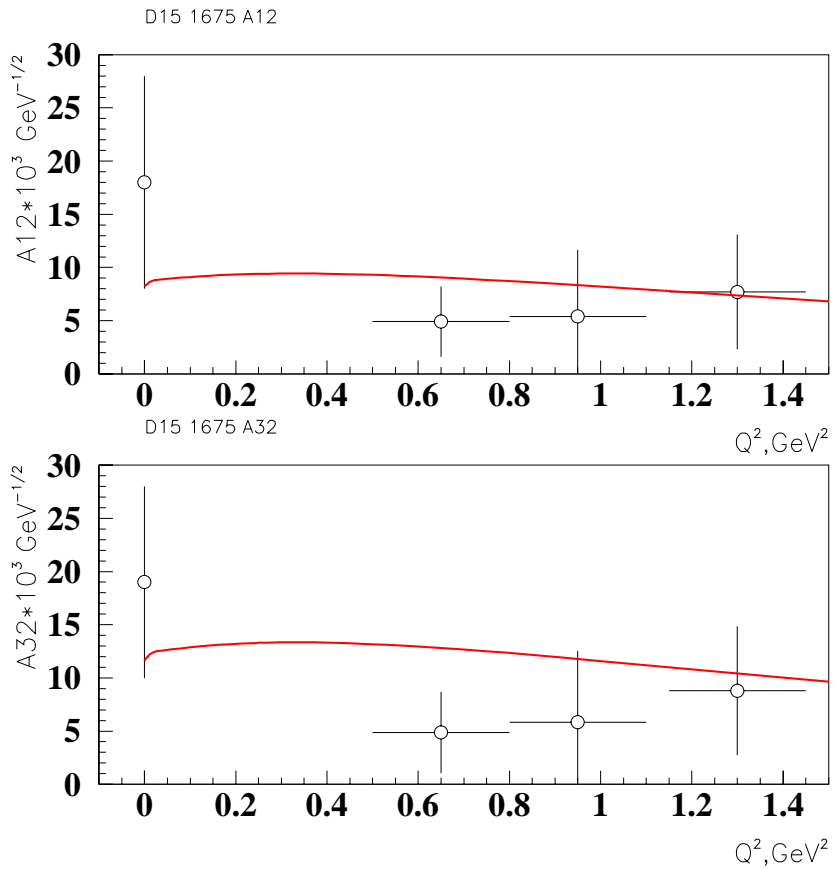


Figure 5.68: Photocouplings of $D_{15}(1675)$ as a function of Q^2 from our fit; photon point is from PDG.

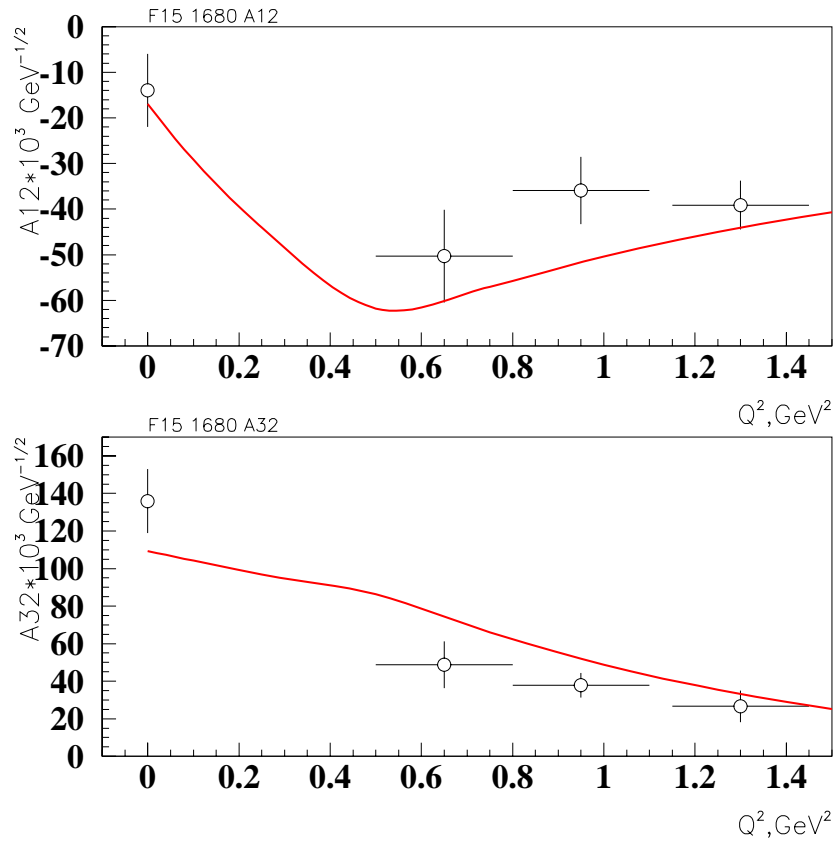


Figure 5.69: Photocouplings of $F_{15}(1680)$ as a function of Q^2 from our fit; photon point is from PDG.

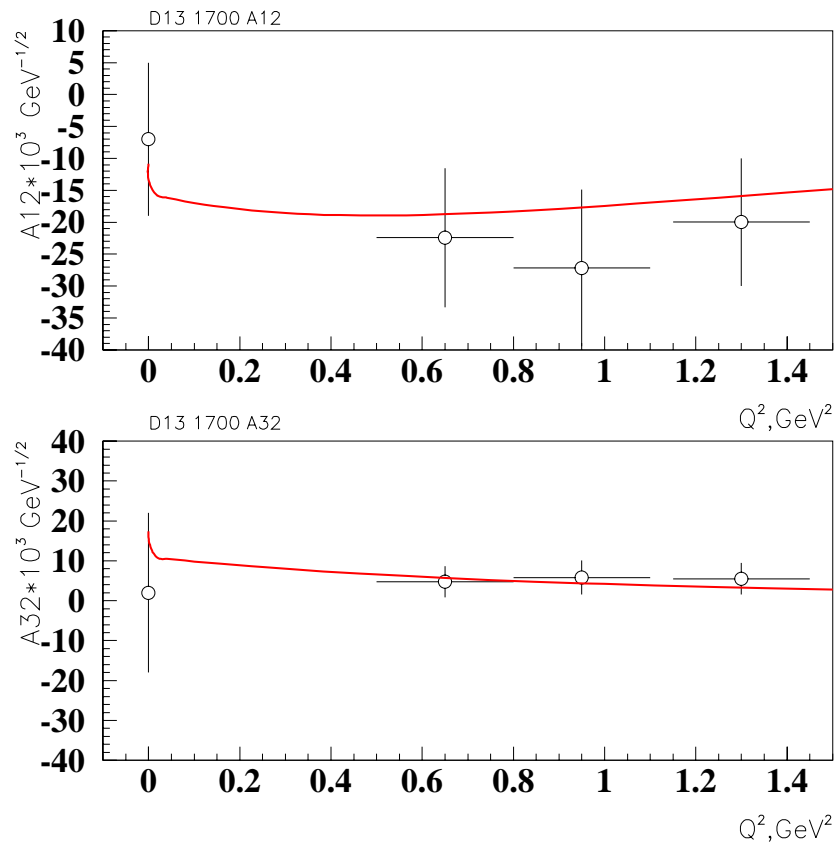


Figure 5.70: Photocouplings of $D_{13}(1700)$ as a function of Q^2 from our fit; photon point is from PDG.

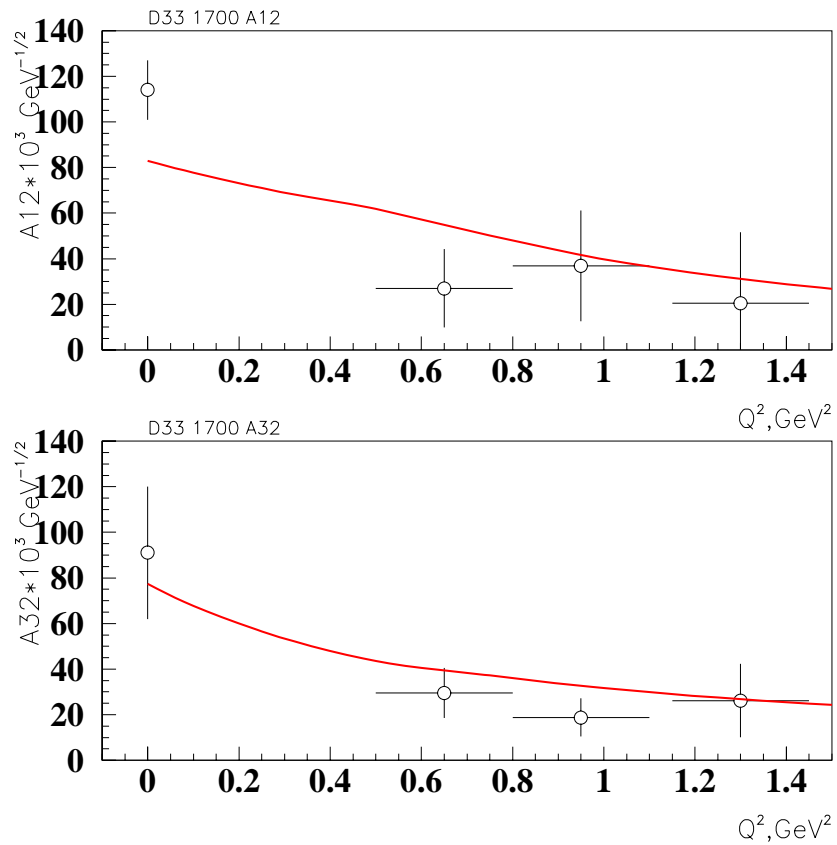


Figure 5.71: Photocouplings of $D_{33}(1700)$ as a function of Q^2 from our fit; photon point is from PDG.

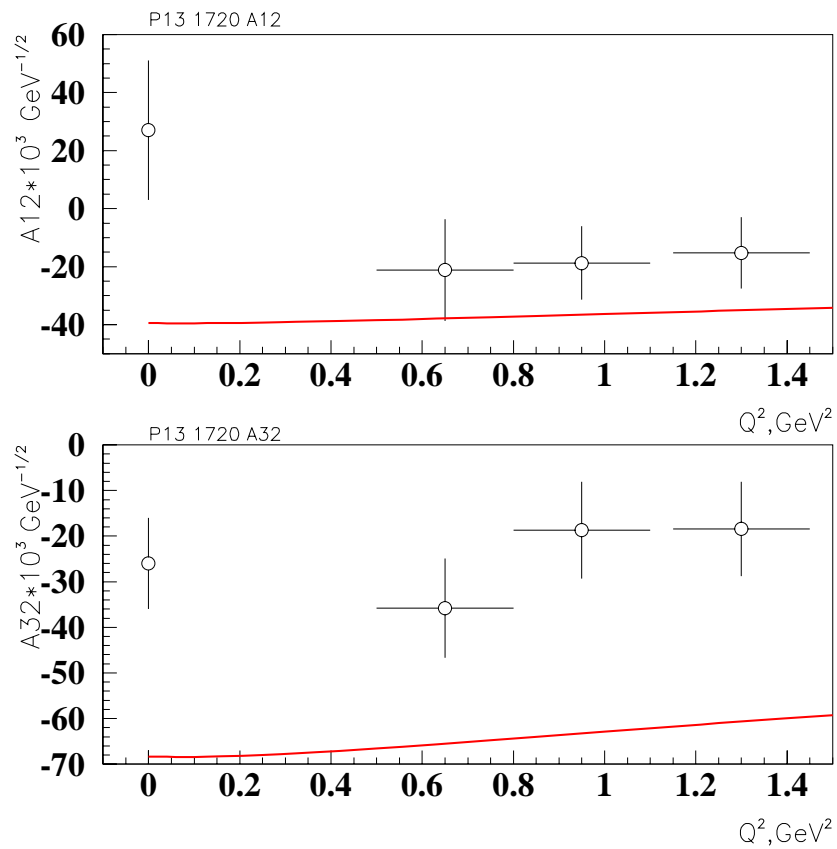


Figure 5.72: Photocouplings of conventional $P_{13}(1720)$ as a function of Q^2 from our fit; photon point is from PDG.

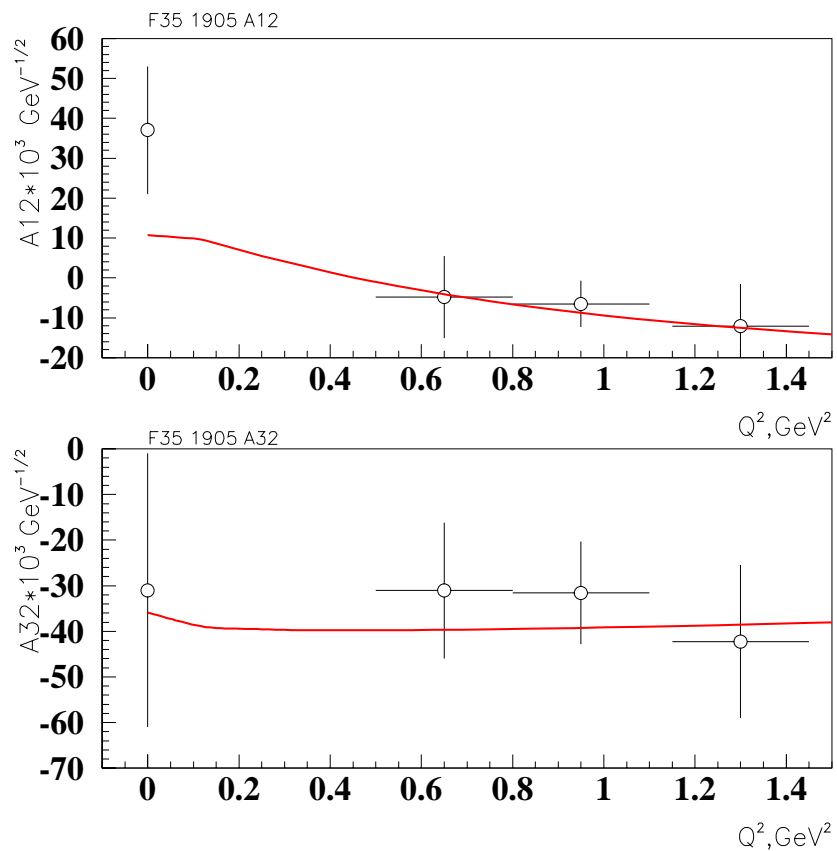


Figure 5.73: Photocouplings of conventional $F_{35}(1905)$ as a function of Q^2 from our fit; photon point is from PDG.

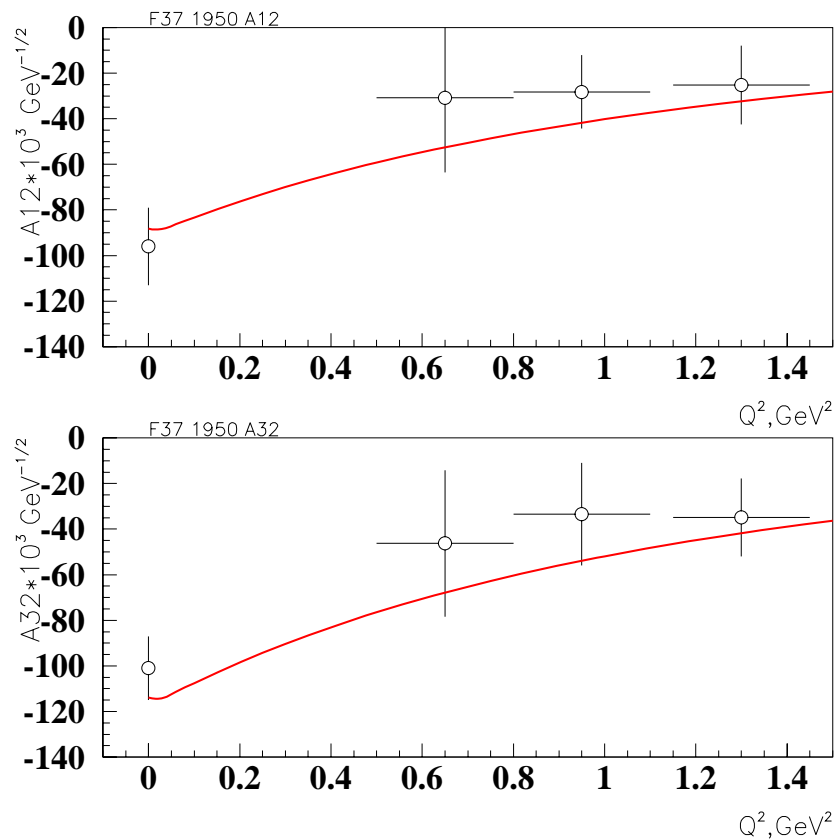


Figure 5.74: Photocouplings of conventional $F_{37}(1950)$ as a function of Q^2 from our fit; photon point is from PDG.

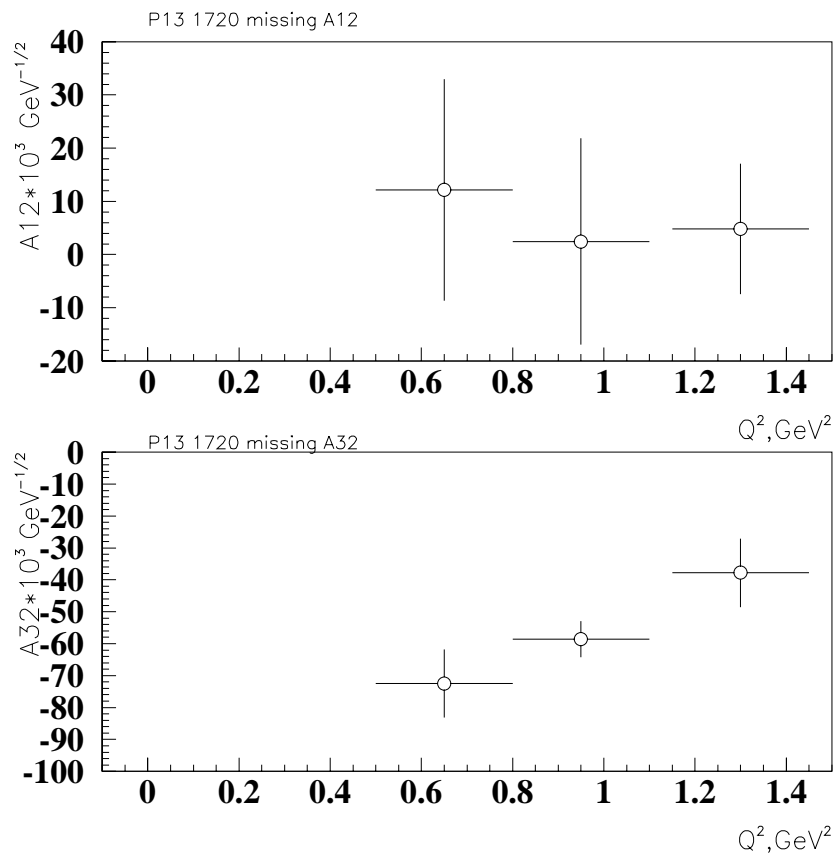


Figure 5.75: Photocouplings of MISSING $P_{13}(1720)$ as a function of Q^2 from our fit.

Table 5.14: Strong parameters for $P_{13}(1720)$ PDG state in S. Dytman's alternative hadronic fit.

| position (GeV) | total width (MeV) | Branching ratio $\pi\Delta$ | Branching ratio ρp |
|-------------------|----------------------|--------------------------------|-----------------------------|
| 1.851 | 545 | 50 % | 27 % |

5.2.1 Resonance Analysis: Further Work After Discussion within SoN Review Committee and Final Fits to be Reported in the Paper

A first comment from S. Dytman was that in the energy region around 1.7 GeV the reliability of hadronic fits may be questioned, due to a series of important effects, such as interference resonance-background, overlap of several states, etc. He suggested that different parameters for the specific $P_{13}(1720)$ state may be extracted, repeating his multichannel unitary fit with different assumptions about the $\Delta\pi$ final channel and the background. A thorough report of many steps of the discussion can be found in <http://www.jlab.org/Hall-B/secure/e1/ripani/review/>. Following this discussion, we therefore decided to repeat our fits under different assumptions, to test whether the alternative results found by Steve could be accommodated within the new CLAS data. Table 5.14 reports the alternative parameters in Steve's new hadronic fit. Our new fit was performed with the following conditions: no missing state; $D_{13}(1700)$ $A_{1/2,3/2}$ were fixed on NRQM predictions; a $P_{13}(1851)$ instead of the $P_{13}(1720)$ was used, according to table 5.14. The strong and electromagnetic couplings of all other states were fixed on our previous best solution without missing state. Variable parameters were $A_{1/2,3/2}$ for $P_{13}(1851)$. In figure 5.82 we report our best fit under the above mentioned conditions, for the total cross section as a function of W , at $Q^2 = 0.65$ GeV 2 . This is clearly not a good fit of the bump at 1.7 GeV, for the simple reason that only the alternative $P_{13}(1851)$ was allowed to float, whose mass is far above the observed bump. A similar situation occurs for $Q^2 = 0.95$ GeV 2 . Therefore, we again filled the gap between calculation and experimental data increasing the $D_{13}(1700)$ photocouplings; according to the discussion in section 2.0.6, this was the only possibility considering the characteristics of various states. In figure 5.83 we report the corresponding best fit under the above mentioned conditions, for the total cross section as a function of W , at $Q^2 = 0.65$ GeV 2 . A similar situation occurs for $Q^2 = 0.95$ GeV 2 . But again, angular distributions are not well described, as shown in figure 5.84.

From the above discussion about the uncertainties of previous hadronic analyses and the errors being perhaps too optimistic, we could conclude that fixing the $P_{13}(1720)$ strong couplings to the values of analysis [44] may not be appropriate. We therefore performed a fit of such resonance, removing the constraint on the partial wave decay branches. In this fit, only the $P_{13}(1720)$ was left floating, without introducing any additional (missing)

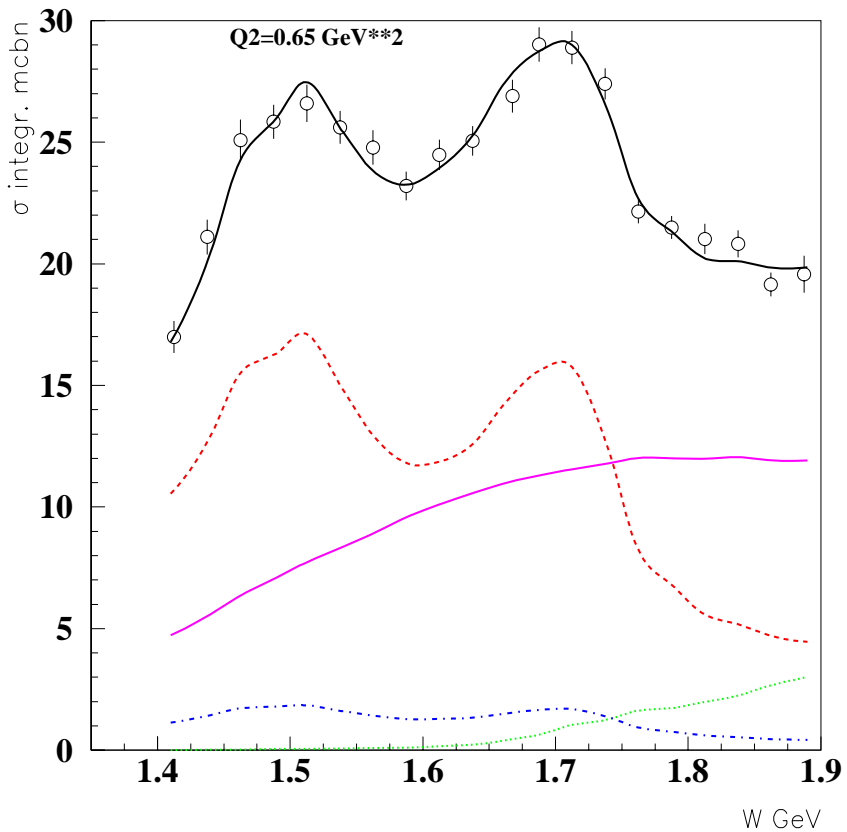


Figure 5.76: Separation between resonant and background contributions in our fit in comparison with CLAS data at $Q^2 = 0.65 \text{ GeV}^2$. Black full curve is the full calculation, dashed red curve is the $\pi^- \Delta^{++}$ contribution, blue dot-dashed curve is the $\pi^+ \Delta^0$, dotted green curve is the ρ meson contribution and finally the magenta full curve is the phase space amount.

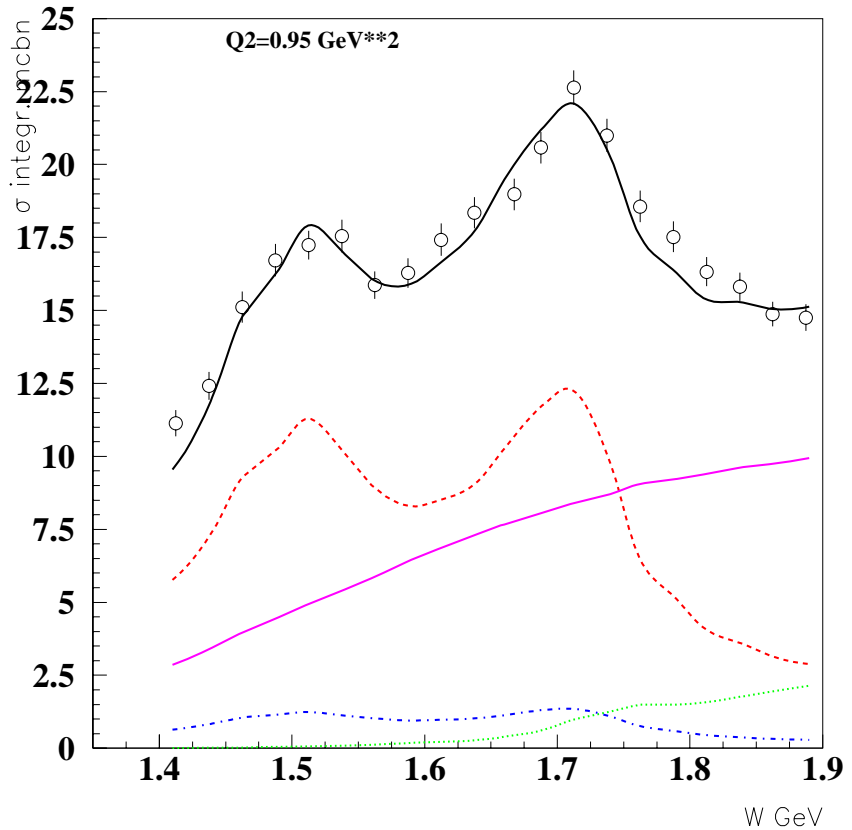


Figure 5.77: Separation between resonant and background contributions in our fit in comparison with CLAS data at $Q^2 = 0.95 \text{ GeV}^2$. Black full curve is the full calculation, dashed red curve is the $\pi^- \Delta^{++}$ contribution, blue dot-dashed curve is the $\pi^+ \Delta^0$, dotted green curve is the ρ meson contribution and finally the magenta full curve is the phase space amount.

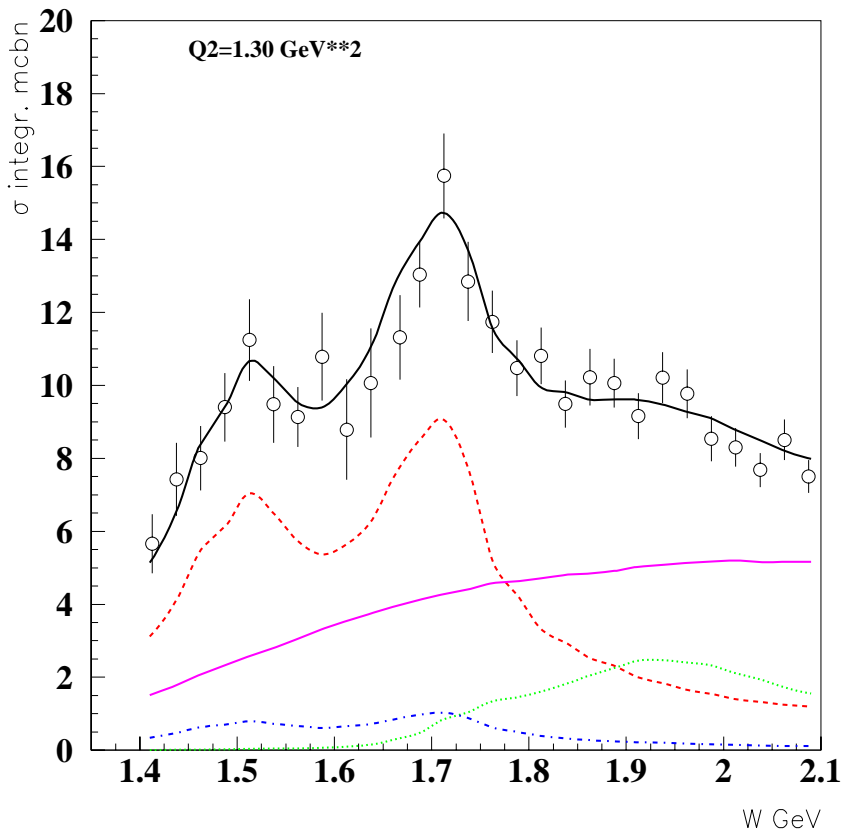


Figure 5.78: Separation between resonant and background contributions in our fit in comparison with CLAS data at $Q^2 = 1.3 \text{ GeV}^2$. Black full curve is the full calculation, dashed red curve is the $\pi^- \Delta^{++}$ contribution, blue dot-dashed curve is the $\pi^+ \Delta^0$, dotted green curve is the ρ meson contribution and finally the magenta full curve is the phase space amount.

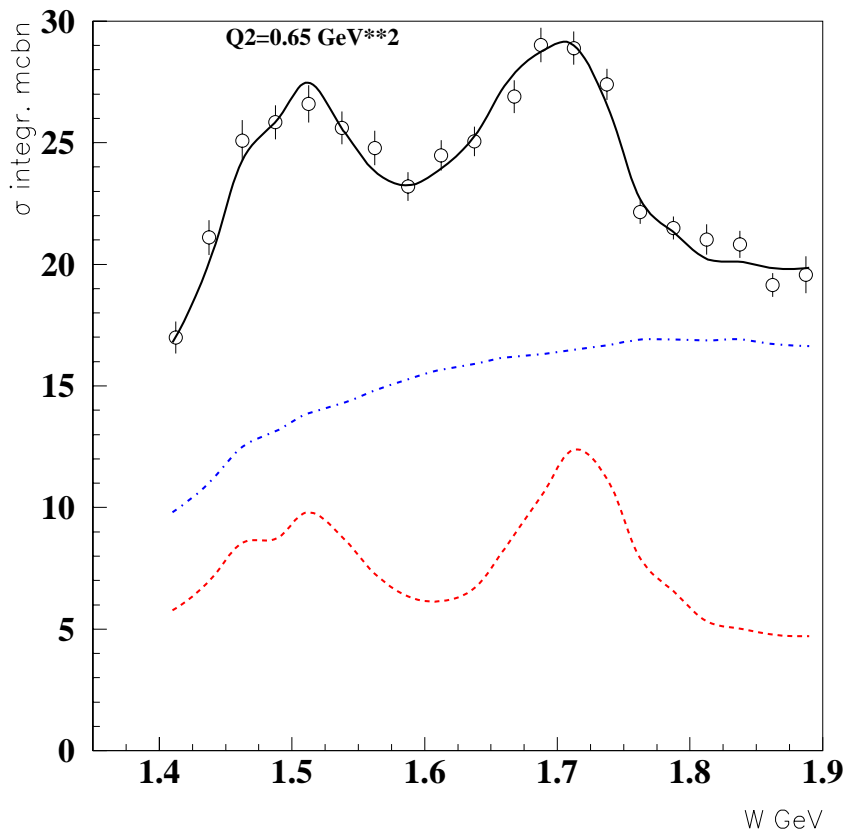


Figure 5.79: Separation between resonant and background contributions in our fit in comparison with CLAS data at $Q^2 = 0.65 \text{ GeV}^2$. Black full curve is the full calculation, blue dot-dashed curve represents the non-resonant contributions, while the dashed red curve is coming from resonant contributions only.

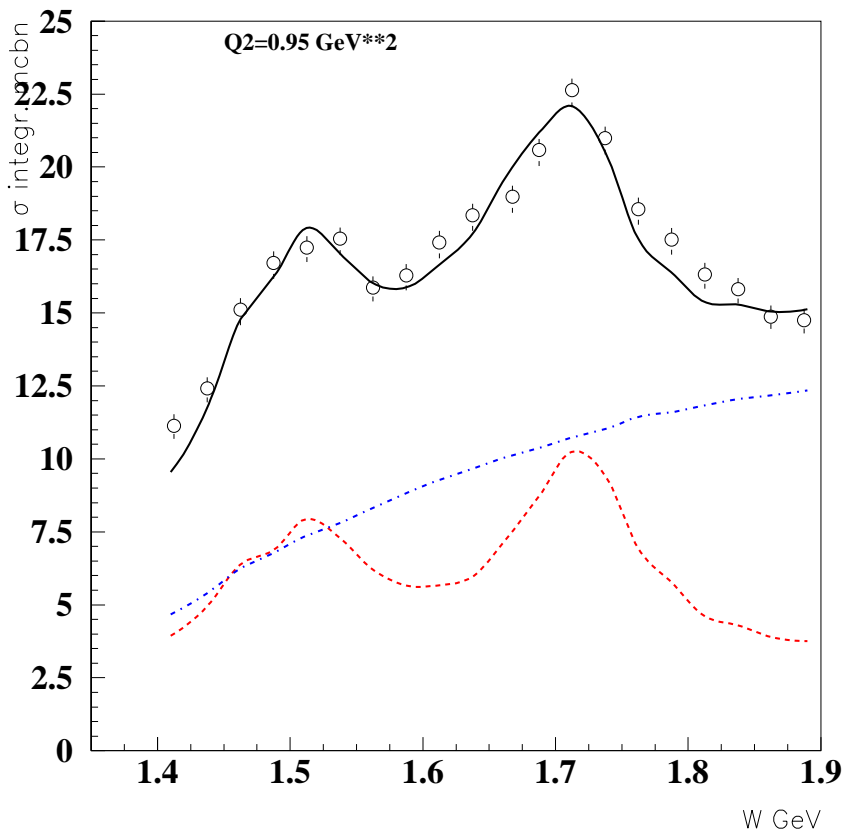


Figure 5.80: Separation between resonant and background contributions in our fit in comparison with CLAS data at $Q^2 = 0.95 \text{ GeV}^2$. Black full curve is the full calculation, blue dot-dashed curve represents the non-resonant contributions, while the dashed red curve is coming from resonant contributions only.

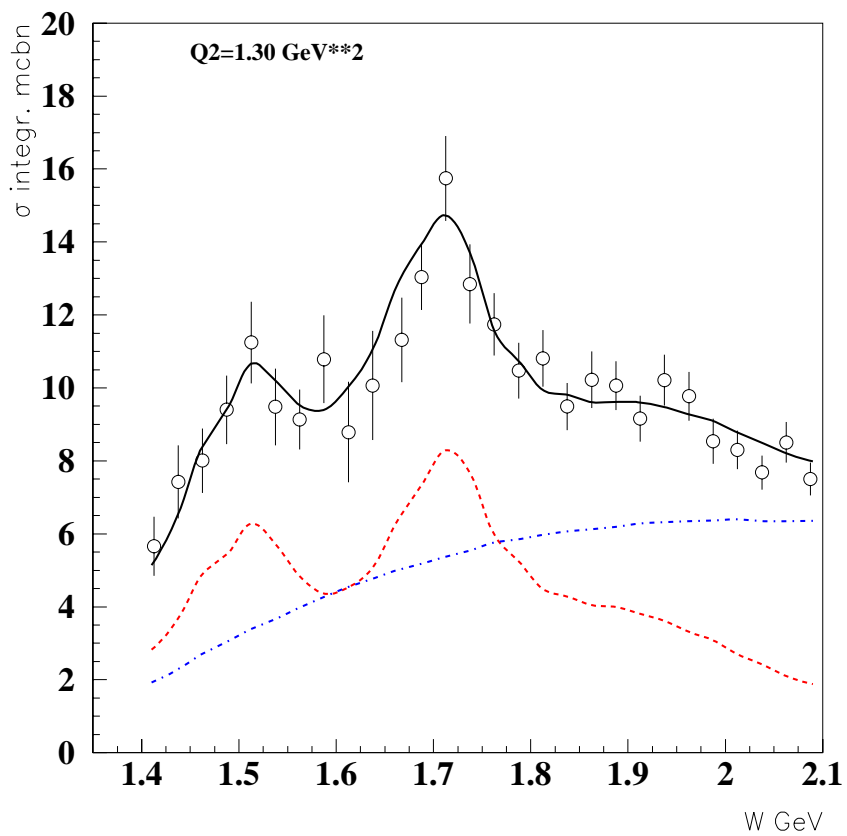


Figure 5.81: Separation between resonant and background contributions in our fit in comparison with CLAS data at $Q^2 = 1.3 \text{ GeV}^2$. Black full curve is the full calculation, blue dot-dashed curve represents the non-resonant contributions, while the dashed red curve is coming from resonant contributions only.

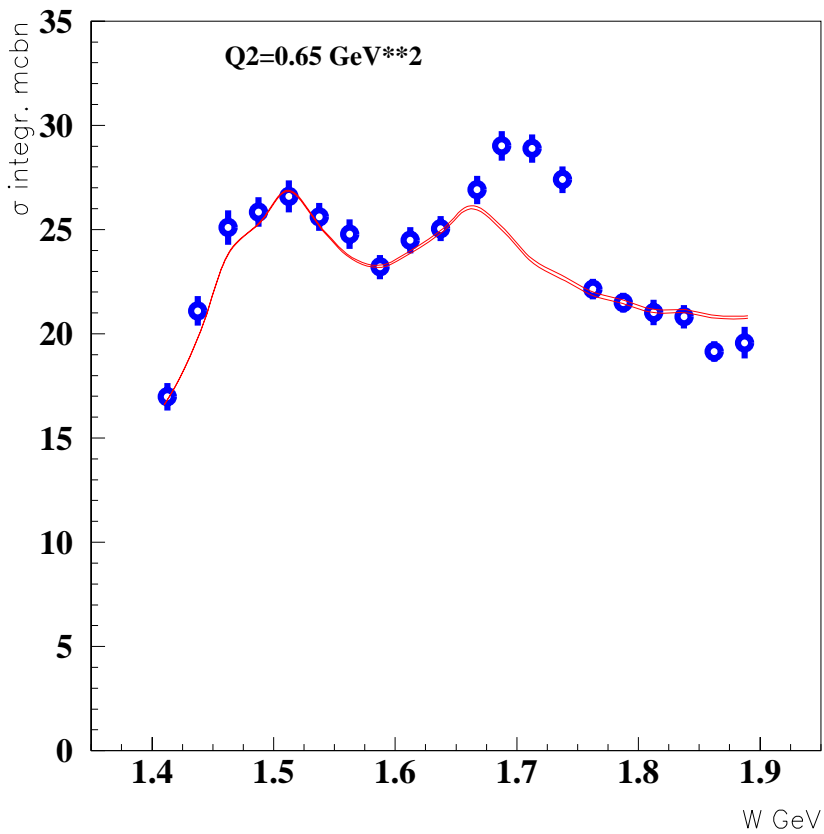


Figure 5.82: New fit of CLAS data at $Q^2 = 0.65 \text{ GeV}^2$. Red full curve is obtained fitting the conventional P_{13} state, assuming new parameters for it according to the alternative fit by Dytman and fixing all other states at previous values, while $D_{13}(1700)$ $A_{1/2,3/2}$ were fixed on NRQM predictions.

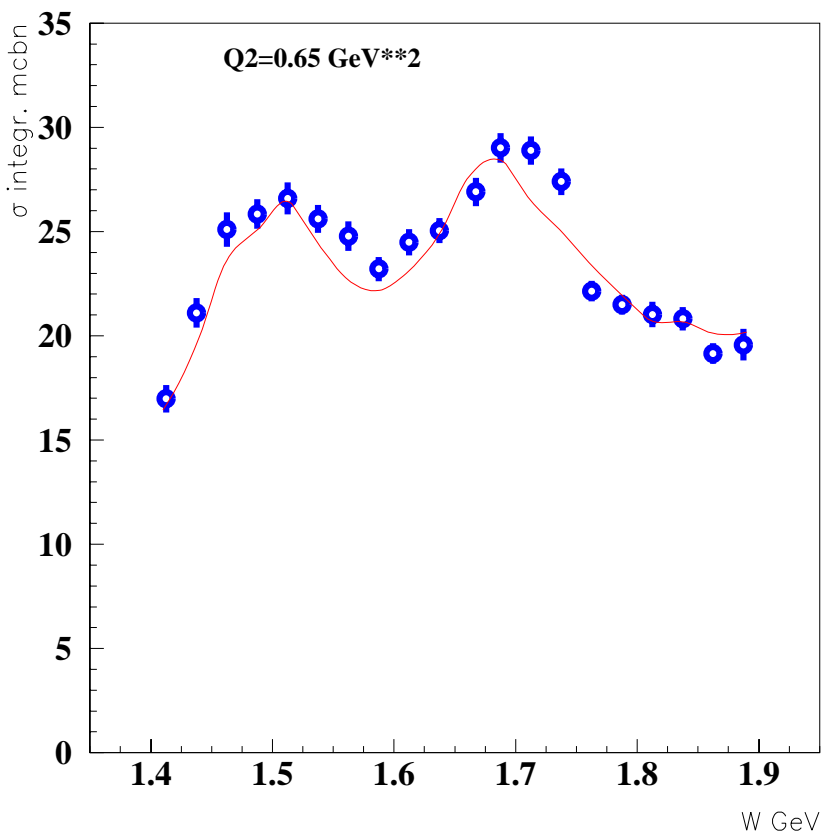


Figure 5.83: New fit of CLAS data at $Q^2 = 0.65 \text{ GeV}^2$. Red full curve is obtained fitting the conventional P_{13} state, assuming new parameters for it according to the alternative fit by Dytman and fixing all other states at previous values, while $D_{13}(1700)$ $A_{1/2,3/2}$ were increased to reproduce the bump.

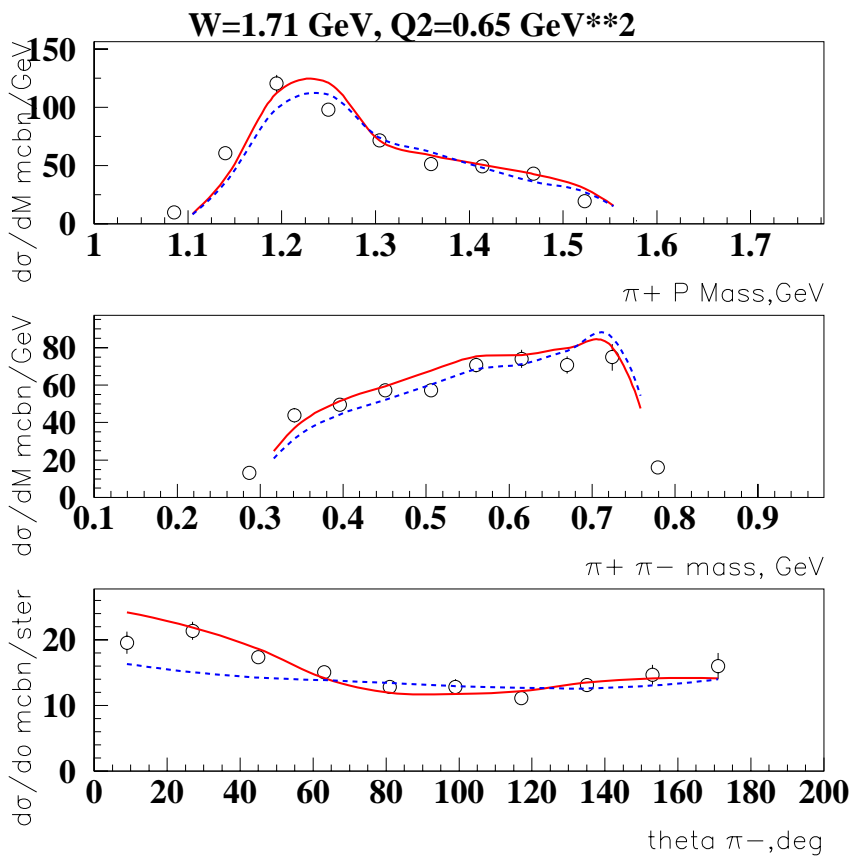


Figure 5.84: New fit of CLAS data at $Q^2 = 0.65 \text{ GeV}^2$. Blue dashed curve is obtained fitting the conventional P_{13} state, assuming new parameters for it according to the alternative fit by Dytman and fixing all other states at previous values, while $D_{13}(1700)$ $A_{1/2,3/2}$ were increased to reproduce the bump. Red full curve is the previous fit with a missing P_{13} .

Table 5.15: PDG $P_{13}(1720)$ parameters when fitting the bump in CLAS data at 1.7 GeV with this state only (B) and new resonance parameters when fitting the bump with a new state (C).

| | mass (MeV) | Γ (MeV) | $\Gamma_{\pi\Delta}/\Gamma$ (%) | $\Gamma_{\rho N}/\Gamma$ (%) |
|------------------|---------------|---------------------|------------------------------------|---------------------------------|
| PDG P_{13} (B) | 1725 ± 20 | $114 \pm 19 \pm 28$ | $63 \pm 12 \pm 15$ | $19 \pm 9 \pm 14$ |
| PDG[32] | 1650-1750 | 100-200 | absent | 70-85 |
| new P_{13} (C) | 1720 ± 20 | $88 \pm 17 \pm 24$ | $41 \pm 13 \pm 20$ | $17 \pm 10 \pm 13$ |

state. Results of this fit are reported in figure 5.85 for the total cross section, while figure 5.85 shows differential cross sections for two W bins at $Q^2 = 0.65$ GeV 2 . It is clear how again a "free" P_{13} resonance (but with a mass still around 1.72 GeV) can fit the data with practically the same quality of the missing resonance fit. The resulting values for the branching fractions were significantly different from previous analyses reported in the literature[32, 44, 45], well outside the reported errors. Table 5.15 shows our results (first row) with statistical (first) and systematic uncertainties (second), in comparison with PDG values. Uncertainties on resonance positions are purely statistical as this parameter is not influenced by systematic errors in data. In Table 5.16 (first three rows) we report the corresponding $A_{1/2,3/2}$ values for the $P_{13}(1720)$ fit, in comparison with SQTM predictions; the first error is a combination of statistical uncertainties in the data and correlations among different resonances; the second error is based on systematics. Resonance parameters and $A_{1/2,3/2}$ values obtained for the new state are reported in Table 5.15 (last row) and 5.16 (last three rows), respectively. As general procedure, the systematic error on the strong parameters was obtained varying them by almost 100 %, then retaining all curves in the total cross section calculation that were overlapping to the data band corresponding namely to the systematic error (this procedure is similar to the one adopted to evaluate statistical errors on the photocouplings in section 2.1). In the case of the systematic error on the photocouplings, we varied all N^* 's and Δ 's photocouplings and then we retained all curves in the total cross section calculation that were overlapping to the data band corresponding namely to the systematic error.

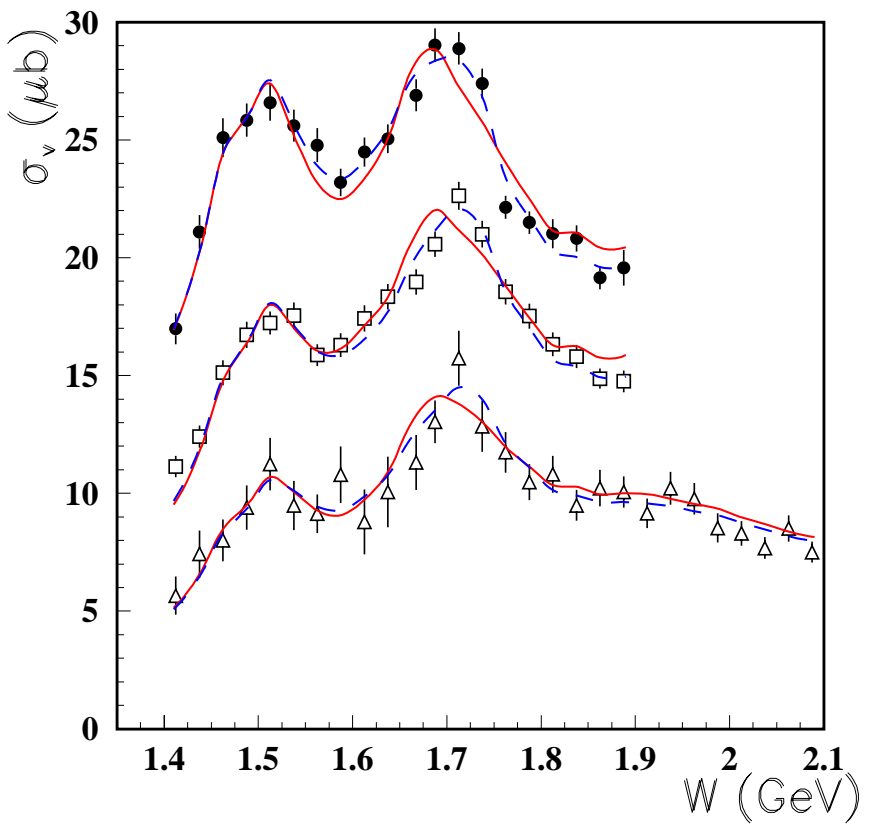


Figure 5.85: Fit of CLAS data at all Q^2 . Blue dashed curve is obtained fitting the conventional P_{13} state, leaving the strong decay couplings to float as well, while all other states were fixed at previous values. Red full curve is the previous fit with the conventional $D_{13}(1700)$.

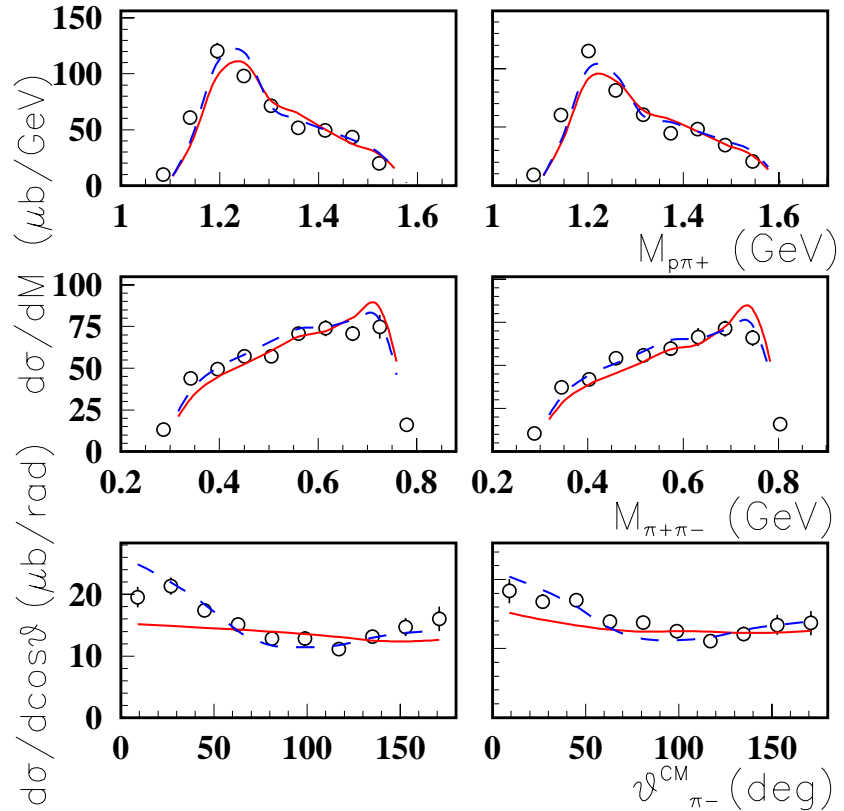


Figure 5.86: Fit of CLAS data at $Q^2=0.5\text{-}0.8 \text{ GeV}^2$, $W=1.7\text{-}1.725 \text{ GeV}$ (left) and $W=1.725\text{-}1.750 \text{ GeV}$ (right), differential in (top to bottom): $p\pi^+$ invariant mass; $\pi^+\pi^-$ invariant mass; π^- angle θ . Curves (see text) where obtained fitting the 1.7 GeV bump with the $D_{13}(1700)$ (full) or the $P_{13}(1720)$ with free strong decay couplings (dashed line).

Table 5.16: PDG $P_{13}(1720)$ photocouplings from fit (B) (first three rows) in comparison with SQTM predictions[43] and new state photocouplings from fit (C) (last three rows) (see caption in previous table for definitions of (B) and (C)).

| Q^2 (GeV^2/c^2) | $A_{1/2}$ ($\frac{10^{-3}}{\sqrt{GeV}}$) (our fit) | $A_{3/2}$ ($\frac{10^{-3}}{\sqrt{GeV}}$) (our fit) | $A_{1/2}$ ($\frac{10^{-3}}{\sqrt{GeV}}$) (SQTM) | $A_{3/2}$ ($\frac{10^{-3}}{\sqrt{GeV}}$) (SQTM) |
|--------------------------|--|--|---|---|
| 0.65 | $2 \pm 21 \pm 27$ | $-83 \pm 5 \pm 10$ | 65 | -38 |
| 0.95 | $3 \pm 29 \pm 33$ | $-63 \pm 8 \pm 11$ | 63 | -37 |
| 1.30 | $2 \pm 12 \pm 13$ | $-45 \pm 27 \pm 27$ | 61 | -35 |
| 0.65 | $15 \pm 25 \pm 29$ | $-74 \pm 8 \pm 9$ | | |
| 0.95 | $12 \pm 20 \pm 20$ | $-53 \pm 6 \pm 6$ | | |
| 1.30 | $3 \pm 14 \pm 14$ | $-41 \pm 18 \pm 18$ | | |

Chapter 6

Conclusions

The Genova-Moscow phenomenological model of double charged pion production by real and virtual photons was used to extract N^* electromagnetic form factors and possible signals from missing baryon states from E-93-006 CLAS Collaboration data.

The Q^2 dependence of $A_{1/2,3/2}$ form factors for 12 baryon states were extracted from the CLAS data fit. For the first time, data on Q^2 dependence for many high-lying N^* 's electromagnetic form factors ($M > 1.6$ GeV) were obtained.

For all states, apart from $P_{13}(1720)$, the extracted values of $A_{1/2,3/2}$ form factors deviate from SQTM predictions by not more than 30%, while correct reproduction of $\pi\pi$ invariant mass distributions imposes a strong reduction of $P_{13}(1720)$ state electromagnetic excitation strength (factor 2-3 in amplitude): it could be an indication of peculiar features in the structure of this state.

The bump around 1.7 GeV in W , observed in total cross section as a function of W at all Q^2 was described in three different assumptions:

1. sizeable enhancement of $D_{13}(1700)$ conventional state (factor 2-3 in amplitude) with respect to Non-Relativistic Quark Model predictions;
2. sizeable enhancement of $P_{13}(1720)$ conventional state (factor 2-3 in amplitude) with respect to Single Quark Transition Model predictions; moreover, the decay branches of this state to $\Delta\pi$ and ρp had to be significantly modified with respect to previous hadronic analysis and to PDG itself;
3. implementing a missing baryon state, whose most probable quantum numbers seem to correspond again to a P_{13} state, but with a strong decay pattern drastically different from the conventional $P_{13}(1720)$ state

Both the modified $P_{13}(1720)$ and the missing baryon state hypothesis provide a systematically better description of cross sections (in particular angular distributions). Our comparative analysis of quantum numbers shows indeed a preference for the P_{13} assignment. Further data on single and multimeson reactions with electromagnetic and hadronic probes may help to make definitive conclusions.

Bibliography

- [1] Particle Data Group, 1998
- [2] R. Koniuk and N. Isgur, Phys. Rev. Lett. 44, 845(1980); Phys. Rev. D21, 1868(1980)
- [3] M.M. Giannini, Rep. Prog. Phys., 54, 453(1990)
- [4] R. Koniuk, Nucl. Phys. , B195 , 452(1982)
- [5] S. Capstick, W. Roberts, Phys. Rev. D49, 4570(1994)
- [6] F. Stancu and P Stassart, Phys. Rev. D47, 2140(1993)
- [7] K.F. Liu and C.W. Wong, Phys. Rev. D28, 170(1983)
- [8] Cambridge Bubble Chamber Group, Phys. Rev., 155, 1477(1967); ABBHHM Collaboration, Phys. Rev., 175, 1669 (1968); D. Lüke and P. Söding - Springer Tracts in Mod. Phys. - 59 (1971)
- [9] A. Piazza et al. , Lettere al nuovo cimento, Vol. III N. 12, 403 (1970)
- [10] V. Eckart et al. , Nucl. Phys. B55, 45 (1973); P. Joos et al., Phys. Lett., B52, 481 (1974); K Wacker et al., Nucl. Phys., B144, 269 (1978)
- [11] A. Braghieri et al., Phys.Lett. B363, 46(1995)
- [12] B. Krusche, Proceedings of Workshop on "N* Physics and Nonperturbative Quantum Chromodynamics, Trento 18-29 May 1998, Few Body Suppl.11, (1999) 284
- [13] F. J. Klein, Bonn University thesis BONN-IR-96-08.
- [14] Byckling and Kajantie, Particle kinematics, Wiley and Sons (1973)
- [15] H.M. Pilkuhn, Relativistic Particle Physics, Springer Verlag (1979)
- [16] K. Egiyan, CLAS-NOTE 99-007 (1999)
- [17] L.W. Mo, Y.S. Tsai, Rev. Mod. Phys. 41, 205(1969)

- [18] W. Brooks, private communication
- [19] ABBHHM Collaboration, Phys. Rev. 175, (1968) 1669
- [20] L.Y. Murphy, J.M. Laget, DAPNIA-SPHN-96-10, Mar. 1996
- [21] J.C. Nacher, Proceedings of the Workshop "NSTAR 2001: the Physics of Excited Nucleons", Mainz, March 2001, World Scientific, eds. D. Drechsel and L. Tiator, and references therein
- [22] A. Thomas, Proceedings of the Workshop "NSTAR 2001: the Physics of Excited Nucleons", Mainz, March 2001, World Scientific, eds. D. Drechsel and L. Tiator
- [23] K. Ochi, M. Hirata, T. Takaki, Phys. Rev., C56, 1472(1997)
- [24] Y. Oh, Proceedings of the Workshop "NSTAR 2001: the Physics of Excited Nucleons", Mainz, March 2001, World Scientific, eds. D. Drechsel and L. Tiator
- [25] Q. Zhao, Proceedings of the Workshop "NSTAR 2001: the Physics of Excited Nucleons", Mainz, March 2001, World Scientific, eds. D. Drechsel and L. Tiator
- [26] M. Vanderhaeghen et al., unpublished
- [27] M. Ripani et al., Nucl. Phys. A 672 (2000) 220; M. Ripani et al., Physics of Atomic Nuclei, Vol. 63, N. 11 (2000) 1943; V.I. Mokeev et al., Phys. Atom. Nucl. 64, (2001) 1292
- [28] V. Mokeev et al., Proceedings of the Workshop "NSTAR 2001: the Physics of Excited Nucleons", Mainz, March 2001, World Scientific, eds. D. Drechsel and L. Tiator, and references therein
- [29] V.D.Burkert, Nucl. Phys. A663–A664 29c (2000); M.Ripani, ibid., 675c
- [30] R.R.Longacre, J.Dolbeau, Nucl. Phys., B122 493 (1977)
- [31] M.Anghinolfi e.a. Phys. of Atom. Nucl. 62 1552 (1999)
- [32] D.E. Groom et al., Eur. Phys. J. C15, 1 (2000)
- [33] D.G.Cassel et al, Phys. Rev., D24 787 (1981)
- [34] D.Lüke, P.Söding, Springer Tracts in Mod. Phys. 59 (1971)
- [35] C.J.Bebek, et. al. Phys. Rev., D17 1693 (1978)
- [36] R.Machleidt in Advances in Nuclear Physics 19 (1979)
- [37] M.Guidal et al., Phys. Lett., B400 6 (1997)

- [38] V.Mokeev, M.Osipenko, Bull. Moscow State Univ. 3 14 (1999)
- [39] M. Ripani et al., Analysis note on “Procedures for the Analysis of the Two Pion Electroproduction Data from CLAS”
- [40] V. Burkert, private communication
- [41] V. Burkert, in Proceedings of PANIC '99, Uppsala, Sweden, 10-16 June 1999, published in Nucl. Phys. A663&664 and CLAS collaboration contributed papers therein
- [42] W. Brooks, in Proceedings of PANIC99, Uppsala, Sweden, 10-16 June 1999, published in Nucl. Phys. A663&664
- [43] V. D. Burkert, Czech. Journ. of Phys., Vol.46, 627(1996)
- [44] D.M.Manley, E.M.Salesky, Phys. Rev. D45, 4002(1992)
- [45] T.P. Vrana et al, Phys.Rept.328, 181(2000)
- [46] V. Burkert, Nucl. Phys. A684, 16(2001)
- [47] S. Capstick et al., Phys.Rev.C59, 3002(1999)
- [48] S. Capstick, private communication
- [49] P. Page in Proceedings of the Workshop ”NSTAR 2000: Excited Nucleons and Hadronic Structure”, Jefferson Lab, February 2000, World Scientific, eds. V. Burkert, L. Elouadrhiri, J. Kelly and R. Minehart
- [50] M. Giannini, E. Santopinto, private communication
- [51] V. Burkert, M. Ripani, JLAB experiment E-99-108